Processing, Microstructure and Mechanical Behavior of Medium Manganese Steels

Binhan Sun

Department of Mining and Materials Engineering McGill University, Montreal

November 2017



A thesis submitted to McGill University in partial fulfillment of the requirements of the degree of Doctor of Philosophy

© Binhan Sun, 2017 All Rights Reserved

ABSTRACT

Developing high strength steels has received increasing attention in steel industry, in order to meet the body-in-white weight reduction strategies pursued by the automotive industry for fuel economy and vehicle safety. In this context, medium manganese (Mn) steels containing 3 to 12 wt.% Mn are one of the strong candidates for the so-called third-generation advanced high-strength steels (AHSS), due to the superior mechanical properties exceeding the first-generation AHSS and the potentially lower cost compared to the high Mn second-generation AHSS. The ultrafine grain size and high fraction of retained austenite, adjustable to various TRIP (transformation-induced plasticity) and/or TWIP (twinning-induced plasticity) effects, constitute the key advantages of this group of steels. This thesis aims to develop a better understanding of the processing-microstructure-property relationship of medium Mn steels with Al and Si additions.

Four experimental steels with compositions of Fe-0.2C-(7~10)Mn-3Al-(0~3)Si (in wt.%) were designed and examined. The phase transformation behavior, with respect to austenite formation and decomposition, of two hot rolled samples with 3 wt.% Al and 3 wt.% Si during intercritical annealing was firstly investigated to develop a better understanding of microstructural control for such steels. The microstructure of the leaner alloy with 7 wt.% Mn was substantially influenced by the annealing temperature, whereas the richer variant 10 wt.% Mn steel exhibited a stable ferrite-austenite duplex microstructure containing a fixed amount of retained austenite, which was found to be independent of the variations of annealing temperature. From these results, controlled annealing was performed for these two hot rolled samples, followed by a further processing by subjecting them to cold rolling and examining the microstructural evolution during cold rolling. Strain partitioning, between austenite and ferrite, and deformation twinning of austenite were found to critically influence the cold rollability of the two steels. Finally, the deformation and fracture mechanisms of the cold rolled and intercritical annealed medium Mn steels were studied, with particular emphasis on the effect of different Si additions (0~3 wt.%).

Results showed that the mechanical property of the steels critically depended on the austenite fraction, TRIP and TWIP effect activated in austenite, as well as the strain partitioning between austenite and ferrite during deformation. The fracture mechanisms altered with different Si levels, which can change from dimpled-type fracture driven by void formation, mainly at the ferrite/strain-induced α' -martensite interfaces, to a combined dimple and cleavage/quasicleavage fracture, which was related to the brittle δ -ferrite in high Si alloys. The work also revealed a strong correlation between strain-induced martensite formation and the serrated plastic flow phenomenon associated with the Portevin-Le Chatelier effect (PLC) effect. Discontinuous behavior of strain-induced transformation was observed, which was due to the localized martensite formation within the PLC bands nucleating intermittently and propagating continuously during tensile straining.

RESUME

Le développement d'aciers à haute résistance a reçu une attention croissante dans l'industrie sid érurgique en vue des stratégies de réduction de poids recherchées par l'industrie automobile pour l'économie de carburant et la sécurité des véhicules. Dans ce contexte, les acier à teneur moyenne en mangan èse (Mn) contenant de 3 à 12 m% de mangan èse sont des candidats d'intérêt pour les aciers à haute résistance dits de troisième génération (AHSS), ceci grâce à leurs propri étés mécaniques supérieures excédant celles des AHSS de première génération mais aussi grâce aux coûts potentiellement plus faibles comparés aux AHSS de deuxième génération à haut taux de Mn. Les grains ultrafins et les hauts taux d'austénite résiduelle, accordables à divers effets TRIP (plasticité induite par transformation) et / ou TWIP (plasticité induite par jumelage), constituent les avantages clés de ce groupe d'aciers. L'objectif de cette thèse est de développer une meilleure compréhension de la relation procédé-microstructure-propriétés des aciers à teneur moyenne en Mn avec comme additifs Al et Si.

Quatre aciers expérimentaux de compositions Fe-0.2C-(7~10)Mn-3Al-(0~3)Si (en m.%) ont été fabriqués et analysés. Le comportement de transformation de phase, en ce qui concerne la formation et la décomposition de la phase austénitique, de deux échantillons laminés à chaud avec 3 m.% d'Al et 3 m.% de Si au cours du recuit intercritique a été d'abord investigué pour développer une meilleure compréhension du contrôle microstructural de tels aciers. La microstructure de l'alliage le plus pauvre avec 7 m.% de Mn a été influencé sensiblement par la température de recuit, alors que la variante la plus riche avec 10 m.% de Mn présentait une microstructure stable en duplex ferrite-austénite contenant une quantité fixe d'austénite résiduelle, qui s'est avérée indépendante des variations des températures de recuit. A partir de ces résultats, un recuit contrôlé a été appliqué à ces deux échantillons laminés à chaud, suivi par un procédé de laminage à froid durant lequel l'évolution microstructurale a été observée. La répartition des contraintes, entre austénite et ferrite, et la déformation de mâclage de l'austénite ont un rôle critique sur la capacité de laminage à froid de ces deux aciers. Enfin, le

comportement de d'éormation et les mécanismes de rupture des aciers àteneur moyenne en Mn ayant subi un recuit intercritique laminés à froid ont été étudiés, en tenant compte plus particulièrement de l'effet des différents taux de Si (0~3 m.%). Les résultats ont montréque les propriétés mécaniques des aciers dépendent de manière critique du taux d'austénite, des effets TRIP et TWIP activés dans l'austénite, ainsi que de la répartition des contraintes entre les phases d'austénite et de ferrite durant la déformation. Les mécanismes de fracture altérés avec différents taux de Si, peuvent être modifiés à partir d'une fissure en cupules due à la formation de pores, principalement aux interfaces martensitique alpha' de transformation caus ét par la ferrite, ou à partir d'une combinaison de fissures en cupule et clivage/quasi-clivage, li ét à la phase de ferrite-delta dans les alliages à haut taux de Si. Ce travail a également d'émontré une corr dation entre la formation de martensite induite par la d'éormation et les phénomènes de flux de matière plastique dentelée associé à l'effet Potevin-Le Chatelier (PLC). Un comportement discontinu de transformation induite par la d'éormation a étéobserv é, d'û à la formation localis ét de martensite au sein des bandes de PLC à la nucl éation par intermittence et à la propagation continue au cours de la traction.

PREFACE

This thesis is compiled using a manuscript-based format, as prescribed by the thesis preparation guidelines of McGill University. The following research articles are included as Chapters 3, 4, 5, and 6 in this thesis, respectively.

- 1. Binhan Sun*, Fateh Fazeli, Colin Scott and Stephen Yue, "Phase transformation behavior of medium manganese steels with 3 wt pct aluminum and 3 wt pct silicon during intercritical annealing", Metall. Mater. Trans. A, 47 (2016), 4869-4882.
- 2. Binhan Sun*, Fateh Fazeli, Colin Scott, Xiaojun Yan, Zhiwei Liu, Xiaoyu Qin and Stephen Yue, "Critical role of strain partitioning and deformation twinning on cracking phenomenon occurring during cold rolling of two duplex medium manganese steels", Scripta Mater., 130 (2017), 49-53.
- 3. Binhan Sun*, Fateh Fazeli, Colin Scott, Nicolas Brodusch and Stephen Yue, "On the deformation and fracture mechanisms of austenite-ferrite duplex medium manganese steels with different silicon additions", to be submitted to Acta Mater., 2017.
- 4. Binhan Sun*, Nicolas Vanderesse, Fateh Fazeli, Colin Scott, Jianqiang Chen, Philippe Bocher, Mohammad Jahazi, Stephen Yue, "Discontinuous strain-induced martensite transformation related to the Portevin-Le Chatelier effect in a medium manganese steel", Scripta Mater., 133 (2017), 9-13.

Author contributions: Binhan Sun designed the alloys, developed the idea for experiments, conducted the main experiments, analyzed the main results and wrote the manuscripts, for all the four articles. Prof. Stephen Yue, actively supervised the research. Dr. Fateh Fazeli and Dr. Colin Scott in CanmetMATERALS, Natural Resources Canada, performed the ingot casting and

rolling, and conducted Thermo-Calc calculation in **Article 1.** They were also actively involved in the discussion of all the results and revised all the manuscripts. Prof. Xiaojun Yan, Mr. Zhiwei Liu and Mr. Xiaoyu Qin in School of Energy and Power Engineering, Beihang University were involved in setting up the *in situ* SEM tensile testing in **Article 2.** In **Article 3**, Mr. Nicolas Brodusch provided assistance in conducing EDX mapping and analyzing the EDX data. The work in **Article 4** was conducted with collaborations with Prof. Mohammad Jahazi and Prof. Philippe Bocher in Department of Mechanical Engineering, École de Technologie Sup érieure. Their postdocs, Dr. Nicolas Vanderesse and Dr. Jianqiang Chen, were involved in setting up the DIC experiments in **Article 4**, and Dr. Nicolas Vanderesse provided the code for analyzing the DIC data.

One additional journal article has been published during the Ph.D. study; it is related to this research but not included in the main chapters. The abstract is provided in **Appendix B**, and the information for this article is shown below:

 Binhan Sun*, Huseyin Aydin, Fateh Fazeli, Stephen Yue, "Microstructure evolution of a medium manganese steel during thermomechanical processing", Metall. Mater. Trans. A, 47 (2016), 1782-1791.

ACKNOWLEDGEMENTS

The journey of the doctoral study has brought me so much happiness that I almost did not feel time flying. The accompany of so many great people certainly constitutes one important part of the happiness, and that is truly fortunate for me. Firstly, I would like to express my sincerest gratitude to my supervisor, Prof. Stephen Yue, who is a person with true wisdom. During my study, he provided me an unremitting support, a high level of trust and a great extent of freedom, which truly motivated my innovations. I have learnt several great qualities from him; these qualities make me not only a better researcher, but also a better person. I could not have imagined having a better supervisor and mentor for my Ph.D study.

I would like to offer my sincere gratitude to Dr. Fateh Fazeli and Dr. Colin Scott from CanmetMATERALS, Natural Resources Canada, for their kind help for my experiment, weekly stimulating discussions and insightful comments on my results, and encouragement for my future career. I would like to thank Dr. Huseyin Aydin, who is a past postdoctoral in our group and a precursor for my research topic. His kind help on both research and communication let me get used to the new research environment more easily.

I would like to thank all my colleagues in my group and other groups of the department for all the technical help for my research. I also appreciate Prof. Xiaojun Yan, Mr. Zhiwei Liu and Mr. Xiaoyu Qin from School of Energy and Power Engineering, Beihang University, for the assistance of setting up the *in situ* SEM tensile testing. Many thanks to Dr. Nicolas Vanderesse, Dr. Jianqiang Chen, Dr. Hossein Monajati, Prof. Mohammad Jahazi and Prof. Philippe Bocher in Department of Mechanical Engineering, École de Technologie Supérieure, for their help in DIC, Feritscope and SEM experiments. I would like to thank Dr. Bengt Hallstedt from Institute for Materials Applications in Mechanical Engineering (IWM), RWTH Aachen University, for providing the modified thermodynamic database. I would like to acknowledge my friend and colleague, Dr. Lucie Nguyen, for the French translation of my thesis abstract.

I am really thankful for all the help and company from my friends in Montreal. They have truly made my life in Montreal more colorful.

I acknowledge the financial assistance from China Scholarship Council (CSC) and the McGill Engineering Doctoral Award (MEDA) program.

I would like to express my most special gratitude to my parents, Mr. Xudong Sun and Mrs. Jiqin Cong. Their unparalleled love and support made this journey possible, and made me concentrate on my research without being distracted. I am also very lucky to have the company of my girlfriend, Ms. Li Guo, for so many years; I can never thank more for her patience and understanding.

TABLE OF CONTENTS

Abstract	I
R ésum é	III
Preface	V
Acknowledgements	VII
Table of Contents	IX
List of Figures	XIII
List of Tables	XXII
Chapter 1 - Introduction	1
1.1 Background	1
1.2 Research Objectives	4
1.3 Thesis Layout	5
1.4 References	6
Chapter 2 - Literature Review	8
2.1 Alloying Strategy in Medium Mn Steels	8
2.1.1 Manganese	8
2.1.2 Carbon	9
2.1.3 Aluminum	10
2.1.4 Silicon	11
2.2 Phase Transformation Behavior During Heat Treatment of Medium Mn Steels	12
2.2.1 Intercritical annealing	12
2.2.2 Other heat treatment methods for medium Mn steels	18
2.3 Austenite Deformation Micromechanics in Medium Mn Steels	21
2.3.1 Transformation-induced plasticity (TRIP)	21
2.3.2 Twinning-induced plasticity (TWIP)	22
2.3.3 Stacking fault energy	23
2.4 Overview of Microstructure-Property Relationship in Medium Mn Steels	27

2.4.1 Overview of tensile properties of medium Mn steels with different structures	27
2.4.2 Effect of austenite fraction	31
2.4.3 Effect of austenite stability	33
2.4.4 Effect of austenite deformation mechanisms	36
2.4.5 Effect of stress/strain distributions	37
2.5 References	40
Chapter 3 - Phase Transformation Behavior of Medium Manganese Steels with 3 wt	t pct
Aluminum and 3 wt pct Silicon during Intercritical Annealing	52
3.1 Abstract	53
3.2 Introduction	54
3.3 Experimental Procedure	56
3.4 Results	58
3.4.1 Hot rolled microstructure	58
3.4.2 Effect of annealing temperature	58
3.4.3 Effect of annealing time	70
3.5 Discussion	74
3.6 Conclusions	80
3.7 References	82
Chapter 4 - Critical Role of Strain Partitioning and Deformation Twinning on Crac	king
Phenomenon Occurring During Cold Rolling of Two Duplex Medium Manganese Se	teels . 87
4.1 Abstract	88
4.2 Introduction	89
4.3 Experimental Procedure	91
4.4 Results and Discussion	93
4.5 Conclusions	103
A C D C	104

Chapter 5 - On the Deformation and Fracture Mechanisms of Austenite-Ferrite D	uplex
Medium Manganese Steels with Different Silicon Additions	106
5.1 Abstract	107
5.2 Introduction	108
5.3 Experimental Procedure	111
5.3.1 Materials and processing	111
5.3.2 Mechanical and microstructural characterization	112
5.4 Results	114
5.4.1 Influence of Si on the microstructure	114
5.4.2 Influence of Si on the tensile properties	119
5.4.3 Deformation micromechanisms and micromechanics	123
5.4.4 Damage and fracture mechanisms	129
5.5 Discussion	134
5.5.1 Effect of Si on deformation micromechanisms and micromechanics	134
5.5.2 Deformation behavior and strain hardening	138
5.5.3 Effect of Si on fracture mechanisms of the LA-structure	143
5.6 Conclusions	146
5.7 References	148
Chapter 6 - Discontinuous Strain-induced Martensite Transformation Related to t	he
Portevin-Le Chatelier Effect in a Medium Manganese Steel	153
6.1 Abstract	154
6.2 Introduction	155
6.3 Experimental Procedure	156
6.4 Results and Discussion	158
6.5 Conclusions	168
6.6 References	169
Chanter 7 - Conclusions	172

Chapter 8 -Contributions to Original Knowledge	176
Chapter 9 -Future Work	178
Appendix A - Supporting Information to Chapter 5	179
Appendix B - Abstract of Published Article Related to this Research	182

LIST OF FIGURES

Figure 1.1 Tensile properties of different groups of AHSS, plotted based on numerous
publications [1.1, 1.2, 1.9-1.15]. (conventional automotive sheet steels: interstitial-free (IF), bake
hardenable (BH), high-strength, low-alloy (HSLA) and mild steels; 1st generation AHSS: dual
phase (DP), complex phase (CP), martensitic (MS) and transformation-induced plasticity (TRIP)
steels; 2 nd generation AHSS: twinning-induced plasticity (TWIP) steels; 3 rd generation AHSS:
quenching and partitioning (Q&P), carbon-free bainite (CFB) and medium Mn steels)2
Figure 2.1 Schematic diagram describing the phase transformation thermodynamics during the
IA process: (a) thermal cycle of the IA process; (b) the influence of annealing temperature on the
austenite fraction before cooling; (c) the influence of annealing temperature on the C and Mn
content of the intercritical austenite; (d) the influence of annealing temperature on the Ms
temperature; (e) the influence of annealing temperature on the retained austenite fraction after
cooling13
Figure 2.2 Schematic diagrams of three stages in austenite growth during intercritical annealing
from a ferrite-pearlite structure: 1st stage: dissolution of pearlite; 2nd stage-1: austenite growth
controlled by C diffusion in austenite; 2 nd stage-2: austenite growth controlled by Mn diffusion in
ferrite; 3 rd stage: final equilibration with Mn diffusion in austenite. (reconstructed based on the
work of Speich et al. [2.28])
Figure 2.3 EBSD phase maps of a 0.05C-9Mn medium Mn steel intercritical annealed from (a)
hot rolled (α' -martensite) structure and (b) cold rolled (deformed α' -martensite) structure.
(reproduced from Ref. [2.70], with permission: © 2014 Elsevier)
Figure 2.4 Schematic Q&P processing cycle. (reproduced from Ref. [2.92], with permission: ©
2016 Springer) 19

Figure 2.5 (a) Schematic diagram of the TRIP-assisted plasticity mechanism; (b) Schematic
diagram of deformation mechanisms in different ranges of deformation temperature: from left to
right is stress-induced martensite formation, strain-induced martensite formation and dislocation
glide. (reproduced from Ref. [2.101], with permission: © 2004 Elsevier)21
Figure 2.6 Mechanisms of plasticity enhancement associated with deformation twinning: (a)
Dynamic Hall-Petch effect; (b) Back stress effect. Here σ_A and τ_A are the applied stress and the
shear stress, respectively, τ_{BS} denotes the back stress, and Λ represents the average twin spacing.
(reproduced from Ref. [2.109], with permission: © 2017 Elsevier)
Figure 2.7 Values of austenite SFE (γ_{SFE}) for different deformation mechanisms of austenite
(deformation-induced martensite, deformation twinning and dislocation glide), proposed by
Allain et al. [2.116] for a Fe-22Mn-0.6C TWIP steel using thermodynamic model and
transmission electron microscropy (TEM), and Lee et al. [2.27] for Fe-18Cr-10Mn-N-C stainless
steels by neutron diffraction (ND) and TEM. (γ : austenite, ϵ : ϵ -martensite, α' : α' -martensite, DT:
deformation twinning)25
Figure 2.8 (a) Comparison of tensile properties of medium Mn steels with other high strength
steels; (b) Tensile properties of medium Mn steels with different heat treatment methods and
microstructures (IA: intercritical annealing; MA: multi-annealing; Q&P: quenching and
partitioning). (plotted based on published data [2.12, 2.30, 2.32, 2.44, 2.59, 2.69, 2.91, 2.94-2.97,
2.111, 2.120, 2.122-2.139])

Figure 2.9 Typical microstructure of medium Mn steels processed with different heat treatments: (a) Secondary electron (SE) imaging and TEM images of a cold rolled Fe-9Mn-0.05C steel heat treated by intercritical annealing, showing a globular-shaped γ + α structure [2.70]; (b) SE imaging and TEM images of a hot rolled Fe-9Mn-0.05C steel heat treated by intercritical

annealing, showing a lath-shaped $\gamma+\alpha$ structure [2.70]; (c) Electron backscatter diffraction
(EBSD) image of a cold rolled 0.12C-5.8Mn-3.1Al steel treated by intercritical annealing,
showing the present of δ -ferrite [2.12]; (d) SE imaging of a cold rolled 0.1C-7Mn steel
intercritical annealed at a relatively high temperature, showing a $\gamma + \alpha + \alpha'$ multi-phase structure
[2.32]; (e) EBSD, TEM bright field (BF) and TEM dark field (DF) images of a
0.2C-4Mn-1.6Si-1Cr steel treated by Q&P process, showing a $\gamma+\alpha'$ two phase structure [2.140].
(reproduced from Ref. [2.70] [2.12] [2.32] and [2.140], with permission: $\ \odot$ 2014 Elsevier, $\ \odot$
2009 Springer, © 2011 Springer and © 2014 Springer)
Figure 2.10 Product of UTS and TE in AHSS as a function of austenite fraction. (reproduced
from Ref. [2.131], with permission: © 2010 Elsevier)

Figure 2.12 Effect of the intercritical annealing temperature (i.e. austenite fraction and stability) on the (a) engineering stress-strain curve, (b) UTS, YS and TE values and (c) the amount of strain-induced α' -martensite in a 10Mn-0.3C-3Al-2Si medium Mn steel with the austenite-ferrite duplex structure. (reproduced from Ref. [2.30], with permission: © 2014 Springer).........34

Figure 2.14 Fig. 2.14 Evolution of von Mises strain fields simulated by microstructure-based
finite element method during plain strain tensile deformation in the Fe-6Mn-0.15C-1.5Si-3A
steel with TRIP and TWIP effect (a) activated and (b) de-activated. (reproduced from Ref.
[2.156], with permission: © 2016 Elsevier)
Figure 3.1 (a) Optical and (b) SEM micrographs of the hot rolled structure of the 7Mn steel; (c)
Optical micrograph of the hot rolled 10Mn steel; (d) XRD patterns of the hot band
microstructures. (P: Pearlite; B: Bainite; γ : Austenite; δ : δ -ferrite, samples were etched by 2 %
nital followed by 10 % aqueous sodium metabisulfite)60
Figure 3.2 Microstructure of the 7Mn steel annealed at 800 ℃ for 1 h: (a) EBSD phase mapping
showing FCC and BCC phases; (b) BCC inverse pole figure (IPF) in the same area of (a); (c)
SEM micrograph in the higher magnification, etched by 2 % nital followed by 10 % aqueous
sodium metabisulfite. (γ_G : globular-shaped austenite; γ_L : lath-shaped austenite; α_G
globular-shaped ferrite; α _L : lath-shaped ferrite)61
Figure 3.3 EBSD images of the 7Mn steel annealed at 1000 °C for 1 h: (a) Phase mapping
showing FCC, BCC and BCT phases; (b) BCC/BCT inverse pole figure in the same area of
(a)
Figure 3.4 Microstructure of the 10Mn steel heat treated at 800 ℃ for 1 h: (a) EBSD phase
mapping showing FCC and BCC phases; (b) BCC inverse pole figure in the same area of (a); (d)
SEM micrograph in the higher magnification, etched by 2 % nital followed by 10 % aqueous
sodium metabisulfite. (γ _{NT} : newly transformed austenite)
Figure 3.5 EBSD images of the 10Mn steel heat treated at 1000 ℃ for 1 h: (a) Phase mapping
showing FCC and BCC phases; (b) BCC inverse pole figure in the same area of (a)

Figure 3.6 Phase fractions of (a) the 7Mn steel and (b) the 10Mn steel under different annealing
temperatures and subsequent quenching (FMNA: ferrite, martensite plus retained austenite
microstructure; FADP: ferrite-austenite duplex phase microstructure)
Figure 3.7 Calculated equilibrium and measured average solute (C, Mn, Al and Si) contents of
the intercritical austenite in (a) the 7Mn steel and (b) the 10Mn steel as a function of annealing
temperature. (The thermodynamic calculation was conducted using Thermo-Calc software with a
modified database)68
Figure 3.8 (a) Calculated Ms temperature of the 7Mn and 10Mn steels as a function of annealing
temperature; (b) Martensite fraction of the 7Mn steel at different annealing temperatures69
Figure 3.9 Phase fractions of (a) the 7Mn steel and (b) the 10Mn steel as a function of annealing
time at 1000 °C
Figure 3.10 (a) Measured and calculated C contents in the austenite phase of the two medium
Mn steels as a function of holding time at 1000 °C; (b) The distribution of Mn, Al and Si across
an austenite island in the 7Mn steel annealed at 1000 °C for 1 min; (c) Manganese contents with
annealing time in austenite and ferrite of both steels; (d) Manganese partition coefficients
between austenite and ferrite in both steels
Figure 3.11 (a) Austenite grain size and calculated M_s temperature of the 7Mn steel as a function
of annealing time; (b) Martensite fraction of the 7Mn steel at different annealing times73
Figure 3.12 Comparison of the austenite fraction between thermodynamic predictions and
experimental measurement in (a) the 7Mn steel and (b) the 10Mn steel

Figure 3.13 Mean diffusion distance of C and Mn in different phases of the 10Mn steel at
1000 ℃
Figure 4.1 EBSD phase mapping of (a) the 7Mn steel and (b) the 10Mn steel after prior heat
treatment at 1000 °C for 10 min, followed by air cooling; (c) Fractions of strain-induced
α' -martensite and retained austenite as a function of cold rolling thickness reduction; (d)
Deformation twins in the 10Mn steel cold rolled to 10% reduction95
Figure 4.2 SEM micrographs of the 7Mn steel after ~20% cold rolling reduction showing
micro-cracks nucleated (a) on the α' -martensite and IA- α phase boundaries and (b) inside the α' - γ
mixed phase; (c) EBSD band contrast (BC) mapping and (d) BCC inverse pole figure (IPF) for
the same sample of (a) and (b), showing micro-cracks and deformation twins inside δ -ferrite (the
coincidence site lattice (CSL) Σ 3 (60°/<111>) twin boundaries were highlighted as thick black
lines in Figure 4.2 (d))97
Figure 4.3 (a) Microscopic tensile strain of austenite (including strain-induced martensite) and
δ-ferrite in the two steels as a function of the overall tensile load; (b) Strain partition coefficient
o-ferrite in the two steels as a function of the overall tensile load; (b) Strain partition coefficient (n) of the two steels, calculated from the data in (a)
(n) of the two steels, calculated from the data in (a)
(n) of the two steels, calculated from the data in (a)
(n) of the two steels, calculated from the data in (a)
(n) of the two steels, calculated from the data in (a)

Figure 5.2 EBSD observation of the (a) LA-structure and (b) HA-structure (a ₁ : LA-0Si, a ₂ :
LA-1Si, a ₃ : LA-3Si; b ₁ : HA-0Si, b ₂ : HA-1Si)
Figure 5.3 EDX mapping of the LA-1Si sample, showing solute (Mn, Al and Si) partitioning
between austenite and ferrite. (The lighter phase in the SE image is ferrite)117
Figure 5.4 Tensile property and SIT behavior for the LA-structure (LA-0Si, LA-1Si and LA-3Si):
(a) Engineering stress-strain curve; (b) Strength (YS and UTS) and elongation (TE, UE and PUE)
values; (c) Rate of strain hardening ($d\sigma/d\epsilon$) and true stress-strain curve; (d) Change of
α'-martensite fraction during tensile straining
Figure 5.5 Tensile property and SIT behavior for the HA-structure (HA-0Si and HA-1Si): (a)
Engineering stress-strain curve and strength (YS and UTS) and elongation (TE, UE and PUE)
values; (b) serrations on the magnified engineering stress-strain curve; (c) Rate of strain
hardening (d σ /d ϵ) and true stress-strain curve; (d) Change of α' -martensite fraction during tensile
straining122
Figure 5.6 TEM observation of austenite deformation mechanisms in LA-structured samples
(macroscopic true strain 0.15): Bright field (BF) images, dark field (DF) images and nanobeam
diffraction (NBD) patterns of (a ₁ -a ₄) the LA-0Si and (b ₁ -b ₄) the LA-1Si sample, showing
formation of deformation twins and strain-induced α' -martensite in separate austenite grains; (c_1)
BF image and (c ₂) DF image and NBD pattern of the LA-3Si sample, showing a high density of
deformation twins in one austenite grain; (c ₃) BF image and NBD pattern for a austenite grain in
the LA-3Si sample, showing the formation of secondary twins and α' -martensite on the
intersections of deformation twins (marked by dot circles)

Figure 5.7 TEM bright field images and NBD patterns of the deformed HA-structure

(macroscopic true strain 0.1), showing deformation twins and strain-induced α' -martensite in the
austenite of (a) the HA-0Si and (b) the HA-1Si sample
Figure 5.8 Microstructure evolution of one local area in the (a) LA-1Si sample and (b) LA-3Si
sample during tensile testing; Measured strain distribution between austenite and ferrite in the
LA-structured samples during tensile testing: (c) LA-0Si; (d) LA-1Si; (e) LA-3Si
Figure 5.9 Strain distribution between austenite and ferrite in the HA-structured samples during
tensile testing: (a) HA-0Si; (b) HA-1Si
Figure 5.10 SEM fractograph of the LA-structured samples: (a) LA-0Si; (b) LA-1Si; (c) LA-3Si
(the edge of the fracture surface is marked by solid lines; local strain at the fracture surface of
each sample is also added); (a_1) , (b_1) and (c_{1-3}) are the magnified areas marked by the rectangular
frames in (a), (b) and (c). (The dashed lines in these images serve to identify the areas of specific
fracture features)
Figure 5.11 SEM observation of the tensile fractured samples (near the fracture surface),
showing damages (voids and cracks) in the (a ₁ -a ₃) LA-1Si and (c ₁ -c ₃) LA-3Si specimen (the
nanovoids are marked by elliptical frames); (b) the density of nanovoids on different nucleation
sites of the LA-0Si and LA-1Si samples
1
Figure 5.12 Evolution of damages in the LA-3Si sample during tensile deformation: (a) 0.2
strain, (b) 0.26 strain, and (c) fractured sample
Figure 5.13 (a) Calculated and experimental (0.6C-18Mn-xSi [5.16], 0.2C-31Mn-xSi [5.52],
0.03C-15Ni-11Cr-1.1Mn-xSi [5.51]) data showing the effect of Si on austenite SFE; (b)
Contribution of the austenite SFE and grain size to the twinning stress for the LA-structure136

Figure 5.14 (a) SIT kinetics of the LA-1Si sample with high strain partitioning and HA-1Si
sample with very mild strain partitioning; (b) Strain-induced martensite fraction after yielding
and martensite transformation rate $(dF_{\alpha'}/d\epsilon)$ of the HA-structured samples. (the dash line in
Figure 5.14 (a) and the solid lines in Figure 5.14 (b) are the fitting curves based on the OC
model)142
Figure 5.15 (a) TEM bright field images and (b) selected area diffraction (SAD) pattern of
δ-ferrite in the LA-3Si sample
Figure 6.1 SEM micrographs of the (a) IA-700 and (b) IA-750 sample
Figure 6.2 (a) True stress-strain curve and (b) the rate of work hardening $(d\sigma/d\varepsilon)$ of the IA-700
and IA-750 sample; (c) Normalized austenite transformed fraction of the two samples during
tensile straining, measured by Feritscope and XRD (the dash line is the fitting curve for the
IA-750 sample based on the OC model)
Figure 6.3 (a) Average engineering strain generated by DIC as a function of deformation time
and strain maps corresponding to the propagation of two successive bands in the IA-750 sample;
(b) Corresponding strain profiles of the two bands along the tensile axis in the analyzed area162
Figure 6.4 Deformation time dependence of (a) engineering strain and normalized austenite
transformed fraction and (b) engineering strain and stress for the IA-750 sample in the plastic
deformation range

LIST OF TABLES

Table 3.1 Steel compositions in weight percent.	56
Table 3.2 Recrystallized fractions (vol.%) of austenite and ferrite in the 10Mn annealing at different temperatures and subsequent quenching (measured by EBSD)	
Table 4.1 Detailed information of each phase in the annealed medium Mn steels	94
Table 5.1 Steel compositions in weight percent.	111
Table 5.2 Detailed information (austenite fraction and composition, grain size, artemperature) in the annealed samples.	
Table 6.1 Fraction and equilibrium composition of austenite in the two samples	159
Table A1 Numerical values and functions used for the calculations (Eq. A1)	180

CHAPTER 1

_

INTRODUCTION

1.1 Background

The automotive industry is facing stringent regulations and significant challenges on weight reduction of road transportation vehicles for fuel economy, as well as improvement of crashworthiness performance to ensure vehicle safety. The response to these challenges requires the development of new lightweight body-in-white assemblies with intensive use of advanced high strength steels (AHSS) [1.1, 1.2]. Compared with conventional high strength steels (HSS) such as bake hardenable (BH) and high-strength, low-alloy (HSLA) steels, AHSS possess better strength and ductility combinations. It is generally classified into categories of first generation AHSS (1st-Gen), second generation AHSS (2nd-Gen) and third generation AHSS (3rd-Gen). The tensile properties for each category, based on numerous publications, are illustrated in Fig. 1.1.

1st-Gen The **AHSS** normally includes dual phase (DP), complex-phase (CP). transformation-induced plasticity (TRIP), and martensitic steels [1.3]. They contain a low amount of Mn (lower than 3 wt.%) and are primarily ferrite-based steels. The product of tensile strength and elongation for this grade is relatively low, which is below 25 GPa% [1.4]. The 2nd-Gen AHSS is mainly referred to as austenitic twinning-induced plasticity (TWIP) steels, which contain a high amount of Mn ranging from roughly 15 to 25 wt.%. Despite the great strength-ductility combinations of such steels (the product of tensile strength and elongation is higher than 50 GPa% [1.4]), the high alloy contents essentially result in some processing challenges and cost issues, relative to low carbon sheet steels [1.5]. Therefore, there is an

increasing interest to develop a new class of steels, 3rd-Gen AHSS, with anticipated properties in the intermediate area identified in Fig. 1.1. Potential candidate grades for the 3rd-Gen AHSS span a vast range of alloying strategies and processing routes, e.g. carbide-free bainite (CFB) [1.6], quenching and partitioning (Q&P) [1.7] and medium Mn steels [1.4, 1.8].

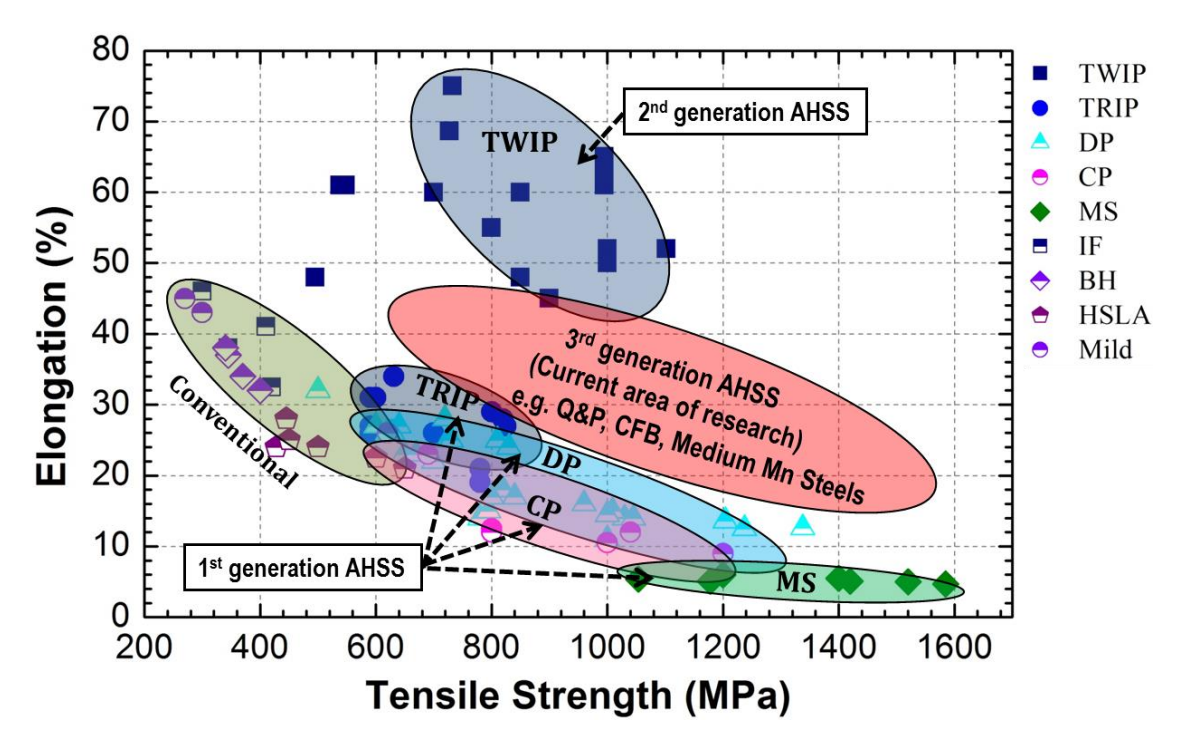


Fig. 1.1 Tensile properties of different groups of AHSS, plotted based on numerous publications [1.1, 1.2, 1.9-1.15]. (conventional automotive sheet steels: interstitial-free (IF), bake hardenable (BH), high-strength, low-alloy (HSLA) and mild steels; 1st generation AHSS: dual phase (DP), complex phase (CP), martensitic (MS) and transformation-induced plasticity (TRIP) steels; 2nd generation AHSS: twinning-induced plasticity (TWIP) steels; 3rd generation AHSS: quenching and partitioning (Q&P), carbon-free bainite (CFB) and medium Mn steels).

Medium Mn steels containing 3 to 12 wt.% Mn have been proven to be one of the strong candidates for the 3rd Gen AHSS, due to mechanical properties exceeding the 1st-Gen AHSS and the potentially lower cost than the high Mn TWIP steels. The concept of such steels originally started in the 1970s with Miller [1.16], but has received considerable attention only recently (in

the early 2010s) due to the increasing demand for strong steels from automotive industry. The increased amount of Mn present in medium Mn steels enhances the stability and volume fraction of retained austenite, which can be tailored by different heat treatments to provide various TRIP and TWIP effects; this can give rise to an increased work hardening, improved plasticity and better fracture toughness.

Currently, most of the work on medium Mn steels is strongly focused on the improvement of basic tensile properties, such as yield strength (YS), ultimate tensile strength (UTS), total elongation (TE), and strength-ductility balance [1.17]. Excellent tensile properties which meet or even exceed the target property shown in Fig. 1.1 have generally been documented for such steels. For example, the product of tensile strength and total elongation for such steels was reported to be as high as ~70 GPa% [1.18]. However, other aspects of medium Mn steels have not attracted enough attention. These include the following:

- (a) The microstructural evolution of medium Mn steels during different processing stages has rarely been examined. A large fraction of metastable austenite is easily retained at different stages of processing; this differs from other steels and would have some influence on processing such steels (e.g. cold rolling);
- (b) The effect of elements on the structure and mechanical behavior of medium Mn steels has not been systematically investigated, such that there is no agreement on the optimized alloying components and composition range. Indeed, the large metallurgical variations (e.g. phase constituents and fractions, austenite stability and deformation mechanisms, grain size and morphology) in such steels pose great challenges in revealing the direct effect of elements;
- (c) Regarding the deformation behavior of medium Mn steels, investigations have mainly centered on the activation of TRIP and TWIP effect in austenite during deformation to explain

the excellent tensile properties of such steels. However, other micromechanical details such as stress/strain partitioning between different phases and the serrated plastic flow phenomenon associated with the Portevin-Le Chatelier (PLC) effect or dynamic strain aging (DSA), have not been properly addressed, and thus remain both poorly documented and poorly understood.

1.2 Research Objectives

The objective of this research is to develop a better understanding of the processing-microstructure-property relationship of Al-Si added medium Mn steels with compositions of Fe-0.2C-(7~10)Mn-3Al-(0~3)Si (in wt.%). The study specifically focuses on the following aspects:

- The phase transformation behavior of hot rolled medium Mn steels with 3 wt.% Al and 3 wt.% Si during intercritical annealing, with emphasis on the austenite formation during reheating and the subsequent decomposition upon quenching;
- The microstructural evolution of the high Al-Si medium Mn steels during cold rolling, and
 the role of austenite deformation mechanisms (strain-induced transformation to martensite
 and deformation twinning) and strain partitioning between austenite and ferrite on the cold
 rollability of the steels;
- Detailed deformation and fracture mechanisms of the cold rolled and intercritical annealed medium Mn steels with different Si additions (0~3 wt.%);
- The correlation between the strain-induced martensite formation and the PLC effect occurred in cold rolled and intercritical annealed medium Mn steels during tensile testing.

1.3 Thesis Layout

This thesis follows the manuscript-based structure and consists of 7 chapters. Chapter 1 introduces the background and objectives of the research. An extensive literature review and the state of the knowledge on medium Mn steels are presented in Chapter 2; this includes (a) the alloying strategy; (b) the heat treatment methods and the phase transformation behavior; (c) the deformation micromechanics of austenite; (d) an overview of structure-property relationship based on the current literature. Chapter 3 concerns the detailed phase transformation behavior of hot rolled medium Mn steels with 3 wt.% Al and 3 wt.% Si additions during intercritical annealing, using various characterization techniques. Chapter 4 focuses on the cold rollability and the microstructural evolution of high Al-Si medium Mn steels during cold rolling. The role of austenite deformation mechanisms and strain partitioning on the cold rollability of the steels is highlighted in this chapter. Chapters 3 and 4 develop a better understanding of processing such high Al-Si medium Mn steels. Chapter 5 presents a detailed investigation on the microstructure and deformation and fracture mechanisms of cold rolled and intercritical annealed medium Mn steels with different Si additions. The results in this chapter again highlight the critical role of strain partitioning on the tensile properties of such steels. Chapter 6 focuses on the correlation between the strain-induced martensite formation and the PLC effect during tensile testing. A discontinuous strain-induced transformation behavior is observed, and a strong correlation between this and the PLC phenomenon is established in this chapter. Chapter 7 provides the major conclusions of the research. Chapter 8 presents the contributions of this thesis to the original knowledge, and an outlook for future work is proposed in **Chapter 9**.

1.4 References

- [1.1] S. Keeler, M. Kimchi, *Advanced High Strength Steel Application Guidelines: Version 5*, WorldAutoSteel 2014, http://www.worldautosteel.org.
- [1.2] Y. Weng, H. Dong, Y. Gan, *Advanced Steels: The Recent Scenario in Steel Science and Technology*, Springer-Verlag Berlin Heidelberg and Metallurgical Industry Press, 2011.
- [1.3] D.K. Matlock, J.G. Speer, *Third generation of AHSS: microstructure design concepts*, in: A. Haldar, S. Suwas, D. Bhattacharjee (Eds.), Microstructure and Texture in Steels and Other Materials, Springer-Verlag London Limited, 2009.
- [1.4] Y.K. Lee, J. Han, *Current opinion in medium manganese steel*, Materials Science and Technology, 31 (2015), 843-856.
- [1.5] B.C. De Cooman, O. Kwon, K.G. Chin, *State-of-the-knowledge on TWIP steel*, Materials Science and Technology, 28 (2012), 513-527.
- [1.6] H.K.D.H. Bhadeshia, *High performance bainitic steels*, Materials Science Forum, 500-501(2005), 63-74.
- [1.7] J. Speer, D. Matlock, B. De Cooman, J. Schroth, *Carbon partitioning into austenite after martensite transformation*, Acta materialia, 51 (2003), 2611-2622.
- [1.8] B.C. De Cooman, *High Mn TWIP steel and medium Mn steel*, in: R. Rana, S.B. Singh (Eds.), Automotive Steels: Design, Metallurgy, Processing and Applications, 2017 Elsevier Ltd., Woodhead Publishing, 2017.
- [1.9] K.G. Chin, C.Y. Kang, S.Y. Shin, S. Hong, S. Lee, H.S. Kim, K.h. Kim, N.J. Kim, *Effects of Al addition on deformation and fracture mechanisms in two high manganese TWIP steels*, Materials Science and Engineering: A, 528 (2011), 2922-2928.
- [1.10] S. Curtze, V.T. Kuokkala, Dependence of tensile deformation behavior of TWIP steels on stacking fault energy, temperature and strain rate, Acta materialia, 58 (2010), 5129-5141.
- [1.11] S. Kang, Y.S. Jung, J.H. Jun, Y.K. Lee, *Effects of recrystallization annealing temperature* on carbide precipitation, microstructure, and mechanical properties in Fe-18Mn-0.6C-1.5Al TWIP steel, Materials Science and Engineering: A, 527 (2010), 745-751.
- [1.12] O. Kwon, Development of high performance high manganese TWIP steels in POSCO, Proceedings of HMnS2011, 2011.
- [1.13] M. Otto, D. John, R. Schmidt-Juergensen, B. Springub, M. Cornelissen, B. Berkhout, J. Patel, *HSD*® *STEELS OPTIMIZED TWIP STEELS*, Proceedings of HMnS2011, 2011.
- [1.14] O. Grässel, G. Frommeyer, *Effect of martensitic phase transformation and deformation twinning on mechanical properties of Fe-Mn-Si-Al steels*, Materials Science and Technology, 14 (1998), 1213-1217.
- [1.15] K. Cho, K. Redkin, M. Hua, C. Garcia, A. DeArdo, Recent development of Nb-containing

- DP590, DP780 and DP980 steels for production on continuous galvanizing lines, in: Y. Weng, H. Dong, Y. Gan (Eds.), Advanced Steels: The Recent Scenario in Steel Science and Technology, Springer-Verlag Berlin Heidelberg and Metallurgical Industry Press, 2011.
- [1.16] R.L. Miller, *Ultrafine-grained microstructures and mechanical properties of alloy steels*, Metallurgical Transaction, 3 (1972), 905-912.
- [1.17] S. Lee, S. Shin, M. Kwon, K. Lee, B.C. De Cooman, *Tensile properties of medium Mn steel with a bimodal UFG* α + γ *and coarse* δ -Ferrite microstructure, Metallurgical and Materials Transactions A, 48 (2017), 1678-1700.
- [1.18] S. Lee, B.C. De Cooman, Annealing temperature dependence of the tensile behavior of 10 pct Mn multi-phase TWIP-TRIP steel, Metallurgical and Materials Transactions A, 45 (2014), 6039-6052.

CHAPTER 2

_

LITERATURE REVIEW

2.1 Alloying Strategy in Medium Mn Steels

In the literature, there is a general consensus that medium Mn falls between 3~12 wt.% [2.1-2.4]. The most common alloying elements in such steels are carbon (C), aluminum (Al), and silicon (Si). Their ranges are quite wide according to the literature, i.e. around 0.01~0.5 wt.% for C [2.5, 2.6], 0~8 wt.% for Al [2.7] and 0~3 wt.% for Si [2.8]. These steels sometimes are micro-alloyed with V [2.9], Nb [2.10] and Ti [2.11]. It has to be noted that, to the best of the author's knowledge, there have been very limited investigations on the effect of alloying elements on the microstructure and mechanical behavior of medium Mn steels [2.12-2.14]. Indeed, the large amounts of metallurgical variations (e.g. phase constituents and fractions, austenite stability and deformation mechanisms, grain size and morphology) in such steels bring great challenges of revealing the direct effect of elements. The following summaries are mainly based on the reports of other types of steels.

2.1.1 Manganese

Manganese, as reflected by the name of the steel, is the most featured element. The most important role of Mn in such steels is to stabilize austenite and retain it at ambient temperature. Adding 1 wt.% Mn in austenite would result in around 30~40 $^{\circ}$ C decrease for the Ms temperature (martensite start temperature) [2.15-2.17] and ~10 $^{\circ}$ C decrease for the Md₃₀ temperature (the temperature where half of the austenite is transformed to martensite at a strain of 30%) [2.18, 2.19]. Therefore, the maximum retained austenite (RA) amount generally increases with higher

Mn; for example, the maximum RA value increased by ~20% for an additional 2~3 wt.% Mn [2.14]. Manganese also decreases the austenite start (Ac1) and finish (Ac3) temperatures. This essentially brings two counter effects: (a) the required annealing temperatures decrease such that grain size can be refined [2.20]; (b) a prolonged time is required to achieve a high fraction of austenite due to the slow transformation kinetics resulting from the sluggish Mn diffusion in austenite at low temperatures [2.14]. It is generally agreed that in binary Fe-Mn systems, austenite stacking fault energy (SFE) at room temperature firstly decreases and then increases with increasing Mn concentrations [2.21-2.23], resulting in a typical parabolic dependence of SFE on Mn content. It is interesting to note that the lowest SFE (the bottom part of the parabolic curve) is obtained for Mn contents in the range of 10 to 16 wt.% [2.23], which is quite similar to the austenite Mn concentration in the most widely investigated medium Mn steels (with 5~10 wt.% Mn). Therefore, the quantitative effect of Mn on austenite SFE in such steels is probably slight. On the other hand, it is predicted by ab-initio calculations [2.24] that Mn can promote the formation of C-Mn pairs, which would reduce the C diffusivity and increase the solubility limit of C in austenite. This might have some effect on mechanical behavior of medium Mn steels.

2.1.2 Carbon

Similar to Mn, C also strongly stabilizes austenite, which suppresses the formation of thermal and mechanical martensite (i.e. increases the Gibbs energy between austenite and martensite, $\Delta G_{\gamma \to \alpha'/\epsilon}$). However, it also possesses many other important influences on medium Mn steels. It is well known that C has a strong solid solution hardening effect. The austenite SFE is substantially increased with higher C contents, i.e. $2.5\sim4$ mJ/m² increase per 0.1 wt.% C [2.25-2.27]. All of these ensure a very strong effect of C on mechanical behavior of medium Mn steels. Due to the limited solubility of C in ferrite, almost all the C partitions into austenite during intercritical annealing, and this always occurs in a very short time [2.28, 2.29] because of the very high diffusivity of C atoms. Thus, the mechanical performance of such steels always has a very high sensitivity to annealing temperatures [2.30-2.34]. The high diffusivity of C atoms is also partly

responsible for some plastic instability phenomena such as the Lüders banding and the Portevin-Le Chatelier (PLC) effect [2.32, 2.35], due to the interactions between C atoms and dislocations.

2.1.3 Aluminum

Aluminum can suppress the austenite to martensite transformation and promote the formation of deformation twins [2.36], due to its increasing effect on austenite SFE. It can be concluded from the experimental data [2.37-2.42] that 1 wt.% Al would result in ~8.5 mJ/m² increase of austenite SFE; this value is in agreement with thermodynamic calculations [2.43]. This could explain the TWIP effect normally observed in Al-added medium Mn steels [2.6, 2.44, 2.45]. Aluminum can also stabilize ferrite and enlarge the two phase (α + γ) domain; higher amounts of Al can promote the formation of δ -ferrite [2.46]. For example, it was observed that δ -ferrite existed in a 0.12C-5Mn-3Al-0.5Si steel but was absent when the Al content was reduced to 1 wt.% [2.46]. The density of the steel can be reduced by Al addition, e.g. 1 wt.% of Al could lead to a ~1.5 wt. % weight reduction in automotive components [2.47]. For this purpose, a very high amount of Al (higher than 3 wt.%) is added sometimes; these high-Al medium Mn steels are also referred to as low-density or lightweight steels [2.47, 2.48].

It should be noted that Al was reported to have some other effects in TWIP and TRIP steels; these effects include: (a) in TWIP steels, Al can improve the resistance to hydrogen embrittlement and delayed fracture [2.49, 2.50]; (b) aluminum could reduce the C diffusivity within the core of dislocations [2.23, 2.51], as indicated by the apparent activation energy increase for the onset of serrations (i.e. the PLC effect) in Al-added TWIP steels [2.51]; (c) it is also known that Al has the ability to retard carbide formation, although less potent than Si in the same concentrations [2.52]; this has been used to promote the C enrichment in austenite during bainite overaging treatments in TRIP steels [2.52-2.54]. However, similar effects of Al on medium Mn steels have not yet been reported.

2.1.4 Silicon

Silicon has a similar effect compared with Al in terms of stabilizing ferrite, raising the austenite transition temperatures, enlarging the two phase range and suppressing the carbide formation [2.52, 2.54]. The suppressive effect on carbides formation is attributed to the fact that Si solubility in carbides is very low, thus Si significantly reduces the driving force for carbide precipitation [2.54]. As well, Si possesses a high degree of solid solution strengthening on both ferrite [2.55-2.58] and austenite [2.38, 2.59]. It was reported that Si can enhance the yield/tensile strengh levels without scrificing uniform elongation in dual phase (DP) steels with a ferrite and martensite structure [2.20, 2.60, 2.61]. Jeong et al. [2.38] investigated the influence of Si on mechanical twinning and strain hardening of an austentic Fe-18Mn-0.6C TWIP steel, and found that the Si can increase the fraction of deformation twins by promoting the formation of secondary twins, thus increasing strain hardening. However, Si also possesses some negative effects on steels, for example, a Si content higher than ~0.5 wt. % was generally reported to be detrimental to the ductility and fracture toughness in low-carbon ferritic steels [2.55-2.57, 2.62, 2.63]. This deteriorating effect becomes rather strong when Si is above 3.5~4 wt. % [2.64, 2.65], mainly because of the occurrence of some ordering phases such as B2 and DO3 promoted by high Si contents, which can induce the formation of dissociated superlattice dislocations and the correlated high stress concentrations [2.65]. This ordering effect can form at a lower Si concentration when Al and Si coexist in the Fe-Al-Si ternary phase [2.56]. The influence of Si on austenite SFE is complex. It has been predicted by Dumay et al. [2.66], using a thermodynamic model, that Si first increases the SFE for small contents and then decreases it at higher levels. However, experimental data showed a decrease effect of Si on austenite SFE (-3.5~-2 mJ/m² per 1 wt.% Si) [2.38, 2.40, 2.67].

2.2 Phase Transformation Behavior During Heat Treatment of Medium Mn

Steels

2.2.1 Intercritical annealing

The high amount of Mn increases the thermal stability of austenite and makes it easily retained at room temperature; therefore, the required processing route can be relatively simple and efficient, consisting of a controlled intercritical annealing (IA) treatment without a need for subsequent bainite overaging or martensite quenching-partitioning [2.12, 2.13, 2.68]. Currently, the IA process is the most widely used method for heat treating such steels. A large fraction of RA as high as ~70% [2.6, 2.30, 2.69] can normally be obtained through controlling the IA parameters.

(A) Phase transformation thermodynamics

A schematic diagram describing the phase transformation thermodynamics during the IA process is shown in Fig. 2.1. The initial microstructure prior to IA is generally composed of mostly α' -martensite [2.31, 2.32, 2.70] or pearlite/bainite [2.8, 2.13] after hot and cold rolling. During intercritical annealing, steels are heated from room temperature, held in the ferrite and austenite two phase domain, followed by rapid cooling or quenching to room temperature (Fig. 2.1 (a)). The phase transformation behavior during the IA process consists of austenite formation or reversion during the heating and holding stages, and austenite decomposition to martensite upon quenching. With increasing temperature in the two phase range, the fraction of equilibrium austenite increases (Fig. 2.1 (b)), and the C and Mn content of the intercritical austenite decreases (Fig. 2.1 (c)) which results in an increased Ms temperature (i.e. lower austenite stability) (Fig. 2.1 (d)).

When the Ms temperature increases to the quenching temperature (normally room temperature), martensite starts to form upon quenching. The fraction of the transformed martensite is closely related to the difference between the Ms temperature and quenching temperature, i.e. the undercooling below the Ms temperature. An empirical equation initially proposed by Koistenen

and Marburger (KM) [2.71] and adjusted by several researchers [2.72-2.75] can be used to quantify this relation. The fundamental form of the equation is:

$$f_{\rm M} = 1 - \exp[\alpha (Ms - T)^{\beta}] \tag{2.1}$$

where f_M is martensite fraction transformed from austenite, α and β are dimensionless constants. This KM equation can also be explained by thermodynamics, based on the assumption that the increase of martensite nucleation sites per unit volume $(dN_{\alpha'})$ is proportional to the free energy change from austenite to α' -martensite [2.75].

At lower annealing temperatures, austenite can completely be retained upon quenching, due to the higher austenite stability (i.e. lower Ms temperature), as such the amount of RA is the same as the austenite fraction before cooling. However, the RA fraction will start to decrease almost immediately when martensite forms on quenching, as shown in Fig 2.1 (d) and (e). Therefore, the RA fraction of medium Mn steels generally increases to a maximum value, followed by a decrease, with increasing annealing temperatures. The peak temperature defines the intercritical annealed microstructure, namely, a ferrite plus austenite duplex structure forms below this critical temperature, and a ferrite, martensite plus retained austenite multi-phase structure prevails when the annealing temperature achieves above this critical value [2.31, 2.76].

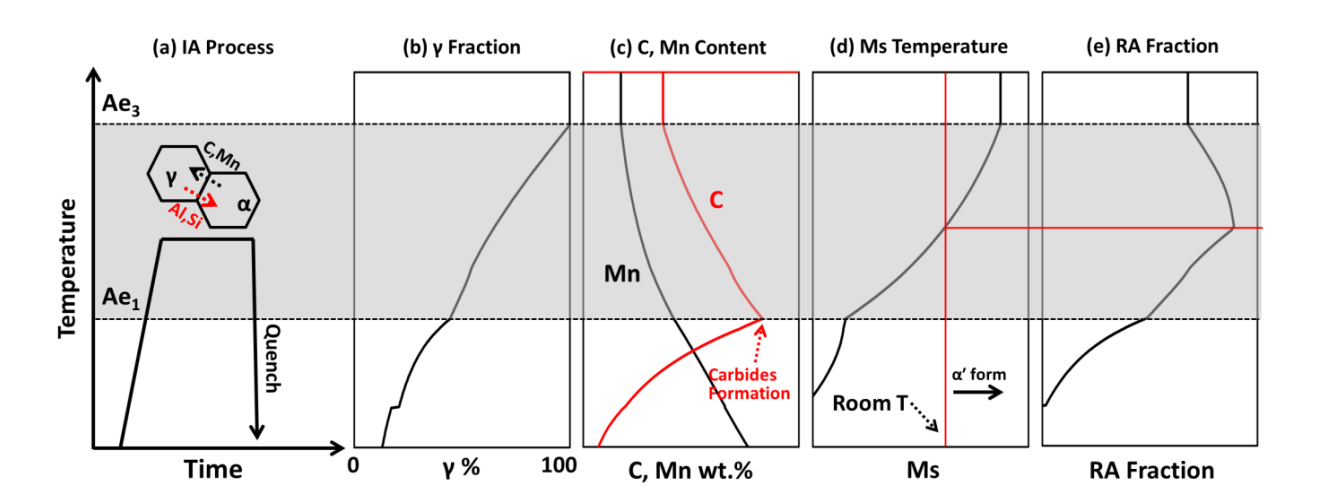


Fig. 2.1 Schematic diagram describing the phase transformation thermodynamics during the IA

process: (a) thermal cycle of the IA process; (b) the influence of annealing temperature on the austenite fraction before cooling; (c) the influence of annealing temperature on the C and Mn content of the intercritical austenite; (d) the influence of annealing temperature on the Ms temperature; (e) the influence of annealing temperature on the retained austenite fraction after cooling.

(B) Austenite formation kinetics

Formation of austenite is generally considered to be a nucleation and diffusion-controlled growth process [2.28, 2.29, 2.31, 2.77-2.81]. The diffusive nucleation sites of austenite are dependent on the initial structure of the steels. The nucleation of austenite in steels with initial ferrite-pearlite microstructure occurs predominantly at the interphase boundaries between pearlite colonies and ferrite grains [2.28, 2.79]. For steels with quenched martensite, austenite nucleation sites have been reported to be at the prior austenite grain boundaries [2.31, 2.77, 2.81] and at martensite lath or packet boundaries [2.31, 2.77, 2.78, 2.80]. In steels consisting of spheroidized carbides and ferrite (i.e. quenched and tempered steels), austenite tends to nucleate primarily at carbide particles located at ferrite grain boundaries [2.29, 2.79]. It was suggested by Garcia et al. [2.79] that carbides located within ferrite grains did not contribute to austenite nucleation but dissolved later in the ferrite matrix with C diffusing to the growing austenite.

It was proposed by Speich et al. [2.28], and supported by many other researchers [2.29, 2.81-2.83], that austenite growth can be separated into three steps in C-Mn steels with a starting structure of ferrite-carbide mixtures. The schematic diagrams of the three stages are shown in Fig. 2.2. The first stage consists of austenite nucleation and carbon-diffusion-controlled growth of austenite following carbide dissolution. Generally, this step is very rapid [2.28, 2.84, 2.85], for example, it only took 0.12 ms in a 0.12C-1.5Mn steel at 900 °C and 50 ms in a 0.1C-3.4 Mn alloy at 740 °C calculated respectively by Speich et al. [2.28] and Lai et al. [2.29], as such this stage normally cannot be observed experimentally. This is due to very high diffusivity of C

atoms and the short diffusion distance (about equal to the interlamellar spacing of the pearlite [2.86] and the thickness of the thin bainite plate [2.87]).

Subsequent growth of austenite into ferrite to achieve a partial equilibrium between the two phases constitutes the second stage. This step is characterized by an intermediate slow growth of austenite, which might be controlled by C diffusion in austenite at high temperatures, or by Mn diffusion in ferrite at low temperatures. The third stage is the final equilibration of ferrite and austenite, which tends to be extremely slow and controlled by sluggish Mn diffusion in austenite (the diffusion rate of Mn in austenite is three orders of magnitude slower than in ferrite [2.28]).

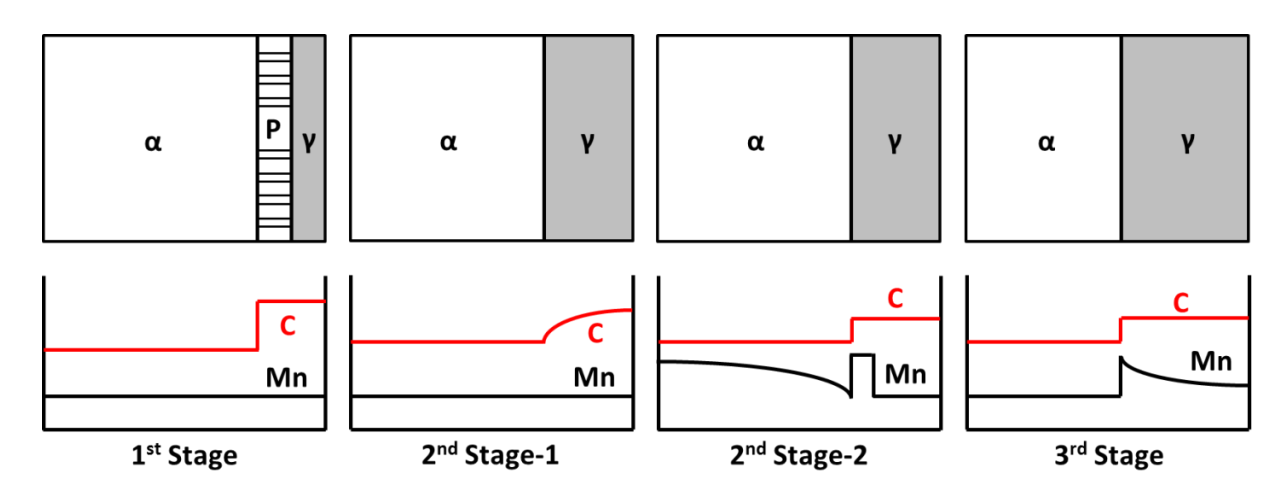


Fig. 2.2 Schematic diagrams of three stages in austenite growth during intercritical annealing from a ferrite-pearlite structure: 1st stage: dissolution of pearlite; 2nd stage-1: austenite growth controlled by C diffusion in austenite; 2nd stage-2: austenite growth controlled by Mn diffusion in ferrite; 3rd stage: final equilibration with Mn diffusion in austenite. (reconstructed based on the work of Speich et al. [2.28])

Similar stages of austenite growth were also established for steels with a quenched martensite structure [2.78, 2.80]. For example, Wei et al. [2.78] investigated growth of austenite from as-quenched martensite during intercritical annealing of a 0.1C–3Mn–1.5Si steel by experiments and DICTRA (diffusion controlled transformation) simulation. It was suggested in their study

that the growth of austenite consisted of three stages, including: (a) initial no-partitioned growth of austenite, controlled by rapid C diffusion in ferrite, which is gradually replaced by C diffusion in austenite, (b) intermediate slow growth, controlled by diffusion of Mn in ferrite, and (c) very slow growth, controlled by Mn diffusion in austenite for final equilibration, which accompanies the shrinkage of austenite. Luo et al. [2.80] studied the austenite reversion behavior of a 0.2C-5Mn steel with a pre-austenitized and quenched martensite structure during intercritical annealing at 650 °C. A similar austenite formation behavior was found, although they separated the formation into four stages (the last two stages correspond to the third stage in Wei's work [2.78]).

The initial microstructure can influence the austenite formation kinetics, despite similar stages of austenite growth for different starting microstructures. It was documented that the initial microstructure can be categorized as ferrite with spheroidized carbides, ferrite with lamellar pearlite, as-quenched, and cold-deformed microstructures, in the order of increasing rate of austenitization [2.88]. Garcia et al. [2.79] investigated austenite formation in the intercritical range for a 0.2C-1.5Mn steel, and found that austenite appeared to form more rapidly from the quenched and tempered (QT) plus cold rolled structure, compared with QT and ferrite/pearlite structures, however, the difference was only slight. Chen et al. [2.89] compared the austenite formation kinetics in a 0.1C-1.5Mn steel with different initial structures in the intercritical range using DICTRA modeling. The results suggested that martensite to austenite transformation was slightly quicker than ferrite/pearlite to austenite transformation.

The morphology of austenite-ferrite mixture can also be controlled by the initial structure. For hot rolled or pre-austenitized and quenched specimens, austenite and ferrite normally show a lath or lamellar morphology after intercritical annealing [2.70, 2.80], whereas a globular or blocky structure forms when the steels are cold rolled, most likely due to the active recovery and recrystallization occurring during the annealing of the deformed samples [2.70]. An example of

the morphology dependence on the initial structure is shown in Fig. 2.3 [2.70].

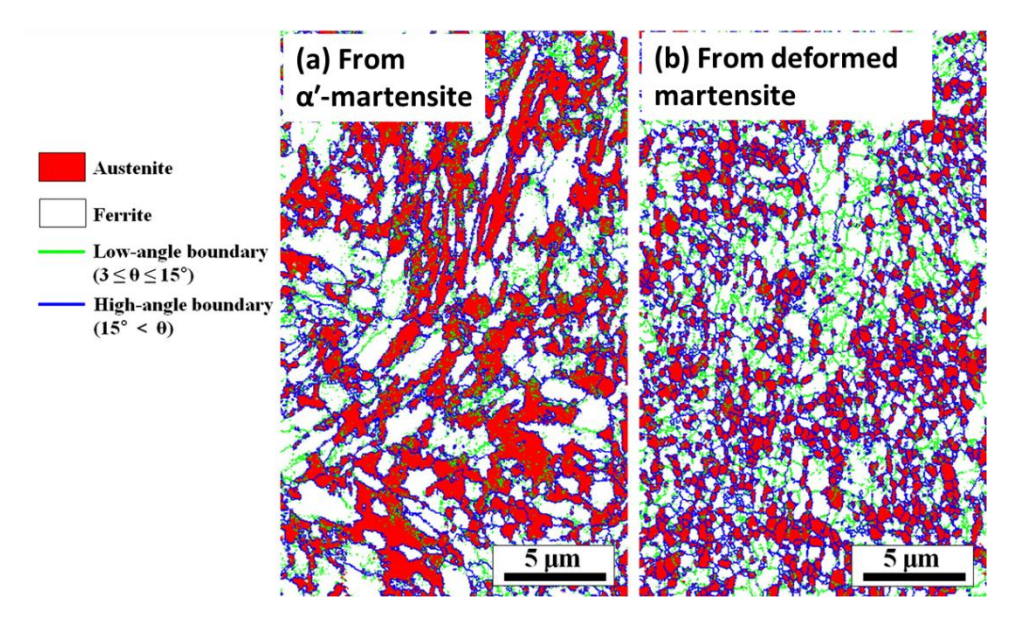


Fig. 2.3 EBSD phase maps of a 0.05C-9Mn medium Mn steel intercritical annealed from (a) hot rolled (α' -martensite) structure and (b) cold rolled (deformed α' -martensite) structure. (reproduced from Ref. [2.70], with permission: © 2014 Elsevier)

The effect of heating rate on austenite reverse transformation behavior of cold rolled 0.05C- $(5\sim9)$ Mn steels with a α' -martensite structure was studied by Han et al. [2.90]. At a heating rate below 15 °C/s, it was observed that cementite formed along various boundaries, and austenite formed near the cementite particles and possessed the globular morphology. When the heating rate was higher than 15 °C/s, austenite reverse transformation occurred without cementite precipitation and lath-shaped austenite grains were formed. It was claimed in their work that diffusive austenite transformation occurred at the slow heating rate, whereas austenite formation was diffusionless for the heating rate higher than 15 °C/s. However, the evidence for this statement seems unconvincing, since neither crystallographic orientation relationships between martensite and the product austenite nor the C concentrations in both phases was given. Cementite formation was also observed at the beginning of annealing (1 min) in the work of Luo et al. [80] who intercritically annealed a 0.2C-5Mn steel with a heating rate of around 40~60 °C/s.

However, they suggested that growth of austenite at the ferrite/cementite interfaces was kinetically sluggish, such that the growth of the intercritical austenite nucleated at the martensite lath boundaries should contribute most to the increase of austenite volume fraction during the annealing.

2.2.2 Other heat treatment methods for medium Mn steels

In addition to intercritical annealing, some other heat treatment methods were proposed recently for medium Mn steels in order to explore the possibilities of further mechanical property improvement. These methods include quenching and partitioning (Q&P) [2.91-2.94], multi-step annealing [2.95, 2.96], and so-called interrupted quenching and intercritical annealing [2.97].

The Q&P process initially proposed by Speer et al. [2.98] for low-alloyed steels have recently been applied in medium Mn steels. The schematic diagram of the thermal cycle used for Q&P process is shown in Fig. 2.4. It consists of four stages: a full or partial austenitization; an initial quench to partially form martensite; a partitioning stage at elevated temperatures to enrich the untransformed austenite with C; a final quenching stage to retain the stable austenite. Due to the increased amount of Mn, applying this process in medium Mn steels can result in a higher fraction of C-enriched austenite compared with low alloyed steels (i.e. a retained austenite fraction of 0.33 was reported by Seo and De Cooman for a 0.2C-4Mn-1.6Si-1Cr steel after Q&P process [2.93]), which can ensure better strength and ductility combinations. Compared with single intercritical annealing, Q&P in medium Mn steels can result in an increase of yield strength due to the present of martensite and suppress static/dynamic strain aging [2.94].

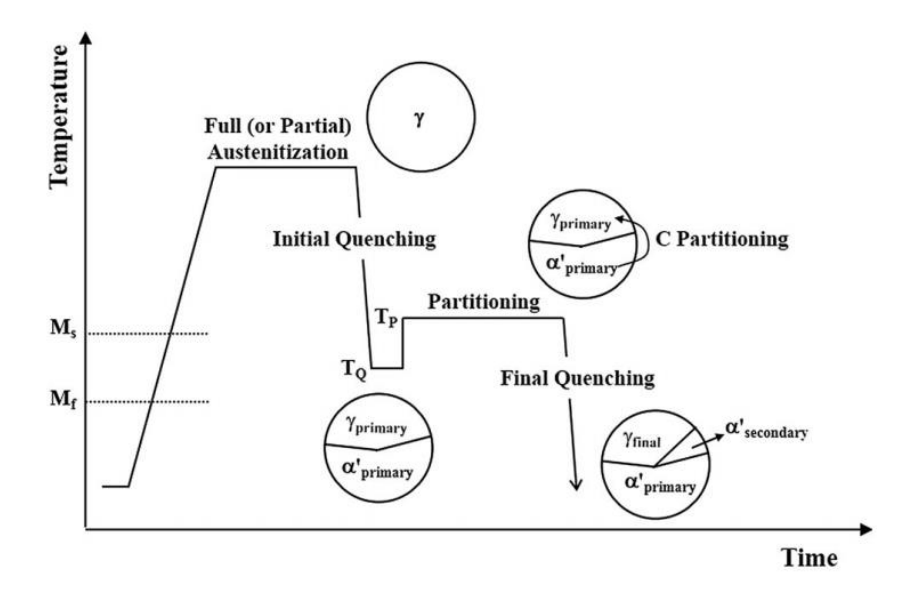


Fig. 2.4 Schematic Q&P processing cycle. (reproduced from Ref. [2.92], with permission: © 2016 Springer)

Some multi-step annealing treatments have also been applied for medium Mn steels, utilizing repeated martensite transformation and austenite reversion [2.95, 2.96]. For example, Heo et al. [2.95] and Liu et al. [2.96] applied a complex four-step anneal, in which steels were firstly annealed at the austenitization temperatures followed by quenching to form a fully martensitic structure, then a very low intercritical temperature (near or slightly lower than A_1 temperature) was used to enrich Mn in austenite; the third step was a rapid annealing at high temperatures (near or higher than A_3 temperature) to form new austenite with lower Mn content and make this austenite transform to martensite upon quenching; the last step was tempering to further increase the stability of the remaining austenite with C partitioning. It was found that the strength of the medium Mn steels after this treatment can be greatly improved without too much loss of ductility compared with one-step intercritical annealed samples [2.96].

Tsuchiyama et al. [2.97] recently proposed a novel interrupted quenching and intercritical annealing treatment for a 0.1C-5Mn-1.2Si steel. The steel was first heated to the austenitization temperatures and then interrupted quenched (IQ) to a temperature between martensite start

temperature and finish temperature to partially form martensite, followed by a subsequent annealing at the lower intercritical range and a final quenching. The untransformed austenite after the IQ stage contained a relatively low Mn content, which remained almost intact during the subsequent annealing due to the low diffusivity of Mn. The austenite reversed in the intercritical annealing stage, however, was enriched with Mn. Upon the final quenching, the untransformed Mn-lean austenite transformed to fresh martensite, whereas the intercritical annealed Mn-rich austenite remained. Therefore, the final microstructure consisted of ferrite, fresh martensite, and Mn-rich austenite. This type of structure was characterized by a higher yield and tensile strength, without too much loss of ductility.

2.3 Austenite Deformation Micromechanics in Medium Mn Steels

2.3.1 Transformation-induced plasticity (TRIP)

The high fraction of retained austenite is the key feature of medium Mn steels, and it is considered to be the main contributor to the high work hardening rate and great strength-ductility combinations. Austenite is generally metastable in such steels and would transform to α' -martensite during deformation, resulting in the well-known TRIP effect.

Figure 2.5 (a) shows schematically the TRIP mechanisms in steels with metastable retained austenite [2.99]. Under deformation the retained austenite transforms to martensite with high C content and high strength, resulting in an increase of strain hardening rate. The transformation is also associated with a volume expansion (around 2~4% [2.100]). Both effects delay the plastic instability (i.e. necking) and extend the range of uniform elongation.

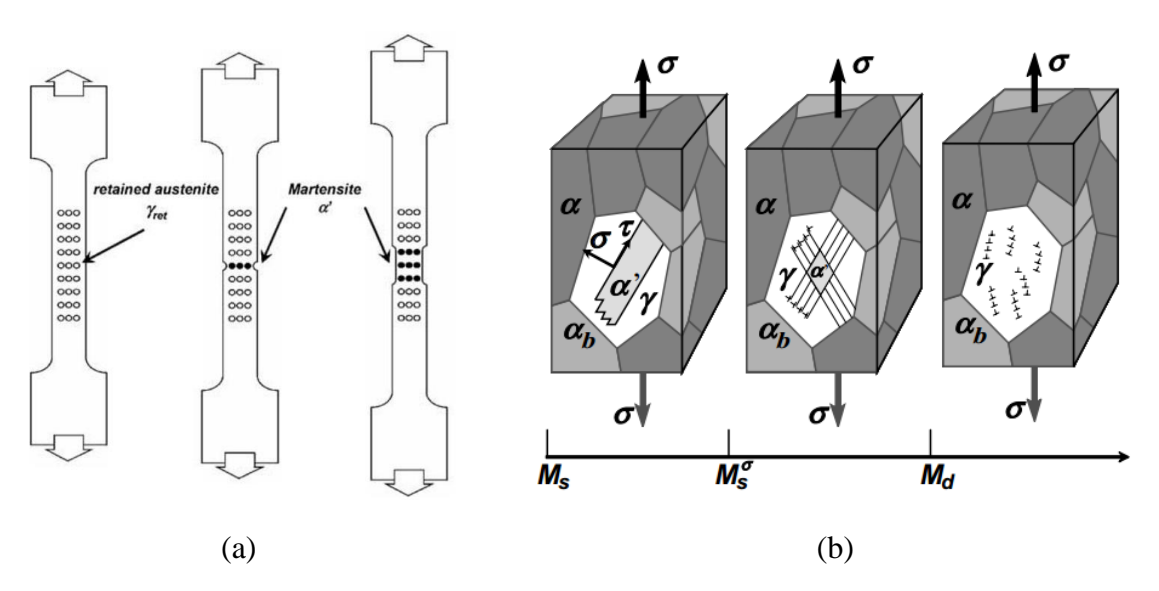


Fig. 2.5 (a) Schematic diagram of the TRIP-assisted plasticity mechanism; (b) Schematic diagram of deformation mechanisms in different ranges of deformation temperature: from left to right is stress-induced martensite formation, strain-induced martensite formation and dislocation glide. (reproduced from Ref. [2.101], with permission: © 2004 Elsevier)

The working hardening behavior of TRIP-assisted steels is critically controlled by the stability of retained austenite. Three deformation temperature ranges should be highlighted with respect to the transformation plasticity mechanisms based on different RA stabilities (Fig. 2.5 (b)): 1. Ms -Ms^o range: stress-induced martensite formation at pre-existing nucleation sites occurs in this range and drives the yielding of austenite. The stress to initiate martensite formation increases with higher temperatures in this range, due to the decreasing transformation driving force. At Ms^o temperature, the stress to initiate martensite formation equals the yield strength of the parent austenite phase. 2. Ms^o-Md range: in this range, the stress for martensite formation is higher than the yield strength of austenite, thus austenite is strained, resulting in strain-induced transformation. It is generally accepted that strain-induced α' -martensite predominantly nucleates at new sites produced by plastic deformation, which consist of ε-martensite, stacking fault bundles and mechanical twins [2.102]. Normally, the ambient temperature should be in this range for the optimal austenite stability and persistent work hardening [2.101]. 3. T > Md range: transformation does not occur in this range due to the high stacking fault energy and low driving force for martensite formation. Therefore, deformation is driven by dislocation glide in this range [2.103].

2.3.2 Twinning-induced plasticity (TWIP)

Another important plasticity-enhanced mechanism of retained austenite in medium Mn steels is the TWIP effect. The high strain hardening rate caused by the TWIP effect is usually attributed to the so-called "dynamical Hall-Petch effect", as illustrated schematically in Fig. 2.6 (a) [2.104]. The formation of deformation twins progressively reduces the effective mean free path or glide distance of dislocations, thus promoting dislocation multiplication and resulting in isotropic strain hardening [2.105]. The back stress effect (i.e. Bauschinger effect) due to dislocation pile-ups at grain or twin boundaries was also proposed to be another important strain hardening source (kinematic hardening) in TWIP steels [2.106]. However, it should be noted that the reported hardening contribution of the back stress effect is still debatable [2.105]. Nevertheless,

it has been documented both experimentally [2.38, 2.107, 2.108] and numerically [2.106] that the strain hardening rate can be enhanced by smaller twin spacing (i.e. higher twin density or fraction). The strain hardening-enhancing effect by deformation twinning is especially useful for the ultra-fine grained structure which normally can be achieved in medium Mn steels, since ultra-fine single phase metals have been widely observed to show a very small strain hardening rate [2.107].

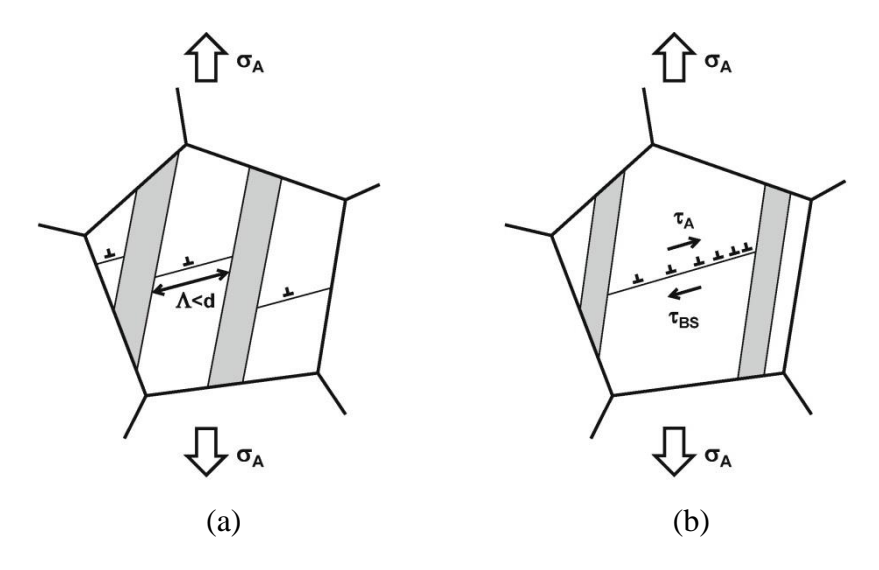


Fig. 2.6 Mechanisms of plasticity enhancement associated with deformation twinning: (a) Dynamic Hall-Petch effect; (b) Back stress effect. Here σ_A and τ_A are the applied stress and the shear stress, respectively, τ_{BS} denotes the back stress, and Λ represents the average twin spacing. (reproduced from Ref. [2.109], with permission: © 2017 Elsevier)

2.3.3 Stacking fault energy

It is now generally accepted that the deformation mechanisms of austenite (deformation-induced martensite or deformation twinning) are related to the SFE of austenite [2.104, 2.109]. For a face-centered cubic (FCC) crystal, a stacking fault is formed by the dissociation of a perfect dislocation into two Shockley partial dislocations of type a/6 <211> which are energetically more favorable. Mechanical twins can result from the collaborative glide of intrinsic Shockley partial dislocations on parallel successive {111} planes, whereas the hexagonal (HCP) ε-martensite

phase can be formed when intrinsic Shockley partial dislocations glide on every second {111} plane [2.110, 2.111].

When SFE is high, perfect dislocation dissociation is unfavorable, such that the only possible deformation mechanism is perfect dislocation glide with frequent cross-slip. With decreasing SFE, dislocation glide becomes more planar, and a large dissociation of dislocations is available, which can result in the nucleation of mechanical twins and their growth by thickening. The critical twinning stress also decreases with lower SFE for FCC metals [2.112, 2.113]. The deformation behavior of austenite will change to ε/α' -martensitic formation when the SFE is getting even lower and at the same time the molar Gibbs energy of the martensitic reaction becomes negative [2.110, 2.111]. Therefore, the deformation modes of austenite (dislocation glide, deformation twinning and phase transformation) normally occur in specific ranges of SFE. Several researchers proposed that the SFE lower than 20 mJ/m² favored ε-martensite formation and higher SFE tended to form mechanical twins [2.36, 2.114]. Frommeyer et al. [2.115] claimed that ε -phase formed a SFE smaller than 16 mJ/m², and a SFE larger than 25 mJ/m² caused deformation twin formation in a stable austenite phase. Allain et al. [2.116] and Lee et al. [2.27] investigated the correlation between SFE and plastic deformation mechanisms in a Fe-22Mn-0.6C TWIP steel and Fe-18Cr-10Mn-N-C stainless steels, respectively. The empirically determined SFE ranges for different deformation behaviors from their studies are plotted in Fig. 2.7.

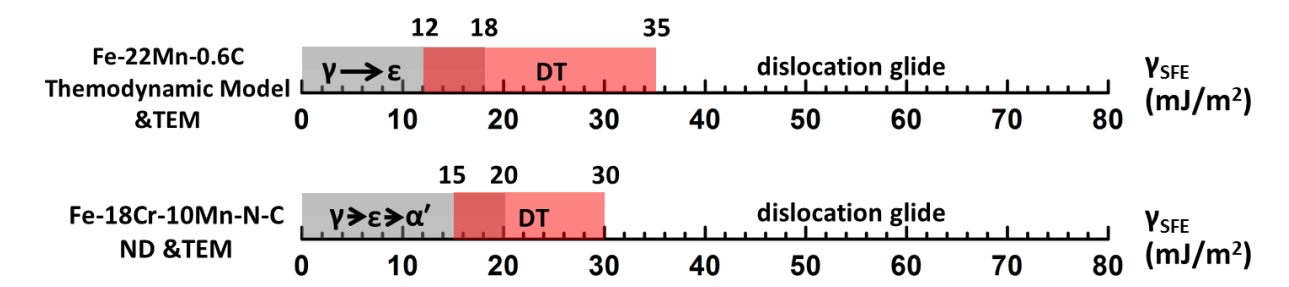


Fig. 2.7 Values of austenite SFE (γ_{SFE}) for different deformation mechanisms of austenite (deformation-induced martensite, deformation twinning and dislocation glide), proposed by Allain et al. [2.116] for a Fe-22Mn-0.6C TWIP steel using thermodynamic model and transmission electron microscopy (TEM), and Lee et al. [2.27] for Fe-18Cr-10Mn-N-C stainless steels by neutron diffraction (ND) and TEM. (γ : austenite, ϵ : ϵ -martensite, α' : α' -martensite, DT: deformation twinning)

Various attempts have been made to determine the values of SFE. The experimental methods include direct TEM method by analyzing dislocation configurations such as extended nodes and stacking fault tetrahedral [2.117], XRD and neutron diffraction methods through analyzing relative peak shifting and broadening [2.27]. There are two basic computational approaches to determine SFE: the thermodynamic method [2.110] and the *ab initio* approach [2.118]. Among all of these methods, the thermodynamic model is probably most widely used due to the relatively simple formula and available thermodynamic data. The model was originally proposed by Olson and Cohen [2.110]. It assumed two atomic planes of HCP stacking (intrinsic stacking fault) separated from the austenite matrix by two interfaces, as such austenite SFE can be expressed by:

$$\gamma_{\rm SFE} = 2\rho(\Delta G^{\gamma \to \varepsilon} + \Delta G_{str}) + 2\sigma_{\gamma/\varepsilon} \tag{2.2}$$

where $\Delta G^{\gamma \to \epsilon}$ is the molar Gibbs energy of austenite to ϵ -martensite phase transformation, which consists of both chemical and magnetic free energies, ΔG_{str} is the strain energy associated with the strain field caused by the different volumes of the γ and ϵ phase, ρ is the molar density along {111} planes, $\sigma_{\gamma/\epsilon}$ is the interfacial energy. The molar Gibbs energy term can be solved by various thermodynamic models, such as sub-regular solution model [2.114, 2.116] and sublattice-type

model [2.117].

It should be highlighted that although austenite SFE is an important factor influencing deformation mechanisms, it is certainly not sufficient on its own. For example, two TWIP steels with similar SFE determined by thermomechanical model, i.e. Fe-30Mn and Fe-22Mn-0.6C, have been reported to show completely different deformation behaviors during tensile straining, with extensive twinning in the Fe-22Mn-0.6C steel and dislocation cell structure formation for the Fe-30Mn steel [2.119]. Sohn et al. [2.120] investigated the tensile behavior of a medium Mn lightweight steel (Fe-0.3C-8.5Mn-5.6Al) with a SFE of around 50 mJ/m², which is above the upper limit of deformation twinning. However, both strain-induced α' -martensite and deformation twins formed during tensile testing. The compositional limitation and the large error sources of SFE determination methods can be argued as one factor responsible for the deviation of the deformation mechanism dependence on SFE. However, the various deformation behaviors should also rely on other metallurgical and mechanical factors, such as C content [2.104], grain size [2.121] and local stress [2.120]. On the other hand, it should be mentioned that there is no direct link between austenite SFE and strain-induced α' -martensite formation, which normally occurs in medium Mn steels [2.30, 2.32].

2.4 Overview of Microstructure-Property Relationship in Medium Mn Steels

2.4.1 Overview of tensile properties of medium Mn steels with different structures

The tensile properties of medium Mn steels reported in the literature are plotted in Fig. 2.8 (a), along with data for other AHSS for comparison. It shows that the property of such steels have been achieved into the target area, which is between the 1st-Gen and 2nd-Gen AHSS. The product of the ultimate tensile strength (UTS) and total elongation (TE) can be as high as ~70 GPa%. This indicates a great potential for the medium Mn steels to become a 3rd-Gen AHSS. Figures 2.8 (b) and 2.9 show the typical microstructure of medium Mn steels after different heat treatments and the corresponding mechanical property. Until now, most of the research has focused on the austenite-ferrite duplex structure (Figs. 2.9 (a~c)), which can be readily produced by annealing at the relatively low intercritical temperature range (i.e. lower than the critical temperature defined in Fig. 2.1 (e)). The morphology of intercritical ferrite (α) and austenite (γ) can be either globular (Fig. 2.9 (a)) or lath (Fig. 2.9 (b)), depending on the starting structure; the grain size of α and γ is generally ultrafine (below 1 µm). Higher amounts of Al and Si will promote the formation of coarse grained δ -ferrite (Fig. 2.9 (c)). Nevertheless, this type of structure shows a great combination of strength and ductility: UTS ranges from ~800 to ~1200 MPa, and TE is generally from ~20 to ~50 %, as shown in Fig. 2.8 (b).

When the IA temperature is relatively high (above the critical value defined in Fig. 2.1 (e)), a multi-phase structure consisting of retained austenite, ferrite and martensite ($\gamma+\alpha+\alpha'$) will form, as shown in Fig. 2.9 (d). The martensite forms upon the rapid cooling stage of IA, and possesses high strength; this increases the yield strength (YS) of the steel. On the other hand, the retained austenite in this type of structure generally possesses a low stability due to the low content of C and Mn (Fig. 2.1 (c)). Deformation-induced transformation from austenite to martensite occurs rapidly at the beginning of deformation and achieves saturated very quickly; this greatly increases the work hardening rate and strength, but significantly reduces the ductility. Therefore, this type of structure always shows a high tensile strength (around 1200~1700MPa) but a limited

total elongation (lower than around 10%) (Fig. 2.8 (b)).

The medium Mn steels heat treated by Q&P and multi-annealing (MA) generally process a $\gamma+\alpha'$ duplex structure or $\gamma+\alpha+\alpha'$ multi-phase structure. In these structures, the austenite is further stabilized by additional C and Mn partitioning, which ensures a more persistent TRIP effect and higher ductility. The martensite phase is also somewhat tempered during the complicated thermal cycles, which also contributes to a higher ductility. Hence, the TE value of this type of structure is higher than the $\gamma+\alpha+\alpha'$ structure processed by IA, whereas the TS value remains similar (Fig. 2.8 (b)).

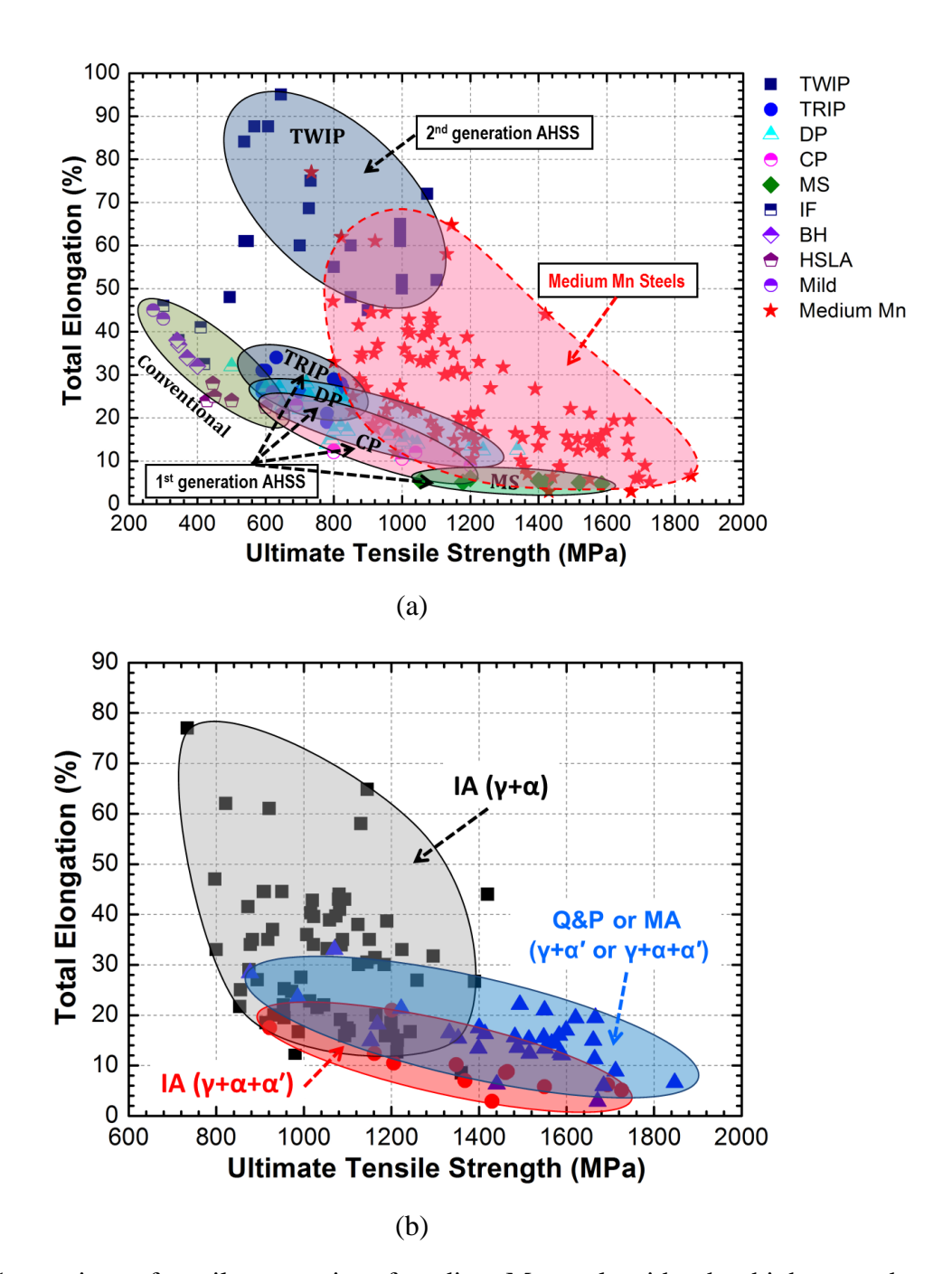


Fig. 2.8 (a) Comparison of tensile properties of medium Mn steels with other high strength steels; (b) Tensile properties of medium Mn steels with different heat treatment methods and microstructures (IA: intercritical annealing; MA: multi-annealing; Q&P: quenching and partitioning). (plotted based on published data [2.12, 2.30, 2.32, 2.44, 2.59, 2.69, 2.91, 2.94-2.97, 2.111, 2.120, 2.122-2.139])

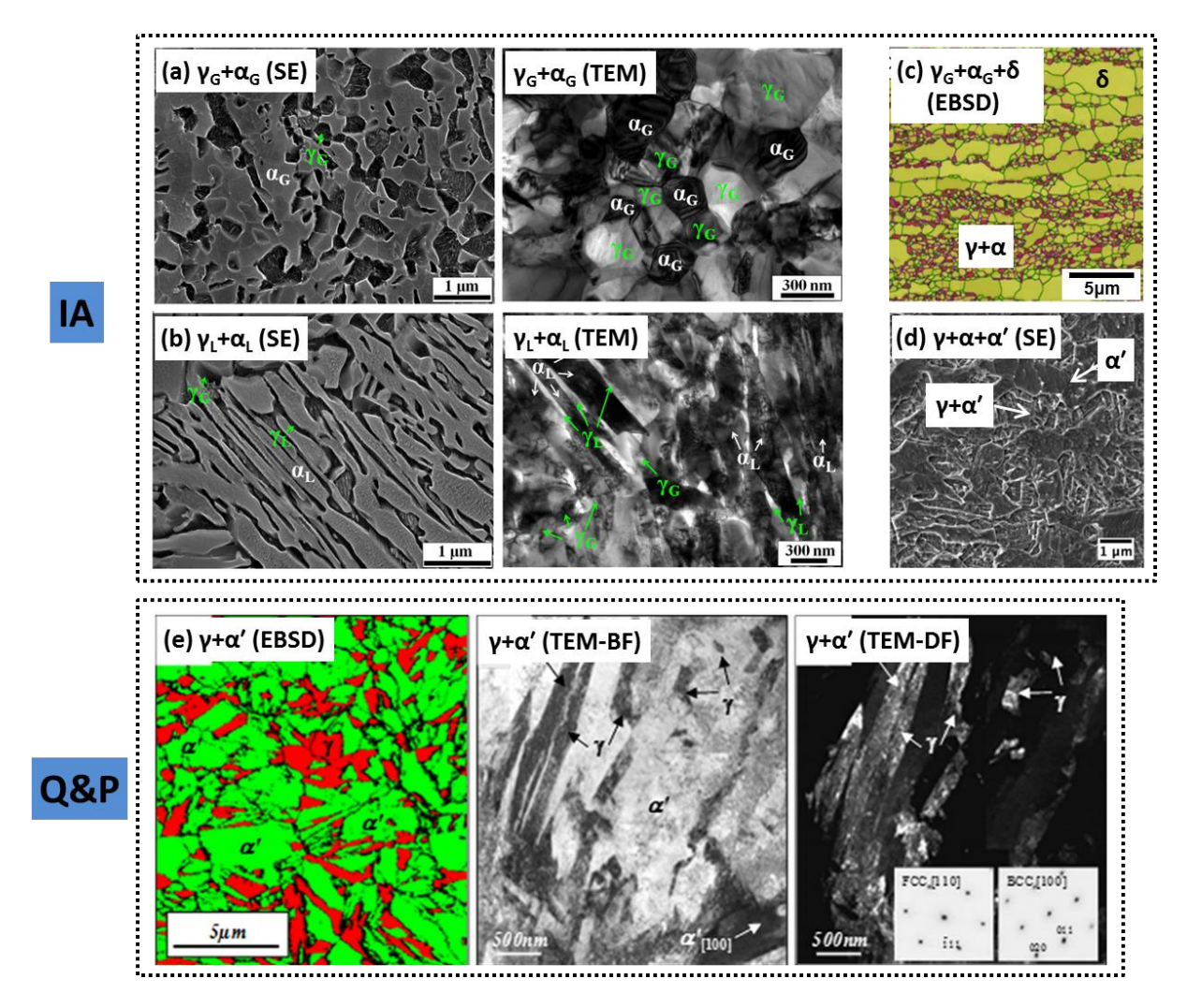


Fig. 2.9 Typical microstructure of medium Mn steels processed with different heat treatments: (a) Secondary electron (SE) imaging and TEM images of a cold rolled Fe-9Mn-0.05C steel heat treated by intercritical annealing, showing a globular-shaped $\gamma+\alpha$ structure [2.70]; (b) SE imaging and TEM images of a hot rolled Fe-9Mn-0.05C steel heat treated by intercritical annealing, showing a lath-shaped $\gamma+\alpha$ structure [2.70]; (c) Electron backscatter diffraction (EBSD) image of a cold rolled 0.12C-5.8Mn-3.1Al steel treated by intercritical annealing, showing the present of δ -ferrite [2.12]; (d) SE imaging of a cold rolled 0.1C-7Mn steel intercritical annealed at a relatively high temperature, showing a $\gamma+\alpha+\alpha'$ multi-phase structure [2.32]; (e) EBSD, TEM bright field (BF) and TEM dark field (DF) images of a 0.2C-4Mn-1.6Si-1Cr steel treated by Q&P process, showing a $\gamma+\alpha'$ two phase structure [2.140]. (reproduced from Ref. [2.70] [2.12] [2.32] and [2.140], with permission: © 2014 Elsevier, ©

2.4.2 Effect of austenite fraction

As aforementioned, austenite is considered to be beneficial for the strength-ductility combinations of AHSS, due to the enhancing effect on work hardening rate and uniform elongation by the activated TRIP and/or TWIP effects. The product of UTS and TE in AHSS generally increases with higher austenite fraction, as revealed in Fig. 2.10. Therefore, increasing the fraction of retained austenite has become an important strategy in medium Mn steels for better mechanical properties.

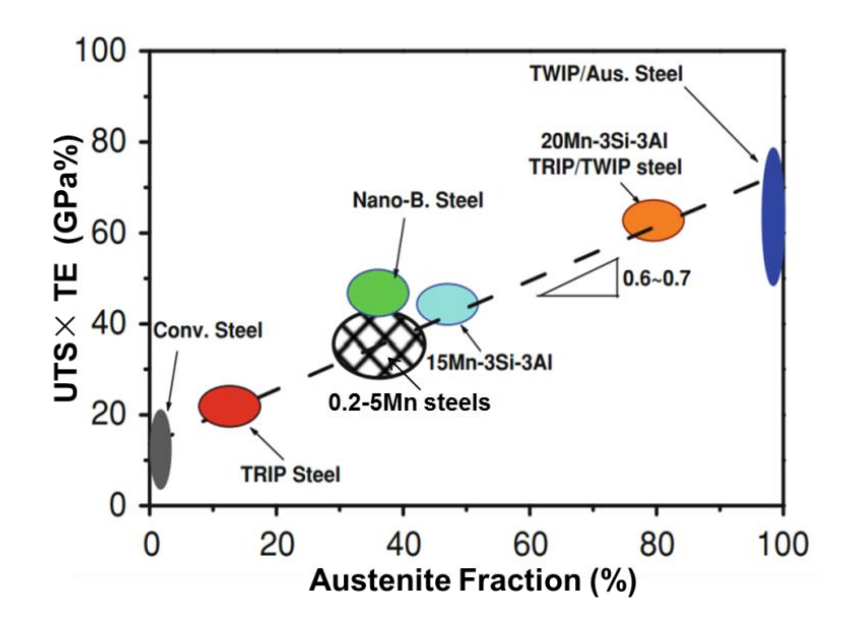


Fig. 2.10 Product of UTS and TE in AHSS as a function of austenite fraction. (reproduced from Ref. [2.131], with permission: © 2010 Elsevier)

The influence of retained austenite fraction on UTS×TE, TE, YS and UTS in intercritical annealed medium Mn steels is shown in Fig. 2.11. In a general scope, the product of UTS and TE in medium Mn steels increases with increasing RA fraction (Fig. 2.11 (a)), which is due to the increase effect of RA on total elongation (Fig. 2.11 (b)). However, both yield strength and tensile

strength decrease when the amount of RA increases up to around 20%, above which the effect of RA fraction on the strength level do not show a clear trend (Fig 2.11 (c) and (d)). The initial strength decrease shown in Figs. 2.11 (c) and (d) is associated with the change in the fraction of fresh martensite in the microstructure. Normally in intercritical annealed medium Mn steels, the formation of fresh martensite upon rapid cooling results in the reduction of retained austenite, such that a lower austenite fraction always corresponds to a higher amount of martensite, which raises the strength level of the steels.

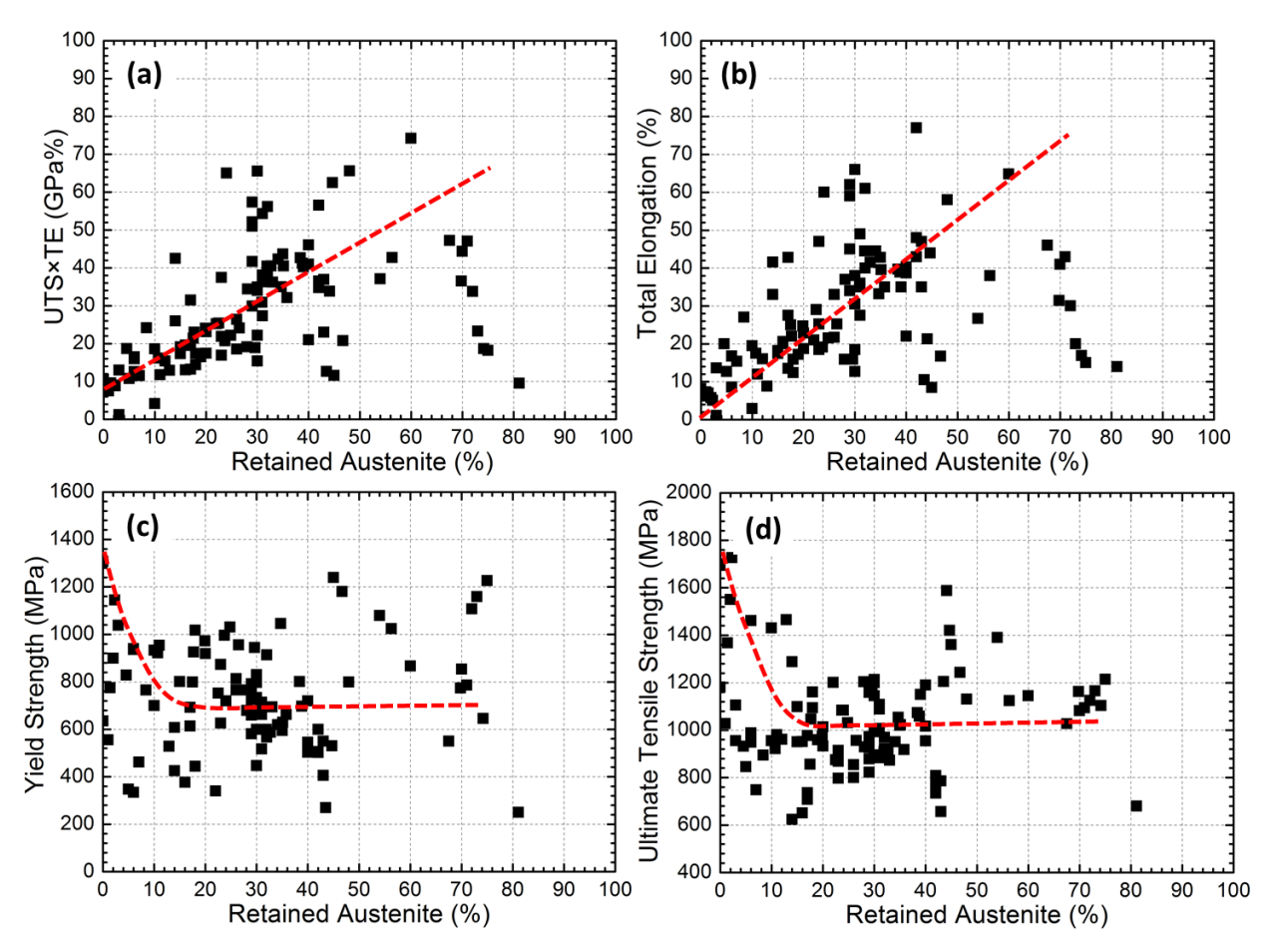


Fig. 2.11 Influence of retained austenite fraction on (a) the product of ultimate tensile strength and total elongation, (b) total elongation, (c) yield strength and (d) ultimate tensile strength in intercritical annealed medium Mn steels. (plotted based on published data [2.6, 2.12, 2.14, 2.30, 2.32, 2.44, 2.69, 2.120, 2.129-2.137, 2.141-2.144])

2.4.3 Effect of austenite stability

For a given medium Mn steel system with an austenite-ferrite duplex structure, the mechanical property is not only dependent on RA fraction. The stability of austenite also plays a key role. A typical example is from the work of Lee and De Cooman [2.30]. In their study, a cold rolled 10Mn-0.3C-3Al-2Si medium Mn steel was subject to intercritical annealing at temperatures from 700 ℃ to 900 ℃, holding for 10min, followed by fast cooling to room temperature. An austenite-ferrite duplex structure was formed after the intercritical annealing. The annealing temperature was reported to have a crucial influence on austenite characteristics, namely, higher annealing temperature increases austenite fraction, but decreases the mechanical stability of austenite. The influence of annealing temperature (i.e. austenite fraction and stability) on the mechanical property of the steel is shown in Figs. 2.12 (a) and (b). The yield strength decreased with higher annealing temperatures, which might be associated with higher austenite fraction (austenite is softer than ferrite in certain medium Mn steel systems as reported by many researchers [2.145-2.147]), larger grain sizes and more complete recrystallization. On the other hand, the lower austenite stability resulted in higher rate of strain-induced martensite formation, as demonstrated in Fig. 2.12 (c); this enhanced the work hardening rate. Therefore, the tensile strength of the steel remained almost unchanged (Fig. 2.12 (a) and (b)), or kept increasing with annealing temperatures, which was observed in many other intercritical annealed medium Mn steels [2.32, 2.147]. One interesting phenomenon is that the TE value first increased and then decreased with higher austenite fractions (i.e. higher annealing temperatures). The maximum TE level was achieved below the peaked austenite fraction. This phenomenon was generally reported in many other reports [2.32, 2.135] and can be explained by the influence of austenite stability. When the austenite stability is too high, the TRIP effect is much reduced thus the work hardening rate drops quickly and necking occurs very early. The ductility is also poor if austenite stability is too low. In this situation, strain or stress induced martensite forms rapidly and replaces the parent austenite phase, and the work hardening cannot be sustained over a large strain range. Therefore, an intermediate level of austenite stability is generally optimum for a

persistent work hardening and a high uniform elongation.

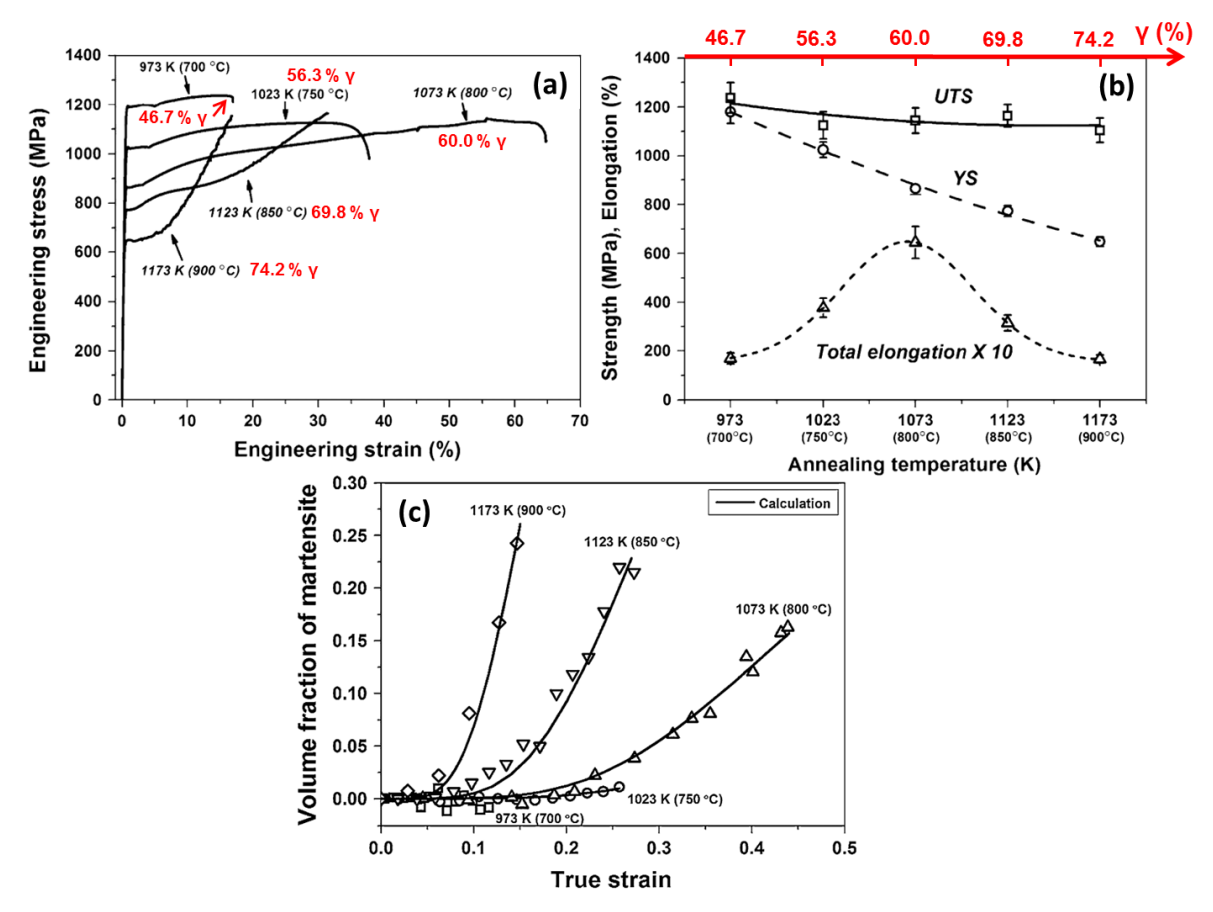


Fig. 2.12 Effect of the intercritical annealing temperature (i.e. austenite fraction and stability) on the (a) engineering stress-strain curve, (b) UTS, YS and TE values and (c) the amount of strain-induced α' -martensite in a 10Mn-0.3C-3Al-2Si medium Mn steel with the austenite-ferrite duplex structure. (reproduced from Ref. [2.30], with permission: © 2014 Springer)

Austenite stability in austenite-ferrite duplex medium Mn steels might also influence the yielding behavior and the PLC effect characterized by serrations in the flow curves. This can be indicated from the work of Gibbs et al. [2.32], who investigated the tensile behavior of a cold rolled 0.1C-7Mn steel subjected to intercritical annealing at different temperatures (Figs. 2.13 (a) and (b)). They showed that a discontinuous yielding behavior, which is associated with the initiation and propagation of Lüders deformation bands, occurred for the samples annealed at low

temperatures, whereas the continuous yielding prevailed at high annealing temperatures. This yielding behavior was studied in more detail by TEM and *in situ* neutron diffraction in their separate articles [2.148, 2.149]. It was proposed that when the room temperature (i.e. testing temperature) was higher than the Ms^{σ} temperature, martensite formation was strain-induced, such that yielding was controlled by localized plastic deformation of strain-aged recrystallized ferrite. This was the situation for the samples annealing at lower temperatures where the stability of austenite was high. When the stability of austenite became lower (for the higher temperature annealed samples), martensite formation can be stress induced and the stress for phase transformation was lower than the yield stress of austenite and ferrite, therefore, yielding was initiated by the stress-induced transformation and behaved as a continuous manner.

On the other hand, it can be seen in Fig. 2.13 (a) that the PLC effect occurred in the samples with the intermediate austenite stability. Lee and De Cooman [2.147] recently pointed out that this PLC effect was associated with strain-induced austenite transformation to martensite. Specifically, they reported that the serrations caused by the PLC effect were generally more pronounced when TRIP effect was activated. In single phase materials, this PLC effect is always associated with dynamic strain aging (DSA), which arises from the dynamic interaction between mobile dislocations and diffusing solute atoms [2.150, 2.151]. However, the in depth characterization of the localized deformation banding behavior, the correlations between the PLC and TRIP effect, and further theories of the PLC effect or DSA in medium Mn steels are currently not available.

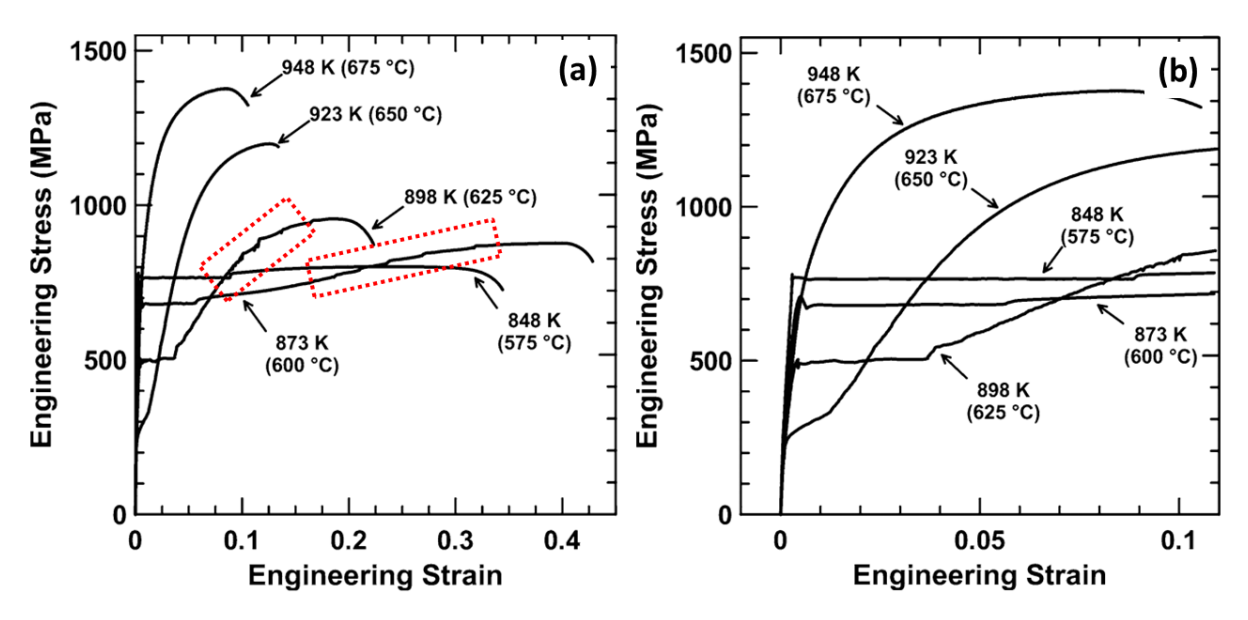


Fig. 2.13 (a) Tensile engineering stress-strain curve and (b) magnified yielding behavior for a 0.1C-7Mn steel intercritical annealed at different temperatures for 1 week, followed by water quench. (the flow curves showing serrations are marked by rectangular frames) (reproduced from Ref. [2.32], with permission: © 2011 Springer)

2.4.4 Effect of austenite deformation mechanisms

Most of the investigated medium Mn steels from the literature show the TRIP effect. However, in some Al-added medium Mn steel systems, the austenite SFE is increased and high enough to activate the TWIP effect, which was experimentally observed by some researchers [2.6, 2.30, 2.44, 2.45, 2.120, 2.143, 2.152, 2.153]. According to the study of Lee and De Cooman [2.30, 2.153], for TRIP and TWIP aided medium Mn steel samples, the work hardening rate is characterized by a typical decrease after the initial Lüders strain, followed by a subsequent increase up to a maximum value. The sample might undergo necking before or after the maximum point [2.30, 2.44, 2.152]. It was proposed in their study that deformation twinning occurred at the first stage of the work hardening. The strain-induced α' -martensite was observed to preferably nucleate at the intersections of deformation twins, and the fraction started to increase when extensive secondary twins formed; the TRIP effect was responsible for the second-stage work hardening increase.

In contrast, Sohn et al. [2.120] defined a three-stage work hardening behavior in an intercritical annealed 0.3C-8.5Mn-5.6Al medium Mn lightweight steel. The first stage corresponded to a continuous decrease to a minimum value, followed by a second stage and a third stage; the last two stages were characterized by two up-down peaks in the strain hardening rate curve. Experiments revealed that austenite grains were deformed by dislocation slipping in the first work hardening stage. In the second stage, deformation twins and strain-induced α' -martensite formed independently in the same grains. Their formations were proposed to be associated with the local orientation variations of austenite grains, which resulted in different resolved shear stresses under tension load. The third stage corresponded to the further thickening or growth of twins and martensite. The mechanical twins did not develop into secondary twins in the whole strain range.

It has to be mentioned that the reports on the TWIP effect in medium Mn steels are still limited, and are generally not conclusive. The effect of different austenite deformation mechanisms on the mechanical behavior of medium Mn steels is expected to be very complicated due to the complex interactions between dislocations, deformation twins and strain-induced martensite. There is an urgent need to quantify the amount of all of these in order to develop a fundamental understanding on the mechanical property dependence on the austenite characteristics, which, indeed, is an extremely challenging work.

2.4.5 Effect of stress/strain distributions

Owing to the multi-phase feature of medium Mn steels and the differences in mechanical behavior among different phases, the distribution of stress or plastic strain under deformation will not be uniform. The strain partitioning between ferrite and martensite has been widely accepted to be one of the important reasons for the initial high strain hardening rate in dual phase (DP) steels [2.154, 2.155]. However, the stress/strain distribution and its effect on the overall mechanical behavior of medium Mn steels have only achieved limited attention. The local

deformation in such steels can be extremely complex due to the dynamically activated TRIP and TWIP effects in austenite, and it will also alter depending on various factors, such as composition, phase fraction and morphology, grain size, and kinetics of TRIP/TWIP. Nevertheless, based on the limited literature [2.70, 2.148, 2.156], the strain partitioning among different phases in medium Mn steels has been reported to have a critical effect on mechanical properties, e.g. yielding behavior [2.70], strain hardening behavior and flow stress [2.148, 2.156]. The research status with respect to this is summarized as follows:

Han et al. [2.70] investigated the tensile behavior of an intercritical annealed α and γ duplex Fe-9Mn-0.05 steel with two different morphologies (lath and globular). The strain distribution between ferrite and the mixed phase of austenite and strain-induced α' -martensite ($\gamma+\alpha'$) was measured through interrupted tensile testing and SEM imaging on the same location of the tensile specimens. It was found that the $\gamma+\alpha'$ phase was more highly strained than α through the entire deformation for the lath-shaped structure, whereas in the globular-shaped structure, the strain concentrated primarily in α up to the yield point elongation and then shifted back to the $\gamma+\alpha'$ phase after the yielding stage. It was claimed that these very different strain partitioning behaviors influenced the yielding behaviors (discontinuous or continuous) for the two structures. However, it should be mentioned that the volume expansion resulted from strain-induced martensite formation would also influence the microscopic strain values measured by SEM imaging.

Gibbs et al. [2.148] used *in situ* neutron diffraction to study the detailed mechanical behavior of each phase in a Fe-7.1Mn-0.1C steel with two types of ultra-fine structures: $\alpha+\gamma+\alpha'$ multi-phase and $\alpha+\gamma$ duplex structures. For the first type of structure, plastic deformation was dominated by stress-induced austenite transformation to martensite at low stresses; it then transferred to a regime determined by ferrite plastic flow at high stresses. However, for the $\alpha+\gamma$ duplex structure, yielding was controlled by strain-aged recrystallized ferrite, after which both ferrite and austenite

were homogeneously deformed.

Latypov et al. [2.156] studied the micromechanical behavior of a Fe-6Mn-0.15C-1.5Si-3Al steel with an $\alpha+\gamma$ duplex microstructure by finite element analysis; the simulations are shown in Fig. 2.14. It was suggested that at low strains during tensile testing, the strain was localized in the initially softer austenite. During further straining, austenite was more strain-hardened due to the activation of coupled TRIP and TWIP effect. The strain started to localize in ferrite when the twinned austenite and martensite mixed phase exceeded the flow stress of strain-hardened ferrite (Fig. 2.14 (a)). However, strain would continuously localize in austenite if the TRIP and TWIP effect are de-activated and the work hardening ability of austenite is decreased, which is the case shown in Fig. 2.14 (b).

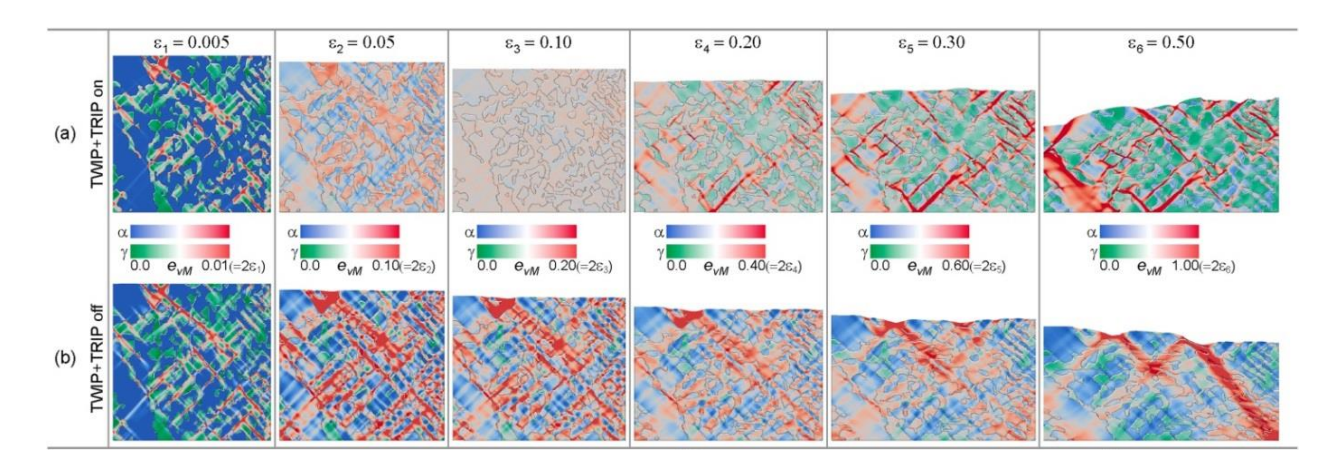


Fig. 2.14 Evolution of von Mises strain fields simulated by microstructure-based finite element method during plain strain tensile deformation in the Fe-6Mn-0.15C-1.5Si-3Al steel with TRIP and TWIP effect (a) activated and (b) de-activated. (reproduced from Ref. [2.156], with permission: © 2016 Elsevier)

2.5 References

- [2.1] S. Lee, W. Woo, B.C. de Cooman, Analysis of the tensile behavior of 12 pct Mn multi-phase $(\alpha + \gamma)$ TWIP+ TRIP steel by neutron diffraction, Metallurgical and Materials Transactions A, 47 (2016), 2125-2140.
- [2.2] S. Lee, B.C. De Cooman, *Influence of intra-granular ferrite on the tensile behavior of intercritically annealed 12 pct Mn TWIP+TRIP steel*, Metallurgical and Materials Transactions A, 46 (2015), 1012-1018.
- [2.3] H. Farahani, W. Xu, S. Van der Zwaag, *Prediction and validation of the austenite phase fraction upon intercritical annealing of medium Mn steels*, Metallurgical and Materials Transactions A, 46 (2015), 4978-4985.
- [2.4] C.H. Seo, K.H. Kwon, K. Choi, K.H. Kim, J.H. Kwak, S. Lee, N.J. Kim, *Deformation behavior of ferrite-austenite duplex lightweight Fe-Mn-Al-C steel*, Scripta Materialia, 66 (2012), 519-522.
- [2.5] D. Raabe, D. Ponge, O. Dmitrieva, B. Sander, *Nanoprecipitate-hardened 1.5 GPa steels with unexpected high ductility*, Scripta Materialia, 60 (2009), 1141-1144.
- [2.6] B. He, H. Luo, M. Huang, Experimental investigation on a novel medium Mn steel combining transformation-induced plasticity and twinning-induced plasticity effects, International Journal of Plasticity, 78 (2016), 173-186.
- [2.7] S.Y. Han, S.Y. Shin, S. Lee, N.J. Kim, J.H. Kwak, K.G. Chin, *Effect of carbon content on cracking phenomenon occurring during cold rolling of three light-weight steel plates*, Metallurgical and Materials Transactions A, 42 (2011), 138-146.
- [2.8] H. Aydin, E. Essadiqi, I.H. Jung, S. Yue, *Development of 3rd generation AHSS with medium Mn content alloying compositions*, Materials Science and Engineering: A, 564 (2013), 501-508.
- [2.9] S. Lee, Y. Estrin, B.C. De Cooman, *Constitutive modeling of the mechanical properties of V-added medium manganese TRIP steel*, Metallurgical and Materials Transactions, 44 (2013), 3136-3146.
- [2.10] M. Cai, Z. Li, Q. Chao, P.D. Hodgson, A novel Mo and Nb microalloyed medium Mn trip steel with maximal ultimate strength and moderate ductility, Metallurgical and Materials Transactions A, 45 (2014), 5624-5634.
- [2.11] Y. Han, J. Shi, L. Xu, W. Cao, H. Dong, Effects of Ti addition and reheating quenching on grain refinement and mechanical properties in low carbon medium manganese martensitic steel, Materials & Design, 34 (2012), 427-434.
- [2.12] D.W. Suh, S.J. Park, T.H. Lee, C.S. Oh, S.J. Kim, *Influence of Al on the microstructural evolution and mechanical behavior of low-carbon, manganese transformation-induced-plasticity steel*, Metallurgical and Materials Transactions A, 41 (2010), 397-408.

- [2.13] H. Aydin, Effect of Microstructure on Static and Dynamic Mechanical Properties of Third Generation Advanced High Strength Steels, Department Mining and Materials Engineering, McGill University, Montreal, Canada, 2013.
- [2.14] P.J. Gibbs: *Design considerations for the third generation advanced high strength steel*, Department of Metallurgical and Materials Engineering, Colorado School of Mines, Golden, CO, United States, 2012.
- [2.15] K.W. Andrews, *Empirical formulae for the calculation of some transformation temperatures*, The Journal of the Iron and Steel Institute, 203 (1965), 721-727.
- [2.16] G. Krauss, *Principles of heat treatment and processing of steels*, American Society for Metals, USA, 1990.
- [2.17] R.A. Grange, H.M. Stewart, *The temperature range of martensite formation*, Trans. AIME, 167 (1946), 467-501.
- [2.18] T.H. Lee, C.S. Oh, S.J. Kim, *Effects of nitrogen on deformation-induced martensitic transformation in metastable austenitic Fe-18Cr-10Mn-N steels*, Scripta Materialia, 58 (2008), 110-113.
- [2.19] T. Angel, Formation of martensite in austenitic stainless steels-effects of deformation, temperature, and composition, The Journal of the Iron and Steel Toostitute, 177 (1954), 165-174.
- [2.20] N. Fonstein, *The effect of chemical composition on formation of ferrite–martensite structures and mechanical properties of dual-phase steels*, in: Advanced High Strength Sheet Steels: Physical Metallurgy, Design, Processing, and Properties, Springer International Publishing Switzerland, 2015.
- [2.21] Y.K. Lee, C. Choi, Driving force for $\gamma \rightarrow \varepsilon$ martensitic transformation and stacking fault energy of γ in Fe-Mn binary system, Metallurgical and Materials Transactions A, 31 (2000), 355-360.
- [2.22] N. Cabanas, J. Penning, N. Akdut, B.C. De Cooman, *High-temperature deformation properties of austenitic Fe-Mn alloys*, Metallurgical and Materials Transactions A, 37 (2006), 3305-3315.
- [2.23] B.C. De Cooman, *High Mn TWIP steel and medium Mn steel*, in: R. Rana, S.B. Singh (Eds.), Automotive Steels: Design, Metallurgy, Processing and Applications, 2017 Elsevier Ltd., Woodhead Publishing, 2017.
- [2.24] J.H. Kang, T. Ingendahl, J. von Appen, R. Dronskowski, W. Bleck, *Impact of short-range ordering on yield strength of high manganese austenitic steels*, Materials Science and Engineering: A, 614 (2014), 122-128.
- [2.25] T.H. Lee, H.Y. Ha, B. Hwang, S.J. Kim, E. Shin, *Effect of carbon fraction on stacking fault energy of austenitic stainless steels*, Metallurgical and Materials Transactions A, 43 (2012), 4455-4459.

- [2.26] P.J. Brofman, G.S. Ansell, On the effect of carbon on the stacking fault energy of austenitic stainless steels, Metallurgical and Materials Transactions A, 9 (1978), 879-880.
- [2.27] T.H. Lee, E. Shin, C.S. Oh, H.Y. Ha, S.J. Kim, Correlation between stacking fault energy and deformation microstructure in high-interstitial-alloyed austenitic steels, Acta Materialia, 58 (2010), 3173-3186.
- [2.28] G.R. Speich, V.A. Demarest, R.L. Miller, *Formation of austenite during intercritical annealing of dual-phase steels*, Metallurgical and Materials Transactions A, 12 (1981), 1419-1428.
- [2.29] Q. Lai, M. Goun & A. Perlade, T. Pardoen, P. Jacques, O. Bouaziz, Y. Br & het, *Mechanism of austenite formation from spheroidized microstructure in an intermediate Fe-0.1C-3.5Mn steel*, Metallurgical and Materials Transactions A, 47 (2016), 3375-3386.
- [2.30] S. Lee, B.C. De Cooman, Annealing temperature dependence of the tensile behavior of 10 pct Mn multi-phase TWIP-TRIP steel, Metallurgical and Materials Transactions A, 45 (2014), 6039-6052.
- [2.31] S. Lee, B.C. De Cooman, *On the selection of the optimal intercritical annealing temperature for medium Mn TRIP steel*, Metallurgical and Materials Transactions A, 44 (2013), 5018-5024.
- [2.32] P.J. Gibbs, E. De Moor, M.J. Merwin, B. Clausen, J.G. Speer, D.K. Matlock, *Austenite stability effects on tensile behavior of manganese-enriched-austenite transformation-induced plasticity steel*, Metallurgical and Materials Transactions A, 42 (2011), 3691-3702.
- [2.33] D.W. Suh, J.H. Ryu, M.S. Joo, H.S. Yang, K. Lee, H. Bhadeshia, *Medium-alloy manganese-rich transformation-induced plasticity steels*, Metallurgical and Materials Transactions A, 44 (2013), 286-293.
- [2.34] T. Furukawa, Dependence of strength-ductility characteristics on thermal history in lowcarbon, 5 wt-% Mn steels, Materials Science and Technology, 5 (1989), 465-470.
- [2.35] X. Wang, L. Wang, M. Huang, Kinematic and thermal characteristics of Lüders and Portevin-Le Châtelier bands in a medium Mn transformation-induced plasticity steel, Acta Materialia, 124 (2017), 17-29.
- [2.36] K. Sato, M. Ichinose, Y. Hirotsu, Y. Inoue, *Effects of deformation induced phase transformation and twinning on the mechanical properties of austenitic Fe-Mn-Al alloys*, ISIJ International. 29 (1989), 868-877.
- [2.37] B.W. Oh, S.J. Cho, Y.G. Kim, Y.P. Kim, W.S. Kim, S.H. Hong, *Effect of aluminium on deformation mode and mechanical properties of austenitic Fe-Mn-Cr-Al-C alloys*, Materials Science and Engineering: A ,197 (1995), 147-156.
- [2.38] K. Jeong, J.E. Jin, Y.S. Jung, S. Kang, Y.K. Lee, The effects of Si on the mechanical twinning and strain hardening of Fe-18Mn-0.6 C twinning-induced plasticity steel, Acta

- Materialia, 61 (2013), 3399-3410.
- [2.39] J. Kim, S.J. Lee, B.C. De Cooman, *Effect of Al on the stacking fault energy of Fe-18Mn-0.6C twinning-induced plasticity*, Scripta Materialia, 65 (2011), 363-366.
- [2.40] G.R. Lehnhoff, K.O. Findley, B.C. De Cooman, *The influence of silicon and aluminum alloying on the lattice parameter and stacking fault energy of austenitic steel*, Scripta Materialia, 92 (2014), 19-22.
- [2.41] J.E. Jin, Y.K. Lee, *Effects of Al on microstructure and tensile properties of C-bearing high Mn TWIP steel*, Acta Materialia, 60 (2012), 1680-1688.
- [2.42] M. Kang, W. Woo, Y.K. Lee, B.S. Seong, *Neutron diffraction analysis of stacking fault energy in Fe-18Mn-2Al-0.6 C twinning-induced plasticity steels*, Materials Letters, 76 (2012) 93-95.
- [2.43] A. Saeed-Akbari, J. Imlau, U. Prahl, W. Bleck, *Derivation and variation in composition-dependent stacking fault energy maps based on subregular solution model in high-manganese steels*, Metallurgical and Materials Transactions A, 40 (2009), 3076-3090.
- [2.44] S. Lee, K. Lee, B.C. De Cooman, *Observation of the TWIP+ TRIP plasticity-enhancement mechanism in Al-added 6 Wt pct medium Mn steel*, Metallurgical and Materials Transactions A, 46 (2015), 2356-2363.
- [2.45] H. Aydin, I.H. Jung, E. Essadiqi, S. Yue, *Twinning and tripping in 10% Mn steels*, Materials Science and Engineering: A, 591 (2014), 90-96.
- [2.46] D.W. Suh, S.J. Park, T.H. Lee, C.S. Oh, S.J. Kim, *Influence of Al on the microstructural evolution and mechanical behavior of low-carbon, manganese transformation-induced-plasticity steel*, Metallurgical and Materials Transactions A, 41 (2010), 397.
- [2.47] S.Y. Han, S.Y. Shin, H.J. Lee, B.J. Lee, S. Lee, N.J. Kim, J.H. Kwak, *Effects of annealing temperature on microstructure and tensile properties in ferritic lightweight steels*, Metallurgical and Materials Transactions A, 43 (2012), 843-853.
- [2.48] S.J. Park, B. Hwang, K. Lee, T.H. Lee, D.W. Suh, H. Han, *Microstructure and tensile behavior of duplex low-density steel containing 5mass% aluminum*, Scripta Materialia, 68 (2013), 365-369.
- [2.49] Y.S. Chun, K.T. Park, C.S. Lee, *Delayed static failure of twinning-induced plasticity steels*, Scripta Materialia, 66 (2012), 960-965.
- [2.50] I.J. Park, K.H. Jeong, J.G. Jung, C.S. Lee, Y.K. Lee, *The mechanism of enhanced resistance to the hydrogen delayed fracture in Al-added Fe-18Mn-0.6C twinning-induced plasticity steels*, International Journal of Hydrogen Energy, 37 (2012), 9925-9932.
- [2.51] T. Shun, C.M. Wan, J.G. Byrne, A study of work hardening in austenitic Fe-Mn-C and Fe-Mn-Al-C alloys, Acta Metallurgica et Materialia, 40 (1992), 3407-3412.
- [2.52] E. Girault, A.I. Mertens, P. Jacques, Y. Houbaert, B. Verlinden, J. Van Humbeeck,

- Comparison of the effects of silicon and aluminium on the tensile behaviour of multiphase TRIP-assisted steels, Scripta materialia, 44 (2001), 885-892.
- [2.53] P.J. Jacques, E. Girault, A. Mertens, B. Verlinden, J.van Humbeeck, F. Delannay, *The developments of cold-rolled TRIP-assisted multiphase steels*. *Al-alloyed TRIP-assisted multiphase steels*, ISIJ International, 41 (2001), 1068-1074.
- [2.54] P.J. Jacques, *Phase transformations in transformation induced plasticity (TRIP)-assisted multiphase steels*, in: E. Pereloma and D.V. Edmonds (Eds.), Phase Transformations in Steels, Vol. 2, Woodhead Publishing Ltd., Philadelphia, 2012.
- [2.55] P. Abramowitz, R.A. Moll, Silicon-carbon interaction and its effect on the notch toughness of mild steel, Metallurgical Transactions, 1 (1970), 1773-1775.
- [2.56] Y.U. Heo, Y.Y. Song, S.J. Park, H. Bhadeshia, D.W. Suh, *Influence of silicon in low density Fe-C-Mn-Al Steel*, Metallurgical and Materials Transactions A, 43 (2012), 1731-1735.
- [2.57] K.D. Sibley, N.N. Breyer, *The effect of silicon on the impact and tensile properties of low-carbon steels*, Metallurgical and Materials Transactions A, 7 (1976), 1602-1604.
- [2.58] C.C. Anya, T.N. Baker, *The effect of silicon on the grain size and the tensile properties of low carbon steels*, Materials Science and Engineering: A, 118 (1989), 197-206.
- [2.59] O. Grässel, G. Frommeyer, *Effect of martensitic phase transformation and deformation twinning on mechanical properties of Fe-Mn-Si-Al steels*, Materials Science and Technology, 14 (1998) 1213-1217.
- [2.60] J.Y. Koo, G. Thomas, *Design of duplex Fe/X/0.1C steels for improved mechanical properties*, Metallurgical Transactions A, 8 (1977), 525-528.
- [2.61] S. Hironaka, H. Tanaka, T. Matsumoto, *Effect of Si on mechanical property of galvannealed dual phase steel*, Materials Science Forum, 638-642 (2010), 3260-3265.
- [2.62] J. Barros, T. Ros-Yanez, L. Vandenbossche, L. Dupr é, J. Melkebeek, Y. Houbaert, *The effect of Si and Al concentration gradients on the mechanical and magnetic properties of electrical steel*, Journal of Magnetism and Magnetic Materials, 290-291 (2005), 1457-1460.
- [2.63] R.G. Davies, Influence of silicon and phosphorous on the mechanical properties of both ferrite and dual-phase steels, Metallurgical Transactions A, 10 (1979), 113-118.
- [2.64] F. Gonz alez, Y. Houbaert, A review of ordering phenomena in iron-silicon alloys, Revista De Metalurgia, 49 (2013), 178-199.
- [2.65] B. Viala, J. Degauque, M. Fagot, M. Baricco, E. Ferrara, F. Fiorillo, *Study of the brittle behaviour of annealed Fe-6.5 wt% Si ribbons produced by planar flow casting*, Materials Science and Engineering: A, 212 (1996), 62-68.
- [2.66] A. Dumay, J.P. Chateau, S. Allain, S. Migot, O. Bouaziz, *Influence of addition elements on the stacking-fault energy and mechanical properties of an austenitic Fe–Mn–C steel*, Materials Science and Engineering: A, 483-484 (2008), 184-187.

- [2.67] X. Tian, Y. Zhang, Effect of Si content on the stacking fault energy in γ-Fe–Mn–Si–C alloys: Part I. X-ray diffraction line profile analysis, Materials Science and Engineering: A, 516 (2009), 73-77.
- [2.68] H. Huang, O. Matsumura, T. Furukawa, *Retained austenite in low carbon, manganese steel after intercritical heat treatment*, Materials Science and Technology, 10 (1994), 621-626.
- [2.69] Q. Han, Y. Zhang, L. Wang, *Effect of annealing time on microstructural evolution and deformation characteristics in 10Mn1.5Al TRIP Steel*, Metallurgical and Materials Transactions A, 46 (2015), 1917-1926.
- [2.70] J. Han, S.J. Lee, J.G. Jung, Y.K. Lee, *The effects of the initial martensite microstructure on the microstructure and tensile properties of intercritically annealed Fe-9Mn-0.05 C steel*, Acta Materialia, 78 (2014), 369-377.
- [2.71] D. Koistinen, R. Marburger, A general equation prescribing the extent of the austenite-martensite transformation in pure iron-carbon alloys and plain carbon steels, Acta Metallurgica, 7 (1959,) 59-60.
- [2.72] S.J. Lee, C.J. Van Tyne, A kinetics model for martensite transformation in plain carbon and low-alloyed steels, Metallurgical and Materials Transactions A, 43 (2012), 422-427.
- [2.73] S. Van Bohemen, *Bainite and martensite start temperature calculated with exponential carbon dependence*, Materials Science and Technology, 28 (2012), 487-495.
- [2.74] S. Van Bohemen, J. Sietsma, *Effect of composition on kinetics of athermal martensite formation in plain carbon steels*, Materials Science and Technology, 25 (2009), 1009-1012.
- [2.75] S.J. Lee, S. Lee, B.C. De Cooman, *Martensite transformation of sub-micron retained austenite in ultra-fine grained manganese transformation-induced plasticity steel*, International Journal of Materials Research, 104 (2013), 423-429.
- [2.76] E. De Moor, D.K. Matlock, J.G. Speer, M.J. Merwin, *Austenite stabilization through manganese enrichment*, Scripta Materialia, 64 (2011), 185-188.
- [2.77] N. Nakada, T. Tsuchiyama, S. Takaki, N. Miyano, *Temperature dependence of austenite nucleation behavior from lath martensite*, ISIJ International, 51 (2011), 299-304.
- [2.78] R. Wei, M. Enomoto, R. Hadian, H.S. Zurob, G.R. Purdy, *Growth of austenite from as-quenched martensite during intercritical annealing in an Fe-0.1 C-3Mn-1.5 Si alloy*, Acta Materialia, 61 (2013), 697-707.
- [2.79] C.I. Garcia, A.J. Deardo, Formation of austenite in 1.5 pct Mn steels, Metallurgical Transactions A, 12 (1980), 521-530.
- [2.80] H. Luo, J. Shi, C. Wang, W. Cao, X. Sun, H. Dong, Experimental and numerical analysis on formation of stable austenite during the intercritical annealing of 5Mn steel, Acta Materialia, 59 (2011), 4002-4014.
- [2.81] X. Cai, A.J. Garratt-Reed, W.S. Owen, The development of some dual-phase steel

- structures from different starting microstructures, Metallurgical and Materials Transactions A, 16 (1985), 543-557.
- [2.82] J. Ågren, Computer simulations of the austenite/ferrite diffusional transformations in low alloyed steels, Acta Metallurgica, 30 (1982), 841-851.
- [2.83] A. Arlazarov, Evolution of Microstructure and Mechanical Properties of Medium Mn Steels and Their Relationship, University of Lorraine, France, 2015, 109-117.
- [2.84] M. Goun & P. Maugis, J. Drillet, A criterion for the change from fast to slow regime of cementite dissolution in Fe–C–Mn steels, Journal of Materials Science & Technology, 28 (2012), 728-736.
- [2.85] Q. Lai, Optimization of the Microstructure of Ferritic-Martensitic Steels with 3.5 wt. % Mn: Phase Transformations and Micromechanical Modeling, Joseph Fourier University, France, 2014, 44-64.
- [2.86] G.R. Speich, A. Szirmae, M.J. Richards, *Formation of austenite from ferrite and ferrite-carbide aggregates*, Transactions of the Metallurgical Society of AIME, 245 (1969), 1063-1074.
- [2.87] J. Yang, H.K.D.H. Bhadeshia, *Reaustenitization experiments on some high-strength steel weld deposits*, Materials Science and Engineering: A, 118 (1989), 155-170.
- [2.88] N. Fonstein: Advanced High Strength Sheet Steels-Physical Metallurgy-Design, Processing, and Properties, Springer International Publishing, 2015.
- [2.89] H. Chen, X. Xu, W. Xu, S. van der Zwaag, *Predicting the austenite fraction after intercritical annealing in lean steels as a function of the initial microstructure*, Metallurgical and Materials Transactions A, 45 (2014), 1675-1679.
- [2.90] J. Han, Y.K. Lee, The effects of the heating rate on the reverse transformation mechanism and the phase stability of reverted austenite in medium Mn steels, Acta Materialia, 67 (2014), 354-361.
- [2.91] Z. Zhao, J. Liang, A. Zhao, J. Liang, D. Tang, Y. Gao, *Effects of the austenitizing temperature on the mechanical properties of cold-rolled medium-Mn steel system*, Journal of Alloys and Compounds, 691 (2017), 51-59.
- [2.92] E.J. Seo, L. Cho, B.C. De Cooman, *Modified methodology for the quench temperature selection in quenching and partitioning (Q&P) processing of steels*, Metallurgical and Materials Transactions A, 47 (2016), 3797-3802.
- [2.93] E.J. Seo, L. Cho, B.C. De Cooman, *Application of quenching and partitioning processing to medium Mn steel*, Metallurgical and Materials Transactions A, 46 (2015), 27-31.
- [2.94] B.C. Cooman, S.J. Lee, S. Shin, E.J. Seo, J.G. Speer, *Combined intercritical annealing and Q&P processing of medium Mn steel*, Metallurgical and Materials Transactions A, 1 (2016), 39-45.

- [2.95] Y.U. Heo, D.H. Kim, N.H. Heo, C.W. Hong, S.J. Kim, *Deformation behavior in medium Mn steel of nanometer-sized* $\alpha'+\gamma$ *lamellar structure*, Metallurgical and Materials Transactions A, 47 (2016), 6004-6016.
- [2.96] S. Liu, Z. Xiong, H. Guo, C. Shang, R.D.K. Misra, *The significance of multi-step partitioning: Processing-structure-property relationship in governing high strength-high ductility combination in medium-manganese steels*, Acta Materialia, 124 (2017), 159-172.
- [2.97] T. Tsuchiyama, T. Inoue, J. Tobata, D. Akama, S. Takaki, *Microstructure and mechanical properties of a medium manganese steel treated with interrupted quenching and intercritical annealing*, Scripta Materialia, 122 (2016), 36-39.
- [2.98] J. Speer, D.K. Matlock, B.C. De Cooman, J.G. Schroth, *Carbon partitioning into austenite after martensite transformation*, Acta Materialia, 51 (2003), 2611-2622.
- [2.99] J.M. Jang, S.J. Kim, N.H. Kang, K.M. Cho, D.W. Suh, *Effects of annealing conditions on microstructure and mechanical properties of low carbon, manganese transformation-induced plasticity steel*, Metals and Materials International, 15 (2009), 909-916.
- [2.100] J.M. Moyer, G.S. Ansell, *The volume expansion accompanying the martensite transformation in iron-carbon alloys*, Metallurgical Transactions A, 6 (1975), 1785-1791.
- [2.101] B.C. De Cooman, Structure–properties relationship in TRIP steels containing carbide-free bainite, Current Opinion in Solid State and Materials Science, 8 (2004), 285-303.
- [2.102] G.B. Olson, M. Cohen, *Kinetics of strain-induced martensitic nucleation*, Metallurgical Transactions A, 6 (1975), 791-795.
- [2.103] G.B. Olson, M. Cohen, A mechanism for the strain-induced nucleation of martensitic transformations, Journal of the Less Common Metals, 28 (1972), 107-118.
- [2.104] O. Bouaziz, S. Allain, C. Scott, P. Cugy, D. Barbier, *High manganese austenitic twinning induced plasticity steels: a review of the microstructure properties relationships*, Current Opinion in Solid State and Materials Science, 15 (2011), 141-168.
- [2.105] Z. Liang, Y. Li, M. Huang, *The respective hardening contributions of dislocations and twins to the flow stress of a twinning-induced plasticity steel*, Scripta Materialia, 112 (2016), 28-31.
- [2.106] O. Bouaziz, S. Allain, C. Scott, Effect of grain and twin boundaries on the hardening mechanisms of twinning-induced plasticity steels, Scripta Materialia, 58 (2008), 484-487.
- [2.107] X. Chen, L. Lu, Work hardening of ultrafine-grained copper with nanoscale twins, Scripta Materialia, 57 (2007), 133-136.
- [2.108] I. Gutierrez-Urrutia, D. Raabe, Dislocation and twin substructure evolution during strain hardening of an Fe–22 wt.% Mn–0.6 wt.% C TWIP steel observed by electron channeling contrast imaging, Acta Materialia, 59 (2011), 6449-6462.
- [2.109] B.C. De Cooman, Y. Estrin, S.K. Kim, Twinning-induced plasticity (TWIP) steels, Acta

- Materialia, In press, 2017.
- [2.110] G.B. Olson, M. Cohen, A general mechanism of martensitic nucleation: Part I. General concepts and the FCC→HCP transformation, Metallurgical Transactions A, 7 (1976), 1897-1904.
- [2.111] S. Curtze, V.T. Kuokkala, Dependence of tensile deformation behavior of TWIP steels on stacking fault energy, temperature and strain rate, Acta Materialia, 58 (2010), 5129-5141.
- [2.112] S. Curtze, Characterization of the Dynamic Behavior and Microstructure Evolution of High Strength Sheet Steels, Tampere University of Technology, 2009.
- [2.113] H. Suzuki, C.S. Barrett, *Deformation twinning in silver-gold alloys*, Acta Metallurgica, 6 (1958), 156-165.
- [2.114] O. Grässel, G. Frommeyer, C. Derder, H. Hofmann, *Phase transformations and mechanical properties of Fe-Mn-Si-Al TRIP-steels*, Journal de Physique Archives, 7 (1997), 383-388.
- [2.115] G. Frommeyer, U. Brüx P. Neumann, Supra-ductile and high-strength manganese -TRIP/TWIP steels for high energy absorption purposes, ISIJ Internatinal, 43 (2003) 438-446.
- [2.116] S. Allain, J.P. Chateau, O. Bouaziz, S. Migot, N. Guelton, *Correlations between the calculated stacking fault energy and the plasticity mechanisms in Fe–Mn–C alloys*, Materials Science and Engineering: A, 387 (2004), 158-162.
- [2.117] D.T. Pierce, J.A. Jiménez, J. Bentley, D. Raabe, C. Oskay, J. Wittig, *The influence of manganese content on the stacking fault and austenite/ɛ-martensite interfacial energies in Fe-Mn-(Al-Si) steels investigated by experiment and theory*, Acta Materialia, 68 (2014), 238-253.
- [2.118] A. Abbasi, A. Dick, T. Hickel, J. Neugebauer, *First-principles investigation of the effect of carbon on the stacking fault energy of Fe–C alloys*, Acta Materialia, 59 (2011), 3041-3048.
- [2.119] O. Bouaziz, H. Zurob, B. Chehab, J.D. Embury, S. Allain, M. Huang, *Effect of chemical composition on work hardening of Fe-Mn-C TWIP steels*, Materials Science and Technology, 27 (2011), 707-709.
- [2.120] S.S. Sohn, K. Choi, J.H. Kwak, N.J. Kim, S. Lee, *Novel ferrite–austenite duplex lightweight steel with 77% ductility by transformation induced plasticity and twinning induced plasticity mechanisms*, Acta Materialia, 78 (2014), 181-189.
- [2.121] S. Takaki, H. Nakatsu, Y. Tokunaga, *Effects of austenite grain size on & martensitic transformation in Fe-15mass*% *Mn alloy*, Materials Transactions, JIM, 34 (1993,) 489-495.
- [2.122] K.G. Chin, C.Y. Kang, S.Y. Shin, S. Hong, S. Lee, H.S. Kim, K.h. Kim, N.J. Kim, *Effects of Al addition on deformation and fracture mechanisms in two high manganese TWIP steels*, Materials Science and Engineering: A, 528 (2011), 2922-2928.
- [2.123] S. Kang, Y.S. Jung, J.H. Jun, Y.K. Lee, Effects of recrystallization annealing temperature on carbide precipitation, microstructure, and mechanical properties in Fe-18Mn-0.6C-1.5Al

- TWIP steel, Materials Science and Engineering: A, 527 (2010), 745-751.
- [2.124] O. Kwon, Development of high performance high manganese TWIP steels in POSCO, Proceedings of HMnS2011, 2011.
- [2.125] S. Keeler, M. Kimchi, *Advanced High Strength Steel Application Guidelines: Version 5*, WorldAutoSteel 2014, http://www.worldautosteel.org.
- [2.126] M. Otto, D. John, R. Schmidt-Juergensen, B. Springub, M. Cornelissen, B. Berkhout, J. Patel, *HSD*® *STEELS OPTIMIZED TWIP STEELS*, Proceedings of HMnS2011, 2011.
- [2.127] Y. Weng, H. Dong, Y. Gan, *Advanced Steels: The Recent Scenario in Steel Science and Technology*, Springer-Verlag Berlin Heidelberg and Metallurgical Industry Press, 2011.
- [2.128] K. Cho, K.V. Redkin, M. Hua, C.I. Garcia, A.J. DeArdo, *Recent development of Nb-containing DP590, DP780 and DP980 steels for production on continuous galvanizing lines*, in: Y. Weng, H. Dong, Y. Gan (Eds.), Advanced Steels: The Recent Scenario in Steel Science and Technology, Springer-Verlag Berlin Heidelberg and Metallurgical Industry Press, 2011.
- [2.129] R.L. Miller, *Ultrafine-grained microstructures and mechanical properties of alloy steels*, Metallurgical Transaction, 3 (1972), 905-912.
- [2.130] H. Dong, W. Cao, J. Shi, C. Wang, M. Wang, *The medium manganese steels: phenomena and industry potentials*, Proceedings of HMnS2011, 2011.
- [2.131] J. Shi, X. Sun, M. Wang, W. Hui, H. Dong, W. Cao, *Enhanced work-hardening behavior and mechanical properties in ultrafine-grained steels with large-fractioned metastable austenite*, Scripta Materialia, 63 (2010), 815-818.
- [2.132] S. Lee, S.J. Lee, S.S. Kumar, K. Lee, B.C. De Cooman, *Localized deformation in multiphase, ultra-fine-grained 6 pct Mn transformation-induced plasticity steel*, Metallurgical and Materials Transactions A, 42 (2011), 3638-3651.
- [2.133] Y. Zhang, L. Wang, K.O. Findley, J.G. Speer, *Influence of temperature and grain size on austenite stability in medium manganese steels*, Metallurgical and Materials Transactions A, 48 (2017), 2140-2149.
- [2.134] H. Jun, O. Yakubovsky, N. Fonstein, *On stability of retained austenite in medium Mn TRIP steels*, Proceedings of HMnS 2011, 2011.
- [2.135] C. Shao, W. Hui, Y. Zhang, X. Zhao, Y. Weng, *Microstructure and mechanical properties of hot-rolled medium-Mn steel containing 3% aluminum*, Materials Science and Engineering: A, 682 (2017), 45-53.
- [2.136] H.W. Yen, S.W. Ooi, M. Eizadjou, A. Breen, C.Y. Huang, H. Bhadeshia, S.P. Ringer, *Role of stress-assisted martensite in the design of strong ultrafine-grained duplex steels*, Acta Materialia, 82 (2015), 100-114.
- [2.137] C. Wang, W. Cao, J. Shi, C. Huang, H. Dong, Deformation microstructures and strengthening mechanisms of an ultrafine grained duplex medium-Mn steel, Materials Science

- and Engineering: A, 562 (2013), 89-95.
- [2.138] L. Cho, E.J. Seo, B.C. De Cooman, *Near-Ac3 austenitized ultra-fine-grained quenching and partitioning (Q&P) steel*, Scripta Materialia, 123 (2016), 69-72.
- [2.139] E.J. Seo, L. Cho, Y. Estrin, B.C. De Cooman, *Microstructure-mechanical properties* relationships for quenching and partitioning (Q&P) processed steel, Acta Materialia, 113 (2016), 124-139.
- [2.140] E.J. Seo, L. Cho, B.C. De Cooman, *Application of quenching and partitioning processing to medium Mn Steel*, Metallurgical and Materials Transactions A, 46 (2015), 27-31.
- [2.141] T. Furukawa, H. Huang, O. Matsumura, *Effects of carbon content on mechanical properties of 5% Mn steels exhibiting transformation induced plasticity*, Materials science and technology 10, (1994), 964-970.
- [2.142] F. Yang, H. Luo, C. Hu, E. Pu, H. Dong, *Effects of intercritical annealing process on microstructures and tensile properties of cold-rolled 7Mn steel*, Materials Science and Engineering: A, 685 (2017), 115-122.
- [2.143] C.Y. Lee, J. Jeong, J. Han, S.J. Lee, S. Lee, Y.K. Lee, Coupled strengthening in a medium manganese lightweight steel with an inhomogeneously grained structure of austenite, Acta Materialia, 84 (2015), 1-8.
- [2.144] A. Arlazarov, M. Goun & O. Bouaziz, A. Hazotte, G. Petitgand, P. Barges, *Evolution of microstructure and mechanical properties of medium Mn steels during double annealing*, Materials Science and Engineering: A, 542 (2012), 31-39.
- [2.145] K. Lee, S.J. Park, Y.S. Choi, S.J. Kim, T.H. Lee, K.H. Oh, H.N. Han, *Dual-scale correlation of mechanical behavior in duplex low-density steel*, Scripta Materialia, 69 (2013), 618-621.
- [2.146] H. Choi, S. Lee, J. Lee, F. Barlat, B.C. De Cooman, *Characterization of fracture in medium Mn steel*, Materials Science and Engineering: A, 687 (2017), 200-210.
- [2.147] S. Lee, S. Shin, M. Kwon, K. Lee, B.C. De Cooman, *Tensile properties of medium Mn steel with a bimodal UFG* $\alpha+\gamma$ *and coarse* δ -ferrite microstructure, Metallurgical and Materials Transactions A, 48 (2017), 1678-1700.
- [2.148] P.J. Gibbs, B.C. De Cooman, D.W. Brown, B. Clausen, J.G. Schroth, M.J. Merwin, D.K. Matlock, *Strain partitioning in ultra-fine grained medium-manganese transformation induced plasticity steel*, Materials Science and Engineering: A, 609 (2014,) 323-333.
- [2.149] B.C. De Cooman, P. Gibbs, S. Lee, D.K. Matlock, *Transmission electron microscopy analysis of yielding in ultrafine-grained medium Mn transformation-induced plasticity steel*, Metallurgical and Materials Transactions A, 44 (2013), 2563-2572.
- [2.150] A.H. Cottrell, B.A. Bilby, *Dislocation theory of yielding and strain ageing of iron*, Proceedings of the Physical Society, 62 (1949), 49-62.

- [2.151] S.J. Lee, J. Kim, S.N. Kane, B.C. De Cooman, *On the origin of dynamic strain aging in twinning-induced plasticity steels*, Acta Materialia, 59 (2011), 6809-6819.
- [2.152] S. Lee, B.C. De Cooman, *Tensile behavior of intercritically annealed ultra fine grained 8% Mn multi-phase steel*, Steel Research International, 86 (2015), 1170-1178.
- [2.153] S. Lee, B.C. De Cooman, *Tensile behavior of intercritically annealed 10 pct Mn multi-phase steel*, Metallurgical and Materials Transactions A, 45 (2014), 709-716.
- [2.154] M. Calcagnotto, Y. Adachi, D. Ponge, D. Raabe, *Deformation and fracture mechanisms in fine- and ultrafine-grained ferrite/martensite dual-phase steels and the effect of aging*, Acta Materialia, 59 (2011), 658-670.
- [2.155] M. Delinc & Y. Brechet, J.D. Embury, M.G.D. Geers, P.J. Jacques, T. Pardoen, *Structure*—property optimization of ultrafine-grained dual-phase steels using a microstructure-based strain hardening model, Acta Materialia, 55 (2007), 2337-2350.
- [2.156] M.I. Latypov, S. Shin, B.C. De Cooman, H.S. Kim, *Micromechanical finite element analysis of strain partitioning in multiphase medium manganese TWIP+TRIP steel*, Acta Materialia, 108 (2016), 219-228.

CHAPTER 3

_

PHASE TRANSFORMATION BEHAVIOR OF MEDIUM MANGANESE STEELS WITH 3 WT PCT ALUMINUM AND 3 WT PCT SILICON DURING INTERCRITICAL ANNEALING

This chapter concerns the phase transformation behavior during intercritical annealing of two hot rolled medium Mn steels with compositions of Fe-0.2C-(7~10)Mn-3Al-3Si (in wt.%). The steel samples have been reported previously to show a coupled TRIP and TWIP effect during tensile straining. However, the detailed phase transformation behavior with respect to the austenite formation during reheating and the subsequent austenite decomposition upon quenching needs clarification. This knowledge can then provide better microstructural control of high Al-Si medium Mn steels, which is beneficial for the subsequent cold rolling process and further improvement of mechanical properties of such steels.

This chapter has been published as: Binhan Sun*, Fateh Fazeli, Colin Scott and Stephen Yue,
 "Phase transformation behavior of medium manganese steels with 3 wt pct aluminum and 3
 wt pct silicon during intercritical annealing", Metall. Mater. Trans. A, 47 (2016),
 4869-4882.

3.1 Abstract

Medium manganese steels alloyed with sufficient aluminum and silicon amounts contain high fractions of retained austenite adjustable to various transformation-induced plasticity (TRIP)/twinning-induced plasticity (TWIP) effects, in addition to a reduced density suitable for lightweight vehicle body-in-white assemblies. Two hot-rolled medium manganese steels containing 3 wt.% aluminum and 3 wt.% silicon were subjected to different annealing treatments in the present study. The evolution of the microstructure in terms of austenite transformation upon reheating and the subsequent austenite decomposition during quenching was investigated. Manganese content of the steels prevailed the microstructural response. The microstructure of the leaner alloy with 7 wt.% Mn (7Mn) was substantially influenced by the annealing temperature, including the variation of phase constituents, the morphology and composition of intercritical austenite, the Ms temperature and the retained austenite fraction. In contrast, the richer variant 10 wt.% Mn steel (10Mn) exhibited a substantially stable ferrite-austenite duplex phase (FADP) microstructure containing a fixed amount of retained austenite which was found to be independent of the variations of intercritical annealing temperature. Austenite formation from hot band ferrite-pearlite/bainite mixtures was very rapid during annealing at 1000 °C, regardless of Mn contents. Austenite growth was believed to be controlled at early stages by carbon diffusion following pearlite/bainite dissolution. The redistribution of Mn in ferrite and particularly in austenite at later stages was too subtle to result in a measureable change in austenite fraction. Further, the hot band microstructure of both steels contained a large fraction of coarse-grained δ-ferrite, which remained almost unchanged during intercritical annealing. A recently developed thermodynamic database was evaluated using the experimental data. The new database achieved a better agreement with the experimental results for the 7Mn steel compared with the existing commercial TCFE database, however, some discrepancy in the predicted phase fractions and compositions still existed. The phase transformation behavior of the two steels during annealing and its implication on the design of high aluminum-silicon medium manganese steels were discussed in detail.

3.2 Introduction

Road transportation vehicles are required to meet stringent standards on fuel economy, emissions and safety by 2025. Vehicle manufacturers are currently developing new lightweight body-in-white assemblies with intensive use of advanced high strength steels (AHSS) to ensure crashworthiness and rigidity. To this end, substantial research and development activities are proceeding globally to deploy superior AHSS grades, so-called third generation AHSS (3rd Gen), with target performance exceeding the properties of conventional dual phase (DP) and transformation induced plasticity (TRIP) steels. One of the strong candidates for 3rd Gen AHSS is medium Mn steels containing nearly 3 to 10 wt.% Mn [3.1-3.3]. High volume fraction of retained austenite (up to 70 vol.%) stabilized by the increased Mn contents constitutes a key advantage of this class of 3rd Gen AHSS and offers excellent mechanical performance [3.2, 3.4-3.10]. In particular, the required processing route is relatively simple and consists of a controlled intercritical annealing (IA) treatment without a need for subsequent bainite overaging or martensite quenching-partitioning [3.8, 3.11, 3.12]. However, numerous microstructures containing different combinations of ferrite, austenite and martensite/bainite with various phase fractions can be produced depending on the IA parameters [3.5, 3.8, 3.13]. Further, partitioning of C and substitutional alloying elements during annealing alters the response of the retained austenite upon subsequent forming operations or in-service deformations [3.8, 3.12, 3.14-3.16]. As such, it is crucial to explore and understand the microstructural evolution during intercritical annealing of medium Mn steels with the main target to define optimized processing parameters for increased fraction and stability of the retained austenite in the final 3rd Gen AHSS sheet or strip products.

Recently, several medium Mn steels alloyed with relatively high Al and/or Si contents, have attracted considerable attentions. The total content of Al and Si is typically higher than ~4 wt.% in these alloys [3.5, 3.15-3.20], leading to a reduced overall density [3.21]. In particular, the stacking fault energy (SFE) of austenite can be tailored by Al and Si additions to promote various

TRIP/TWIP effects, giving rise to a further improvement of mechanical property [3.15, 3.16, 3.18-3.20, 3.22-3.24]. For example, our previous study found that both TRIP and TWIP effect could be activated to achieve a noticeable combination of strength-ductility balance of 27,000 MPa.% in a hot rolled 10Mn-3Al-3Si alloy [3.5, 3.22]. However, high amounts of Al and Si in these steels stabilize ferrite and enlarge the two phase (α + γ) domain so that thermomechanical processing in the two phase range cannot be avoided [3.17]. The ensuing hot/cold rolled microstructure is often complicated containing a certain amount of δ -ferrite along with retained austenite and other phases [3.19, 3.25-3.27]. To our knowledge, there are no detailed literature reports on the evolution and response of this complex microstructure upon subsequent intercritical processing. Further, accurate thermodynamic data for this group of medium Mn steels is unavailable currently, which constitutes extra challenges to preselect suitable annealing parameters.

The scope of the present study was the microstructural evolution of 7 and 10 wt.% medium Mn hot-rolled steels containing 3 wt.% Al and Si upon different intercritical annealing treatments, with the main objective to provide a better understanding on the microstructural control for this type of medium Mn steels. The work focused on hot rolled products, which share similar features with cold rolled sheets in terms of intercritical austenite formation and alloy partitioning. As such, the ensuing insights especially the effect of annealing parameters on fraction, composition and stability of retained austenite can be readily exploited for processing of cold rolled high Si-Al, medium Mn 3rd Gen AHSS sheets. Further, considering the lack of accurate thermodynamic description for these high Al-Si medium Mn steels, the current results are deemed very beneficial for development of more reliable thermodynamic database for similar steels. The assessment of microstructure-property correlations of the studied steels is the subject of ongoing study and is not presented here.

3.3 Experimental Procedure

The chemical compositions of the investigated medium Mn steels are shown in Table 3.1, and herein they are referred to as 7Mn and 10Mn. The steel melts were prepared in a vacuum induction furnace and cast into 100 kg ingots. Following homogenization at 1200 $^{\circ}$ C for 3 h, the ingots were hot rolled in the temperature range from 1100 $^{\circ}$ C to 750 $^{\circ}$ C and air cooled. The coiling process was then simulated by maintaining the hot bands at ~600 $^{\circ}$ C and furnace cooling.

Table 3.1 Steel compositions in weight percent

Alloy	С	Mn	Al	Si	Mo	Fe
7Mn	0.22	7.15	3.11	3.21	0.05	balance
10Mn	0.20	10.02	3.17	3.19	0.06	balance

Specimens were cut from the hot rolled plates and subjected to heat treatments in a box furnace with a protective argon atmosphere, followed by water quenching. A secondary thermocouple was positioned in contact with the samples to ensure a precise control of the temperature. The effect of annealing temperature and time on microstructural evolution was investigated separately. The first set of samples was annealed at various temperatures ranging from 700 $\,^{\circ}$ C to 1200 $\,^{\circ}$ C with 100 $\,^{\circ}$ C increments for 1 h. The second set was subjected to a constant temperature of 1000 $\,^{\circ}$ C for different holding times between 1 min and 5 h.

Microstructure observations were performed with a Nikon Epiphot 200 optical microscope (OM) and a Hitachi SU3500 Scanning Electron Microscope (SEM) equipped with an electron backscattered diffraction (EBSD) detector. Samples for OM and SEM examinations were etched with 2 % nital followed by 10 % aqueous sodium metabisulfite (Na₂S₂O₅). For EBSD observation, samples were finally polished with 0.05 μ m colloidal silica for 4~8 hours in a vibratory polisher. The austenite fraction of the samples was determined by X-ray diffraction (XRD) using Co K_{α} radiation, operated at 35 kV and 45 mA with scan step size of 0.02 °. The

acquired data was analyzed by the Reitveld whole diffraction pattern fitting procedures [3.28] implemented by the TOPAS 4 software. The pearlite, bainite and martensite volume fractions were measured based on the ASTM E1245-03 standard [3.29], using the image processing software ImageJ; more than 15 OM micrographs taken in a relatively low magnification (200×) were randomly selected for this measurement. Austenite grain size was determined by the standard linear intercept method [3.30] based on the OM and SEM images; about 200 intercepts were yielded for each measurement for a standard deviation of less than 20 %.

Composition analysis (Mn, Al and Si) for specific phases were performed in SEM using Energy-Dispersive X-Ray Spectrometer (EDS). The average C content of austenite was determined from the XRD data by adopting the equation proposed by Dyson and Holmes [3.31, 3.32]:

$$\alpha_{\gamma}$$
 (Å) = 3.556 + 0.0453 $x_{\rm C}$ + 0.00095 $x_{\rm Mn}$ + 0.0056 $x_{\rm Al}$,

where α_{γ} is austenite lattice parameter, x_C , x_{Mn} , and x_{Al} are concentrations of C, Mn and Al in austenite (wt.%). In the present study, α_{γ} was determined from the interplanar spacing (d_{hkl}) of the (111) peak of austenite [3.33], which is the most pronounced peak in the XRD pattern and should yield the highest accuracy. The phase composition measurements by EDS/XRD were conducted for different randomly selected locations of each specimen, and the values were averaged. It should be noted that all the error bars shown in this paper reflect the relative deviation from several measurements for different sample locations; the precision of the techniques were not included.

3.4 Results

3.4.1 Hot rolled microstructure

Figure 3.1 shows the hot band microstructures of the 7Mn and 10Mn steel illustrating elongated bands due to hot rolling in two-phase region. In the 7Mn steel (Figs. 3.1 (a) and (b)), three different phases are identified: δ -ferrite (δ), pearlite (P) and bainite (B). Pearlite in conjunction with bainite transformed from the prior austenite during the coiling simulation process. The volume fractions of pearlite and bainite in the hot rolled 7Mn steel are 32.2 \pm 1.5 % and 8.2 \pm 0.7 %, respectively, measured by the image analysis using OM micrographs. Retained austenite was not found in the hot-rolled microstructure of the 7Mn steel, as also confirmed by XRD measurements (Fig. 3.1 (d)). In contrast for the 10Mn steel, a large amount of retained austenite (γ) exists (37.9 \pm 2.7 vol.% calculated by XRD) in the microstructure of the hot bands. Only a small amount of pearlite (7.4 \pm 0.6 vol.% measured by OM image analysis) is present on the edge of the austenite islands.

3.4.2 Effect of annealing temperature

The microstructure of the 7Mn steel is highly influenced by the reheating temperature during subsequent annealing of the hot bands. As shown in Fig. 3.2, the initial pearlite and bainite transform completely to austenite and ferrite after 1 h annealing at 800 °C. However, the banded features of the hot rolled microstructure remain unchanged, consisting of contiguous δ -ferrite regions engulfing austenite/ferrite bands. EBSD and SEM images (Figs. 3.2) show that both intercritical austenite (γ) and ferrite (α) adopt two distinct morphologies: lath shape and globular shape annotated by elliptical and rectangular frames, respectively in Figs. 3.2 (a) and (b) and labelled by γ_G , γ_L , α_G and α_L . It was confirmed in the previous work [3.27] that the globular-shaped phases were transformed from pearlite, whereas the austenite and ferrite formed from bainite have the lath morphology. It seems that γ_L nucleates from the fine lath-like carbide particles in the initial bainite, as also reported by Huang et al. [3.11] who studied a 0.1C-5Mn steel with an initial bainite plus martensite microstructure. The grain size of γ and α is fine, i.e.

~2.5 µm for globular-shaped phases and less than 1 µm in width for lath-shaped phases, whereas the δ -ferrite grains are coarse (50~100 µm). The Mn content of γ_L is 8.7 \pm 0.2 wt.%, which is lower than that of γ_G (9.6 \pm 0.1 wt.%). Conversely, α_L has a higher Mn concentration (6.8 \pm 0.2 wt.%) than α_G (6.1 \pm 0.2 wt.%). When the 7Mn hot rolled specimen is subjected to a heat treatment at 1000 °C, some portion of austenite grains transforms to martensite upon quenching, giving rise to a multi-phase microstructure of ferrite, martensite plus retained austenite (FMNA), as illustrated by Fig. 3.3. The α' -martensite with the BCT crystal structure in Fig. 3.3 was identified by its higher dislocation density which yields a higher local misorientation value [3.34]. Lath-shaped morphology was no longer observed for this scenario, which could be due to recrystallization or most likely coarsening driven by the decrease in the total surface energy.

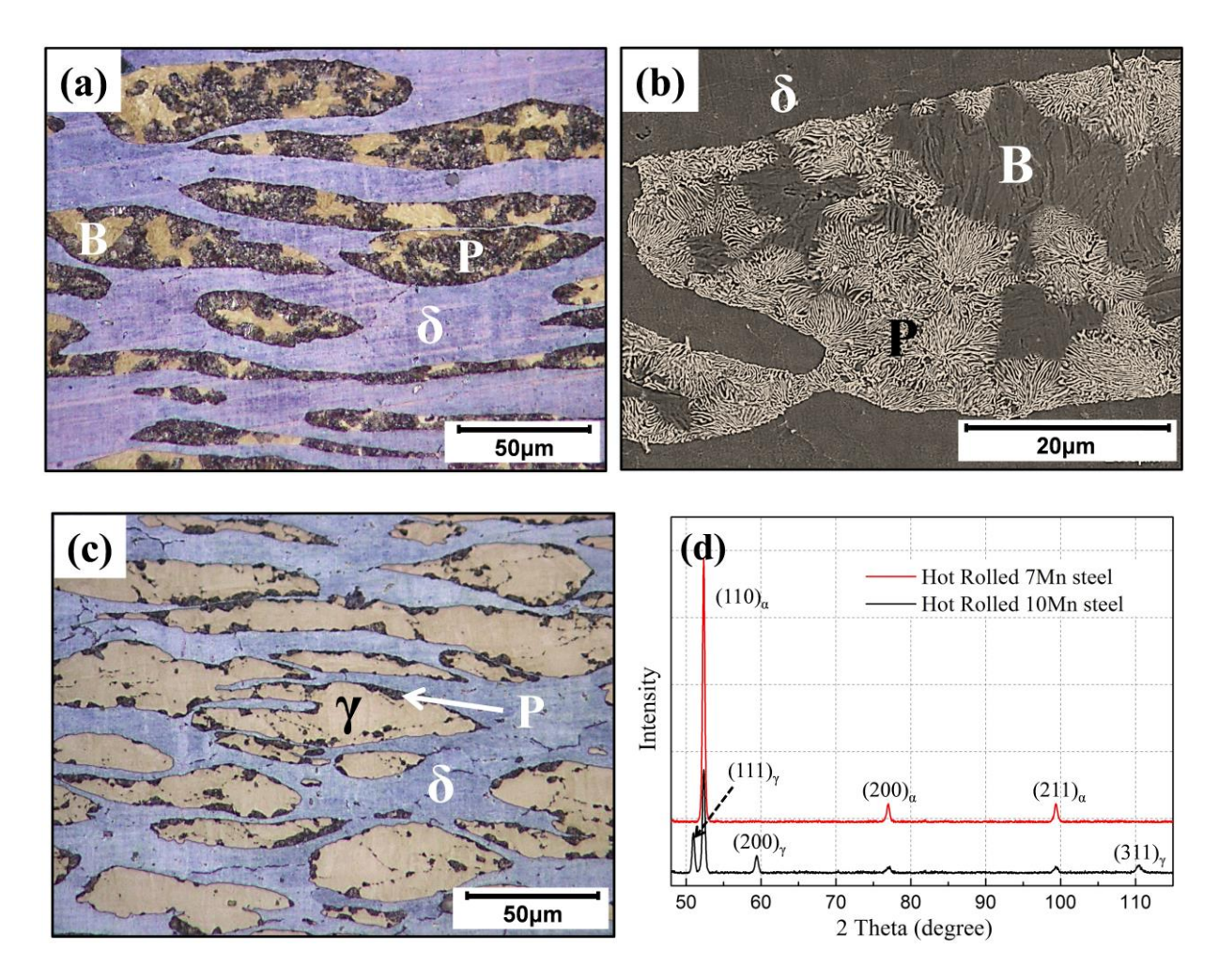
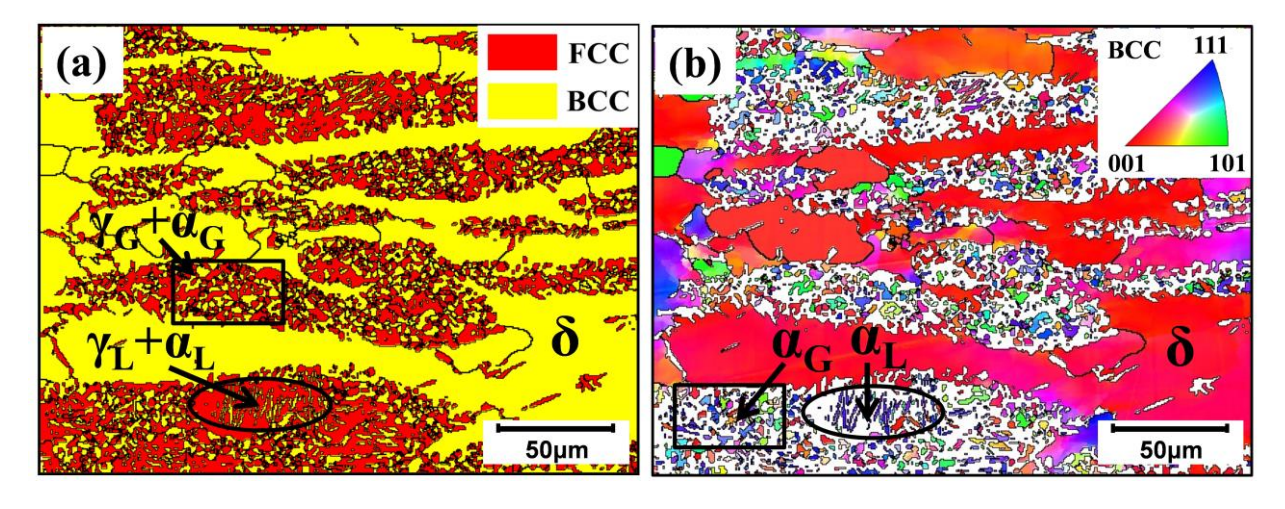


Fig. 3.1 (a) Optical and (b) SEM micrographs of the hot rolled structure of the 7Mn steel; (c) Optical micrograph of the hot rolled 10Mn steel; (d) XRD patterns of the hot band microstructures. (P: Pearlite; B: Bainite; γ : Austenite; δ : δ -ferrite, samples were etched by 2 % nital followed by 10 % aqueous sodium metabisulfite)



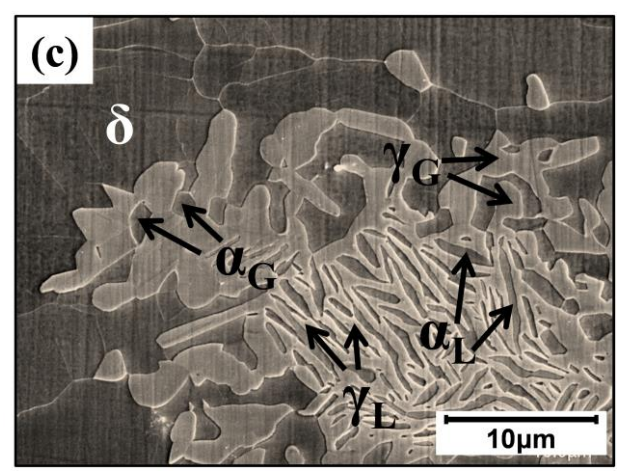


Fig. 3.2 Microstructure of the 7Mn steel annealed at 800 °C for 1 h: (a) EBSD phase mapping showing FCC and BCC phases; (b) BCC inverse pole figure (IPF) in the same area of (a); (c) SEM micrograph in the higher magnification, etched by 2 % nital followed by 10 % aqueous sodium metabisulfite. (γ_G : globular-shaped austenite; γ_L : lath-shaped austenite; α_G : globular-shaped ferrite; α_L : lath-shaped ferrite)

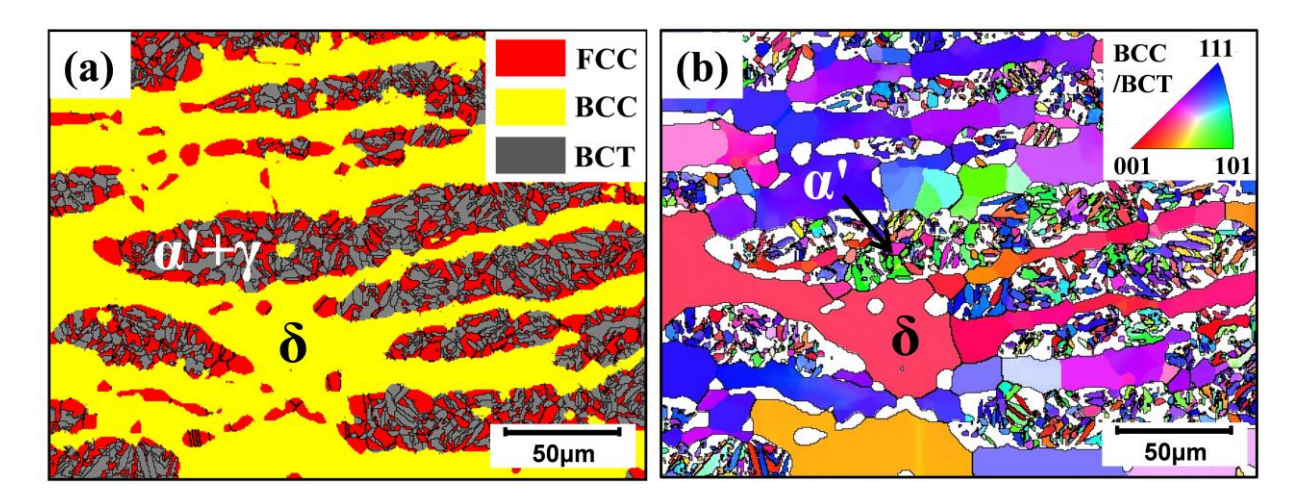


Fig. 3.3 EBSD images of the 7Mn steel annealed at 1000 °C for 1 h: (a) Phase mapping showing FCC, BCC and BCT phases; (b) BCC/BCT inverse pole figure in the same area of (a).

Figure 3.4 shows the microstructure of the 10Mn steel after annealing at 800 °C for 1 h. The initial austenite and δ -ferrite aggregate bands remained intact during annealing. A small amount of newly formed austenite (γ_{NT}) and ferrite with a globular-shape has transformed from the pearlite in the hot-rolled microstructure, as seen more clearly in Fig. 3.4 (c). The grain size of the globular austenite and ferrite was estimated to be ~2 µm. EDX measurement revealed that γ_{NT} had a higher Mn content (14.2 \pm 0.2 wt.%) than the initial γ austenite (11.4 \pm 0.1 wt.%), whereas α had a lower Mn content (8.9 \pm 0.3 wt.%) than the δ -ferrite (9.5 \pm 0.1 wt.%). At a higher annealing temperature of 1000 °C, the γ_{NT} tends to merge with the initial austenite and cannot be differentiated, leading to a smoother edge of the austenite bands (Fig. 3.5). Further, the small α -ferrite grains seems to have lower volume fraction and larger grain size (~4 µm); probably due to some coarsening. Nonetheless, it is obvious that the microstructure of the 10Mn steel is not very sensitive to the annealing temperature.

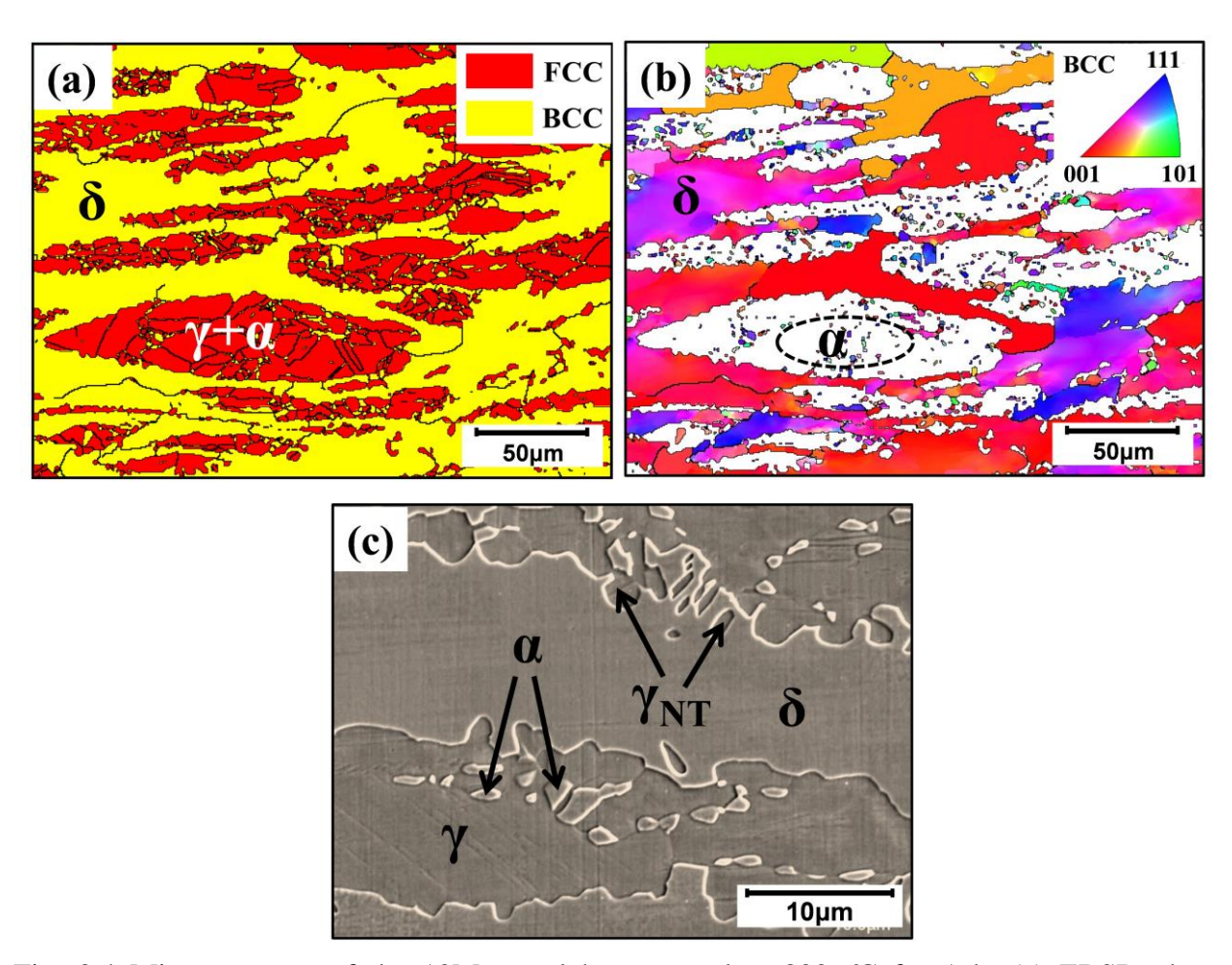


Fig. 3.4 Microstructure of the 10Mn steel heat treated at 800 °C for 1 h: (a) EBSD phase mapping showing FCC and BCC phases; (b) BCC inverse pole figure in the same area of (a); (d) SEM micrograph in the higher magnification, etched by 2 % nital followed by 10 % aqueous sodium metabisulfite. (γ_{NT} : newly transformed austenite)

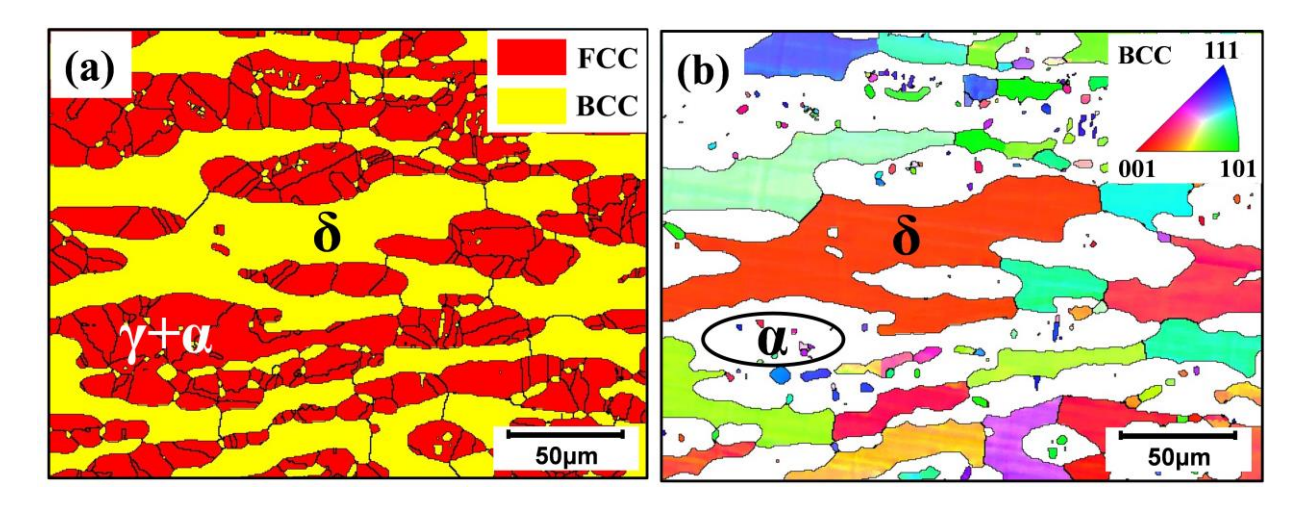


Fig. 3.5 EBSD images of the 10Mn steel heat treated at 1000 ℃ for 1 h: (a) Phase mapping showing FCC and BCC phases; (b) BCC inverse pole figure in the same area of (a).

For both alloys, the EBSD results (Figs. $3.2\sim3.5$) indicate that at the higher annealing temperature, 1000~C, δ -ferrite exhibits a wider range of crystallographic orientations and a finer grain size. This may be attributed to the enhanced recrystallization of δ -ferrite grains at higher annealing temperatures. It is likely that dynamic recrystallization in both phases during hot rolling was not completed, and the microstructure still remained somewhat deformed after subsequent cooling. The complex response of the ferrite-austenite mixture to different hot deformation temperatures and respective restoration scenarios for the 10Mn alloy have been studied in detail elsewhere [3.17]. Table 3.2 compares the recrystallized fraction of each phase in the 10Mn steel after annealing at different temperatures and subsequent quenching. In general, more austenite and ferrite recrystallized at the higher annealing temperature. It is also interesting to note that ferrite has a higher recrystallized fraction than austenite at both annealing temperatures, which is related to the different recrystallization kinetics of the two phases [3.17].

Table 3.2 Recrystallized fractions (vol.%) of austenite and ferrite in the 10Mn steel after annealing at different temperatures and subsequent quenching (measured by EBSD).

Austenite Phase	800 ℃	1000 °C	Ferrite Phase	800 ℃	1000 ℃
Recrystallized	9.85	42.1	Recrystallized	38.65	71.15
Substructured	50.2	56.85	Substructured	57.25	27.5
Deformed	39.95	1.05	Deformed	4.1	1.35

The phase fractions of the 7Mn and 10Mn steels under different annealing temperatures and subsequent quenching are shown in Fig. 3.6. For both steels, microstructural characterization reveals that the onset of austenite formation occurs above 700 °C. The 7Mn steel (Fig. 3.6(a)) shows a ferrite-austenite duplex phase (FADP) microstructure at 800 °C and 900 °C, whereas the FMNA microstructure was observed for higher annealing temperatures. The martensite fraction increases with increasing annealing temperature above 1000 °C, which results in a lower fraction of retained austenite. Any diffusional phase transformation during water quench was unlikely to occur due to very fast cooling rate, i.e. ~85 °C/s. Therefore, the fraction of initial austenite at annealing temperatures can be estimated simply by the combined volume fractions of retained austenite and martensite at room temperature. The result was plotted as a blue dashed line in Fig. 3.6 (a). It appears that the volume fraction of initial austenite prior to cooling increases rapidly from 700 $\,^{\circ}$ C to 900 $\,^{\circ}$ C and then stabilizes with a very slight decrease at 1200 $\,^{\circ}$ C in the 7Mn steel. However for the 10Mn steel, only the FADP microstructure was observed after quenching from annealing temperatures above 800 °C (Fig. 3.6 (b)). The findings imply that initial austenite in the 10Mn steel is sufficiently stable to resist subsequent decomposition during cooling. The austenite fraction in the 10Mn steel first increases with increasing temperature to 800 °C, stabilizes, and slightly decreases at 1200 °C. It was also found that the 10Mn steel had around 10 vol.% more austenite than the 7Mn steel at temperatures higher than 800 °C prior to quenching, which indicates the significant role of Mn on stabilizing austenite.

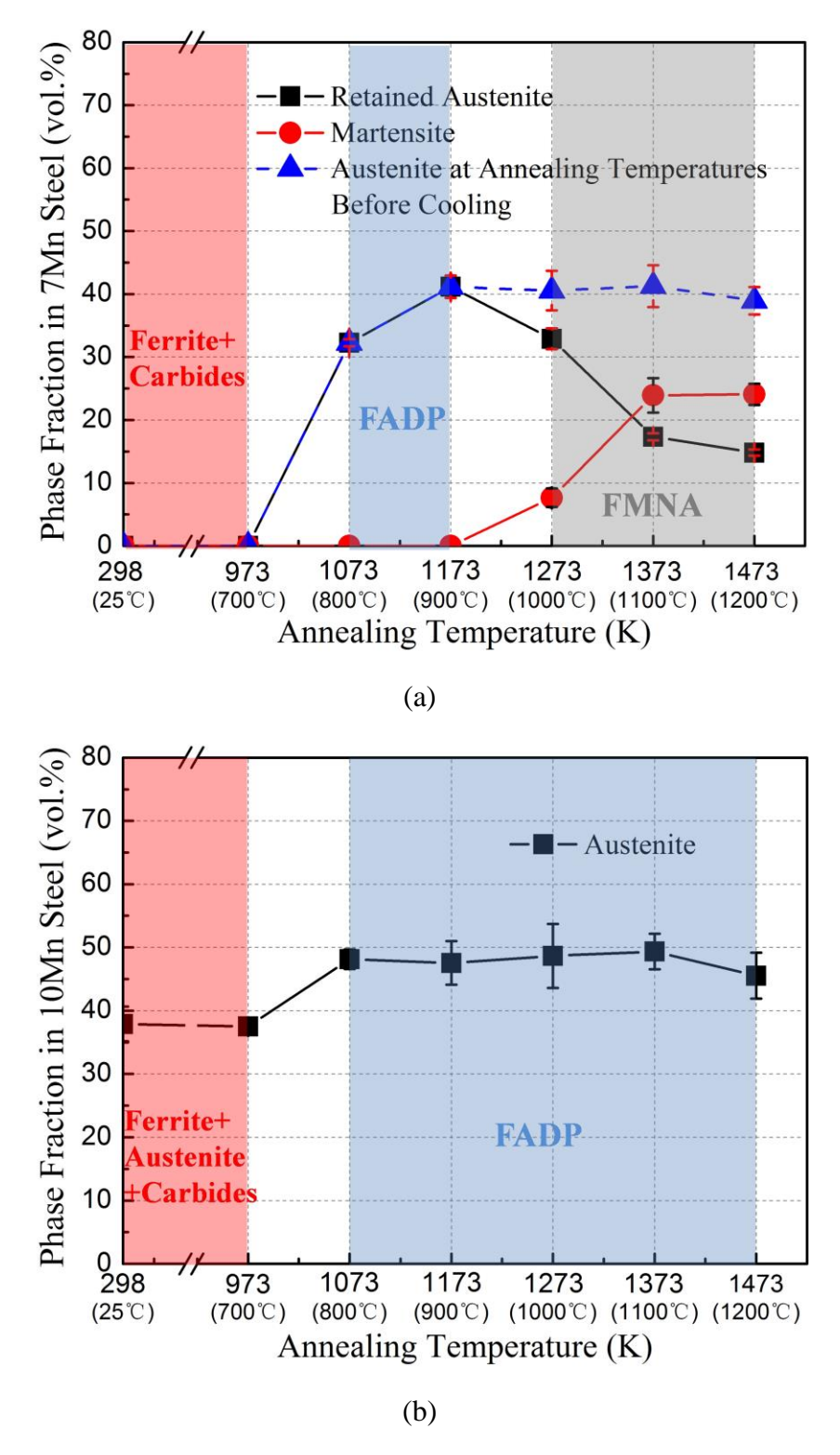


Fig. 3.6 Phase fractions of (a) the 7Mn steel and (b) the 10Mn steel under different annealing temperatures and subsequent quenching (FMNA: ferrite, martensite plus retained austenite microstructure; FADP: ferrite-austenite duplex phase microstructure).

The experimental average solute contents of the intercritical austenite with annealing temperature are illustrated in Fig. 3.7. The thermodynamic calculation for the austenite composition was also plotted together and the comparison will be discussed in Section 3.5. As mentioned above, the austenite composition (Mn, Al and Si) of the 7Mn steel also depends on its morphology, i.e. lath shape and globular shape, which is transformed from prior bainite and pearlite, respectively. The volume fractions of γ_L and γ_G could be estimated, based on an assumption that the volume fraction ratio of γ_L to γ_G in the annealed samples equals the fraction ratio of prior bainite to pearlite (8.2/32.2). Therefore, the average austenite Mn, Al and Si contents shown in Fig. 3.7(a) were calculated by the following equation:

$$w_i(\gamma, average) = \left[w_i(\gamma_L) \times f(\gamma_L) + w_i(\gamma_G) \times f(\gamma_G)\right] / f(\gamma)$$
(3.1)

where w_i is the contents of Mn, Al or Si (in wt.%), $f(\gamma_L)$ and $f(\gamma_G)$ are the volume fraction of the lath-shaped austenite and globular-shaped austenite, respectively. However, the lath-shaped phases in the 7Mn steel disappeared when the annealing temperature is above 900 °C, therefore, only the composition of γ_G was taken into account at these conditions. In addition, although the newly transformed austenite (γ_{NT}) appeared in the 10Mn steel also possesses a slight different composition, it can only be observed in the samples annealed at 800 $\,^{\circ}$ C and the fraction is quite small, therefore, the composition values in γ_{NT} were not counted in Fig. 3.7 (b). For the 7Mn steel, as shown in Fig. 3.7 (a), Mn, Al and Si contents show a monotonic trend with temperature; a decrease of Mn and a slight increase of Al and Si. Carbon concentration first decreases from 800 °C to 1100 °C and then slightly increases at higher temperatures. However, regarding the 10Mn steel (Fig. 3.7 (b)), Mn, Al and Si contents of the intercritical austenite remain unchanged at different annealing temperatures. The C concentration of the austenite increases initially from 700 °C to 800 °C, presumably due to carbides dissolution in austenite at 800 °C. Subsequently, a decrease of C content is observed up to 1100 °C, followed by an increase at 1200 °C. It is noticed that the annealing temperature has a more pronounced influence on the austenite composition of the 7Mn steel.

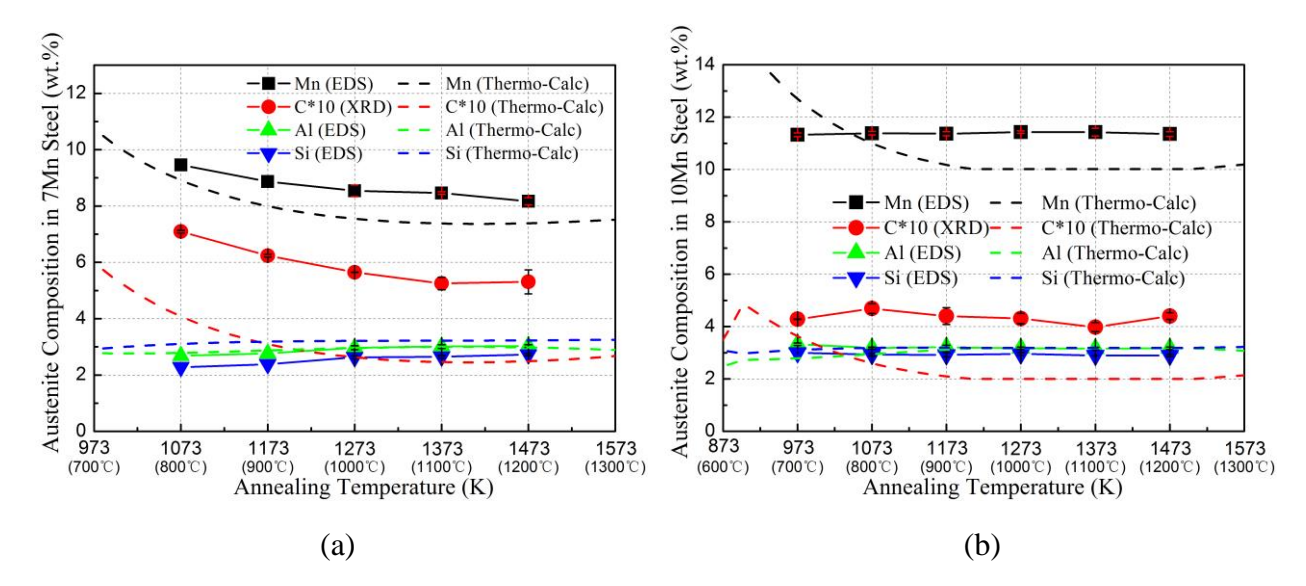


Fig. 3.7 Calculated equilibrium and measured average solute (C, Mn, Al and Si) contents of the intercritical austenite in (a) the 7Mn steel and (b) the 10Mn steel as a function of annealing temperature. (The thermodynamic calculation was conducted using Thermo-Calc software with a modified database)

The martensite start (Ms) temperature of the intercritical austenite at different annealing temperatures was calculated for the two steels. The following empirical equation accounting for composition and grain size effect was selected [3.35]:

$$Ms(\mathcal{C}) = 545 - 423w_C - 30.4w_{Mn} - 60.5V_{\gamma}^{-1/3}$$
 (3.2)

where w_C and w_{Mn} are the C and Mn contents of the austenite (in wt.%); the experimental values in Fig. 3.7 were used in the calculation, and V_{γ} is the effective grain volume of the austenite (in μm^3). The Koistenen-Marburger (KM) empirical equation [3.36] was adopted to estimate the fraction of martensite:

$$f_M = \{1 - \exp[-\alpha (M_s - T_q)^{\beta}]\} \times f_{\gamma}$$
 (3.3)

where f_M is the martensite fraction transformed from austenite, f_{γ} is the austenite fraction under annealing temperatures before cooling, T_q is the quenching temperature (here 25 °C), and α and β are constants [3.37]: $\alpha = 0.0231 - 0.0105 \ w_C$; $\beta = 1.4304 - 1.1836 \ w_C + 0.7527 \ w_C^2$.

Figure 3.8 (a) illustrates the calculated Ms temperature of the 7Mn and 10Mn steels at different annealing temperatures, without austenite grain size consideration. For the 7Mn steel, it shows that the Ms temperature increases with annealing temperature. The Ms temperature of the 7Mn steel remains above room temperature, 25 $^{\circ}$ C, for annealing temperatures higher than 1000 $^{\circ}$ C, which could explain the transition of FADP to FMNA microstructure at higher annealing temperatures for the 7Mn steel. The calculated martensite fraction in the 7Mn steel adopting KM equation is shown in Fig. 3.8 (b); a good agreement between the calculation and measurement can be found. Martensite in the 7Mn steel increases rapidly from 900 $^{\circ}$ C to 1100 $^{\circ}$ C and approaches a plateau at higher temperatures. However, although the austenite in the 10Mn steel contains slightly less C than that in the austenite of the 7Mn steel (Fig. 3.7), the higher Mn content of the 10Mn steel maintains the Ms temperature below room temperature for all the examined annealing temperatures. Therefore, only the FADP microstructure can be obtained in the 10Mn steel.

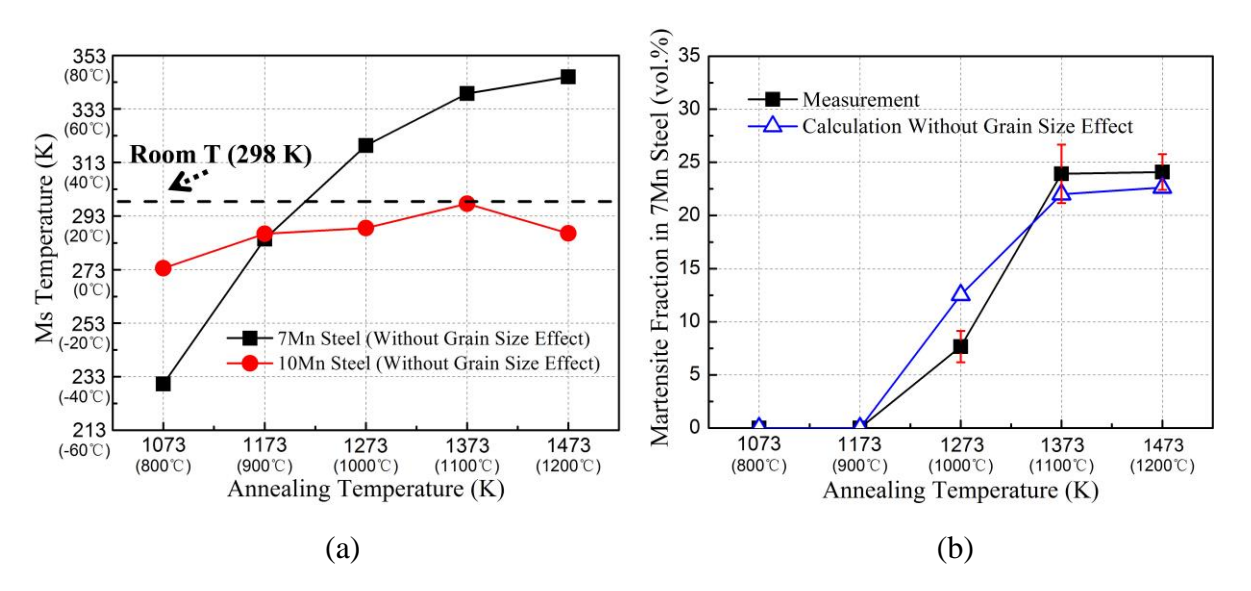


Fig. 3.8 (a) Calculated Ms temperature of the 7Mn and 10Mn steels as a function of annealing temperature; (b) Martensite fraction of the 7Mn steel at different annealing temperatures.

3.4.3 Effect of annealing time

Different annealing times were conducted at 1000 °C, followed by water quenching to study the kinetics of phase transformation in the two medium Mn steels. Figure 3.9 shows the volume fractions of different phases as a function of annealing time at 1000 °C for the two medium Mn steels. Austenite transformation is very rapid in both steels, e.g. nearly 40 vol.% austenite has been transformed in the 7Mn steel after only 1 min holding (the microstructures can be found elsewhere [3.27]). In the 7Mn steel, as shown in Fig. 3.9 (a), the retained austenite fraction is the highest after annealing for 1 min, and martensite starts to form after 2 min and increases with time continuously, consuming some of the retained austenite. However, the austenite fraction before quenching in the 7Mn steel is almost constant after 1 min. For the 10Mn steels (Fig. 3.9 (b)), martensite was never observed under any condition. The initial austenite fraction is 37.9 \pm 2.7 vol.% in the hot-rolled microstructure. After 1 min annealing, it increases to 46.9 \pm 5.9 vol.%, however, with increasing annealing time, the austenite fraction changes slightly (45~49 vol.%) without a clear trend with holding time.

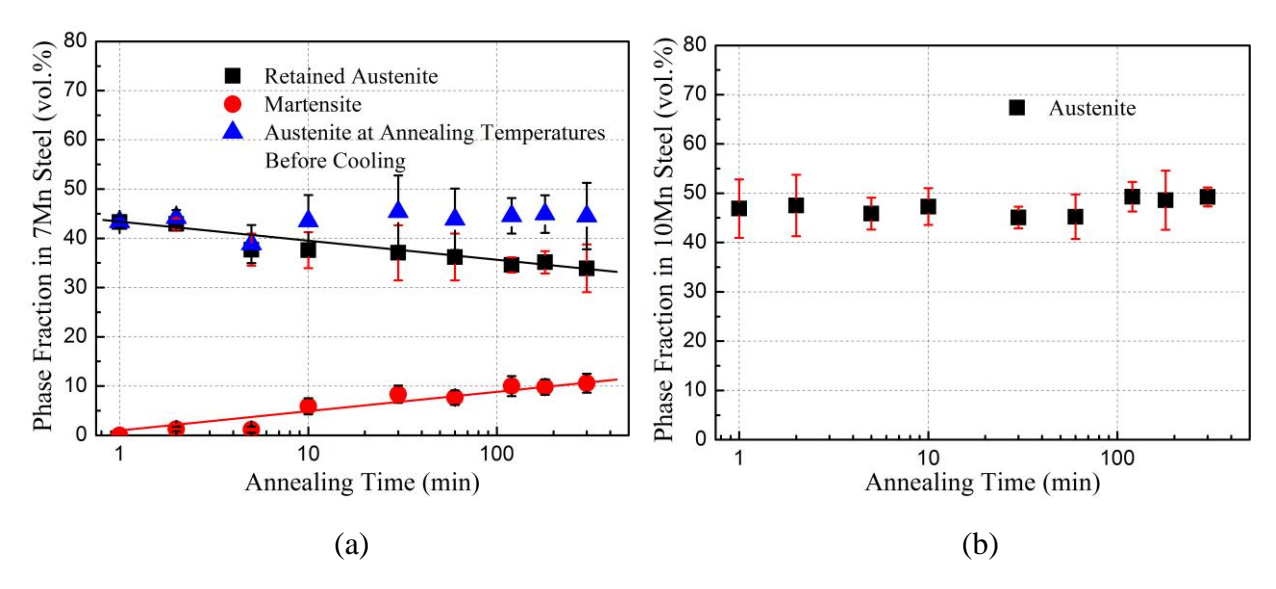


Fig. 3.9 Phase fractions of (a) the 7Mn steel and (b) the 10Mn steel as a function of annealing time at $1000 \, \text{C}$.

The austenite C contents measured by XRD in the two medium Mn steels annealed for different times at 1000 °C are shown in Fig. 3.10 (a). The figure also plotted the calculated values based on the lever rule under the assumption that C was not soluble in ferrite; a strong match is observed between the measured and calculated values. There is no clear relationship between austenite C concentration and annealing time for both grades. Additionally, both measured and calculated C concentrations show some scatter, which is believed to stem from several error sources (e.g. XRD measurements and Dyson's equation). Solute partitioning occurs during intercritical annealing, as reported by several researchers [3.12, 3.14, 3.15, 3.38]. Figure 3.10 (b) gives the distribution of Mn, Al and Si across a fine intercritical austenite island in the 7Mn steel annealed at 1000 °C for 1 min. It shows that austenite is enriched by Mn but depleted with respect to Al and Si after annealing, even for a short 1 min holding. Figure 3.10 (c) plots the Mn contents in austenite and ferrite of the two steels, and the Mn partition coefficients between austenite and ferrite were calculated and shown in Fig. 3.10 (d). For both steels, Mn concentration is increasing in austenite and reducing in ferrite in the global trend during annealing (Fig. 3.10 (c)), resulting in a more pronounced Mn partitioning between austenite and ferrite, illustrated in Fig. 3.10 (d). However, the change of Mn content in the two phases of both steels can be divided into two stages: in stage 1, Mn keeps depleting in ferrite while remaining stabile, or slightly increasing, in austenite; then the Mn content maintains an almost constant level in ferrite while increases in austenite, which characterizes stage 2 in Fig. 3.10 (c). This separate Mn diffusion stages will be discussed in Section 3.5. It is also interesting to note that intercritical ferrite (α) in the 7Mn steel has a lower Mn concentration than δ -ferrite (leading to a higher Mn partition coefficient), however, these two curves almost converge at longer annealing times. It is illustrated by Fig. 3.10 (d) that the 7Mn steel has higher Mn partition coefficients than the 10Mn steel.

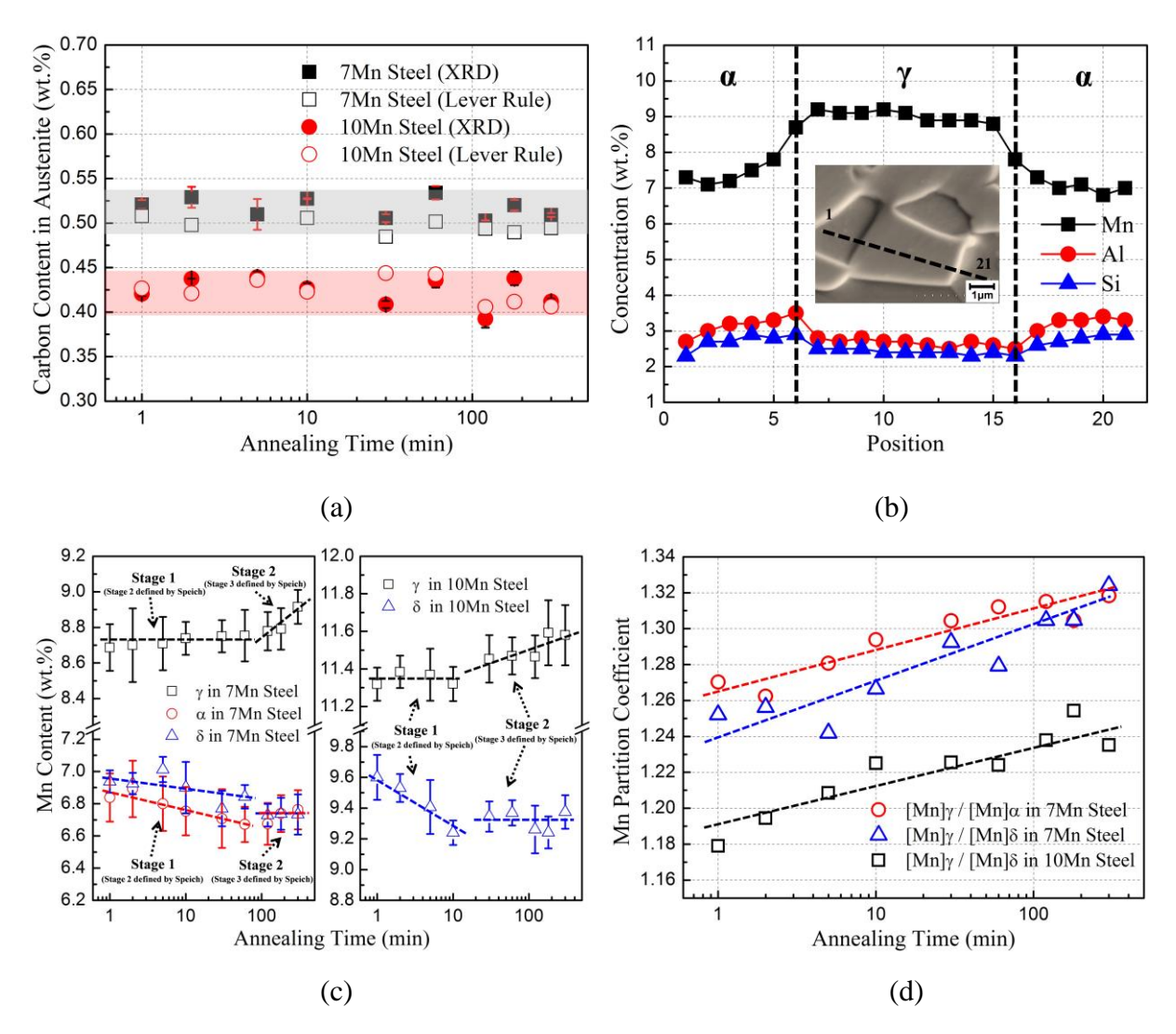


Fig. 3.10 (a) Measured and calculated C contents in the austenite phase of the two medium Mn steels as a function of holding time at $1000 \, \text{C}$; (b) The distribution of Mn, Al and Si across an austenite island in the 7Mn steel annealed at $1000 \, \text{C}$ for 1 min; (c) Manganese contents with annealing time in austenite and ferrite of both steels; (d) Manganese partition coefficients between austenite and ferrite in both steels.

The calculated Ms temperature and martensite fraction for the 7Mn steel at different annealing times are illustrated in Fig. 3.11. Accounting for compositional effect, the Ms temperature maintains almost stable with annealing time at 1000 °C due to the little change of C and Mn content in austenite, as shown in Fig. 3.11(a). Accordingly the calculated martensite fraction

without grain size effect only changes slightly (less than 2 vol.%), as observed in Fig. 3.11(b). However by taking into account the austenite grain size, the Ms temperature shows a significant increase initially during the early 1 min to 2 minutes and it stabilizes subsequently with annealing time. This reveals that the effect of grain size is dominant at early stages where the austenite grains are small, whereas this effect becomes almost negligible above certain sizes (here about 5 µm). The calculated martensite fraction accounting for grain size, as shown in Fig. 3.11 (b), exhibits a similar trend compared with the experimental data, although the calculated value is slightly higher; it first increases at the beginning and remains almost unchanged after certain amount of time.

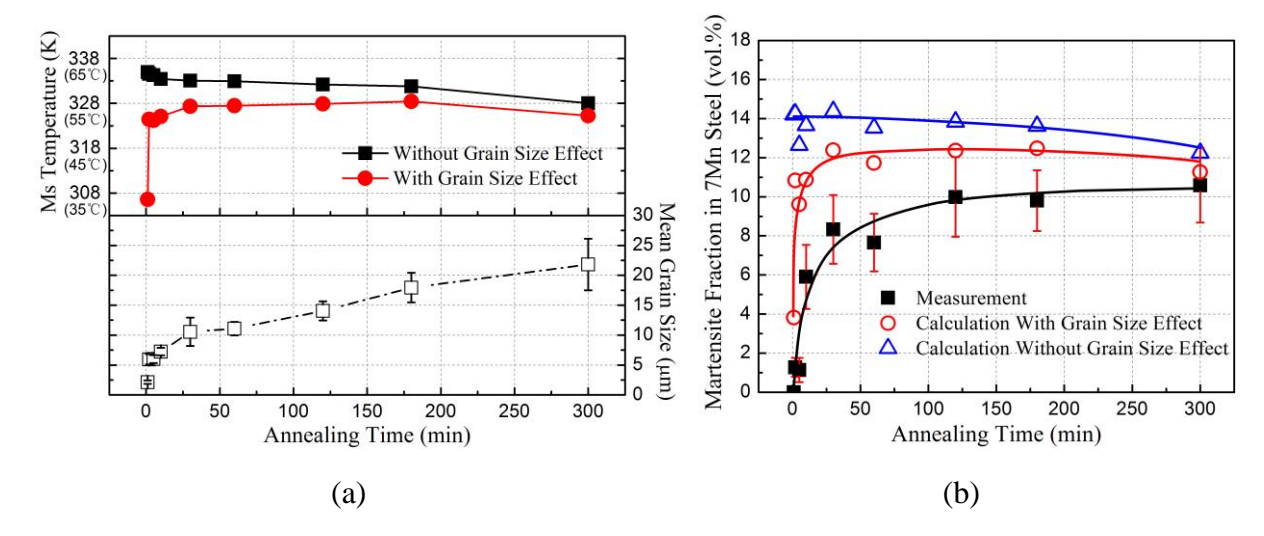


Fig. 3.11 (a) Austenite grain size and calculated M_s temperature of the 7Mn steel as a function of annealing time; (b) Martensite fraction of the 7Mn steel at different annealing times.

3.5 Discussion

The observed results in Section 3.4 suggested that that the final microstructure of the 7Mn steel depended substantially on the annealing temperatures. Higher temperatures promote austenite formation but dilute the C and Mn contents and degrade the stability of the austenite which tends to transform to martensite upon quenching. The volume fraction of retained austenite could range from 0 to ~40 %, and the martensite fraction was between 0 to ~25 vol.%, revealing a strong microstructural diversity, which was also reported by other researchers in medium Mn steels [3.8, 3.12, 3.13, 3.39]. The mechanical property of the 7Mn steel was highly influenced by its microstructure. Micro-shear punch tests revealed that the FADP microstructure is superior to the FMNA microstructure in terms of both strength and ductility (the data can be found elsewhere [3.27]). In contrast, the 10Mn steel exhibited a FADP microstructure containing ~50 vol.% austenite which was found to be independent of the variations of intercritical annealing temperature. This noticeable stable ferrite-austenite duplex microstructure, to our knowledge, was never reported in medium Mn steels; similar structure could only be found in high alloyed steels, e.g. duplex stainless steels [3.40] or a Fe-0.6C-20Mn-9Al steel reported by Hwang et al. [3.41]. The mechanical properties for the 10Mn steel are also expected to be unaffected by annealing temperatures, as demonstrated in the previous work by shear punch tests [3.27]. Reported data for medium Mn steels indicated that the optimal combinations of strength and ductility can only be achieved in a very narrow annealing temperature range, i.e. ~50 °C [3.1, 3.7-3.9, 3.16, 3.42, 3.43]. Therefore, the processing robustness of the examined 10Mn steel constitutes an important advantage for its industrial production because a wide processing window exists in terms of optimum annealing temperature and subsequent cooling.

It has to be noted that upon reheating the δ -ferrite phase remains greater than 50 vol.% even at the highest annealing temperatures for both steels. This feature differs from the typical medium Mn TRIP steels that contain small amounts of Al and Si. For example, Han et al. [3.44] investigated the effect of the heating rate on austenite formation in a 7 wt.% Mn steel with 0.3

wt.% Si and 0.1 wt.% Al, and found that the structure achieved 100 % austenite at 766 $^{\circ}$ C for 3 $^{\circ}$ C/s heating rate. Obviously the addition of 3 wt.% Al and Si effectively stabilizes ferrite and enlarges the ferrite-austenite domain in the examined steels. This is also confirmed by Suh et al. [3.25] who studied the effect of Al content on the microstructure of 5 wt.% Mn steels, and found that a single austenite phase domain disappeared as Al content exceeded beyond 3 wt.%. Although this stable δ -ferrite increases the complexity of the microstructure, it could bring about two benefits: (1) It promotes additional C and Mn partitioning between austenite and ferrite to further enrich the intercritical austenite (as shown in Fig. 3. 10), as such it enhances the stability of austenite. (2) It was reported by Lee et al. [3.26] that localized deformation (Lüders bands propagation) could be suppressed by the coarse-grained δ -ferrite. However, the detailed effect of such a large amount of δ -ferrite on the mechanical properties of medium Mn steels is still unclear and requires further exploration in the future.

CALPHAD method is commonly used to preselect suitable heat treatment parameters in multicomponent systems. The austenite equilibrium fraction and composition at different temperatures were calculated using the commercial thermodynamic software, Thermo-Calc®, with both the commercial TCFE7 database and a modified thermodynamic database which was proposed by Hallstedt et al. [3.45] initially for high Mn steels. The calculated austenite fractions from both databases, together with the experimental data are shown in Fig. 3.12. The two databases predict similar results for the 10Mn steel and the 7Mn steel at lower temperatures. However, the modified database achieves some improvement for the 7Mn steel at the higher temperature range (Fig. 3.12 (a)), e.g. a fully austenite domain should exist with the temperature above 1103 °C predicted by the TCFE7 database, whereas the modified database predicts a dual phase microstructure at this temperature range, matching the experimental observations. Nevertheless, the predicted austenite fractions in both alloys exhibit a large deviation from the measurements, although a similar trend with annealing temperature can be observed. The calculated austenite compositions of the two alloys from the modified database are also

compared with the experimental measurements in Fig. 3.7. The predicted austenite Al and Si contents agree very well with the experimental results. However, the calculated austenite Mn contents in both alloys have nearly 1 wt.% deviation from the experimental results. Further, it should be noted that in the 10Mn steel, the experimental austenite Mn content does not follow the trend of the prediction at low temperatures. The difference of the austenite C content between the calculation and the experimental data is even larger for both alloys. This discrepancy of the austenite C and Mn contents compared to the measured values stem from the overestimation of austenite volume fraction by the thermodynamic data. It has to be noted that the annealing time was insufficient to permit the alloying elements reaching their equilibrium partitioned state. However, as shown in Fig. 3.10 (a), C contents in austenite of both steels seem to be unchanged during annealing, indicating a constraint equilibrium is achieved rapidly. On the other hand, the Mn enrichment in austenite is very small (Fig. 3.10 (c)), so that prolonged annealing beyond 1 h would not help to eliminate the discrepancy between the experimental and calculated Mn contents of the austenite. Further, the Mn contents in austenite keep increasing with time, which means the experimental austenite Mn contents will always exceed the prediction even with sufficient diffusion because most of the experimental data is already higher than the calculation after 1 h annealing (Fig. 3.7). This implies the deviation between the thermodynamic data and the experimental results would not be reduced even sufficient annealing time could be applied to reach equilibrium state. Therefore, this deviation could most likely to be derived from the inaccuracy of the thermodynamic database, which needs to be checked and further optimized for this type of medium Mn steels.

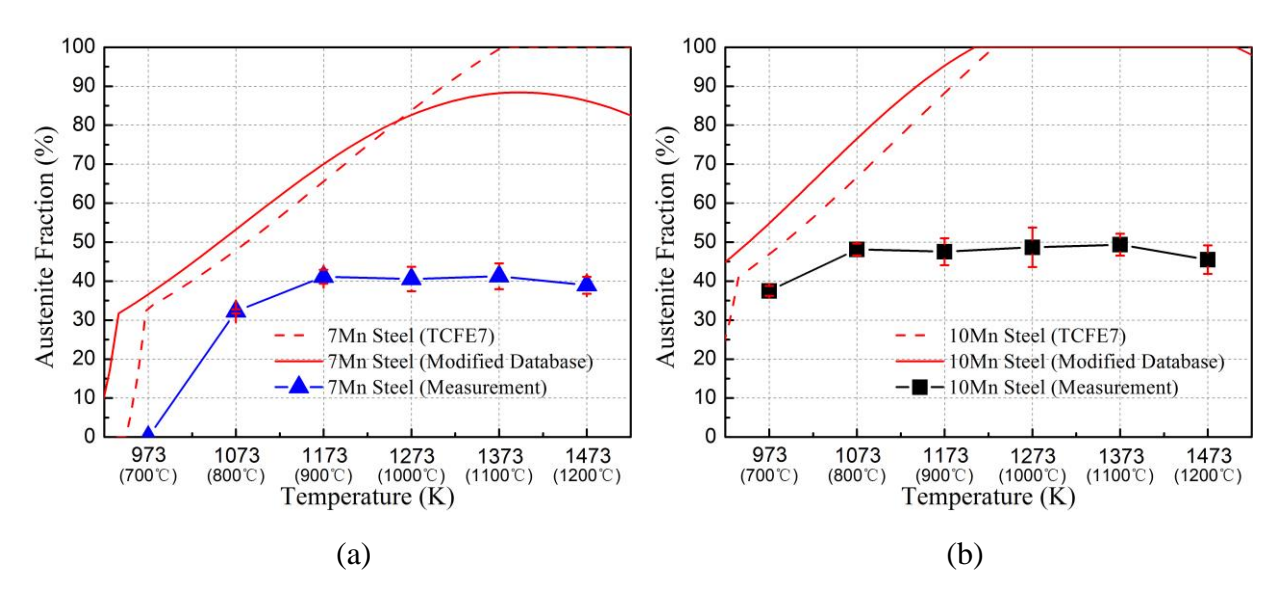


Fig. 3.12 Comparison of the austenite fraction between thermodynamic predictions and experimental measurement in (a) the 7Mn steel and (b) the 10Mn steel.

As mentioned in Section 3.4.3, austenite formation was very rapid at 1000 °C and the fraction of austenite remained invariably unchanged with annealing time in the examined medium Mn steels (Fig. 3.9). However, it was proposed by Speich et al. [3.46] and confirmed by other researchers [3.47-3.50], that austenite formation could be separated into three steps in dual-phase (DP) steels with ferrite-carbide mixtures: 1. austenite nucleation and carbon-diffusion-controlled growth of austenite following carbides dissolution; 2. further austenite growth into ferrite, controlled by Mn diffusion in ferrite in the intercritical temperature range; 3. final equilibration of ferrite and austenite controlled by sluggish Mn diffusion in austenite.

Generally, the first step is very rapid [3.46, 3.50, 3.51], for example, it only took 0.12 ms in a 0.12C-1.5Mn steel at 900 °C and 50 ms in a 0.1C-3.4 Mn alloy at 740 °C calculated respectively by Speich et al. [3.46] and Lai [3.50], as such this stage normally cannot be observed experimentally. This is due to very high diffusivity of C atoms and the short diffusion distance (about equal to the interlamellar spacing of the pearlite [3.52] and the thickness of the thin bainite plate [3.53]). The traditional mean diffusion distance ($\sqrt{D}t$) of C and Mn atoms in

different phases of the 10Mn steel at 1000 $^{\circ}$ C was calculated and shown in Fig. 3.13, where D is the diffusion coefficient selected from the literatures [3.54-3.57] and t is the diffusion time. It shows that at this temperature, C diffuses almost 25 times faster than Mn in ferrite and 250 times faster than Mn in austenite. As shown in Fig. 3.10 (a), C content in austenite remains almost unchanged after 1 min, on the other hand, the calculated value based on lever rule is quite close to the XRD measured value, indicating the carbides are completely dissolved after 1 min. Therefore, in the present work, it is highly possible that the carbon-controlling step was completed before 1 min or even during the course of heating. It should be noted that the austenite formation kinetics from pearlite and bainite would possess some difference depending on the carbide distribution, composition and morphology, but this difference could be in a very small magnitude which would be detected hardly by conventional experiments.

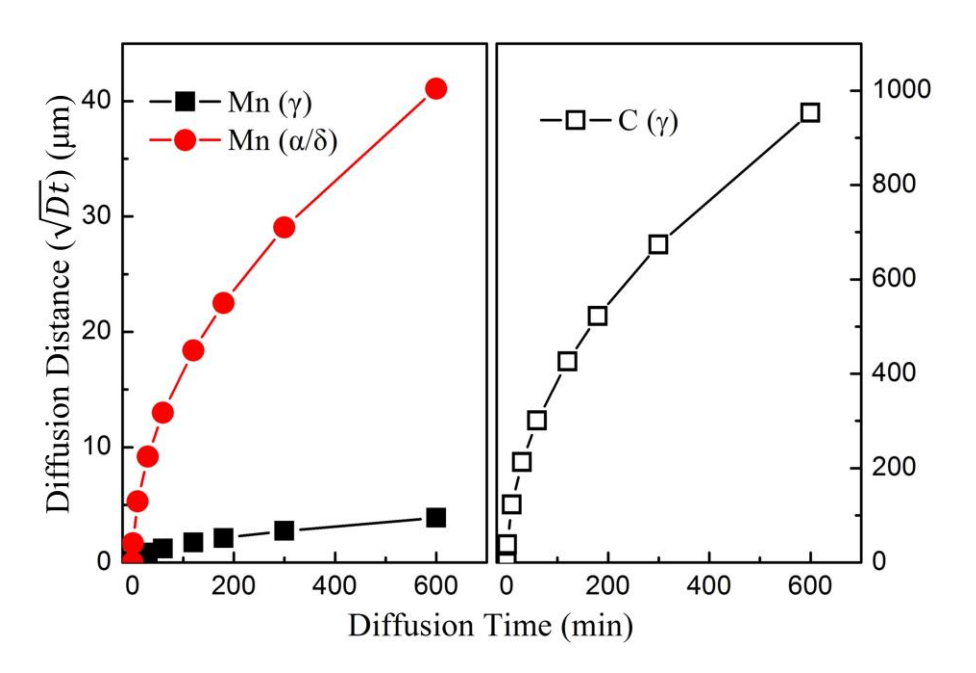


Fig. 3.13 Mean diffusion distance of C and Mn in different phases of the 10Mn steel at 1000 ℃.

The second austenite formation step proposed by Speich et al. is characterized by an intermediate slow growth of austenite $(10^3 \sim 10^6 \text{ s } [3.48])$, followed by the third equilibration step which tends to be extremely slow [3.46]. Obviously, there was no direct evidence for additional growth of

austenite during isothermal holding beyond one minute during annealing at 1000 °C, as illustrated by Fig. 3.9, namely the second austenite formation step is "absent". It can be argued that the second step which is controlled by Mn diffusion in ferrite is also very rapid and could be almost finished before 1 min or during heating, as proposed in Lai's study [3.50]. This seems reasonable considering the relatively high annealing temperature selected in this work. However, the fraction of δ -ferrite is almost unchanged during annealing, for instance, the hot rolled 7Mn steel consists of 59.6 vol.% δ-ferrite, which is quite similar to the values after annealing (55~61 vol.%). This reveals no tangible austenite growth into ferrite occurred, which was also confirmed by careful comparison of the microstructures before and after annealing in the same area [3.27]. Nevertheless it was found that Mn atoms had chance to redistribute slightly in the two phases after 1 min, as shown in Fig. 3.10 (c). Apparently two different kinetic regimes can be identified. Firstly, Mn continued depleting in ferrite while almost invariant in austenite, which could correspond to the step 2 proposed by Speich et al. [3.46]. Secondly, at longer holding time, Mn content of ferrite remained almost constant while ramped up in austenite, corresponding to the final equilibration stage (stage 3) in Speich et al. and other researchers' work [3.46-3.50]. This observation implied that the Mn redistribution in ferrite actually could occur and most likely complete before the final equilibration stage. However, due to very slight amount of redistribution (<0.5 wt.%) which is controlled by the probably small ferrite to austenite transformation driving force, a tangible change in austenite fraction could not be detected experimentally. In terms of processing implication, the results suggest that a long annealing time is irrelevant for these steels and a short annealing time, in the order of a few minutes, is adequate; showing another advantage of these medium Mn grades to enhance production rate and energy saving.

3.6 Conclusions

The microstructural evolution of two high Al-Si medium Mn (7 and 10 wt.%) hot rolled steels upon intercritical annealing and subsequent quenching to room temperature were investigated. The following conclusions can be summarized:

- 1. The annealing temperature had a substantial influence on the microstructure of the 7Mn steel, including the variation of phase constituents, austenite morphology and composition (mainly C and Mn content), the Ms temperature and retained austenite fraction. The fraction of retained austenite peaked at ~40 vol.% for intercritical treatment at 900 °C. However, the 10Mn steel was not sensitive to the annealing temperature, showing an invariant ferrite-austenite duplex microstructure with ~50 vol.% austenite regardless of the annealing temperature. The Mn content of austenite in the 10Mn steel also remained nearly unchanged at different annealing temperatures; this higher Mn value enhanced the austenite stability and maintained the Ms temperature below ambient temperature. Both steels possessed a large fraction of δ-ferrite (higher than 50 vol.%) before heat treatments, which was stabilized by Al and Si and maintained intact during intercritical annealing.
- 2. Transformation of initial ferrite-pearlite/bainite hot band microstructure into austenite is very rapid upon heating and additional isothermal holding in both steels. Austenite growth is believed to be first controlled by C diffusion in austenite following pearlite/bainite dissolution. Subsequently, Mn atoms tend to redistribute first in ferrite and at later stages in austenite. However, the amount of Mn partitioning and redistribution was too subtle (less than 0.5 wt.%) to result in a tangible change in austenite fraction for the examined annealing time.
- 3. A modified thermodynamic database was evaluated using the experimental data. Although the new database achieved a better agreement with the experimental results for the 7Mn steel

compared with TCFE7, some discrepancy in the predicted phase fractions and compositions over a range of intercritical temperatures still existed for the examined steels. The experimental results in the present work could be exploited to optimize the existing thermodynamic database for such high Al-Si medium Mn steels.

3.7 References

- [3.1] N. Fonstein: Advanced High Strength Sheet Steels-Physical Metallurgy-Design, Processing, and Properties, Springer International Publishing, 2015, 297-323.
- [3.2] Y.K. Lee, J. Han, *Current opinion in medium manganese steel*, Materials Science and Technology, 31 (2015), 843-856.
- [3.3] O. Bouaziz, H. Zurob, M. Huang, *Driving force and logic of development of advanced high strength steels for automotive applications*, Steel Research International, 84 (2013), 937-947.
- [3.4] R.L. Miller, *Ultrafine-grained microstructures and mechanical properties of alloy steels*, Metallurgical Transaction, 3 (1972), 905-912.
- [3.5] H. Aydin, E. Essadiqi, I.H. Jung, S. Yue, *Development of 3rd generation AHSS with medium Mn content alloying compositions*, Materials Science and Engineering: A, 564 (2013), 501-508.
- [3.6] A. Arlazarov, M. Goun & O. Bouaziz, A. Hazotte, G. Petitgand, P. Barges, *Evolution of microstructure and mechanical properties of medium Mn steels during double annealing*, Materials Science and Engineering: A, 542 (2012), 31-39.
- [3.7] P. Gibbs, E. De Moor, M. Merwin, B. Clausen, J. Speer, D. Matlock, *Austenite stability effects on tensile behavior of manganese-enriched-austenite transformation-induced plasticity steel*, Metallurgical and Materials Transactions A, 42 (2011), 3691-3702.
- [3.8] S. Lee, B.C. De Cooman, On the selection of the optimal intercritical annealing temperature for medium Mn TRIP steel, Metallurgical and Materials Transactions A, 44 (2013), 5018-5024.
- [3.9] S.Lee, S.J. Lee, S.S. Kumar, K. Lee, and B.C. De Cooman, *Localized deformation in multiphase, ultra-fine-grained 6 pct Mn transformation-induced plasticity steel*, Metallurgical and Materials Transactions A, 42 (2011), 3638-3651.
- [3.10] W. Cao, C. Wang, J. Shi, M. Wang, W. Hui, H. Dong, *Microstructure and mechanical properties of Fe-0.2C-5Mn steel processed by ART-annealing*, Materials Science and Engineering: A, 528 (2011), 6661-6666.
- [3.11] H. Huang, O. Matsumura, T. Furukawa, *Retained austenite in low carbon, manganese steel after intercritical heat treatment*, Materials Science and Technology, 10 (1994), 621-626.
- [3.12] E. De Moor, D.K. Matlock, J.G. Speer, M.J. Merwin, *Austenite stabilization through manganese enrichment*, Scripta Materialia, 64 (2011), 185-188.
- [3.13] P.J. Gibbs: *Design Considerations For the Third Generation Advanced High Strength Steel*, Department of Metallurgical and Materials Engineering, Colorado School of Mines, Golden, CO, United States, 2012,1-79.
- [3.14] S. Lee, S.J. Lee, B.C. De Cooman, Austenite stability of ultrafine-grained transformation-induced plasticity steel with Mn partitioning, Scripta Materialia, 65 (2011),

- 225-228.
- [3.15] S. Lee, B.C. De Cooman, *Tensile behavior of intercritically annealed ultra-fine grained 8% Mn multi-phase steel*, Steel Research International, 86 (2015), 1170-1178.
- [3.16] S. Lee, B.C. De Cooman, Annealing temperature dependence of the tensile behavior of 10 pct Mn multi-phase TWIP-TRIP steel, Metallurgical and Materials Transactions A, 45 (2014) 6039-6052.
- [3.17] B. Sun, H. Aydin, F. Fazeli, S. Yue, *Microstructure evolution of a medium manganese steel during thermomechanical processing*, Metallurgical and Materials Transactions A, 47 (2016) 1782-1791.
- [3.18] S.S. Sohn, K. Choi, J.H. Kwak, N.J. Kim, S. Lee, *Novel ferrite–austenite duplex lightweight steel with 77% ductility by transformation induced plasticity and twinning induced plasticity mechanisms*, Acta Materialia, 78 (2014), 181-189.
- [3.19] C.Y. Lee, J. Jeong, J. Han, S.J. Lee, S. Lee, Y.K. Lee, Coupled strengthening in a medium manganese lightweight steel with an inhomogeneously grained structure of austenite, Acta Materialia, 84 (2015), 1-8.
- [3.20] S. Lee, K. Lee, B.C. De Cooman, *Observation of the TWIP+TRIP plasticity-enhancement mechanism in Al-added 6 wt pct medium Mn steel*, Metallurgical and Materials Transactions A, 46 (2015), 2356-2363.
- [3.21] H. Kim, D.W. Suh, N.J. Kim, Fe-Al-Mn-C lightweight structural alloys: a review on the microstructures and mechanical properties, Science and Technology of Advanced Materials, 14 (2013), 1-11.
- [3.22] H. Aydin, I.H. Jung, E. Essadiqi, S. Yue, *Twinning and tripping in 10% Mn steels*, Materials Science and Engineering: A, 591 (2014), 90-96.
- [3.23] K. Jeong, J.E. Jin, Y.S. Jung, S. Kang, Y.K. Lee, *The effects of Si on the mechanical twinning and strain hardening of Fe-18Mn-0.6C twinning-induced plasticity steel*, Acta Materialia, 61 (2013), 3399-3410.
- [3.24] B.W. Oh, S.J. Cho, Y.P. Kim, Y.P. Kim, W.S. Kim, S.H. Hong, *Effect of aluminium on deformation mode and mechanical properties of austenitic Fe-Mn-Cr-Al-C alloys*, Materials Science and Engineering: A, 197 (1995), 147-156.
- [3.25] D.W. Suh, S.J. Park, T.H. Lee, C.S. Oh, S.J. Kim, *Influence of Al on the microstructural evolution and mechanical behavior of low-carbon, manganese transformation-induced-plasticity steel*, Metallurgical and Materials Transactions A, 41 (2010), 397-408.
- [3.26] S. Lee, Y. Estrin, B.C. De Cooman, *Constitutive modeling of the mechanical properties of V-added medium manganese TRIP steel*, Metallurgical and Materials Transactions A, 44 (2013), 3136-3146.
- [3.27] B. Sun, H. Aydin, F. Fazeli, and S. Yue, Effect of annealing on the microstructure and

- properties of two medium manganese steels, Proceeding of Materials Science and Technology Conference and Exhibition 2015, Columbus, OH, United States, 2015, 893-900.
- [3.28] R.A. Young: *The Rietveld Method*, International Union of Crystallograhy, Oxford, New York, 1995.
- [3.29] ASTM Standard E1245-03: Standard Practice for Determining the Inclusion or Second-Phase Constituent Content of Metals by Automatic Image Analysis, ASTM International, West Conshohocken, PA, 2012, www.astm.org.
- [3.30] ASTM Standard E112-12: Standard Test Methods for Determining Average Grain Size, ASTM International, West Conshohocken, PA, 2012, www.astm.org.
- [3.31] N.H. Van Dijk, A.M. Butt, L. Zhao, J. Sietsma, S.E. Offerman, J.P. Wright, S. van der Zwaag, *Thermal stability of retained austenite in TRIP steels studied by synchrotron X-ray diffraction during cooling*, Acta Materialia, 53 (2005), 5439-5447.
- [3.32] D.J. Dyson and B. Holmes, *Effect of alloying additions on the lattice parameter of austenite*, The Journal of the Iron and Steel Institute, 208 (1970) 469-474.
- [3.33] B.D. Cullity: *Elements of X-Ray Diffraction*, 2nd edition, Addison-Wesley Publishing Company, 1978, 459.
- [3.34] M. Calcagnotto, D. Ponge, E. Demir, D. Raabe, *Orientation gradients and geometrically necessary dislocations in ultrafine grained dual-phase steels studied by 2D and 3D EBSD*, Materials Science and Engineering: A, 527 (2010), 2738-2746.
- [3.35] S.J. Lee, S. Lee, B.C. De Cooman, *Martensite transformation of sub-micron retained austenite in ultra-fine grained manganese transformation-induced plasticity steel*, International Journal of Materials Research, 104 (2013), 423-429.
- [3.36] D.P. Koistinen and R.E. Marburger, A general equation prescribing the extent of the austenite-martensite transformation in pure iron-carbon alloys and plain carbon steels, Acta Metallurgica, 7 (1959), 59-60.
- [3.37] S.J. Lee, C.J. Van Tyne, A Kinetics model for martensite transformation in plain carbon and low-alloyed steels, Metallurgical and Materials Transactions A,43 (2012), 422-427.
- [3.38] S.J. Lee, S. Lee, B.C. De Cooman, *Mn partitioning during the intercritical annealing of ultrafine-grained 6% Mn transformation-induced plasticity steel*, Scripta Materialia, 64 (2011) 649-652.
- [3.39] M. Cai, Z. Li, Q. Chao, P.D. Hodgson, *A novel Mo and Nb microalloyed medium Mn TRIP steel with maximal ultimate strength and moderate ductility*, Metallurgical and Materials Transactions A, 45 (2014), 5624-5634.
- [3.40] Practical guidelines for the fabrication of duplex stainless steels, 2nd edition, International Molybdenum Association (IMOA), London, UK, 2009, 10-13.
- [3.41] S.W. Hwang, J.H. Ji, E.G. Lee, K.T. Park, Tensile deformation of a duplex Fe-20Mn-9Al-

- 0.6 C steel having the reduced specific weight, Materials Science and Engineering: A, 528 (2011) 5196-5203.
- [3.42] D.W. Suh, J.H. Ryu, M.S. Joo, H.S. Yang, K. Lee, H.K.D.H. Bhadeshia, *Medium-alloy manganese-rich transformation-induced plasticity steels*, Metallurgical and Materials Transactions A, 44 (2013), 286-293.
- [3.43] T. Furukawa, Dependence of strength-ductility characteristics on thermal history in lowcarbon, 5 wt-% Mn steels, Materials Science and Technology, 5 (1989), 465-470.
- [3.44] J. Han, Y.K. Lee, The effects of the heating rate on the reverse transformation mechanism and the phase stability of reverted austenite in medium Mn steels, Acta Materialia, 67 (2014) 354-361.
- [3.45] B. Hallstedt, A.V. Khvan, B.B. Lindahl, and M. Selleby, *Thermodynamic database for high-manganese steels*, *CALPHAD XLIV*, Loano, Italy, unpublished research, 2015.
- [3.46] G.R. Speich, V.A. Demarest, R.L. Miller, *Formation of austenite during intercritical annealing of dual-phase steels*, Metallurgical and Materials Transactions A, 12 (1981), 1419-1428.
- [3.47] X.L. Cai, A.J. Garratt-Reed, W.S. Owen, *The development of some dual-phase steel structures from different starting microstructures*, Metallurgical Transactions A, 16 (1985) 543-557.
- [3.48] J. Ågren, Computer simulations of the austenite/ferrite diffusional transformations in low alloyed steels, Acta Metallurgica, 30 (1982), 841-851.
- [3.49] A. Arlazarov, Evolution of microstructure and mechanical properties of medium Mn steels and their relationship, University of Lorraine, France, 2015, 109-117.
- [3.50] Q. Lai, Optimization of the Microstructure of Ferritic-Martensitic Steels with 3.5 wt. % Mn: Phase Transformations and Micromechanical Modeling, Joseph Fourier University, France, 2014, 44-64.
- [3.51] M. Goun & P. Maugis, J. Drillet, A criterion for the change from fast to slow regime of cementite dissolution in Fe-C-Mn steels, Journal of Materials Science & Technology, 28 (2012) 728-736.
- [3.52] G.R. Speich, A. Szirmae, M.J. Richards, *Formation of austenite from ferrite and ferrite-carbide aggregates*, Transactions of the Metallurgical Society of AIME, 245 (1969), 1063-1074.
- [3.53] J.R. Yang, H.K.D.H. Bhadeshia, *Reaustenitization experiments on some high-strength steel weld deposits*, Materials Science and Engineering: A, 118 (1989), 155-170.
- [3.54] C. Wells, R.F. Mehl, *Rate of diffusion of manganese in gamma iron in low-carbon and high-carbon manganese steels*, Transactions of the American Institute of Mining, Metallurgical and Petroleum Engineers, 145 (1941), 315-328.

- [3.55] J. Ågren, A revised expression for the diffusivity of carbon in binary Fe-C austenite, Scripta Metallurgica, 20 (1986), 1507-1510.
- [3.56] G. Neumann and C. Tuijn: *Self-diffusion and impurity diffusion in pure metals: handbook of experimental data*, 1st edition, Elsevier Ltd., 2009, 261-274.
- [3.57] J.S. Kirkaldy, P.N. Smith, R.C. Sharma, *Diffusion of manganese in paramagnetic BCC iron*, Metallurgical and Materials Transactions B, 4 (1973), 624-625.

CHAPTER 4

_

CRITICAL ROLE OF STRAIN PARTITIONING AND DEFORMATION TWINNING ON CRACKING PHENOMENON OCCURRING DURING COLD ROLLING OF TWO DUPLEX MEDIUM MANGANESE STEELS

In Chapter 3, the detailed phase transformation behavior of hot rolled medium Mn steels with high Al and Si content during intercritical annealing was investigated. This leads to a better understanding on the microstructural control for such medium Mn hot bands, which is helpful for the subsequent cold rolling process. This chapter thus focuses on the cold rollability of the high Al-Si medium Mn steels and their microstructural evolutions during cold rolling. The results reveal a critical role of austenite deformation mechanisms and strain partitioning on the cold rollability of the steels. The knowledge facilitates the successful processing of these high Al-Si medium Mn steels.

• This chapter has been published as: Binhan Sun*, Fateh Fazeli, Colin Scott, Xiaojun Yan, Zhiwei Liu, Xiaoyu Qin and Stephen Yue, "Critical role of strain partitioning and deformation twinning on cracking phenomenon occurring during cold rolling of two duplex medium manganese steels", Scripta Mater., 130 (2017), 49-53.

4.1 Abstract

Two ferrite-austenite duplex medium manganese steels with very similar phase fractions and grain sizes were subjected to cold rolling. The 10Mn steel presented a much better cold rollability compared with the 7Mn steel, which is believed to stem from two critical factors. Firstly, the larger strain partitioning in the 10Mn steel resulted in a less deformation accommodated by the brittle δ -ferrite, which delayed or even inhibited micro-crack formation inside the ferrite phase; Secondly, the deformation twinning activated in the austenite of the 10Mn steel during rolling effectively enhanced the ductility of the austenite-martensite (γ - α') mixed phase.

4.2 Introduction

Medium Mn steels alloyed with 3~10 wt.% Mn feature a large fraction of retained austenite (RA) [4.1] which can be tailored to provide various TRIP (transformation-induced plasticity) and TWIP (twinning-induced plasticity) effects [4.2, 4.3]. This can result in an excellent mechanical performance, making the steel a strong candidate material for the third-generation of advanced high strength steels (AHSS). The austenite is retained by the stabilization effect of the relatively high initial Mn addition and extra Mn partitioning due to intercritical treatment. However, this large amount of RA would easily transform to the hard and brittle martensite phase during deformation if its mechanical stability is not well controlled, which essentially deteriorates the ductility and the cold rollability of the steel. Currently, while great progresses have been achieved on the optimization of alloying, heat treatments and mechanical properties, the cold rolling performance of this type of steel and the corresponding microstructural evolution have rarely been reported.

A complicated deformation behavior is expected for medium Mn steels with multi-phases when they are subjected to cold rolling for two main reasons. First, the distribution of plastic strain will not be uniform due to the differences in mechanical behavior of different constituting phases. It has been reported that strain partitioning between austenite and ferrite in medium Mn steels largely influences the overall flow behavior, e.g. flow stress and strain-hardening behavior [4.4, 4.5]. Second, the deformation modes activated in austenite would also affect the cold rollability. It is well established that both TRIP and TWIP effect can improve the ductility of steels, by providing large enhancements of the work-hardening rate. The objective of this study is better understanding of the microstructural response of two variants of ferrite-austenite duplex medium Mn steels during cold rolling. This allows to assess the production of medium Mn steel sheets by conventional processing lines. The dominating factors on the cold rollability was revealed by comparing the two steels produced with similar initial phase fractions and grain sizes but very

different strain distribution and austenite deformation modes. The results generated in this work might also be applied to some low-density steels, which share similar microstructures [4.6].

4.3 Experimental Procedure

The chemical compositions of the rolled medium steels two hot Mn are Fe-0.2C-7/10Mn-3Al-3Si (in wt.%); they are referred to as 7Mn and 10Mn steel. Casting and hot rolling schedules for the 7Mn steel have been presented in Chapter 3. The 10Mn steel was newly hot rolled in this study; its ingot was reheated to 1200 °C and hot rolled to 3 mm above ~800 °C. Small strip specimens (6 cm × 1 cm) with a thickness of ~2 mm for cold rolling were machined from the hot rolled sheets. Before cold rolling, samples were intercritically annealed at 1000 °C for 10 min, followed by air cooling, in order to produce ferrite plus austenite duplex microstructures with similar phase fractions and grain sizes for the two steels.

Cold rolling was conducted in a two-high laboratory rolling mill with the roll diameter of 10.2 cm and a rolling speed of around 35 revolutions per minute (RPM). The rolling direction was the same as for the hot rolling; an average of ~5% reduction in thickness was applied for each pass. After ~20% reduction, small edge cracking in the 7Mn steel occurred, and in the final stage, i.e. ~50% reduction, the edge areas were seriously cracked. However, the 10Mn steel showed a much better cold rollability with no edge cracks or any other defects formed up to ~50% reduction.

Microstructure observations were performed with electron backscattered diffraction (EBSD), scanning electron microscope (SEM, Hitachi SU3500) and transmission electron microscope (TEM, FEI Tecnai G2 F20, operated at 200 kV). The austenite fraction of the samples was determined by X-ray diffraction (XRD) using Co K_{α} radiation. The hardness of each phase in the two samples was measured inside the grains using a Vickers micro-hardness tester. Compositional analysis for specific phases was performed in SEM using Energy-Dispersive X-ray Spectrometer (EDX).

The strain distribution between austenite and ferrite in the two alloys during deformation was

measured by an in-situ SEM tensile test. A MTI SEMtester 1000 micro load frame was used to load the samples inside the electron microscope vacuum chamber (ZEISS EV018), with a constant loading rate of 0.1 mm/min. The surface of the tensile samples (with the gage length of 12.5 mm) were polished and etched before testing. Concurrent loading and imaging of the sample for the same area were performed during each test. The microscopic strain (*e*) of each phase was calculated by the length change of more than five grains along the tensile direction divided by their initial length.

4.4 Results and Discussion

Figure 4.1 shows the ferrite-austenite duplex microstructures of the two steels after prior annealing, which consists of mostly δ -ferrite and austenite (γ) elongated bands resulting from hot deformation in the two-phase range [4.7]. A very small amount of intercritically annealed ferrite $(IA-\alpha)$ is present inside the austenite grains, which is transformed from prior bainite and pearlite. The well-known Kurdjumov-Sachs (K-S) orientation relationship exists between the IA- α and γ , with the phase boundaries highlighted as the red color in Figs. 4.1 (a) and (b). Detailed information of each phase in the annealed samples is listed in Table 4.1. The two steels exhibit very similar retained austenite fractions and grain sizes despite the different Mn additions; the fraction of δ -ferrite is also expected to be similar due to the very small amount of IA- α . This similar phase fraction is most likely due to the slow austenite formation kinetics at later stages of intercritical annealing which is controlled by the sluggish Mn diffusion. Solute partitioning is observed after intercritical annealing, resulting in a higher Mn enrichment in austenite and a higher Al and Si concentration in δ -ferrite, as shown in Table 4.1. The austenite is softer than the δ-ferrite in both steels, although some amount of stress/strain-induced martensite might form during the indentation which essentially increases the austenite hardness value [4.8]. Figure 4.1 (c) plots the fractions of retained austenite and strain-induced α' -martensite in the two steels cold rolled to different stages (measured by XRD); no ε-martensite was observed after deformation, either from the microstructure or the XRD patterns. The amounts of transformed α' -martensite with overall cold rolling reduction are very similar for the two steels. In the 10Mn steel, deformation twins were also formed inside austenite grains during cold rolling (Fig. 4.1 (d)), showing the TWIP effect; however, no such features were observed in any samples of the 7Mn steel.

Table 4.1 Detailed information of each phase in the annealed medium Mn steels

Alloy	Phase	Grain Size (um)	Phase Fraction (wt.%)	C-lever rule* (wt.%)	Mn-EDX (wt.%)	Al-EDX (wt.%)	Si-EDX (wt.%)	Vickers Hardness (HV)	Ms (℃)**	Md ₃₀ (°C) **
7Mn	austenite (γ)	49.3 (4.3)	39.9 (1.7)	0.55	8.3	2.7	2.4	412.3 (20.1)	27.6	206.4
Steel	δ -ferrite (δ)	111.6 (3.0)	-	-	6.5	3.4	2.9	438.9 (12.1)	-	-
10Mn	austenite (γ)	43.5 (8.9)	41.0 (0.8)	0.49	11.7	3.1	2.8	369.7 (26.6)	-54.8	193.4
Steel	δ -ferrite (δ)	118.0 (6.1)	-	-	9.4	3.8	3.2	425.8 (27.6)	-	-

^{*}Carbon content was calculated based on the lever rule under the assumption that C was not soluble in ferrite;

(values in the parentheses are the standard errors)

^{**}Ms (°C) = $539-423w_C-30.4w_{Mn}-11w_{Si}$ [4.9], Md_{30} (°C) = $608-515w_C-7.8w_{Si}-12w_{Mn}$ [4.10], where w_C , w_{Mn} , w_{Si} are austenite C, Mn and Si contents (in wt.%).

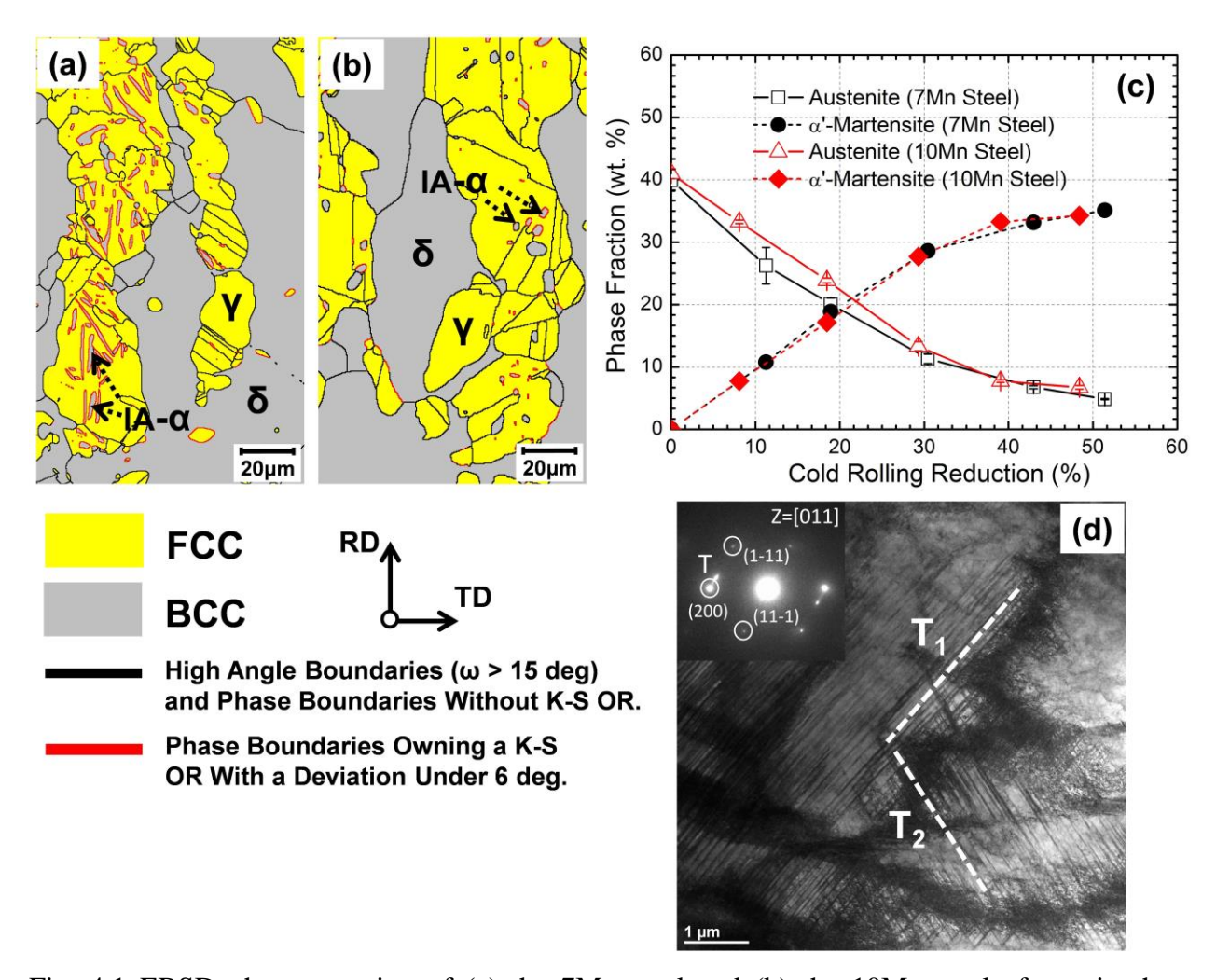


Fig. 4.1 EBSD phase mapping of (a) the 7Mn steel and (b) the 10Mn steel after prior heat treatment at 1000 $^{\circ}$ C for 10 min, followed by air cooling; (c) Fractions of strain-induced α' -martensite and retained austenite as a function of cold rolling thickness reduction; (d) Deformation twins in the 10Mn steel cold rolled to 10% reduction.

Figure 4.2 shows the SEM and EBSD images of the 7Mn steel samples cold rolled to ~20% reduction, which was observed as the starting stage of the edge cracking. Several micro-cracks were observed in the vicinity of the edge cracks; they are nucleated at the interface of strain-induced α' -martensite and IA- α , or inside the α' - γ mixture, as marked by an elliptic and a rectangular frames in Figs. 4.2 (a) and (b), respectively. The ferrite/martensite interface decohesion and martensite cracking were facilitated by the local stress concentration and low

toughness of fresh martensite; they have been widely observed and well explained in dual-phase (DP) steels [4.11, 4.12]. However, the cracking also initiates inside the coarse-grained δ -ferrite (Figs. 4.2 (c) and (d)), which is quite unexpected because the ferrite phase is normally considered as a soft/ductile phase at room temperature, and used as the soft matrix in plain carbon steels and most first generation AHSS such as DP and TRIP steels. The embrittlement of δ -ferrite could be derived from two possible reasons: firstly high enrichment of Si in ferrite; and secondly due to large grain size (110~120 μm). It is established that Si higher than ~0.5 wt.% could worsen the ductility and fracture toughness of ferrite [4.13, 4.14], due to the high degree of solid solution strengthening, although the overall tensile elongation of the steel might be enhanced depending on the microstructural change by Si addition [4.15]. This deteriorating effect becomes rather strong when the Si level is above certain value (3.5~4 wt.%) [4.16], mainly because of the occurrence of some ordering phases such as B2 and DO3 promoted by high Si content, which can induce the formation of dissociated superlattice dislocations and the correlated high stress concentration [4.16]. The Si content of the δ -ferrite phase in the annealed 7Mn and 10Mn steel is 2.9 and 3.2 wt.% (Table 4.1), respectively, which are quite close to this value. A large grain size would also promote fracture, by decreasing the critical fracture stress [4.17]. Actually, there is a synergic effect between the two factors; on one hand, the addition of Si promotes the growth of large ferrite grains during annealing [4.17], on the other hand, since solutes tend to segregate on the boundaries, the coarse grain of ferrite which yields less boundaries could essentially increase the degree of solid solution hardening by Si [4.18], further reducing the ductility. This detrimental effect of grain size was supported by the experimental work of Kim et al. [4.19] who studied a Fe-0.1C-2Si DP steel and found the coarse dual-phase structure has a higher strength than the fine structures, but demonstrates a much lower elongation and ductility. This was attributed to the initiation of cleavage cracks in the coarse-grained ferrite region. It is also interesting to observe the formation of deformation twins inside the δ -ferrite grains close to the micro-cracks, which could be promoted by the large grain size [4.20, 4.21] and high deformation rates [4.21]; they are either crossing the whole grains or terminated by the micro-cracks, as

revealed in Figs. 4.2 (c) and (d). Theses twins might also behave as the nucleation sites of cracks and induce a cleavage fracture in ferrite, as reported by many researchers [4.20, 4.21].

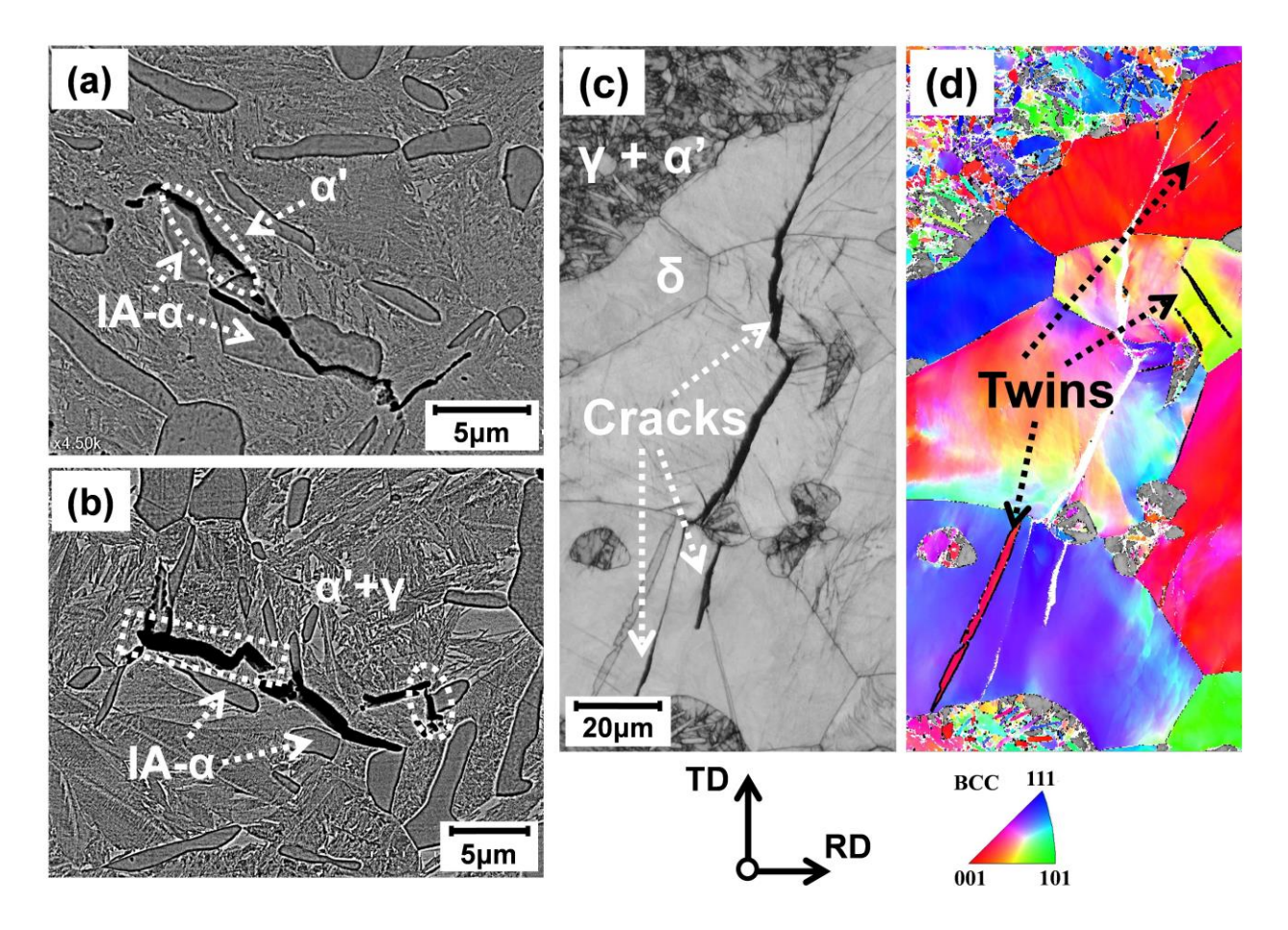


Fig. 4.2 SEM micrographs of the 7Mn steel after ~20% cold rolling reduction showing micro-cracks nucleated (a) on the α' -martensite and IA- α phase boundaries and (b) inside the α' - γ mixed phase; (c) EBSD band contrast (BC) mapping and (d) BCC inverse pole figure (IPF) for the same sample of (a) and (b), showing micro-cracks and deformation twins inside δ -ferrite (the coincidence site lattice (CSL) Σ 3 (60°/<111>) twin boundaries were highlighted as thick black lines in Fig. 4.2 (d)).

As illustrated above, both steels have high Si additions and large δ -ferrite grains, which are undesired and detrimental for ductility, however, the ensuing adverse effect is much more pronounced for the 7Mn steel, for example, no cracking was observed during the whole cold

rolling process of the 10Mn steel. In order to explain this, the heterogeneous distribution of plastic strains between the two phases can be further analyzed. Figure 4.3 (a) shows the microscopic tensile strain of the δ -ferrite and austenite phase in both steels as a function of the macroscopic tensile load, measured by in-situ SEM tensile tests; note that the austenite phase here includes both the martensite transformed during straining and the remained austenite. It is obvious that the strain partitioning between ferrite and austenite occurs in both steels under deformation, and most strain is accommodated by the softer austenite. However, the distribution of plastic strain is much more heterogeneous in the 10Mn steel, which can also be indicated by the much larger ferrite/austenite hardness difference shown in Table 4.1. Note that the micro-hardness tests were conducted only inside of the grains without including the grain boundaries. It was mentioned by Lee et al. [4.6] that the grain boundaries could also influence the macroscopic mechanical property of each phase and might alter the strain/load distribution behavior in two phase steels, however, their work showed that this effect is only prominent when the grain size is lower than 1 μ m. The strain partition coefficient (n) could be defined as the ratio of the austenite strain to the ferrite strain in the plastic deformation range at the same macroscopic load ($n = e_{\gamma} / e_{\alpha}$). The average value was estimated to be 2.3 for the 10Mn steel and 1.3 for the 7Mn steel, as shown in Fig. 4.3 (b). It has to be noted that these values could decrease at higher strains since the continuous formation of strain-induced martensite and deformation twins would enhance the work hardening of austenite and might eventually result in the strain transferring from austenite to ferrite [4.5]. Nevertheless, it is reasonable to conclude that the larger strain partitioning in the 10Mn steel lowers the deformation accommodated by the brittle δ-ferrite during cold rolling, which can be one factor delaying the cracking.

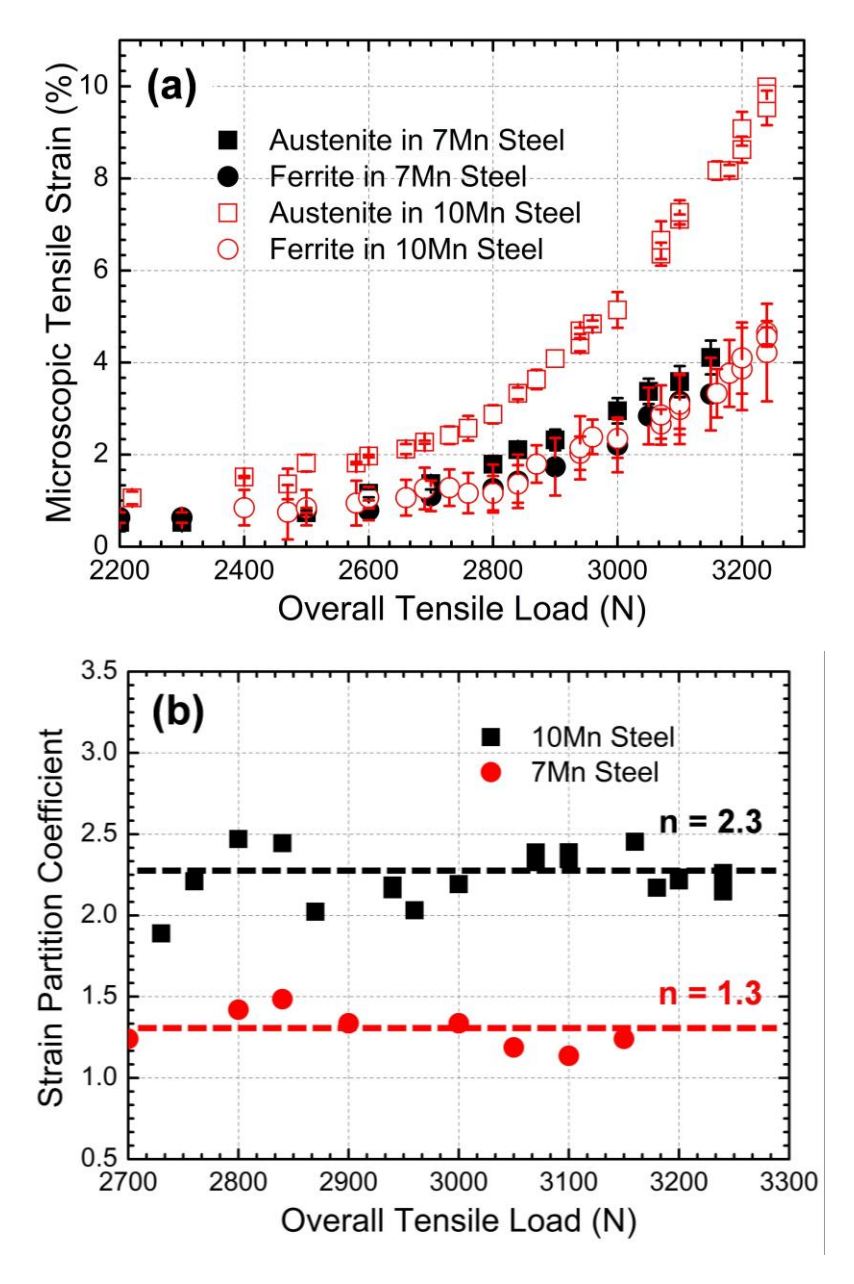


Fig. 4.3 (a) Microscopic tensile strain of austenite (including strain-induced martensite) and δ -ferrite in the two steels as a function of the overall tensile load; (b) Strain partition coefficient (n) of the two steels, calculated from the data in (a).

As mentioned above, micro-cracking during cold rolling is also related to the formation of strain-induced martensite. It is expected that the fraction of this martensite and the plasticity of the neighboring austenite are both important factors. Although the amount of strain-induced

martensite is similar for the two steels at a given overall rolling reduction, the stability of austenite is actually different. The lower austenite stability is confirmed by the higher Ms and Md₃₀ temperatures (Md₃₀ is the temperature where half of the austenite is transformed to martensite at a strain of 30%) for the 7Mn steel estimated in Table 1. As such, higher fractions of strain-induced martensite tend to form in the 7Mn steel compared to the 10Mn alloy at the same local strain of austenite. This becomes evident by compiling the data of Figs. 4.1 (c) and 4.3 (b), i.e. due to different strain partitioning coefficients the local strain is significantly lower in austenite of the 7Mn steel at a given overall reduction regardless of similar martensite fractions. Nevertheless, in the overall behavior, if there is a critical martensite fraction existing as a critical micro-crack nucleation threshold, such as ~20 wt. % α'-martensite in the 7Mn steel sample cold rolled to ~20% reduction, then it is difficult to explain that the 10Mn steel, with nearly 35 wt. % α'-martensite after cold rolling to ~50% reduction, does not show any microscopic voids or cracks inside the α' - γ mixed phase. Hence, there must be some distinct features in the 10Mn steel which effectively reduce the possibility of micro-crack formation. It is demonstrated that the austenite in the 10Mn steel shows a coupled TRIP and TWIP effect during cold rolling, whereas only the TRIP effect is activated in the austenite of the 7Mn steel. It is general that steels with a TWIP effect present a higher ductility and toughness compared with those aided by TRIP effect. For instance, Frommeyer et al. [4.22] investigated three high Mn TRIP/TWIP steels with compositions of Fe-15/20/25Mn-3Al-3Si; it was found that the 15Mn alloy showing only a TRIP effect possessed a 46% tensile elongation, whereas the 20Mn alloy aided by both TRIP and TWIP effects showed 81% elongation, and this value increased to 95% for the 25Mn alloy which only showed the TWIP effect. A similar result was found by Lee and De Cooman [4.3], who studied the tensile behavior of a Fe-0.3C-10Mn-3Al-2Si alloy and showed the ductility was significantly improved when suitable intercritical annealing treatments were applied to activate some TWIP effect in the austenite. However, the differences on phase constituents and fractions between the general TRIP-aided and TWIP-aided steels make it very difficult to directly compare these two effects in terms of their contributions on ductility. Therefore, one novelty of this work

is providing an approach to compare the TRIP and TWIP effect directly, by comparing two steels with similar initial structures but different austenite deformation behaviors. It is probable that the extra TWIP effect in the 10Mn steel improves its ductility and toughness, which essentially enhances its cold rollability. When strain-induced martensite is transformed from austenite and the α' - γ mixture is subsequently deformed, dislocation pile-ups and stress concentrations will occur at the intersections of two martensite plates [4.23, 4.24] or between martensite plates and other boundaries [4.25], which can initiate micro-cracks. This stress concentration cannot be relieved by the cross slip of dislocations due to the low austenite stacking fault energy (SFE) of both steels. However, deformation twinning formed in the 10Mn steel might relieve certain amount of stress concentration by allowing dissociated dislocation glide and lattice realignment inside twins, thus suppressing the nucleation of micro-cracking. On the other hand, the deformation twins would also provide an extra enhancement of the work hardening rate in austenite, which inhibits the local deformation. This beneficial effect of the deformation twining on ductility can be confirmed by checking the fracture surfaces of both steels. As shown in Fig. 4.4, the δ -ferrite phase in both steels presents a complete cleavage fracture, which confirms that it is quite brittle. The fracture surfaces of the γ - α' mixed phase show a mixture of quasi-cleavage and dimple behavior, however, the dimple area in the 10Mn steel is clearly much larger than that in the 7Mn steel, which indicates a better ductility.

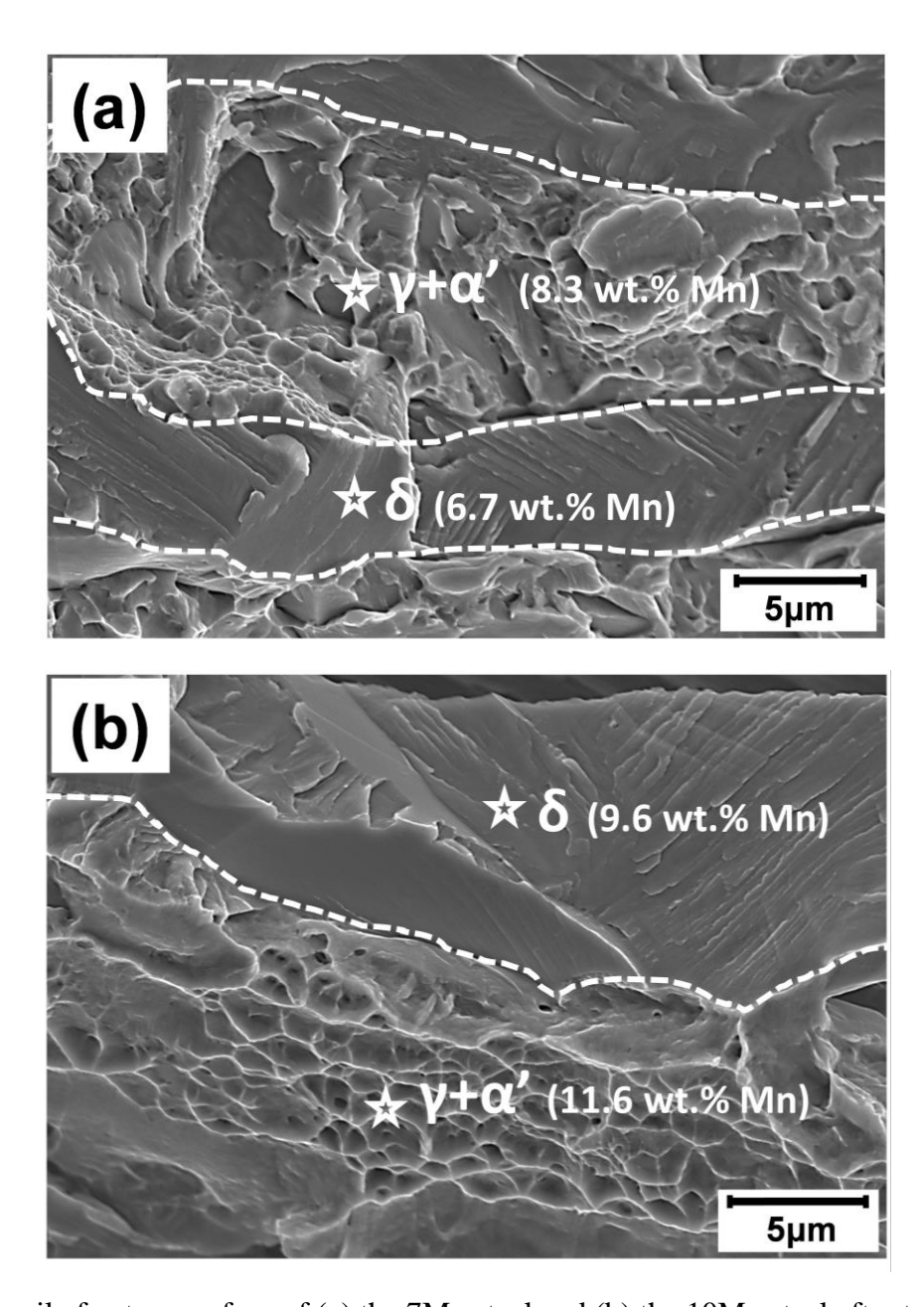


Fig. 4.4 Tensile fracture surface of (a) the 7Mn steel and (b) the 10Mn steel after tensile tests.

4.5 Conclusions

In summary, two medium Mn steels with ferrite-austenite duplex microstructures were subjected to cold rolling. The 10Mn steel presented a much better cold rollability, which is believed to stem from two factors: (a) the larger strain partitioning in the 10Mn steel resulted in a less deformation accommodated by the brittle δ -ferrite, which delays or even inhibits the micro-cracking formation inside the ferrite phase. The low ductility of the δ -ferrite is related to its high Si content and large grain size; (b) the deformation twinning (TWIP effect) activated in the 10Mn steel during rolling effectively enhanced the ductility of γ - α' mixed phase. This study shows that deformation twinning presents a superior contribution to the ductility of steels compared with strain-induced martensite.

4.6 References

- [4.1] S. Lee, B.C. De Cooman, On the selection of the optimal intercritical annealing temperature for medium Mn TRIP steel, Metallurgical and Materials Transactions A, 44 (2013), 5018-5024.
- [4.2] H. Aydin, I.H. Jung, E. Essadiqi, S. Yue, *Twinning and tripping in 10% Mn steels*, Materials Science and Engineering: A, 591 (2014), 90-96.
- [4.3] S. Lee, B.C. De Cooman, *Annealing temperature dependence of the tensile behavior of 10 pct Mn multi-phase TWIP-TRIP Steel*, Metallurgical and Materials Transactions A, 45 (2014), 6039-6052.
- [4.4] P.J. Gibbs, B.C. De Cooman, D.W. Brown, B. Clausen, J.G. Schroth, M.J. Merwin, D.K. Matlock, *Strain partitioning in ultra-fine grained medium-manganese transformation induced plasticity steel*, Materials Science and Engineering: A, 609 (2014), 323-333.
- [4.5] M.I. Latypov, S. Shin, B.C. De Cooman, H.S. Kim, *Micromechanical finite element analysis of strain partitioning in multiphase medium manganese TWIP+TRIP steel*, Acta Materialia, 108 (2016), 219-228.
- [4.6] K. Lee, S.J. Park, Y.S. Choi, S.J. Kim, T.H. Lee, K.H. Oh, H.N. Han, *Dual-scale correlation of mechanical behavior in duplex low-density steel*, Scripta Materialia, 69 (2013), 618-621.
- [4.7] B. Sun, H. Aydin, F. Fazeli, S. Yue, *Microstructure evolution of a medium manganese steel during thermomechanical processing*, Metallurgical and Materials Transactions A, 47 (2016) 1782-1791.
- [4.8] H.S. Park, J.C. Han, N.S. Lim, J.B. Seol, C.G. Park, *Nano-scale observation on the transformation behavior and mechanical stability of individual retained austenite in CMnSiAl TRIP steels*, Materials Science and Engineering: A, 627 (2015), 262-269.
- [4.9] K.W. Andrews, *Empirical formulae for the calculation of some transformation temperatures*, The Journal of the Iron and Steel Institute, 203 (1965) 721-727.
- [4.10] T.H. Lee, C.S. Oh, S.J. Kim, *Effects of nitrogen on deformation-induced martensitic transformation in metastable austenitic Fe-18Cr-10Mn-N steels*, Scripta Materialia, 58 (2008), 110-113.
- [4.11] D.L. Steinbrunner, D.K. Matlock, G. Krauss, *Void formation during tensile testing of dual phase steels*, Metallurgical Transactions A, 19 (1988), 579-589.
- [4.12] M. Calcagnotto, Y. Adachi, D. Ponge, D. Raabe, *Deformation and fracture mechanisms in fine- and ultrafine-grained ferrite/martensite dual-phase steels and the effect of aging*, Acta Materialia, 59 (2011), 658-670.
- [4.13] K.D. Sibley, N.N. Breyer, The effect of silicon on the impact and tensile properties of

- low-carbon steels, Metallurgical and Materials Transactions A, 7 (1976), 1602-1604.
- [4.14] P. Abramowitz, R.A. Moll, Silicon-carbon interaction and its effect on the notch toughness of mild steel, Metallurgical Transaction, 1 (1970), 1773-1775.
- [4.15] R.G. Davies, *Influence of silicon and phosphorous on the mechanical properties of both ferrite and dual-phase steels*, Metallurgical Transactions A, 10 (1979), 113-118.
- [4.16] B. Viala, J. Degauque, M. Fagot, M. Baricco, E. Ferrara, F. Fiorillo, *Study of the brittle behaviour of annealed Fe-6.5 wt% Si ribbons produced by planar flow casting*, Materials Science and Engineering: A, 212 (1996), 62-68.
- [4.17] A.S. Tetelman, A.J. McEvily Jr, *Fracture of Structural Materials*, John Wiley & Sons, Inc., New York, 1967.
- [4.18] C.C. Anya, T.N. Baker, *The effect of silicon on the grain size and the tensile properties of low carbon steels*, Materials Science and Engineering: A, 118 (1989), 197-206.
- [4.19] N.J. Kim, G. Thomas, *Effects of morphology on the mechanical behavior of a dual phase Fe/2Si/0.1 C steel*, Metallurgical Transactions A, 12 (1981), 483-489.
- [4.20] D. Hull, Effect of grain size and temperature on slip, twinning and fracture in 3% silicon iron, Acta Metallurgica, 9 (1961), 191-204.
- [4.21] T. Šmida, J. Bošanský, *Deformation twinning and its possible influence on the ductile brittle transition temperature of ferritic steels*, Materials Science and Engineering: A, 287 (2000), 107-115.
- [4.22] G. Frommeyer, U. Brux, P. Neumann, *Supra-ductile and high-strength manganese-TRIP/TWIP steels for high energy absorption purposes*, ISIJ International, 43 (2003) 438-446.
- [4.23] S.Y. Jo, J. Han, J.H. Kang, S. Kang, S. Lee, Y.K. Lee, *Relationship between grain size and ductile-to-brittle transition at room temperature in Fe-18Mn-0.6C-1.5Si twinning-induced plasticity steel*, Journal of Alloys and Compounds, 627 (2015), 374-382.
- [4.24] S. Takaki, T. Furuya, Y. Tokunaga, *Effect of Si and Al additions on the low temperature toughness and fracture mode of Fe-27Mn alloys*, ISIJ International, 30 (1990), 632-638.
- [4.25] M. Koyama, T. Sawaguchi, K. Tsuzaki, *Premature fracture mechanism in an Fe-Mn-C austenitic steel*, Metallurgical and Materials Transactions A, 43 (2012,) 4063-4074.

CHAPTER 5

_

ON THE DEFORMATION AND FRACTURE MECHANISMS OF AUSTENITE-FERRITE DUPLEX MEDIUM MANGANESE STEELS WITH DIFFERENT SILICON ADDITIONS

In Chapter 4, the cold rollability of the high Al-Si medium Mn steels and their microstructural evolutions during cold rolling were studied. The knowledge helped the successful cold rolling of such steels. This chapter investigates the microstructure, deformation behavior and fracture mechanisms of cold rolled and intercritical annealed medium Mn steels. It was hypothesized that Si could be a key factor in dictating the properties. Therefore, particular emphasis is paid on the effect of different Si additions (0~3 wt.%). The influence of the plasticity-enhancing mechanisms (TRIP and TWIP effect) of austenite and strain partitioning between austenite and ferrite on the mechanical property of different Si-alloyed samples is also a focus. A more fundamental understanding on the microstructure-property relationship of such steels is developed through this chapter.

• This chapter is to be submitted to Acta Mater., as: Binhan Sun*, Fateh Fazeli, Colin Scott, Nicolas Brodusch and Stephen Yue, "On the deformation and fracture mechanisms of austenite-ferrite duplex medium manganese steels with different silicon additions", 2017.

5.1 Abstract

The present study concerns the detailed deformation and fracture mechanisms of a 0.2C-10Mn-3Al medium Mn steel with different Si additions. Austenite-ferrite duplex microstructures with almost identical austenite fractions and austenite C, Mn and Al concentrations for different Si-alloyed steels were produced by intercritical annealing. The mechanical property of the annealed samples relied on the activation and kinetics of the transformation-induced plasticity (TRIP) and twinning-induced plasticity (TWIP) effect in austenite, as well as the strain partitioning between phase constituents during deformation. For the duplex structure with a lower fraction of austenite (i.e. ~30 %), the tensile strength was only slightly changed with Si levels, whereas the total and uniform elongation were significantly influenced, with a first increase and then decrease trend with increasing Si contents. This was associated with the different behavior of deformation twinning in austenite and strain partitioning between austenite and ferrite in different Si-alloyed samples. Silicon also decreased the post-uniform elongation and the degree of necking for this structure. With increasing Si contents, the fracture mechanisms changed from dimpled-type fracture driven by void formation, mainly ferrite/strain-induced α'-martensite interfaces, to a combined dimple and cleavage/quasi-cleavage fracture, which was governed by cracking inside δ -ferrite or along the δ-ferrite related interfaces. Conversely, when the austenite fraction was higher (i.e. ~45 %), the tensile strength and ductility values of the steel samples became insensitive to the Si content. In this structure, the more rapid martensite formation at the beginning of the deformation decreased the strain partitioning between austenite and ferrite, and was believed to be the main factor influencing the strain hardening rate.

5.2 Introduction

Developing high strength steels has received increasing attention in the steel industry, in order to meet the body-in-white weight reduction strategies pursued by the automotive industry for fuel economy and vehicle safety. In this context, medium manganese (Mn) steels containing 3 to 12 wt.% Mn have recently been developed and proven to be one of the strong candidates for the third-generation advanced high-strength steels (AHSS), due to the mechanical properties that exceed the first-generation AHSS and a potentially lower cost than the high Mn second-generation AHSS [5.1-5.6].

Investigations of medium Mn steels start from the Fe-C-Mn ternary system [5.2, 5.5-5.8]; the original work is from Miller [5.6] in the 1970s. The increased content of Mn compared with the first-generation AHSS effectively stabilizes austenite and increases the retained austenite (RA) fraction [5.2, 5.5, 5.8]. The transformation-induced plasticity (TRIP) effect in austenite of the Fe-C-Mn medium Mn steels contributes to great strength-ductility combinations [5.2, 5.5, 5.7, 5.8]. More recently, Al was added in medium Mn steels [5.9], in order to raise the intercritical temperatures, thus shortening the intercritical annealing time. The two phase $(\gamma + \alpha)$ range can also be enlarged by Al, such that the processing window, in terms of annealing temperatures, can be expanded [5.9]. More interestingly, the twinning-induced plasticity (TWIP) effect was observed in Al-added medium Mn steels [5.1, 5.4], which further improves the mechanical performance of such steels [5.1].

Silicon levels lower than 4 wt.% have also been added in medium Mn steels by some researchers [5.1, 5.3, 5.4, 5.10-5.13]; however, the purpose has rarely been mentioned and the effect of Si in such steels has never been established. It can be expected that Si possesses a similar effect as Al in terms of stabilizing ferrite, increasing austenite formation temperatures and enlarging the intercritical range. Silicon is also well established as an effective solid solution strengthening element for both ferrite and austenite [5.14-5.16]. It was reported that Si can enhance the

yield/tensile strengh levels without scrificing uniform elongations in dual phase (DP) steels with a ferrite and martensite structure [5.17-5.19]. Hironaka et al. [5.19] attributed this to the increased strain hardening rate of ferrite by Si, due to the retardation effect of Si on the formation of dislocation cell structure and the resulting higher rate of dislocation storage. Jeong et al. [5.16] investigated the influence of Si on the mechanical twinning and strain hardening of an austentic Fe-18Mn-0.6C TWIP steel, and found that the Si can promote the formation of deformation twins, thus increasing straining hardening. Despite all these reported beneficial influences, Si also possesses some negative effects on steels. For example, a Si content higher than ~0.5 wt. % was generally reported to be detrimental to the ductility and fracture toughness in low-carbon ferritic steels [5.14].

For medium Mn steels with multi-phases, the mechanical properties rely on the deformation behavior of each individual phase and their interactions [5.4, 5.20]. Therefore, the documented Si effects on single phase steels might not be applicable for medium Mn steels. It is thus worthwhile to investigate the effect of Si on the overall mechanical behavior of such steels, and explore the suitability of Si alloying from the perspective of mechanical metallurgy. Great challenges exist for isolating the Si effect on medium Mn steels, since many other microstructural variations (e.g. austenite fractions and C/Mn contents upon intercritical annealing) could also influence the mechanical properties.

In addition, most investigations on medium Mn steels have mainly focused on the plasticity-enhancing mechanisms (TRIP and/or TWIP) of austenite, in order to explain the excellent tensile properties of such steels. The interaction between austenite and its neighboring phases in terms of strain partitioning during deformation and its influence on the mechanical property, however, have not attracted enough attention. Only limited reports can be found regarding this topic [5.4, 5.20]. Considering each individual phase in such steels can have very different mechanical properties, this factor cannot be neglected.

The present work aims to investigate the deformation and fracture mechanisms of a 0.2C-10Mn-3Al medium Mn steel with different Si additions. In an effort to reveal the Si effect, we first attempt to produce similar austenite-ferrite duplex microstructures for different steels by carefully controlling the intercritical annealing parameters. Then the tensile properties are compared among different Si-alloyed steels. The deformation behaviors with respect to the plasticity-enhancing mechanisms of austenite and strain partitioning between austenite and ferrite are studied in detail. Finally, we investigate the effect of Si on fracture mechanisms of medium Mn steels, which is a topic rarely studied in such steels [5.11].

5.3 Experimental Procedure

5.3.1 Materials and processing

The chemical compositions of the investigated medium Mn steels are shown in Table 5.1. They possess various Si contents (0~3 wt.%) but approximately same amounts of other elements (C, Mn and Al). The steels are referred to as 0Si, 1Si and 3Si in this study for convenience.

Table 5.1 Steel compositions in weight percent

Alloy	С	Mn	Al	Si	Fe
0Si	0.185	10.41	2.85	0.025	Bal.
1Si	0.185	10.24	2.78	1.0	Bal.
3Si	0.183	9.66	3.18	3.39	Bal.

The steel ingots were cast in a vacuum induction furnace, reheated to $1200\sim1230~$ °C and hot rolled to $2.5\sim3~$ mm (3 mm for the 0Si and 1Si steel, 2.5~ mm for the 3Si steel) above $\sim750~$ °C. The hot bands were then heat treated at 500~ °C for the 0Si and 1Si steel and at 800~ °C for the 3Si steel to soften the materials, after which cold rolling was conducted with a thickness reduction of $\sim50\%$. The cold rolled microstructures of the 0Si and 1Si steel are predominantly deformed martensite, whereas the 3Si steel consists of δ -ferrite (δ) and about 40 vol.% strain-induced α' -martensite after cold rolling.

Since the fraction of retained austenite critically influences the mechanical properties of medium Mn steels [5.1, 5.2, 5.5], it needs to be maintained constant for the three steels in order to reveal the effect of Si; this requires a careful control of annealing parameters. The CALPHAD method is not suitable for guiding the heat treatments in this study due to the inaccuracy of the thermodynamic database for Si-added medium Mn systems. Therefore, intercritical annealing was first carried out in a box furnace for the cold rolled steels at various temperatures for 5 min, followed by water quenching, after which suitable austenite-ferrite duplex microstructures with a

fixed austenite fraction were selected to investigate the effect of Si on mechanical behaviors. The intercritical ranges (austenite start (Ac1) and austenite finish (Ac3) temperatures) of the three alloys were determined by dilatometry (DIL 805A/D); the experimental parameters can be found elsewhere [5.21].

5.3.2 Mechanical and microstructural characterization

Room temperature uniaxial tensile tests were carried out on the annealed specimens at a constant crosshead speed corresponding to a macroscopic engineering strain rate of 6×10^{-4} s⁻¹; two to five tensile samples were repeated. The tensile samples were machined according to ASTM E-8 subsize standard (25 mm gage length) and oriented parallel to the rolling direction.

The microstructure of undeformed and deformed specimens, damage and fracture surface were characterized by scanning electron microscopy (SEM) and electron backscatter diffraction (EBSD) (a FEI Inspect F-50 field-emission SEM for secondary electron (SE) imaging; a Hitachi SU-3500 SEM and a Hitachi SU-8230 cold-field emission SEM for EBSD). Samples for EBSD observations were finally polished with 0.04 µm colloidal silica in a vibratory polisher. The acquired EBSD data (phase, grain size and local misorientation) were analyzed using the HKL Channel 5 (Tango) software package. The micromechanical details associated with the deformation-induced phase transformation and deformation twinning were studied using a transmission electron microscope (TEM, FEI Tecnai G2 F20, operated at 200 kV). Thin foil specimens for TEM investigations were prepared by mechanical grinding and electro-polishing in a twin-jet polisher (Struers, Tenupol-5) at a voltage of 20 V and room temperature. The electrolyte contained 90% glacial acetic acid and 10 % perchloric acid.

Retained austenite fraction was quantified by X-ray diffraction (XRD) using Co K_{α} radiation, operated at 35 kV and 45 mA with scan step size of 0.02 °. The acquired data was analyzed by the Reitveld whole diffraction pattern fitting procedures [5.22] implemented by the TOPAS 5

software. The change in the fraction of retained austenite due to α' -martensite formation during tensile tests was analyzed by an *in situ* magnetic induction method implemented by a Feritscope (Fischer, FMP 30). The probe of the Feritscope was tightly attached to the center of the tensile samples during the tensile testing, and the value was recorded every 2.5 s. Since a linear relationship exists between the Feritscope and XRD values [5.23], the retained austenite fraction generated from the Feritscope was calibrated in advance using XRD values.

Composition analysis (Mn, Al and Si) of the phases was performed using Energy-Dispersive X-Ray Spectrometer (EDX), operated at an accelerating voltage of 10 kV in the Hitachi SU-8230 SEM fitted with a Bruker Flat Quad 5060F annular silicon drift detector (SDD). The contents of Mn, Al and Si of austenite are averaged from more than 15 grains selected randomly from different locations in each specimen. EDX area mapping was used to show the chemical distributions of Mn, Al and Si. The weight fraction values in EDX mapping was computed based on the f-ratio method [5.24] applied to a four elements system, i.e. Fe, Mn, Al and Si. The average C content of austenite was determined from the XRD data by adopting the equation proposed by Dyson and Holmes [5.25]:

$$\alpha_{\gamma}$$
 (Å) = 3.556 + 0.0453 $x_{\rm C}$ + 0.00095 $x_{\rm Mn}$ + 0.0056 $x_{\rm Al}$,

where α_{γ} is austenite lattice parameter which was determined from the interplanar spacing (d_{hkl}) of the austenite peaks [5.26], x_C , x_{Mn} , and x_{Al} are concentrations of C, Mn and Al in austenite (wt.%).

5.4 Results

5.4.1 Influence of Si on the microstructure

The experimental Ac1 and Ac3 temperatures of the three steels and their retained austenite fractions, as a function of annealing temperatures, are shown in Fig. 5.1. The austenite transition temperatures are effectively increased by Si addition. This effect is more pronounced for the austenite finish temperature (Ac3), that is, the intercritical range is enlarged by Si. It needs to be noted that the Ac3 temperature of the 3Si sample cannot be detected up to $1200 \, \text{C}$, namely, the single phase austenite range disappears for this steel. With increasing annealing temperature, the retained austenite fraction in the 0Si and 1Si steels shows a typical increase to a maximum value, followed by a decrease due to martensite formation upon quenching [5.5]. However, the 3Si steel always presents an austenite-ferrite duplex structure without martensite formation even after quenching from high temperatures, and the fraction of austenite keeps increasing with temperature. This is derived from the existence of the large fraction of δ -ferrite stabilized by the high Si content, which promotes C and Mn enrichment in austenite thus resulting in a higher austenite stability. The detailed phase transformation behavior of the hot rolled 3Si steel upon intercritical annealing was described in Chapter 3.

Nevertheless, it is revealed in Fig. 5.1 that similar austenite fractions can be obtained for the three steels by simply adjusting the annealing temperatures. Specifically, we focus on the mechanical behavior of the austenite-ferrite duplex microstructure with two variants of austenite fractions: (a) low-fraction austenite (LA) structure, which possesses ~30 % retained austenite and high stability. This is almost the lowest austenite fraction that can be achieved in the 0Si steel without carbides formation for the current intercritical annealing time; (b) high-fraction austenite (HA) structure with ~45 % austenite and lower stability. This is the maximum austenite value for the 0Si and 1Si samples (Fig. 5.1). It should be noted that the austenite fraction in the 3Si steel cannot reach this value up to 1000 °C. Again for convenience, the selected samples are referred to as LA-0Si, LA-1Si, LA-3Si for the LA-structure, and HA-0Si and HA-1Si for the

HA-structure.

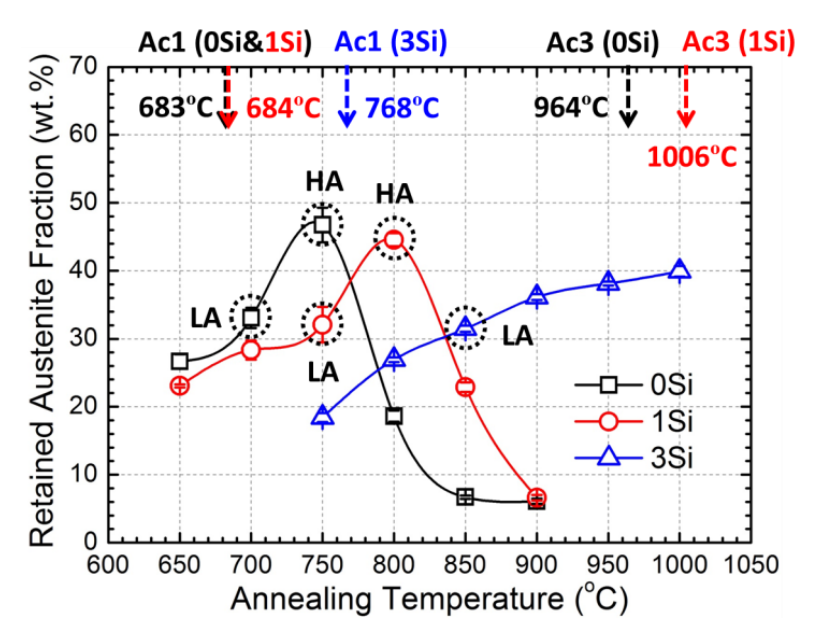


Fig. 5.1 Retained austenite fraction of the three steels annealed at different annealing temperatures for 5 min, followed by water quench. (the austenite transition temperatures for the three steels measured by dilatometry are marked by arrows, and the selected two types of microstructures are highlighted by dot circles).

The two types of microstructures (LA and HA) imaged by EBSD are presented in Fig. 5.2. The detailed information with respect to the fraction and composition of austenite, the grain size of each phase, and the calculated Ms and Md₃₀ temperatures are listed in Table 5.2. Both the 0Si and 1Si steels consist of sub-micron grained γ and α , regardless of the annealing temperatures. However, the LA-3Si sample contains a bimodal grain structure with ultra-fine γ and α transformed from martensite during annealing, and certain fraction of coarse grained δ -ferrite (around 10 μ m). The δ -ferrite phase was retained from the hot rolling stage and underwent fast recrystallization and grain growth during intercritical annealing [5.27]. However, further growth of δ -ferrite grains perpendicular to the rolling direction was constrained by the neighboring γ/α bands; as such these grains are still elongated along the rolling direction after annealing at

In each group of microstructures, a similar austenite fraction and austenite C, Mn and Al contents are maintained for different Si-alloyed steels (Table 5.2). However, the Si content essentially raises the annealing temperature for achieving similar austenite fractions, which increases the grain size; this linked effect on grain size is evident in Table 5.2. The chemical distributions of Mn, Al, and Si in the LA-1Si sample are shown in Fig. 5.3. It demonstrates a strong solute partitioning between austenite and ferrite, by Mn enrichment in austenite and Si/Al enrichment in ferrite. It has to be noted that an additional Si contribution came from the EDX detector itself, which resulted in an overestimation of the absolute Si weight fraction; however, this does not affect the difference of the Si concentration between the two phases.

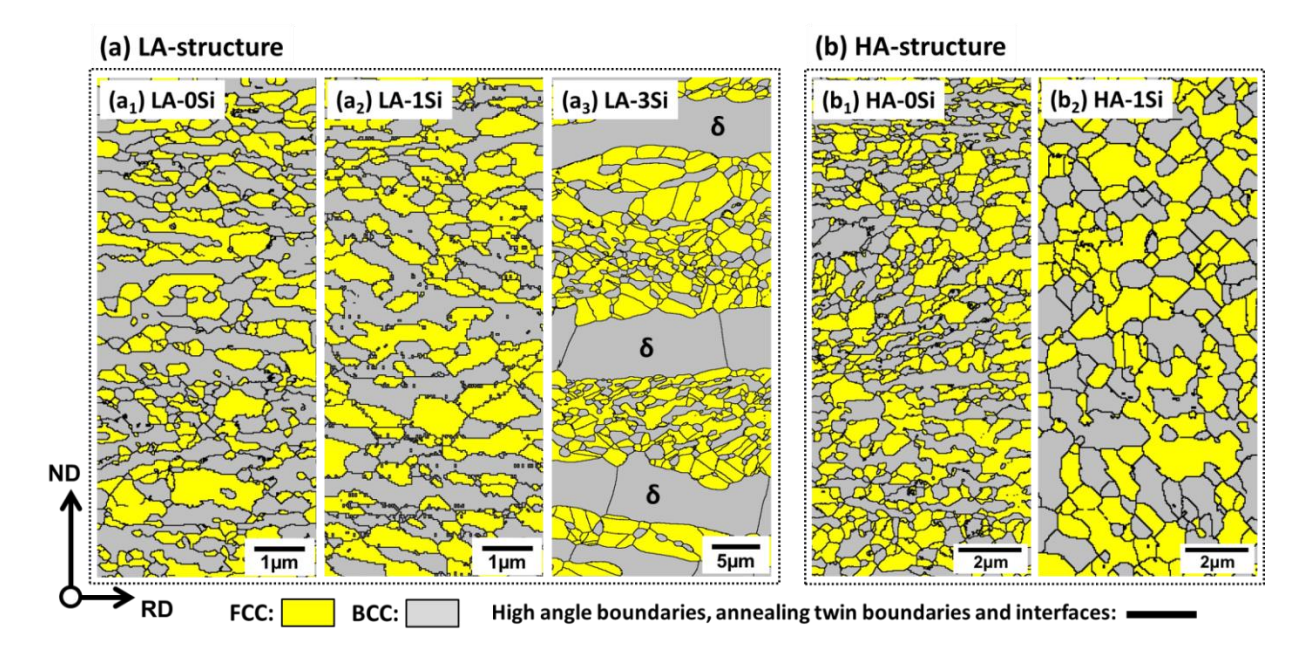


Fig. 5.2 EBSD observation of the (a) LA-structure and (b) HA-structure (a₁: LA-0Si, a₂: LA-1Si, a₃: LA-3Si; b₁: HA-0Si, b₂: HA-1Si).

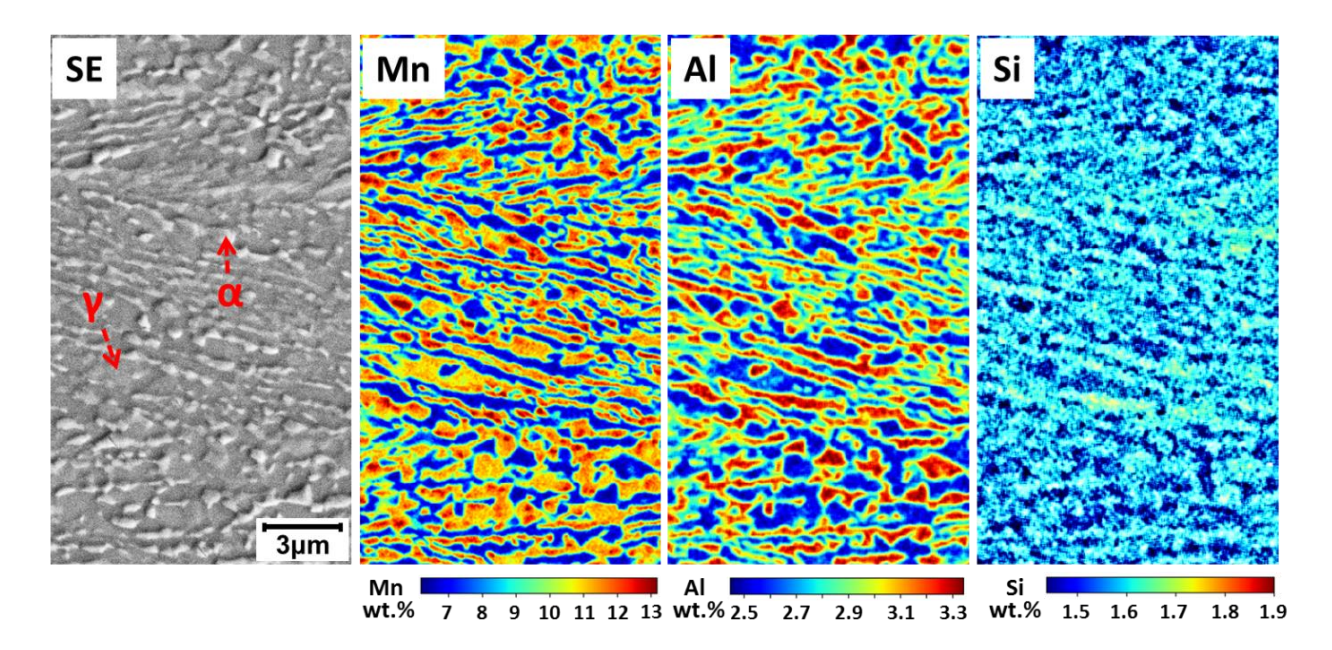


Fig. 5.3 EDX mapping of the LA-1Si sample, showing solute (Mn, Al and Si) partitioning between austenite and ferrite. (The lighter phase in the SE image is ferrite)

Table 5.2 Detailed information (austenite fraction and composition, grain size, and Ms/Md₃₀ temperature) in the annealed samples.

Sample	Austenite Fraction		Grain Size (μm)-EBSD		Ms	Md ₃₀				
	(wt.%)-XRD	C-lever rule ^a	C-XRD	Mn-EDX	Al-EDX	Si-EDX	austenite	α-ferrite	$- (\mathcal{C})_{p}$	$(\mathcal{C})^{c}$
LA-0Si	33.1 (1.5)	0.56	0.61	12.4 (0.6)	2.2 (0.1)	-	0.25	0.27	-155.7	173.1
LA-1Si	32.1 (2.6)	0.58	0.63	11.7 (0.5)	2.1 (0.1)	0.9 (0.1)	0.38	0.39	-134.5	162.9
LA-3Si	31.5 (0.5)	0.58	0.63	12.3 (0.4)	2.5 (0.1)	2.4 (0.1)	1.21	0.68	-143.7	149.8
HA-0Si	46.7 (2.5)	0.40	0.56	11.3 (0.4)	2.2 (0.1)	-	0.34	0.39	-60.7	257.5
HA-1Si	44.6 (1.0)	0.41	0.56	11.1 (0.3)	2.2 (0.05)	0.9 (0.04)	0.77	0.68	-48.6	249.0

a. Carbon content calculated by lever rule was based on the assumption that C was not soluble in ferrite.

(values in the parentheses are the standard errors).

b. Ms (C) = 475.9-335.1C (wt.%)-34.5 Mn (wt.%)-1.3 Si (wt.%)+11.67 ln (d_{γ}), where d_{γ} is the austenite grain size (in μ m) [5.28].

c. Md_{30} (°C) = 551-462C (wt.%)-8.1 Mn (wt.%)-9.2Si (wt.%)-1.42{(-3.2877-6.6439log₁₀l)-8)} [5.29, 5.30], where Md_{30} is the temperature at which half of the austenite is transformed to martensite after a strain of 30%, l is the mean linear intercept length of austenite grains (measured based on EBSD phase mappings).

5.4.2 Influence of Si on the tensile properties

The tensile properties and strain-induced transformation (SIT) from austenite to α' -martensite behavior for the LA and HA structures are shown in Fig. 5.4 and Fig. 5.5, respectively. For the LA-structure (Fig. 5.4), the yield strength (YS) decreases with increasing Si content, likely due to the larger grain size at high annealing temperatures necessary to achieve the similar microstructure. However, the ultimate tensile strength (UTS) is only slightly influenced by Si, although a first increase and then decrease trend can be established. The effect of Si on the ductility of the LA-structure is pronounced. It first increases the total elongation (TE) from ~29 % for the LA-0Si sample to ~45 % for the LA-1Si sample, then decreases the value to ~31 % for the LA-3Si sample (Fig. 5.4 (b)). The increase effect by a small amount of Si on both UTS and TE was also reported by Furukawa [5.13] who studied the tensile properties of 0.1-5Mn steels with 0 and 2 wt.% Si, although the microstructure was not given and no detailed analysis can be found in the study. The change of TE in Fig. 5.4 (b) is due to the variation of the uniform elongation (UE), which is related to the strain hardening ability of the materials. However, the post-uniform elongation (PUE) keeps decreasing with higher Si content, and this value reaches almost 0 for the LA-3Si sample, indicating the occurrence of some embrittlement or premature fracture at high Si level.

As shown from Fig. 5.4 (c), the strain hardening behavior of the three steels alters depending on the Si content. The strain hardening rate of the LA-0Si sample shows a one-stage monotonic decrease after yielding, until the occurrence of necking defined by the well-known Considère criterion. However, the LA-1Si and LA-3Si samples consist of a second-stage strain hardening (labeled in Fig. 5.4 (c)), characterized by an increase following the first-stage decrease; this postpones the plastic instability (i.e. necking) and contributes to a larger uniform elongation. Note that this second-stage increase is more pronounced in the 1Si sample compared with that in the 3Si sample. In the LA-1Si sample, the strain hardening rate also features a third stage decrease after around 0.23 true strain, whereas this stage is clearly absent in the LA-3Si sample

due to the premature fracture.

The change of strain-induced α' -martensite fraction was computed by the difference between the fraction of initial austenite and the remaining austenite during straining; this calculation is valid given that no ϵ -martensite formation was observed after deformation either from the microstructure or the XRD patterns. The results for the LA-structure are shown in Fig. 5.4 (d). Note that the magnetic induction measurement was deviated for the LA-3Si sample, most likely due to the presence of banded δ -ferrite and the thinner tensile specimens of the 3Si steel (~0.3 mm thinner than the other two steels). Therefore, only the XRD value was given for the LA-3Si sample. Nevertheless, it shows that the fraction of α' -martensite at a given macroscopic strain is similar for the three steels, despite their different austenite Si contents and grain sizes.

Two noticeable changes due to the different Si contents for the LA-structure can also be observed from the tensile curves (Fig. 5.4 (a)). The LA-0Si and LA-1Si steels show the discontinuous yielding resulting from Lüders banding. However, continuous yielding prevails in the LA-3Si sample, which is likely due to the suppression effect of the large fraction δ -ferrite on the initial localization of plastic flow [5.3]. On the other hand, the flow curve of the LA-1Si sample presents some serrations at the late stage of the plastic deformation (see the magnified part of the tensile curve as illustrated by the inset figure in Fig. 5.4 (a)), which indicates the occurrence of the Portevin-Le Chatelier (PLC) phenomenon associated with dynamic strain again (DSA). However, the other two samples do not show this PLC effect in the whole plastic range. Nevertheless, it can be concluded that Si mainly influences the ductility of the LA-structure in terms of the uniform elongation related to the strain hardening behavior and the post-uniform elongation pertaining to the fracture mechanisms.

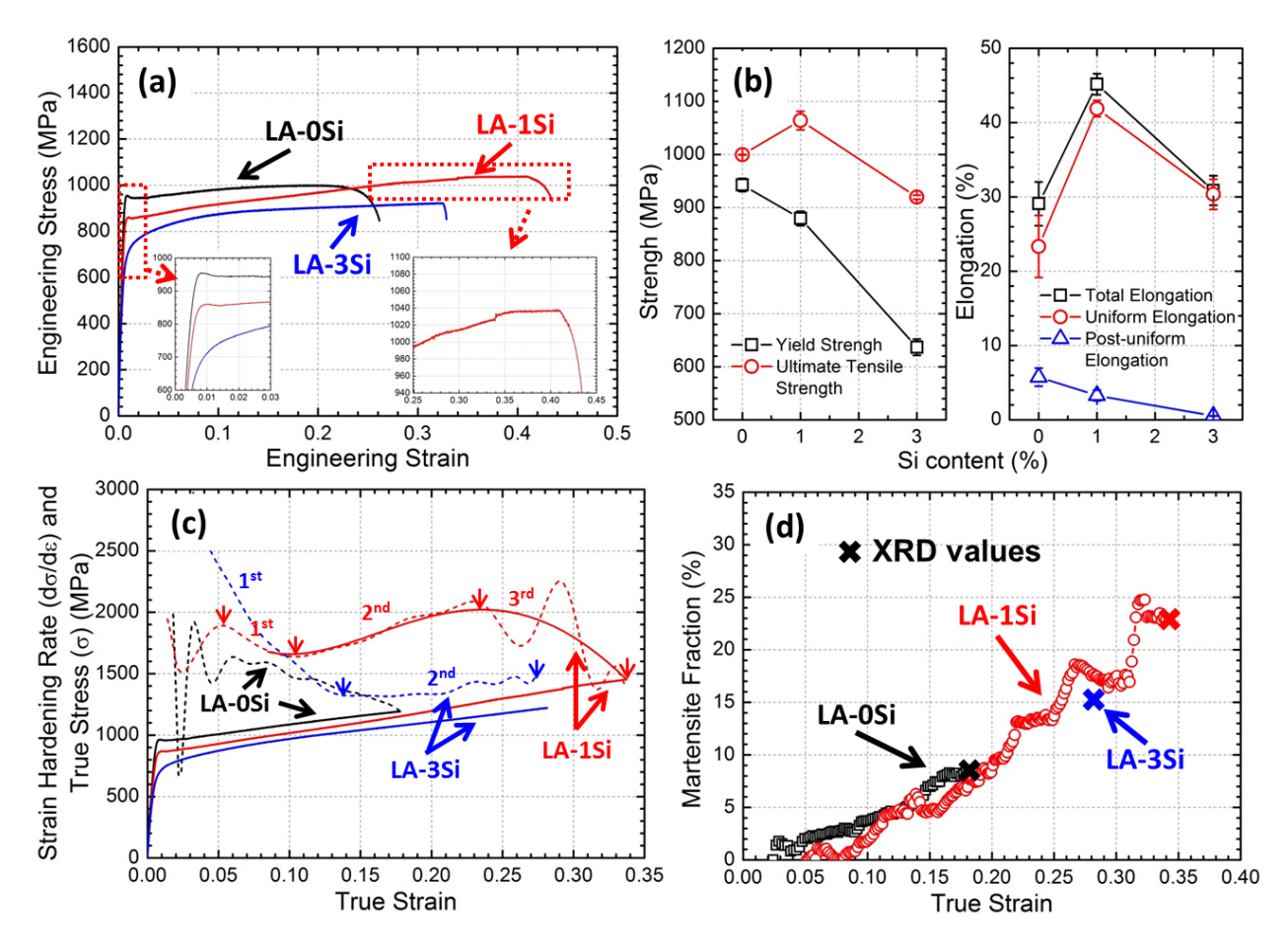


Fig. 5.4 Tensile property and SIT behavior for the LA-structure (LA-0Si, LA-1Si and LA-3Si): (a) Engineering stress-strain curve; (b) Strength (YS and UTS) and elongation (TE, UE and PUE) values; (c) Rate of strain hardening ($d\sigma/d\epsilon$) and true stress-strain curve; (d) Change of α' -martensite fraction during tensile straining.

Both the strength and ductility of the HA-structure, unlike the LA-structure, are not very sensitive to Si content. The HA-1Si sample possesses a slightly lower YS, higher UTS and lower elongations (TE, UE and PUE) compared with the HA-0Si sample (Fig. 5.5 (a)). Both samples exhibit a similar strain hardening behavior, characterized by a general increase to a maximum value followed by a decrease. However, it can be revealed in Fig. 5.5 (c) that Si enhances the strain hardening rate by a maximum value of around 2000 MPa. Regarding the SIT behavior, the amount of α' -martensite is similar for the two samples at high strains, but differs at the beginning of tensile deformation (Fig. 5.5 (d)); this is believed to be responsible for the different strain

hardening rates and will be discussed in Section 5.5.

Compared with the LA-structure, much more α' -martensite forms during tensile straining in the HA-structure, which is due to the initial higher fraction and lower stability of retained austenite (i.e. lower C and Mn concentrations). As such, a higher strain hardening rate and a higher tensile strength can be obtained for this type of structure. In addition, this type of microstructure shows a clear PLC effect (Fig. 5.5 (b)) and a discontinuous behavior of SIT (Fig. 5.5 (d)) in both samples. These two phenomena are closely correlated due to the localized strain-induced α' -martensite inside the PLC bands forming and propagating continuously during tensile straining, as will be described in Chapter 6.

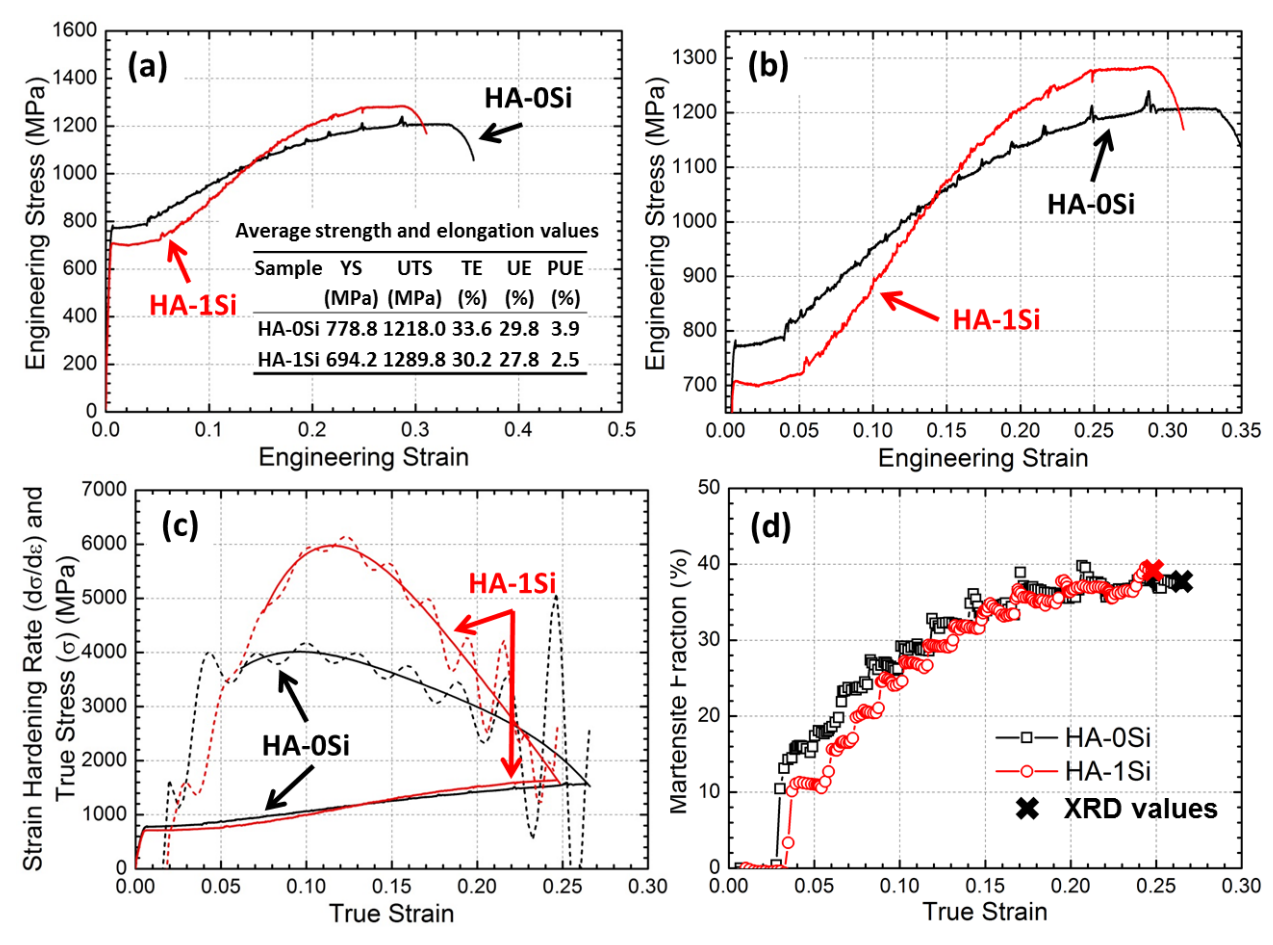


Fig. 5.5 Tensile property and SIT behavior for the HA-structure (HA-0Si and HA-1Si): (a) Engineering stress-strain curve and strength (YS and UTS) and elongation (TE, UE and PUE)

values; (b) serrations on the magnified engineering stress-strain curve; (c) Rate of strain hardening ($d\sigma/d\epsilon$) and true stress-strain curve; (d) Change of α' -martensite fraction during tensile straining.

5.4.3 Deformation micromechanisms and micromechanics

TEM observation was used to study the austenite deformation mechanisms in more detail. Interrupted tensile test specimens were investigated and the results for the LA-structured samples (deformed at a true strain of 0.15) are shown in Fig. 5.6. For all three specimens (LA-0Si/1Si/3Si), both strain-induced α' -martensite and deformation twins form in austenite during tensile straining, i.e. the steels underwent coupled TRIP-TWIP effect. In the LA-0Si and LA-1Si samples, deformation twins and α' -martensite tend to form in separate austenite grains (Figs. 5.6 (a₁-a₄) and (b₁-b₄)). In general, these twins nucleate on the α/γ interfaces (Fig. 5.6 (a₁)) and grow into the grains along one active twinning plane. Only a few twins are well developed and traverse the whole grain (Figs. 5.6 (a₂) and (b₂)). The twin lamellae spacing was measured based on TEM observations along the <011> beam direction. The average spacing between these well-developed twins is around 20 to 30 nm for the LA-0Si and LA-1Si sample.

However, the behaviors are very different in the LA-3Si sample. Compared with the lower Si samples, many more deformation twins are well developed in the 3Si sample (Fig. 5.6 (c₁)), with a smaller average twin spacing of less than 15 nm. This demonstrates a higher deformation twin density and fraction in the 3Si sample. Further, secondary twins form in some grains and intersect with the primary twins, and the interior angle between the primary and secondary twins were measured to be \sim 69°, which agrees well with previous reports of TWIP steels [5.16]. The twin platelet intersections also act as additional nucleation sites for α' -martensite, as shown in Fig. 5.6 (c₃). The underlying mechanism of α' -martensite nucleation on the twin intersections is well established in the literature [5.31].

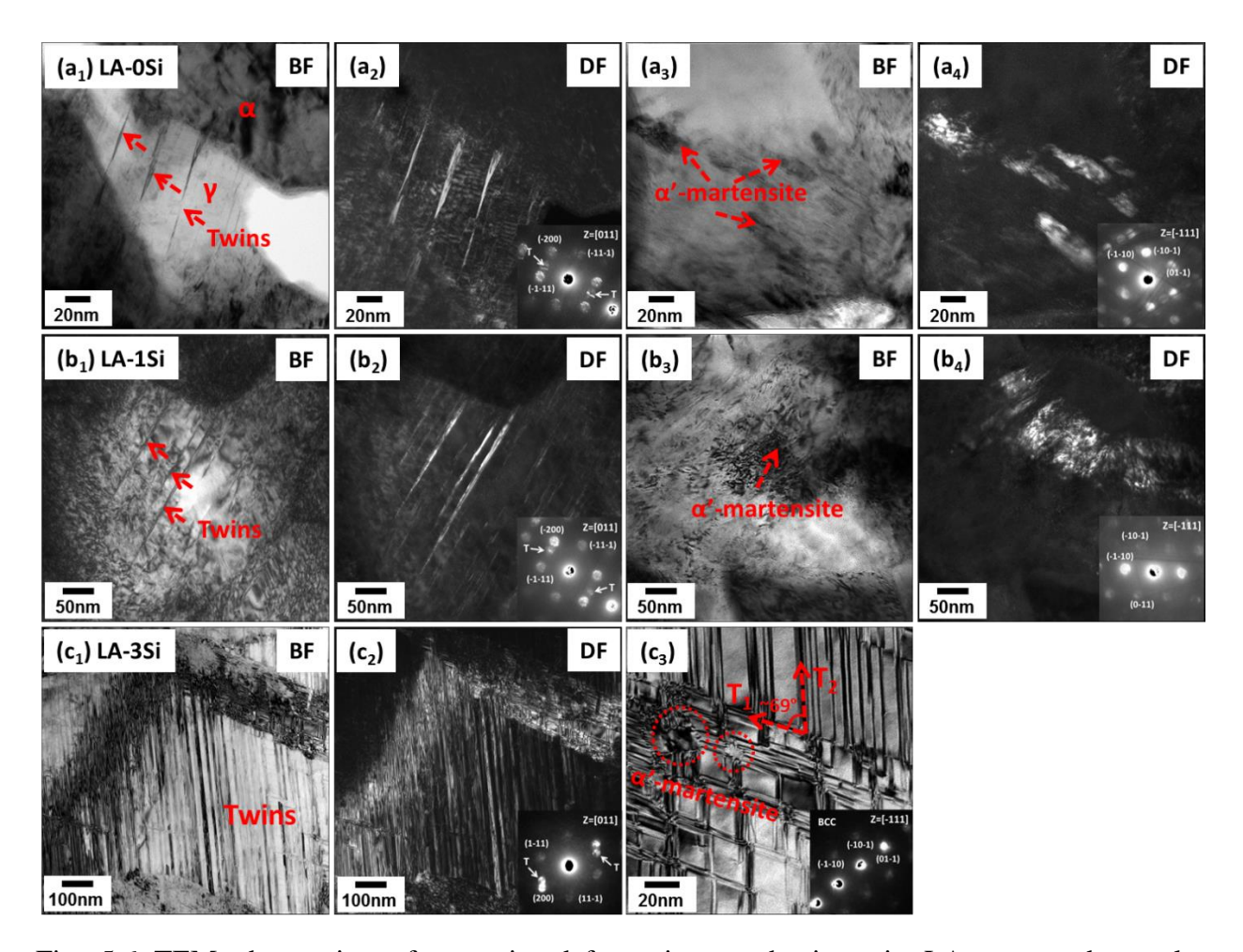


Fig. 5.6 TEM observation of austenite deformation mechanisms in LA-structured samples (macroscopic true strain 0.15): Bright field (BF) images, dark field (DF) images and nanobeam diffraction (NBD) patterns of (a_1-a_4) the LA-0Si and (b_1-b_4) the LA-1Si sample, showing formation of deformation twins and strain-induced α' -martensite in separate austenite grains; (c_1) BF image and (c_2) DF image and NBD pattern of the LA-3Si sample, showing a high density of deformation twins in one austenite grain; (c_3) BF image and NBD pattern for a austenite grain in the LA-3Si sample, showing the formation of secondary twins and α' -martensite on the intersections of deformation twins (marked by dot circles).

For the HA-structure, although the stability of austenite is lower and much more α' -martensite forms under deformation compared with the LA-structure (e.g. more than 25 wt.% martensite has already transformed in both samples at an overall true strain of 0.1), some deformation twins can

still be observed in TEM images (as shown in Fig. 5.7), but with a lower frequency. Similar to the low Si alloys of the LA-structure, no secondary twins can be found in both the HA-0Si and HA-1Si samples at the strain level of 0.1. For this type of structure, the twins and α' -martensite are possible to be independently formed in one austenite grain with different nucleation sites. This might be related to local orientation variations which result in different resolved shear stresses under tension load. This orientation dependence of the TRIP and TWIP mechanisms has been shown by Sohn et al. [5.32] who studied the tensile behaviors of a Fe-0.3C-8.5Mn-5.6Al lightweight steel.

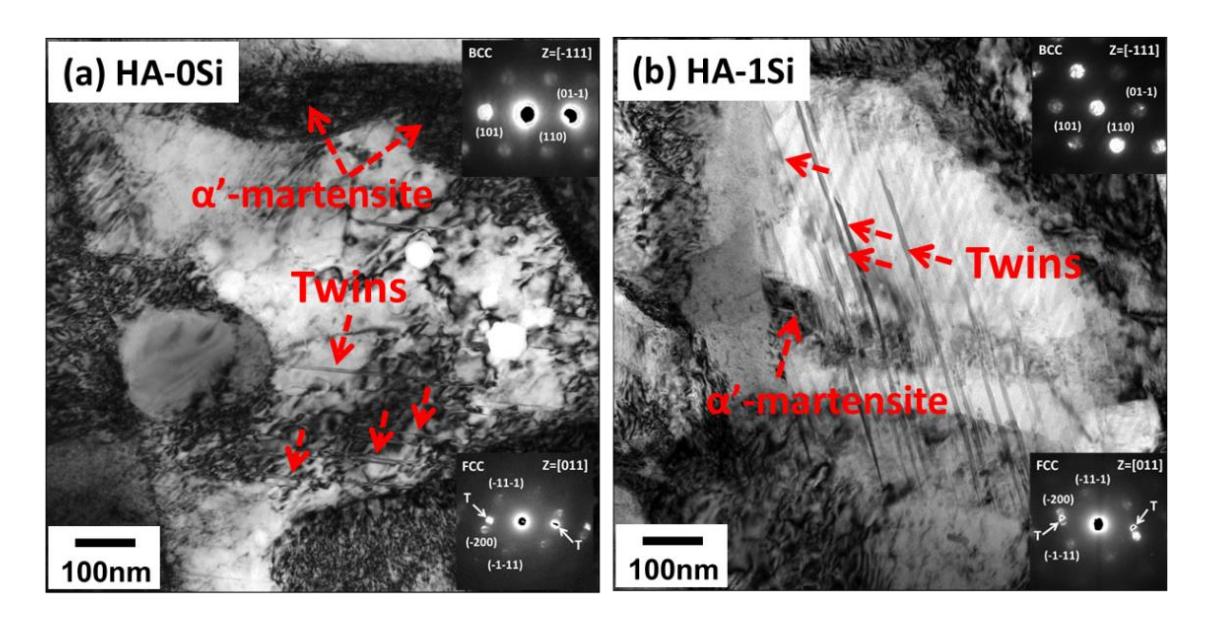


Fig. 5.7 TEM bright field images and NBD patterns of the deformed HA-structure (macroscopic true strain 0.1), showing deformation twins and strain-induced α' -martensite in the austenite of (a) the HA-0Si and (b) the HA-1Si sample.

Owing to the dual phase feature in the investigated steels and the differences in mechanical behavior between austenite and ferrite, the distribution of plastic strain during tensile testing will not be uniform. This heterogeneous strain distribution between the two constituting phases in the two types of microstructures was investigated by *ex situ* tensile tests in this work. Prior polished and etched specimens were subjected to tensile testing. SE imaging for the same locations of the

tensile specimens was performed every ~5 % strain. The microscopic strain (e) of each phase was calculated based on the length change of the selected grains along the tensile direction (Δl) divided by their initial length (l_0), i.e. $e = \Delta l / l_0$. In order to minimize the effect of some localized deformation due to the PLC effect, more than 8 different areas throughout the whole gage length of each sample were selected, which yielded a measurement of more than 30 grains for each phase. This is a unique advantage of this test compared with *in situ* measurements where normally only one area can be analyzed for each sample. Two notes need to be mentioned for this measurement. Firstly, due to the limited ability of SE imaging on differentiating strain-induced α' -martensite from the remaining austenite, the austenite phase here includes both phases. Secondly, in the LA-3Si sample, since the fraction of α is low, austenite is considered as the whole γ/α clusters, and strain partitioning between austenite and δ -ferrite was evaluated.

Strain distributions between austenite and ferrite for the LA-structure and HA-structure during tensile testing are shown in Figs. 5.8 (c)~(e) and Fig. 5.9, respectively. All the investigated samples except LA-3Si show different extent of strain partitioning, and most strain localizes in the austenite phase, for the following two reasons: (a) austenite in medium Mn systems could be softer than ferrite, as validated in some literature for similar steel systems [5.4, 5.11, 5.33, 5.34]; (b) the volume expansion of α' -martensite transformation (normally around 2~4% [5.35]) probably results in a net increase of local plastic strain in the γ - α' mixed phase; it might also make the adjacent ferrite subject to a state of compression, thus decreases the local strain of α [5.36, 5.37].

The case is different in the LA-3Si sample where no strain partitioning can be detected. The microstructure evolution of one local area in the LA-1Si sample and the LA-3Si sample during straining is shown in Figs. 5.8 (a) and (b). As shown in Fig. 5.2 (a₃) and Fig. 5.8 (b), δ -ferrite and austenite in the LA-3Si sample are largely continuous and elongated, and they are located alternatively with each other along the normal and transverse directions, forming a hierarchical

or fibrous structure. When this structure is subjected to tensile tests with the tensile axis parallel to the "fiber" direction, the two phases need to be equally strained to maintain the strain compatibility, even though the hardness of one phase (austenite, $327.1\pm11.4~\text{HV}^1$) is lower than the other (δ -ferrite, $367.0\pm6.5~\text{HV}^1$). Nonetheless, through comparing the 0Si and 1Si samples in Figs. 5.8 and 5.9, it can be observed that that the stain partitioning is enhanced by Si content for the ultrafine γ - α structure. This enhancement effect is much more pronounced for the LA-structured samples (Figs. 5.8 (c) and (d)). The heterogeneity of strain distribution achieves the highest in the LA-1Si sample, which could be the reason for its high strain hardening rate, as will be discussed in Section 5.5.

¹ The hardness of austenite and δ-ferrite in the LA-3Si sample was measured by a Vickers micro-hardness tester. More than 10 indents for each phase were performed and analyzed. The γ/α clusters was considered as the austenite phase here due to the small fraction of α .

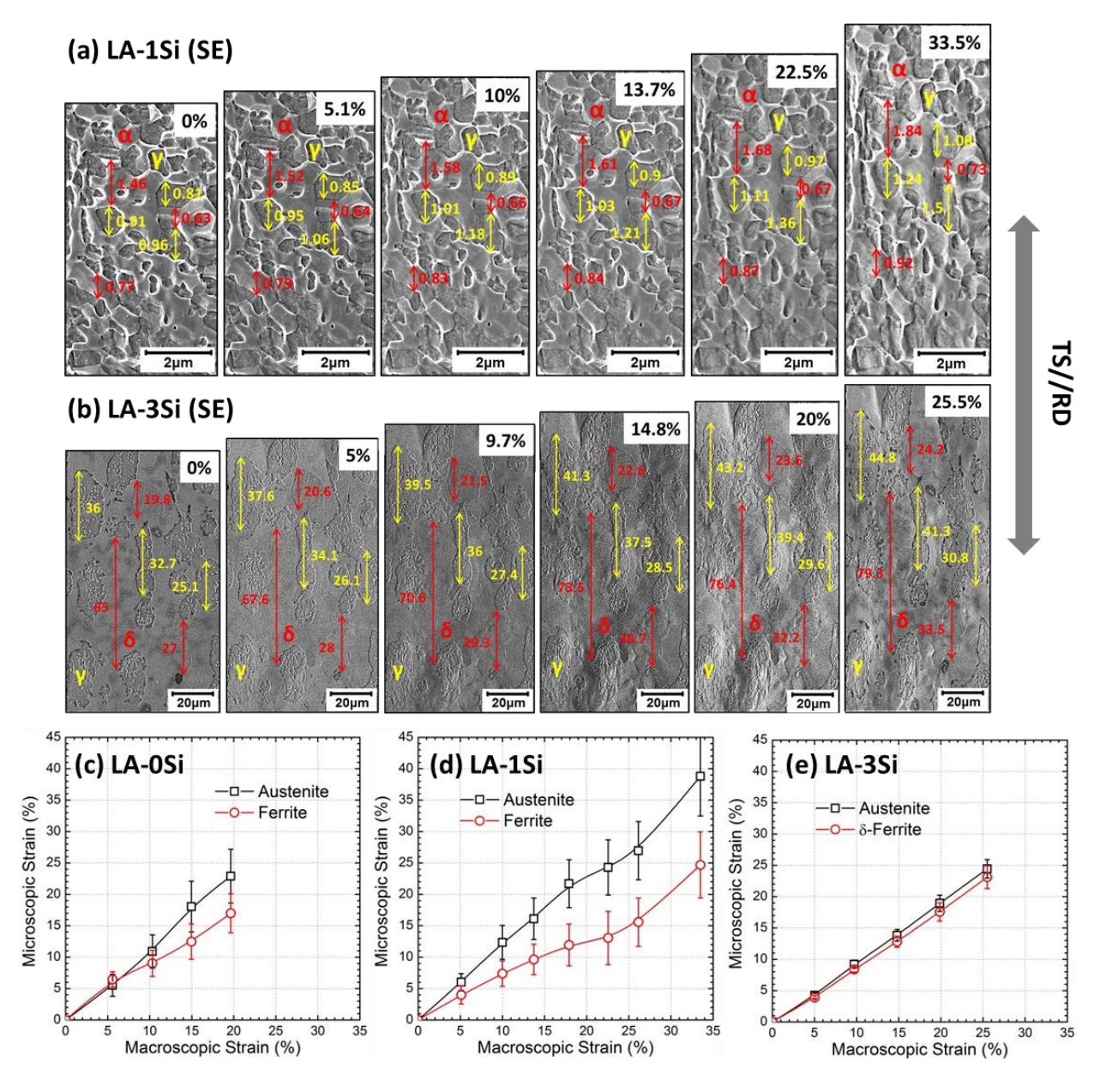


Fig. 5.8 Microstructure evolution of one local area in the (a) LA-1Si sample and (b) LA-3Si sample during tensile testing; Measured strain distribution between austenite and ferrite in the LA-structured samples during tensile testing: (c) LA-0Si; (d) LA-1Si; (e) LA-3Si.

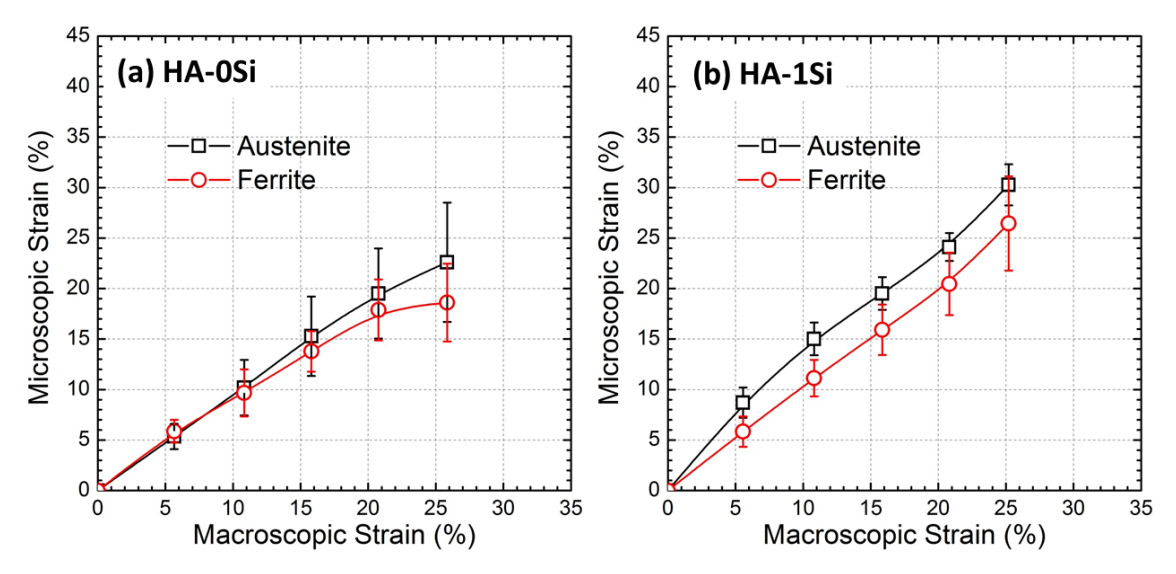


Fig. 5.9 Strain distribution between austenite and ferrite in the HA-structured samples during tensile testing: (a) HA-0Si; (b) HA-1Si.

5.4.4 Damage and fracture mechanisms

As mentioned in Section 5.4.2, the PUE values of both kinds of microstructure decrease with increasing Si content. For the LA-structure, there is a significant PUE decrease from ~6% to almost 0% when the Si amount increases from 0 to 3 wt.%. The damage and fracture mechanisms for the LA-structured samples are mainly focused here. SEM fractographs of the LA-structured samples are shown in Fig. 5.10. The area of the fracture surface, as marked by solid lines in Figs. 5.10 (a~c), clearly increases with increasing Si content, meaning a gradually decreased reduction of area. The local strain at the fracture region (ε_{loc}) was calculated using both the initial cross-sectional area (A_0) of gauge portion and the measured cross-sectional area of the fractured region (A_f):

$$\varepsilon_{\rm loc} = \ln \left(A_0 / A_{\rm f} \right) \tag{5.1}$$

The local strain value decreases from 0.91 for the LA-0Si sample, to 0.82 for the LA-1S sample, and further down to 0.46 for the LA-3Si sample; this decreased local strain with Si content corresponds well with the trend of the PUE values. Both exhibit that Si decreases the degree of necking. The lower Si steels (LA-0Si/1Si) are ductile, as documented by well-defined dimples shown in Figs. 5.10 (a₁) and (b₁). The dimple size of the LA-1Si sample is smaller than that of

the LA-0Si sample, despite the slightly larger grain size. The fracture mode of the LA-3Si sample is more complicated; it contains both ductile areas with mostly dimples and brittle areas with mainly cleavage or quasi-cleavage behavior. In the ductile areas (Fig. 5.10 (c₁)), there are some islands showing a complete cleavage behavior featured by the flat facet. These islands are characterized as δ -ferrite by their lower Mn contents. For the brittle areas (marked by dashed lines in Fig. 5.10 (c)), the δ -ferrite generally remains cleavage-type fracture, whereas some regions which are identified as γ - α ' mixed phase by the higher Mn contents exhibit either dimple behavior (Fig. 5.10 (c₂)) or quasi-cleavage fracture (Fig. 5.10 (c₃)). Some cracking along the interfaces between coarse δ -ferrite and fine γ - α ' mixed phase can also be observed in these brittle areas, as shown in Fig. 5.10 (c₂). The results suggest a quite different failure process between the lower and higher Si alloys, namely, the lower Si (LA-0Si/1Si) samples undergo a failure process of void nucleation, growth and coalescence, whereas the fracture of the higher Si alloy (LA-3Si) is associated with both cracking in δ -ferrite or along the interfaces and voids formation in the γ - α ' region.

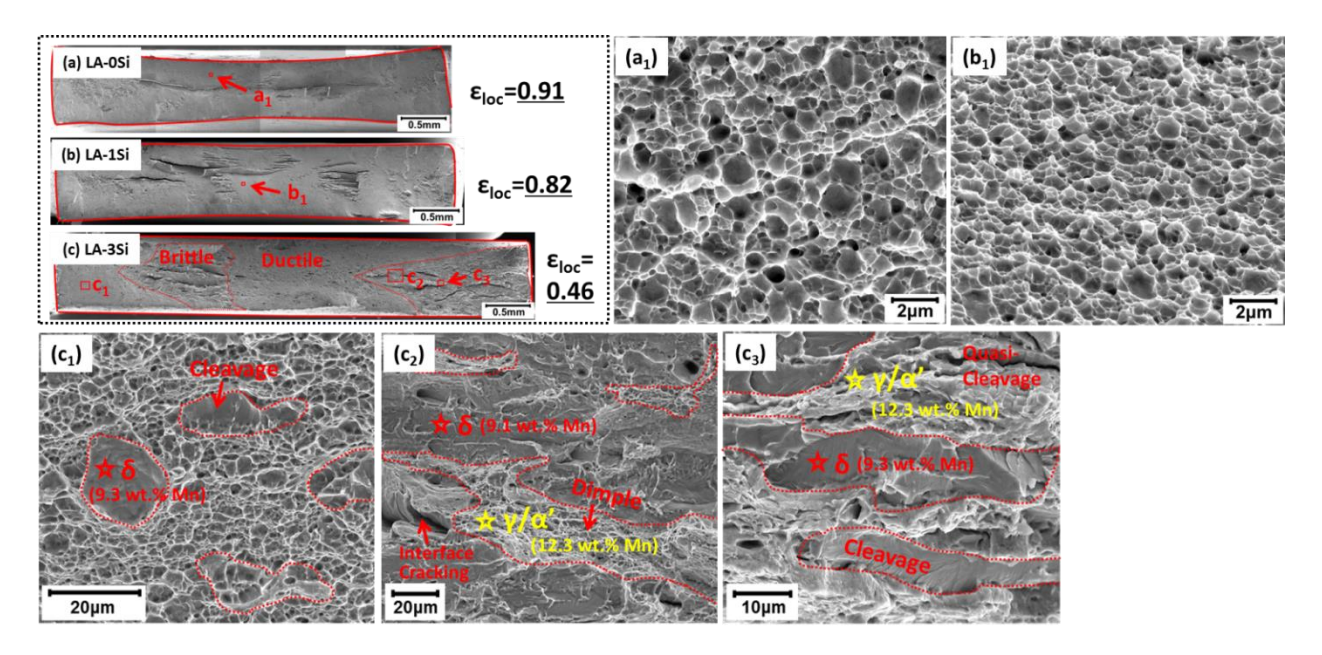


Fig. 5.10 SEM fractograph of the LA-structured samples: (a) LA-0Si; (b) LA-1Si; (c) LA-3Si (the edge of the fracture surface is marked by solid lines; local strain at the fracture surface of

each sample is also added); (a_1) , (b_1) and (c_{1-3}) are the magnified areas marked by the rectangular frames in (a), (b) and (c). (The dashed lines in these images serve to identify the areas of specific fracture features)

In order to investigate the fracture behavior of the three samples in more detail, the damage (voids or cracks) near the fracture surface of the cross-sectioned tensile samples was examined, and the results are shown in Fig. 5.11. Since the scope here is to investigate the effect of Si on damage and fracture mechanisms, the role of inclusions on the failure process is neglected. For the lower Si samples (LA-0Si/1Si), due to the large local strain in the necking areas, austenite near the fracture surfaces could completely transform to α'-martensite. Three void nucleation sites were identified in the two samples: at α/α' interface (Fig. 5.11 (a₁)), inside α' (Fig. 5.11 (a₂)) and inside α (Fig. 5.11 (a₃)). These voids generally remain nano-scaled (the diameter is lower than 100 nm), even at these high local strain regions. The ferrite/martensite interface decohesion and martensite cracking were facilitated by the local stress concentration and low toughness of fresh martensite, respectively. These two nucleation sites have been widely documented in dual-phase (DP) steels. However, reports on DP steels showed that the damage could initiate primarily at ferrite/martensite interface [5.38] or inside martensite [5.39], or in both locations for equal proportions [5.40], depending on the phase fractions [5.41] and grain sizes [5.39]. In addition to these two sites, Kadkhodapour et al. [5.42] observed void nucleation at ferrite grain boundaries in the neighborhood of martensite grains during the failure process of a commercial DP800 steel.

In order to identify the preferred void nucleation sites for the LA-0Si and LA-1Si sample, a statistical analysis was established by studying a large number of nanovoids (more than 300) near the fracture surface through the whole thickness. The density of nanovoids (defined by the nanovoid number divided by the detected area) for the two samples is shown in Fig. 5.11 (b). The results exhibit a much higher nanovoid density at the α/α' interface for both samples, which

reveals the voids are mainly initiated by ferrite/martensite interface decohesion. It can also be observed that for all the three nucleation sites, the nanovoid density of the LA-0Si sample is higher compared with the LA-1Si sample. Since the density of voids normally increases with local plastic strain [5.40, 5.43], the higher void density in the LA-0Si sample could be due to the higher local strain at the necking area (Fig. 5.10).

For the LA-3Si sample, it is similar to the lower Si samples that voids mostly nucleate at various interfaces (α/α' and δ/α') (Figs. 5.11 (c_1) and (c_3)); they are also nano-sized (around 200 nm) but slightly larger compared with those in lower Si samples. In addition, some larger cracks are observed at two locations: (a) at the interface of δ -ferrite and γ/α' mixed phase along the tensile direction (Fig. 5.11 (c_2)); (b) inside the δ -ferrite phase and orient perpendicular or ~45 ° with respect to the tensile axis; these cracks either stop at the interface (Fig. 5.11 (c_3)) or penetrate into the surrounding γ/α' (Fig. 5.11 (c_4)). The cracks at the first location are generally of larger width.

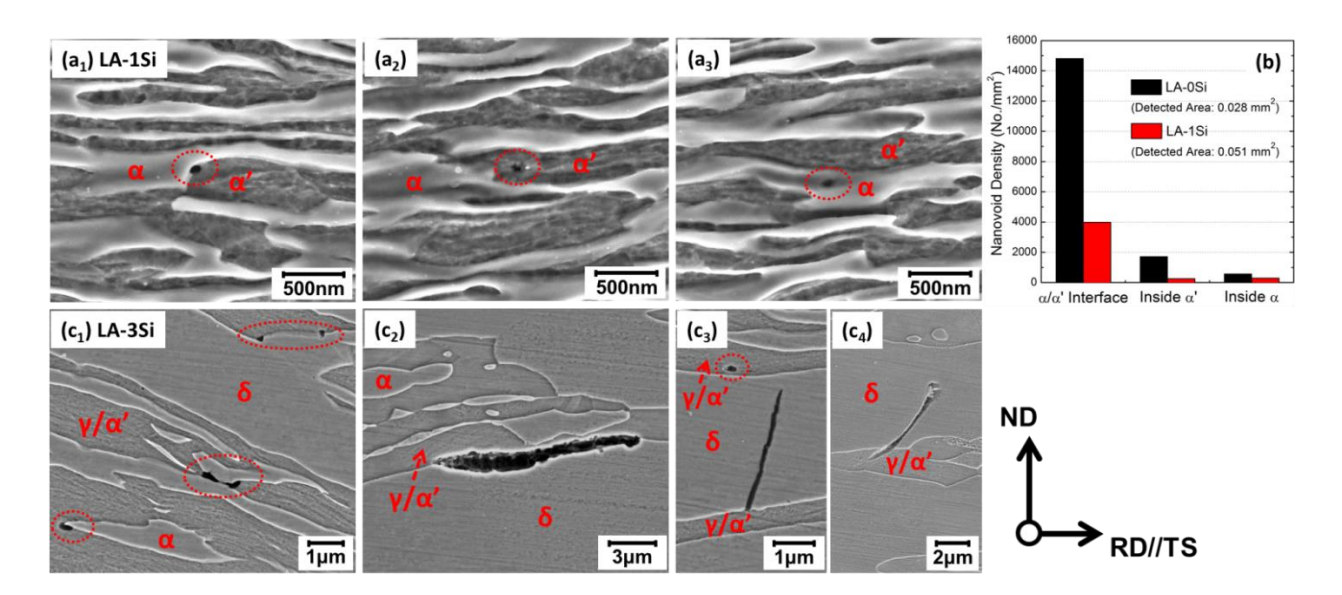


Fig. 5.11 SEM observation of the tensile fractured samples (near the fracture surface), showing damages (voids and cracks) in the (a_1-a_3) LA-1Si and (c_1-c_3) LA-3Si specimen (the nanovoids are marked by elliptical frames); (b) the density of nanovoids on different nucleation sites of the

LA-0Si and LA-1Si samples.

In order to investigate the dominant failure process of the LA-3Si sample, interrupted *ex situ* tensile tests were carried out, and the evolution of damage during tensile deformation is shown in Fig. 5.12. It is observed that the voids at various locations formed at 0.2 strain, as marked by the elliptical frames in Fig. 5.12 (a). However, they only dilate a little with further straining, but do not show growth or propagation until fracture. This suggests that the fracture of the LA-3Si sample is mainly due to the cracking inside δ -ferrite or along the interfaces of δ -ferrite and γ/α' mixed phase.

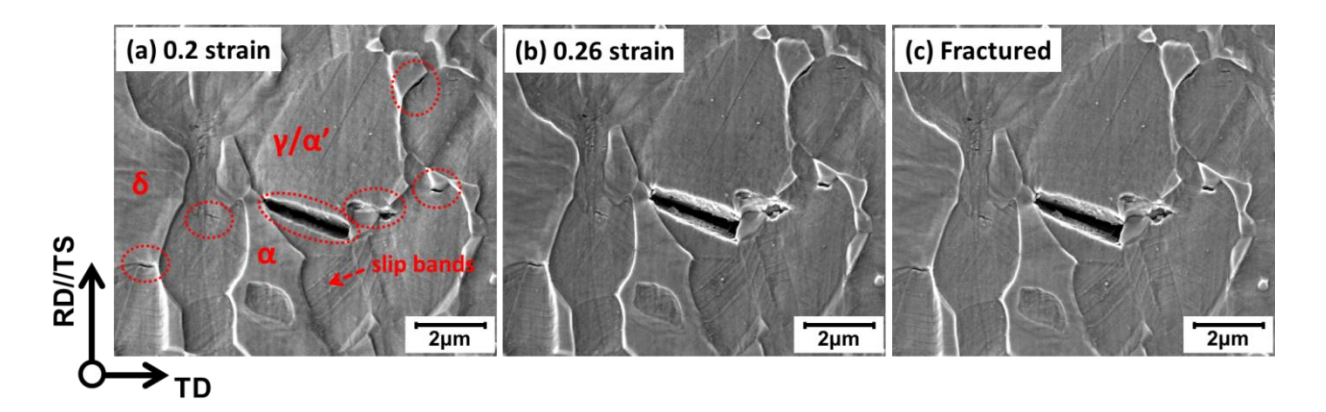


Fig. 5.12 Evolution of damages in the LA-3Si sample during tensile deformation: (a) 0.2 strain, (b) 0.26 strain, and (c) fractured sample.

5.5 Discussion

5.5.1 Effect of Si on deformation micromechanisms and micromechanics

The results in Section 5.4 have shown that the main differences of deformation details in different Si-alloyed samples are: (a) deformation twinning (i.e. TWIP effect) and (b) strain partitioning between austenite and ferrite. The fraction and density of deformation twins significantly increase in the 3Si sample with also the activation of secondary twins. For both types of structures, the strain partitioning is higher in the 1Si sample compared with that in the 0Si sample. However, the effect of Si on strain partitioning is much more pronounced for the LA-structure. The 3Si sample does not show any strain partitioning due to its fibrous morphology, despite the hardness difference between austenite and δ -ferrite.

It is generally accepted that deformation twinning in austenite is closely related to the SFE. Lower SFE (generally reported to be around $18\sim45$ mJ/m² in austenitic TWIP steels [5.10, 5.44-5.47]) favors deformation twinning, due to the energetically favorable dissociation of perfect dislocations and the lower critical twinning stresses [5.44, 5.48]. Allen et al. [5.49] also defined a linear relationship between SFE and twin thickness which is related to the twin distance and fraction. In order to explain the deformation twinning behavior of different Si alloyed steels, the austenite SFE ($\gamma_{\rm SFE}$) was calculated based on a thermodynamic model originally proposed by Olson and Cohen [5.50]. It assumes two atomic planes of hexagonal (hcp) stacking (intrinsic stacking fault) separated from the austenite matrix by two interfaces, as such austenite SFE ($\gamma_{\rm SFE}$) can be expressed by:

$$\gamma_{\rm SFE} = 2\rho(\Delta G^{\gamma \to \varepsilon} + \Delta G_{str}) + 2\sigma_{\gamma/\varepsilon}$$
 (5.2)

where $\Delta G^{\gamma \to \epsilon}$ is the molar Gibbs energy of austenite to ϵ -martensite phase transformation, ΔG_{str} is the strain energy associated with the strain field caused by the different volumes of the γ and ϵ phase, ρ is the molar density along {111} planes, $\sigma_{\gamma/\epsilon}$ is the interfacial energy. Detailed calculation of γ_{SFE} is described in Appendix A.

The calculated austenite SFE of the three steels for the LA-structure is plotted in Fig. 5.13 (a), along with some experimental SFE data from literature [5.16, 5.51, 5.52]. Both the calculated and experimental results reveal a decrease effect of Si on SFE (-3.5~-2 mJ/m² per 1 wt.% Si); this corresponds well with the work by Das [5.53] who investigated the effect of elements on SFE using a Bayesian neural network model based on an extensive literature data. Therefore, it is likely that the higher fraction or density of deformation twins and the activation of secondary twins in the LA-3Si sample are partly due to its lower SFE. This can be supported by the work of Jeong et al. [5.16] who studied 0.6C-18Mn-xSi steels with similar grain sizes and phenomenologically proposed that the total twin volume fraction proportionally decreased by around 0.13% per SFE of 1 mJ/m², and secondary twin fraction also significantly increased with lower SFE (i.e. higher Si content).

However, the effect of austenite grain size on the formation of deformation twins cannot be neglected. It has been shown from the work of Gutierrez-Urrutia and Raabe [5.54] in a Fe-22Mn-0.6C TWIP steel with a SFE of 22 mJ/m², that grain refinement can strongly reduce the twin area fraction although this does not completely suppress the twins. They also developed a Hall-Petch type relation between the twinning stress (τ_{tw}) and grain size (d); the relation can be described as follows:

$$\tau_{tw} = \tau_0 + \frac{\kappa_{tw}}{\sqrt{d}} \tag{5.3}$$

where K_{tw} is the Hall–Petch constant for twinning; τ_0 is the twinning stress for a single crystal, which can be considered as the critical resolved shear stress to separate a leading Shockley partial from the trailing partial and create a twin [5.48, 5.49, 5.54]. Thus τ_0 can be expressed by:

$$\tau_0 = \gamma_{SFE}/b \tag{5.4}$$

where b is the Burgers vector, can be taken as 0.25 nm [5.4, 5.54]. The Taylor factor (M = 3.06 [5.4]) can be used to transfer the shear stress to normal stress, therefore:

$$\sigma_{tw} = M\tau_{tw} = \frac{M\gamma_{SFE}}{b} + \frac{MK_{tw}}{\sqrt{d}}$$
 (5.5)

Rahman et al. [5.48] experimentally studied the effect of grain size on the twinning stress in a

Fe-15Mn-0.7C-2Al-2Si TWIP steel; the composition is very similar to the austenite composition of the LA-structured sample in the current study. A value of 232.2 μ m^{1/2} for $M \times K_{tw}$ can be determined from their study. Using equation (5.5), the contribution of the austenite SFE and grain size to the twinning stress can be analyzed; the results for the LA-structured samples are given in Fig. 5.13 (b). The twinning stresses for all the samples are smaller than their yield strength, which can explain the deformation twins observed in the three samples. It also shows that the twinning stress is decreased by both the lower SFE and larger grain size of the higher Si-alloyed samples, which indicates that the more active twinning formation in the LA-3Si sample should be attributed to both factors. However, to the best of the authors' knowledge, the detailed deformation twinning behavior in ultrafine grained steels with grain size lower than 500 nm, has not been reported. Therefore, it is worth to mention that this Hall-Petch type relation between τ_{tw} and d has not yet been validated for this fine grain level.

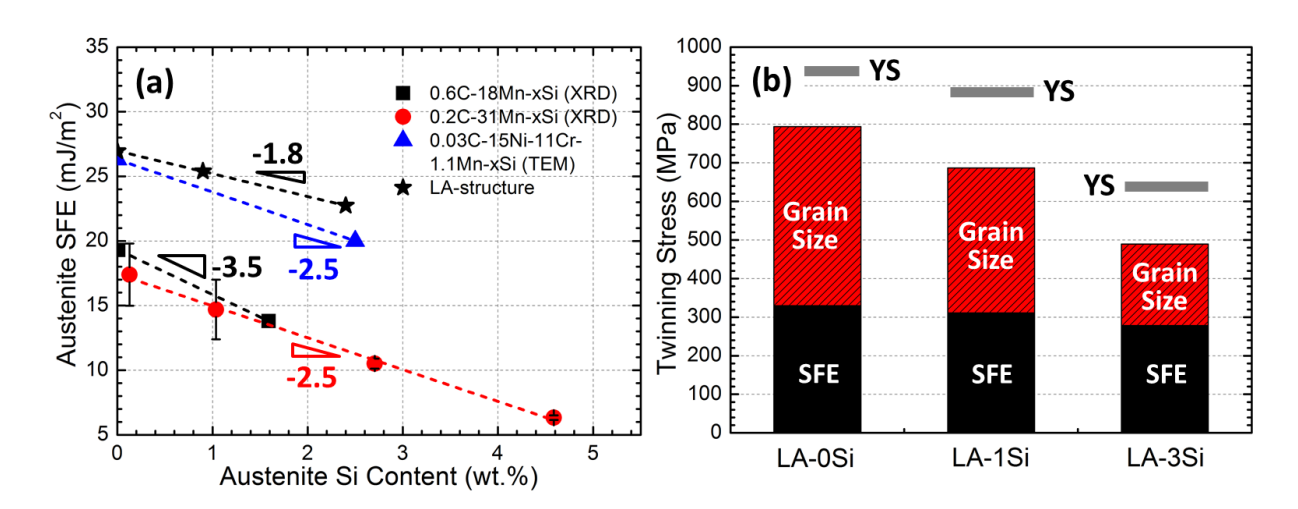


Fig. 5.13 (a) Calculated and experimental (0.6C-18Mn-xSi [5.16], 0.2C-31Mn-xSi [5.52], 0.03C-15Ni-11Cr-1.1Mn-xSi [5.51]) data showing the effect of Si on austenite SFE; (b) Contribution of the austenite SFE and grain size to the twinning stress for the LA-structure.

Another noticeable effect of Si is that it changes the strain distribution between austenite and ferrite for the 0Si and 1Si steels with the ultra-fine γ - α structure, and this effect is more obvious

for the LA-structure. Although Si is an effective solid solution strengthening element for both ferrite and austenite, the relative strengthening effect of Si on these two phases might be different. The solution strengthening hardening effect of Si in ferritic steels is already well established with reports of an increase in frictional stress (σ_0) as high as 117.2 MPa per 1 wt.% Si [5.14]. This value might even be enhanced when the steel is highly alloyed with Al, due to the formation of some ordered phase [5.12]; for example, Heo et al. [5.12] observed a significant ferrite hardness increase from 272 to 413 HV, with the Si level increased from 1 to 1.8 wt.% in a steel system of Fe-0.2C-8Mn-5Al. On the other hand, it seems that the solid solution strengthening effect of Si on austenite is relatively smaller. We determined a yield strength increase of around 54~65 MPa per 1 wt.% Si for our Fe-0.98C-17.6Mn-(0~2)Si TWIP steels; this is remarkably close to the value reported in the work of Jeong et al. [5.16] (65 MPa per 1 wt.% Si for Fe-18Mn-0.6C-xSi TWIP steels). The different strengthening effect of Si on the two phases and the extra Si enrichment in ferrite (Fig. 5.3) can enlarge hardness/strength difference between ferrite and austenite, therefore enhancing the strain partitioning.

However, regarding the HA-structure, the Si influence on strain partitioning is weaker (Fig. 5.9). This is believed to be due to the rapid martensite formation especially at the early stage of deformation (Fig. 5.5 (d)), i.e. 10~15% martensite has already transformed after yielding (Lüders banding). Once a large fraction of martensite is transformed, it will tend to be less strained due to the much higher hardness, thus more strain will start to concentrate on the surrounding ferrite. Therefore, both samples for the HA-structure show a small strain partitioning, regardless of the Si level. Note that the initial dislocation density can be different in austenite and ferrite resulting from the different recrystallization kinetics at annealing temperatures [5.27], which might also affect strain partitioning. However, this difference was not observed based on the kernel average misorientation (KAM) value from EBSD data.

5.5.2 Deformation behavior and strain hardening

Since the microstructures of the low Si alloys (0Si and 1Si) are different compared with the 3Si alloy, despite similar austenite fractions can be obtained. The presence of coarse grained δ -ferrite in the 3Si alloy changes the morphology and thus alters the strain partitioning behavior. Therefore, in this section, we will first focus on discussing the strain hardening behavior of the 0Si and 1Si samples, starting from the LA structure and then to the HA structure. The deformation and strain hardening behavior for the LA-3Si sample will be discussed in the later part independently.

(A) LA-0Si and LA-1Si samples

As demonstrated from Fig. 5.4 (c) and Section 5.4.2, the LA-1Si sample possesses a higher strain hardening rate than the LA-0Si sample in the whole strain range, and a distinct three-stage strain hardening behavior. Strain-induced α'-martensite formation (TRIP effect) and deformation twinning (TWIP effect) in austenite are well established as effective strain-hardening contributors [5.1-5.3, 5.32]. The amount of strain-induced α'-martensite for the LA-structure is low at small strains (Fig. 5.4 (d)), and the *in situ* magnetic induction measurement does not detect a large difference of overall SIT kinetics between the LA-0Si and LA-1Si samples at true strains below 0.2 (where the LA-0Si sample necks). The deformation twinning behavior for these two samples is also similar; both show a small fraction of well-developed deformation twins with no secondary twins activated. Thus, the TRIP and TWIP effects in austenite are not deemed to be the reason for the different strain hardening behaviors between LA-0Si and LA-1Si.

It was reported in Chapter 4 and other literature [5.4, 5.20] that the strain partitioning between austenite and ferrite in medium Mn steels can have a critical effect on the mechanical behavior, e.g. cold rollability or ductility, yielding [5.20] and strain-hardening behavior [5.4]. Here we relate the unexpected high strain hardening rate in the LA-1Si sample to its more heterogeneous strain distribution, in terms of two factors. Firstly, strain partitioning reflects a certain level of

strain incompatibility of the two phases during plastic deformation, which essentially increases the numbers of geometrically necessary dislocations (GNDs) along the austenite-ferrite interfaces. This additional source of dislocations enhances dislocation multiplication thus increases the strain hardening. Some local dislocation pile-ups could also be produced by the plastic incompatibility, giving rise to the long-range elastic back stresses, i.e. kinematic hardening [5.55, 5.56]. These points were widely used to interpret the initial high strain hardening rate in DP steels where a high strain partitioning exists between the soft ferrite and hard martensite [5.39, 5.55, 5.56]. Considering the ultrafine grain size in the investigated samples, this positive effect of strain partitioning on strain hardening can be significant, due to the large number of GNDs resulted from the high phase boundary fractions [5.39].

Secondly, it is known that austenite possesses a higher strain hardening ability than ferrite [5.57] regardless of the activated deformation mechanisms (planar glide of dislocations, strain-induced martensite or deformation twinning) associated with the low SFE in the face-centered cubic (fcc) lattice. Therefore, strain localization in austenite would increase the overall strain hardening rate [5.57].

The different strain hardening behaviors between LA-0Si and LA-1Si can be explained based on these two factors. The 1st stage strain hardening of the LA-1Si sample is characterized by a continuous decrease. This is similar to the strain hardening behavior of the LA-0Si sample, which corresponds to the classical stage III strain hardening regime of polycrystals and is attributed to the dynamic recovery of dislocations [5.47, 5.58, 5.59]. The LA-1Si sample has a higher strain hardening rate at this stage than the LA-0Si sample, which can be explained by the higher amount of GNDs associated with strain partitioning. This is reasonable because both TRIP and TWIP effects are mild at this stage and similar for the two samples; the SFE difference is also small between the 0Si and 1Si steel which will not create a large difference on the cross-slip of dislocations [5.47].

The 2nd strain hardening stage in the LA-1Si sample features an increase up to about 2000 MPa, which is much higher than the LA-0Si sample (Fig. 5.4 (c)). The formation of GNDs due to strain partitioning fails to explain this 2nd stage increase, because its increasing effect on strain hardening is normally most pronounced at the initial plastic deformation stages, and decays with higher strain, as widely observed in DP steels [5.39, 5.56]. As such, it is believed that the second factor, i.e. strain localization in the austenite, plays a dominant role at the 2nd stage. Specifically, the TRIP and TWIP effects and the associated dislocation multiplication in austenite can be enhanced by the strain concentration.

The strain partitioning-enhanced TRIP effect can be verified by analyzing the SIT kinetics, which generally refers to the normalized austenite transformed fraction (F_{α}/F_{γ} , where $F_{\alpha'}$ and F_{γ} are the fraction of α' -martensite and initial austenite, respectively) as a function of macroscopic true strain [5.60, 5.61]. The SIT kinetics of the LA-1Si sample is shown in Fig. 5.14 (a), along with a reference sample, HA-1Si, which shows a very small strain partitioning. Reports have shown that the overall SIT kinetics generally presents a sigmoidal shape [5.2, 5.60, 5.61], which is characterized by a first slow increase of α' -martensite, followed by a rapid increase with higher strain and a saturation below 100%. The relation between $F_{\alpha'}/F_{\gamma}$ and overall true strain (ε) can be depicted by the well-known Olson-Cohen (OC) model [5.61]:

$$F_{\alpha}/F_{\gamma} = 1 - exp\{-\beta[1 - exp(-\alpha\varepsilon)]^n\}$$
(5.6)

where α , β and n are constants. This relation is true for austenitic stainless steels [5.61] or some multiphase steels [5.60] where the strain distribution among different phase constituents is roughly homogeneous; however, the behavior will be altered when large strain partitioning exists. As exhibited in Fig. 5.14 (a), the more homogeneously strain distributed sample, HA-1Si, follows the OC model, despite the discontinuous SIT behavior due to the PLC effect; the curve fitting yields the values of 13.0, 2.1 and 2.8, for α , β and n, respectively. However, the SIT behavior in the LA-1Si sample cannot be described by the sigmoidal shape and the OC model; the high strain localization in austenite results in an increasing SIT kinetics with macroscopic true strain, and

martensite formation is clearly not saturated even after ~80% austenite has transformed. This means that the contribution of the TRIP effect to the strain hardening of the LA-1Si sample continuously increases with higher global plastic strain, which gives rise to the 2nd stage increase of the strain hardening rate. Similarly, the TWIP effect and the dislocation multiplication in the austenite are also possibly enhanced by the strain partitioning, thus would have the same influence on strain hardening.

With further straining of the LA-1Si sample, a 3rd stage strain hardening, characterized by a general decrease, prevails after a true strain of around 0.23 until the occurrence of necking. Although the overall rate of SIT still keeps increasing, the behavior changes to a discontinuous behavior due to the occurrence of the PLC effect at this stage (Fig. 5.4 (a)), meaning martensite formation starts to localize in the PLC band. This might reduce the contribution of the TRIP effect on the overall strain hardening. On the other hand, the reduced capability of the substructure (martensite and/or twins) in the austenite to trap more dislocations might also limit the strain hardening capacity at high strains [5.59].

(B) HA-0Si and HA-1Si samples

Unlike the LA-structure, the two samples of the HA-structure do not show much difference in the strain partitioning behavior. However, the difference of the strain hardening rate between the two samples can be as high as 2000 MPa at around 0.1~0.15 true strain (Fig. 5.5 (c)). This can be explained by the different strain-induced martensite fraction at the beginning of deformation. As shown in Fig. 5.5 (d), the first burst of martensite is due to the localized martensite transformation in the Lüders band (as will be validated in Chapter 6), and the amount of this localized martensite is different between the two steels. When this amount of martensite is subtracted and only the martensite fraction after the Lüders strain is plotted as a function of true strain (as shown in Fig. 5.14 (b)), a large difference can be observed, namely, the rate and amount of martensite formation after yielding is much larger in the HA-1Si sample compared

with that in the HA-0Si sample. The rate of transformation can be defined as the derivative of an OC fit to the martensite fraction vs. true strain; it was also plotted in Fig. 5.14 (b). The rates of martensite formation for the two samples peak at around 0.8 strain, close to the peak strain of the strain hardening curve (~0.9 for the HA-0Si sample and ~0.11 for the HA-1Si sample, as shown in Fig. 5.5 (c)). This strongly suggests that the different SIT kinetics after yielding is the main reason for the different strain hardening rate between the HA-0Si and HA-1Si sample.

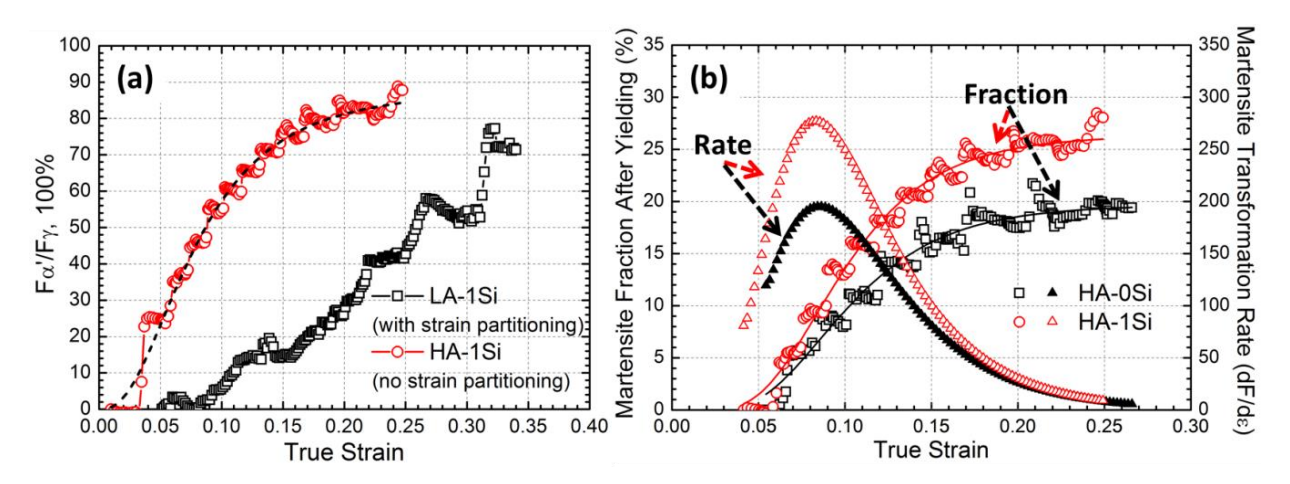


Fig. 5.14 (a) SIT kinetics of the LA-1Si sample with high strain partitioning and HA-1Si sample with very mild strain partitioning; (b) Strain-induced martensite fraction after yielding and martensite transformation rate $(dF_{\alpha}/d\epsilon)$ of the HA-structured samples. (the dash line in Fig. 5.14 (a) and the solid lines in Fig. 5.14 (b) are the fitting curves based on the OC model)

(C) 3Si steel

The LA-3Si sample exhibits a two-stage strain hardening (Fig. 5.4 (c)), similar to the first two stages in the LA-1Si sample. The 1^{st} stage strain hardening rate in the LA-3Si sample is remarkably higher than the other two LA-structured samples, which might be due to the different dislocation motion related to the continuous yielding, coarse grained δ -ferrite and more completely recrystallized structure; the explanation for this is deemed to be very completed and requires future studies. Nevertheless, the 2^{nd} stage strain hardening characterized by a slight increase in the LA-3Si sample is the reason for the higher uniform elongation compared with

LA-0Si. Since no strain partitioning can be detected in this sample, the 2nd stage strain hardening can only be interpreted by its more active TWIP effect. It has been well documented both experimentally [5.16, 5.59, 5.62] and numerically [5.63] that the strain hardening rate can be enhanced by smaller twin spacing (i.e. higher twin density or fraction), due to the so-called "dynamical Hall-Petch effect" and the Bauschinger effect (i.e. kinematic hardening) initially proposed by Bouaziz et al. [5.63]. This is evident by the fact that the strain hardening behavior of the LA-0Si sample, which possesses a low density of well-developed twins and also a low strain partitioning, only shows a one-stage monotonic decrease of strain hardening. In fact, the strain hardening feature of the LA-3Si sample is quite similar to that reported in some TWIP steels (e.g. Fe-18Mn-0.6C-1.5Al [5.64] and Fe-18Mn-0.6C-1.5Si [5.16]). However, it should be noted that value of the strain hardening rate at this stage for the LA-3Si sample is smaller than the value at the same strain hardening stage in the LA-1Si sample, indicating the strain hardening behavior of the investigated alloys is more pronouncedly affected by strain partitioning compared with the TWIP effect in austenite. Another noticeable phenomenon of the LA-3Si sample is the absent of the 3rd stage strain hardening decrease, which is due to the early fracture of the sample resulted from the embrittlement of the δ -ferrite phase, as will be discussed in the next section.

5.5.3 Effect of Si on fracture mechanisms of the LA-structure

It has been established in Section 5.4 that the PUE values or the degree of necking decreases with higher Si content. The promoting effect of Si on embrittlement has also been observed in single phase ferritic [5.14, 5.65] and austenitic steels [5.15], and explained in terms of the high degree of solid solution strengthening [5.12, 5.14], the void formation behavior associated with dislocation interactions [5.15] and the formation of ordered phase [5.12, 5.65]. Compared with the LA-0Si sample, the decreased PUE value in the LA-1Si sample (Fig. 5.4 (b)) can be explained by the solid solution strengthening effect of Si. It was also proposed by Koyama et al. [5.15] that the reduced austenite SFE by Si could result in an increasing rate of dislocation density and promote vacancy formation, thus promoting the so-called dislocation/dislocation

interaction-induced vacancy/void formation. This can be reflected by the smaller dimple size in the LA-1Si sample, since the voids grown from vacancies are smaller than those grown from other sources such as inclusions [5.15]. Further, the fracture of the LA-0Si and LA-1Si sample is mainly caused by the void formation at the α/α' interfaces (Fig. 5.11 (b)). It is expected that the stress/strain concentrations at the interfaces is higher in the LA-1Si sample due to the more heterogeneous deformation, which might accelerate the void nucleation, growth and coalescence. One can also argue that the occurrence of the PLC phenomenon associated with DSA in the LA-1Si sample can result in the reduced necking [5.66]. However, Si also reduces the PUE value of the HA-structure where the PLC effect occurs in both samples; this suggests that the PLC effect is not the main reason for the reduced PUE value in the LA-1Si sample.

Nevertheless, the post-uniform elongation is only slightly decreased with Si level increasing from 0 to 1 wt.%, and the fracture modes of the 0Si and 1Si samples are still dimpled fracture. However, when the Si content increases to 3 wt.% (i.e. the LA-3Si sample), the fracture surface consists of both dimple and cleavage/quasi-cleavage behaviors, and the cleavage region is associated with δ -ferrite (Fig. 5.10). The micro-cracks observed inside the δ -ferrite (Fig. 5.11 ($c_3\sim c_4$)) also suggest that the δ -ferrite phase is brittle. In Chapter 4, we observed similar embrittlement of δ -ferrite in the hot rolled and annealed 3Si steel, and we attributed this to its very large grain size (110~120 μ m) and high enrichment of Si. Here we demonstrate that even the grain size of δ -ferrite is successfully reduced to ~10 μ m by cold rolling and annealing, the phase still shows a high degree of embrittlement. In order to investigate the origin of this embrittlement, TEM analysis was conducted on the δ -ferrite and the results are shown in Fig. 5.15. The diffraction pattern of δ -ferrite clearly shows the formation of B2 (FeSi type) ordered phase, which is promoted by the high Si and Al contents. This ordering effect can induce the formation of dissociated superlattice dislocations and the correlated high stress concentration [5.65], thus embrittling the δ -ferrite phase.

Another noticeable cracking location is the interface of δ -ferrite and γ/α' mixed phase (Fig. 5.11 (c₂)); micro-cracks at this location are generally along the tensile direction. The different mechanical properties between δ -ferrite and austenite can produce a large plasticity mismatch between the two phases and shear stresses around the interfaces, which tends to nucleate cracks. Since the interface of δ -ferrite and γ/α' mixed phase is generally continuous over a long range, the growth of cracks at this location will encounter few obstacles and occur very fast; this might be another reason for the embrittlement of the LA-3Si sample. In addition, the crack formation develops a significant local stress triaxiality near the crack tips, which can accelerate the void growth and coalescence inside the neighboring γ/α' mixed phase [5.66]. Sometimes, microcracks penetrate into the surrounding γ/α' (Fig. 5.11 (c₄)), which might induce the quasi-cleavage fracture of the γ/α' mixed phase.

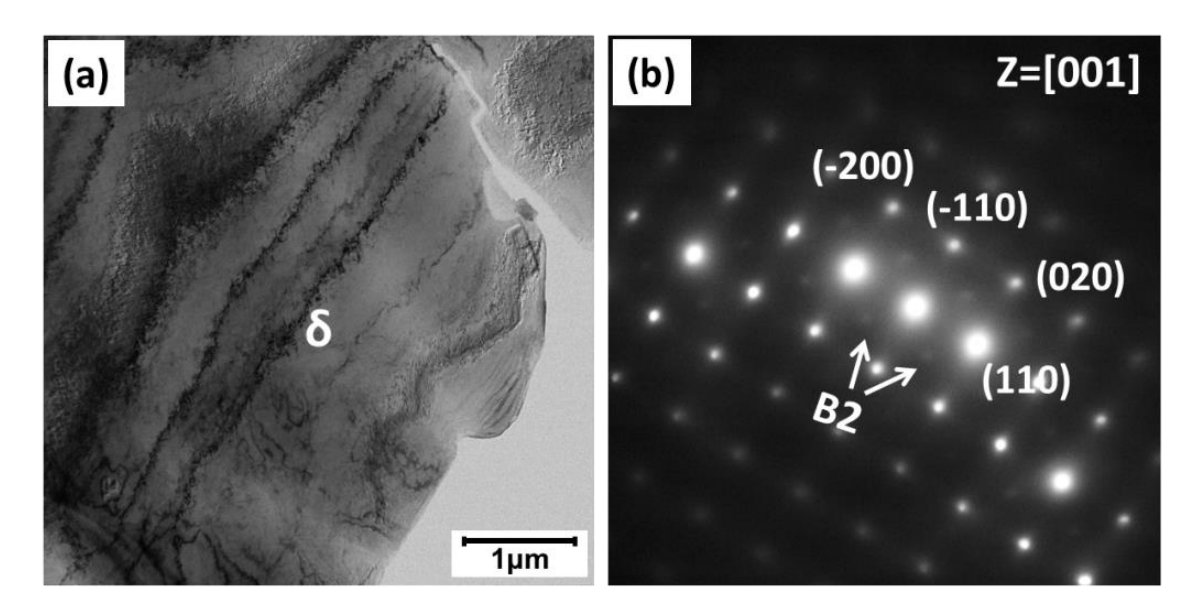


Fig. 5.15 (a) TEM bright field images and (b) selected area diffraction (SAD) pattern of δ -ferrite in the LA-3Si sample.

5.6 Conclusions

In the present study, the detailed deformation behavior and fracture mechanisms of austenite-ferrite duplex medium Mn steel with different Si additions was investigated, with particular emphasis on two variants of austenite fraction, lower austenite (LA) fraction of ~30 % and higher austenite (HA) fraction of ~45 %. The main conclusions can be summarized:

- 1. Silicon raised the austenite transition temperatures and enlarged the ferrite-austenite two phase domain. 3 wt.% Si added in the steel resulted in the formation of a large fraction of δ-ferrite, which remained coarse grained after intercritical annealing. Similar austenite-ferrite duplex microstructures with fixed austenite fractions and C, Mn, Al contents were produced for different Si-alloyed steels by controlling annealing temperatures. All the investigated samples showed a coupled TRIP and TWIP effect during tensile straining.
- 2. For the LA-structure, the tensile strength was only slightly changed by Si, whereas the total and uniform elongation was significantly influenced, with a first increase and then decrease trend with increasing Si contents. This was related to the different strain hardening behavior, resulted from the difference of strain distributions between austenite and ferrite and deformation twinning in austenite for different Si-alloyed samples. The enhanced strain partitioning between austenite and ferrite in the LA-1Si sample was believed to be the main reason for its high strain hardening rate. For the high Si sample (LA-3Si), the density and fraction of deformation twins were much higher, and secondary twins were activated during deformation. This resulted in a more active TWIP effect in the austenite and a higher strain hardening rate at high strain levels compared with the LA-0Si sample.
- 3. The mechanical property of the HA-structure was not sensitive to the Si content. Strain partitioning was only slight for this microstructure, due to the rapid martensite transformation at the beginning of deformation. The different strain hardening rate between the HA-0Si and

HA-1Si sample resulted from the different kinetics of strain-induced α' -martensite formation after yielding (i.e. the Lüders strain).

- 4. The post-uniform elongation decreased with increasing Si content. The lower Si (LA-0Si/1Si) samples were ductile with dimpled fracture, and voids formed mainly at the α/α' interfaces. However, the higher Si alloy (LA-3Si) underwent premature fracture during tensile tests, and the fracture surface consisted of both dimple and cleavage/quasi-cleavage features. The failure of the LA-3Si sample was governed by the cracking in the brittle δ -ferrite phase or along the interfaces of δ -ferrite and γ/α' mixed phase. The embrittlement of δ -ferrite in this sample was due to the formation of B2 ordered phase.
- 5. The significance of this work also lies in revealing the fact that austenite characteristics (fraction, size, stability and deformation mechanisms) are not the single factors controlling the mechanical properties of ferrite-austenite duplex medium Mn steels. The condition of the ferrite phase and the interactions between austenite and ferrite in terms of strain partitioning also play important roles for achieving better mechanical performances.

5.7 References

- [5.1] S. Lee, B.C. De Cooman, Annealing temperature dependence of the tensile behavior of 10 pct Mn multi-phase TWIP-TRIP steel, Metallurgical and Materials Transactions A, 45 (2014), 6039-6052.
- [5.2] P. Gibbs, E. De Moor, M. Merwin, B. Clausen, J. Speer, D. Matlock, *Austenite stability effects on tensile behavior of manganese-enriched-austenite transformation-induced plasticity steel*, Metallurgical and Materials Transactions A, 42 (2011), 3691-3702.
- [5.3] S. Lee, Y. Estrin, B.C. De Cooman, *Constitutive modeling of the mechanical mroperties of V-added medium manganese TRIP steel*, Metallurgical and Materials Transactions A, 44 (2013), 3136-3146.
- [5.4] M.I. Latypov, S. Shin, B.C. De Cooman, H.S. Kim, *Micromechanical finite element analysis of strain partitioning in multiphase medium manganese TWIP+TRIP steel*, Acta Materialia, 108 (2016), 219-228.
- [5.5] S. Lee, B.C. De Cooman, On the selection of the optimal intercritical annealing temperature for medium Mn TRIP steel, Metallurgical and Materials Transactions A, 44 (2013), 5018-5024.
- [5.6] R.L. Miller, *Ultrafine-grained microstructures and mechanical properties of alloy steels*, Metallurgical Transaction, 3 (1972), 905-912.
- [5.7] T. Furukawa, H. Huang, O. Matsumura, *Effects of carbon content on mechanical properties of 5% Mn steels exhibiting transformation induced plasticity*, Materials Science and Technology, 10 (1994), 964-970.
- [5.8] H. Luo, J. Shi, C. Wang, W. Cao, X. Sun, H. Dong, *Experimental and numerical analysis on formation of stable austenite during the intercritical annealing of 5Mn steel*, Acta Materialia, 59 (2011), 4002-4014.
- [5.9] D.W. Suh, S.J. Park, T.H. Lee, C.S. Oh, S.J. Kim, *Influence of Al on the microstructural evolution and mechanical behavior of low-carbon, manganese transformation-induced-plasticity steel*, Metallurgical and Materials Transactions A, 41 (2010), 397-408.
- [5.10] O. Grässel, L. Krüger, G. Frommeyer, L.W. Meyer, *High strength Fe-Mn-(Al,Si) TRIP/TWIP steels development-properties-application*, International Journal of Plasticity, 16 (2000), 1391-1409.
- [5.11] H. Choi, S. Lee, J. Lee, F. Barlat, B.C. De Cooman, *Characterization of fracture in medium Mn steel*, Materials Science and Engineering: A, 687 (2017), 200-210.
- [5.12] Y.U. Heo, Y.Y. Song, S.J. Park, H.K.D.H. Bhadeshia, D.W. Suh, *Influence of silicon in low density Fe-C-Mn-Al Steel*, Metallurgical and Materials Transactions A, 43 (2012), 1731-1735.
- [5.13] T. Furukawa, Dependence of strength-ductility characteristics on thermal history in low

- carbon, 5 wt-% Mn steels, Materials Science and Technology, 5 (1989), 465-470.
- [5.14] K.D. Sibley, N.N. Breyer, *The effect of silicon on the impact and tensile properties of low-carbon steels*, Metallurgical Transactions A, 7 (1976), 1602-1604.
- [5.15] M. Koyama, T. Sawaguchi, K. Tsuzaki, Effects of Si on Tensile Properties Associated with Deformation-Induced ε-Martensitic Transformation in High Mn Austenitic Alloys, Materials Transactions, 56 (2015), 819-825.
- [5.16] K. Jeong, J.E. Jin, Y.S. Jung, S. Kang, Y.K. Lee, *The effects of Si on the mechanical twinning and strain hardening of Fe–18Mn–0.6C twinning-induced plasticity steel*, Acta Materialia, 61 (2013), 3399-3410.
- [5.17] N. Fonstein, *The effect of chemical composition on formation of ferrite—martensite structures and mechanical properties of dual-phase steels*, in: Advanced High Dtrength Sheet Steels: Physical Metallurgy, Design, Processing, and Properties, Springer International Publishing, 2015, 139-181.
- [5.18] J.Y Koo, G. Thomas, *Design of duplex Fe/X/0.1C steels for improved mechanical properties*, Metallurgical Transactions A, 8 (1977), 525-528.
- [5.19] S. Hironaka, H. Tanaka, T. Matsumoto, *Effect of Si on mechanical property of galvannealed dual phase steel*, Materials Science Forum, 638-642 (2010), 3260-3265.
- [5.20] P.J. Gibbs, B.C. De Cooman, D.W. Brown, B. Clausen, J.G. Schroth, M.J. Merwin, D.K. Matlock, *Strain partitioning in ultra-fine grained medium-manganese transformation induced plasticity steel*, Materials Science and Engineering: A, 609 (2014), 323-333.
- [5.21] B. Sun, F. Fazeli, C. Scott, S. Yue, *Role of Mn and Si on the phase characteristics and mechanical properties of duplex (ferrite plus austenite) medium Mn steels*, Proceedings in ICAS2016 & HMnS2016, Chengdu, China, 2016, 95-98.
- [5.22] R.A. Young: *The Rietveld Method*, International Union of Crystallograhy, Oxford, New York, 1995.
- [5.23] J. Talonen, P. Aspegren, H. Hänninen, Comparison of different methods for measuring strain induced α -martensite content in austenitic steels, Materials Science and Technology, 20 (2004), 1506-1512.
- [5.24] P. Horny, E. Lifshin, H. Campbell, R. Gauvin, *Development of a new quantitative X-ray microanalysis method for electron microscopy*, Microscopy and Microanalysis, 16 (2010), 821-830.
- [5.25] D. Dyson, B. Holmes, *Effect of alloying additions on the lattice parameter of austenite*, The Journal of the Iron and Steel Institute, 208 (1970), 469-474.
- [5.26] B.D. Cullity: *Elements of X-Ray Diffraction*, 2nd edition, Addison-Wesley Publishing Company, 1978, 459.
- [5.27] B. Sun, H. Aydin, F. Fazeli, S. Yue, Microstructure evolution of a medium manganese steel

- during thermomechanical processing, Metallurgical and Materials Transactions A, 47 (2016) 1782-1791.
- [5.28] S.J. Lee, K.S. Park, *Prediction of martensite start temperature in alloy steels with different grain sizes*, Metallurgical and Materials Transactions A, 44 (2013), 3423-3427.
- [5.29] J. Talonen, H. Hänninen, P. Nenonen, G. Pape, Effect of strain rate on the strain-induced $\gamma \rightarrow \alpha'$ -martensite transformation and mechanical properties of austenitic stainless steels, Metallurgical and Materials Transactions A, 36 (2005), 421-432.
- [5.30] K. Nohara, Y. Ono, N. Ohashi, Composition and grain size dependencies of strain-induced martensitic transformation in metastable austenitic stainless steels, Tetsu-to-Hagane, 63 (1977), 772-782.
- [5.31] F. Lecroisey, A. Pineau, *Martensitic transformations induced by plastic deformation in the Fe-Ni-Cr-C system*, Metallurgical and Materials Transactions B, 3 (1972), 391-400.
- [5.32] S.S. Sohn, K. Choi, J.H. Kwak, N.J. Kim, S. Lee, *Novel ferrite–austenite duplex lightweight steel with 77% ductility by transformation induced plasticity and twinning induced plasticity mechanisms*, Acta Materialia, 78 (2014), 181-189.
- [5.33] K. Lee, S.J. Park, Y.S. Choi, S.J. Kim, T.H. Lee, K.H. Oh, H.N. Han, *Dual-scale correlation of mechanical behavior in duplex low-density steel*, Scripta Materialia, 69 (2013), 618-621.
- [5.34] S. Lee, S. Shin, M. Kwon, K. Lee, B.C. De Cooman, *Tensile properties of medium Mn steel with a bimodal UFG* α + γ *and coarse* δ -ferrite microstructure, Metallurgical and Materials Transactions A, 48 (2017), 1678-1700.
- [5.35] J.M. Moyer, G.S. Ansell, *The volume expansion accompanying the martensite transformation in iron-carbon alloys*, Metallurgical Transactions A, 6 (1975), 1785-1791.
- [5.36] P. Jacques, Q. Furn émont, A. Mertens, F. Delannay, On the sources of work hardening in multiphase steels assisted by transformation-induced plasticity, Philosophical Magazine A, 81 (2001), 1789-1812.
- [5.37] D.L. Bourell, A. Rizk, *Influence of martensite transformation strain on the ductility of dual-phase steels*, Acta Metallurgica, 31 (1983), 609-617.
- [5.38] C. Landron, O. Bouaziz, E. Maire, J. Adrien, *Characterization and modeling of void nucleation by interface decohesion in dual phase steels*, Scripta Materialia, 63 (2010), 973-976.
- [5.39] M. Calcagnotto, Y. Adachi, D. Ponge, D. Raabe, *Deformation and fracture mechanisms in fine- and ultrafine-grained ferrite/martensite dual-phase steels and the effect of aging*, Acta Materialia 59, (2011), 658-670.
- [5.40] E. Maire, O. Bouaziz, M. Di Michiel, C. Verdu, *Initiation and growth of damage in a dual-phase steel observed by X-ray microtomography*, Acta Materialia, 56 (2008), 4954-4964.
- [5.41] E. Ahmad, T. Manzoor, K.L. Ali, J.I. Akhter, Effect of microvoid formation on the tensile

- properties of dual-phase steel, Journal of Materials Engineering and Performance, 9 (2000), 306-310.
- [5.42] J. Kadkhodapour, A. Butz, S.Z. Rad, *Mechanisms of void formation during tensile testing in a commercial, dual-phase steel*, Acta Materialia, 59 (2011), 2575-2588.
- [5.43] M.M. Wang, C.C. Tasan, D. Ponge, A.C. Dippel, D. Raabe, *Nanolaminate transformation-induced plasticity–twinning-induced plasticity steel with dynamic strain partitioning and enhanced damage resistance*, Acta materialia, 85 (2015), 216-228.
- [5.44] S. Curtze, V.T. Kuokkala, Dependence of tensile deformation behavior of TWIP steels on stacking fault energy, temperature and strain rate, Acta materialia, 58 (2010), 5129-5141.
- [5.45] A. Dumay, J.P. Chateau, S. Allain, S. Migot, O. Bouaziz, *Influence of addition elements on the stacking-fault energy and mechanical properties of an austenitic Fe–Mn–C steel*, Materials Science and Engineering: A, 483 (2008), 184-187.
- [5.46] S. Allain, J.P. Chateau, O. Bouaziz, S. Migot, N. Guelton, *Correlations between the calculated stacking fault energy and the plasticity mechanisms in Fe–Mn–C alloys*, Materials Science and Engineering: A, 387 (2004), 158-162.
- [5.47] D.T. Pierce, J.A. Jim énez, J. Bentley, D. Raabe, J.E. Wittig, *The influence of stacking fault energy on the microstructural and strain-hardening evolution of Fe–Mn–Al–Si steels during tensile deformation*, Acta Materialia, 100 (2015), 178-190.
- [5.48] K.M. Rahman, V.A. Vorontsov, D. Dye, *The effect of grain size on the twin initiation stress in a TWIP steel*, Acta Materialia, 89 (2015), 247-257.
- [5.49] S. Allain, J.P. Chateau, D. Dahmoun, O. Bouaziz, *Modeling of mechanical twinning in a high manganese content austenitic steel*, Materials Science and Engineering: A, 387 (2004), 272-276.
- [5.50] G.B. Olson, M. Cohen, A general mechanism of martensitic nucleation: Part I. General concepts and the FCC→HCP transformation, Metallurgical Transactions A, 7 (1976), 1897-1904.
- [5.51] G. Lehnhoff, K. Findley, B.C. De Cooman, *The influence of silicon and aluminum alloying on the lattice parameter and stacking fault energy of austenitic steel*, Scripta Materialia, 92 (2014), 19-22.
- [5.52] X. Tian, Y. Zhang, Effect of Si content on the stacking fault energy in γ-Fe–Mn–Si–C alloys: Part I. X-ray diffraction line profile analysis, Materials Science and Engineering: A, 516 (2009), 73-77.
- [5.53] A. Das, *Revisiting stacking fault energy of steels*, Metallurgical and Materials Transactions A, 47 (2016), 748-768.
- [5.54] I. Gutierrez-Urrutia, S. Zaefferer, D. Raabe, *The effect of grain size and grain orientation on deformation twinning in a Fe-22 wt.% Mn-0.6 wt.% C TWIP steel*, Materials Science and

- Engineering: A, 527 (2010), 3552-3560.
- [5.55] A. Sarosiek, W. Owen, *The work hardening of dual-phase steels at small plastic strains*, Materials Science and Engineering, 66 (1984), 13-34.
- [5.56] M. Delinc & Y. Brechet, J. Embury, M. Geers, P. Jacques, T. Pardoen, *Structure-property optimization of ultrafine-grained dual-phase steels using a microstructure-based strain hardening model*, Acta Materialia, 55 (2007), 2337-2350.
- [5.57] S.W. Hwang, J.H. Ji, E.G. Lee, K.T. Park, *Tensile deformation of a duplex Fe*–20Mn–9Al–0.6 C steel having the reduced specific weight, Materials Science and Engineering: A, 528 (2011), 5196-5203.
- [5.58] U. Kocks, H. Mecking, *Physics and phenomenology of strain hardening: the FCC case*, Progress in Materials Science, 48 (2003), 171-273.
- [5.59] I. Gutierrez-Urrutia, D. Raabe, Dislocation and twin substructure evolution during strain hardening of an Fe-22 wt.% Mn-0.6 wt.% C TWIP steel observed by electron channeling contrast imaging, Acta Materialia, 59 (2011), 6449-6462.
- [5.60] L. Samek, E. De Moor, J. Penning, B.C. De Cooman, *Influence of alloying elements on the kinetics of strain-induced martensitic nucleation in low-alloy, multiphase high-strength steels*, Metallurgical and Materials Transactions A, 37 (2006), 109-124.
- [5.61] G.B. Olson, M. Cohen, *Kinetics of strain-induced martensitic nucleation*, Metallurgical Transactions A, 6 (1975), 791-795.
- [5.62] X. Chen, L. Lu, Work hardening of ultrafine-grained copper with nanoscale twins, Scripta materialia 57, (2007), 133-136.
- [5.63] O. Bouaziz, S. Allain, C. Scott, Effect of grain and twin boundaries on the hardening mechanisms of twinning-induced plasticity steels, Scripta Materialia, 58 (2008), 484-487.
- [5.64] J.E. Jin, Y.K. Lee, *Strain hardening behavior of a Fe-18Mn-0.6C-1.5Al TWIP steel*, Materials Science and Engineering: A, 527 (2009), 157-161.
- [5.65] B. Viala, J. Degauque, M. Fagot, M. Baricco, E. Ferrara, F. Fiorillo, *Study of the brittle behaviour of annealed Fe-6.5 wt% Si ribbons produced by planar flow casting*, Materials Science and Engineering: A, 212 (1996), 62-68.
- [5.66] H.Y. Yu, S.M. Lee, J.H. Nam, S.J. Lee, D. Fabrègue, M.h. Park, N. Tsuji, Y.K. Lee, Post-uniform elongation and tensile fracture mechanisms of Fe-18Mn-0.6C-xAl twinning-induced plasticity steels, Acta Materialia, 131 (2017), 435-444.

CHAPTER 6

_

DISCONTINUOUS STRAIN-INDUCED MARTENSITE TRANSFORMATION RELATED TO THE PORTEVIN-LE CHATELIER EFFECT IN A MEDIUM MANGANESE STEEL

Chapter 5 studied the microstructure and mechanical behavior of cold rolled and intercritical annealed medium Mn steels with different Si additions. It was documented in Chapter 5 that some intercritical annealed medium Mn steel samples showed obvious serrations on the flow curves, which was related to the PLC effect associated with DSA. The localized deformation derived from the PLC effect and the strain-induced martensite formation could be interrelated. This chapter specifically focuses on the correlations between the strain-induced martensite formation and the PLC effect in medium Mn steels during tensile testing, using the *in situ* magnetic induction measurements and digital image correlation (DIC). The knowledge can provide some valuable information on the fundamental mechanisms of the PLC and strain induced transformation phenomena in medium Mn steels.

• This chapter has been published as: Binhan Sun*, Nicolas Vanderesse, Fateh Fazeli, Colin Scott, Jianqiang Chen, Philippe Bocher, Mohammad Jahazi, Stephen Yue, "Discontinuous strain-induced martensite transformation related to the Portevin-Le Chatelier effect in a medium manganese steel", Scripta Mater., 133 (2017), 9-13.

6.1 Abstract

The correlation between the strain-induced martensite transformation (SIMT) and the Portevin-Le Chatelier (PLC) effect during tensile testing of a ferrite-austenite duplex medium manganese (Mn) steel was investigated in this study. A discontinuous SIMT phenomenon (D-SIMT) was observed in the steel by *in situ* magnetic induction measurements complemented with *ex situ* X-ray diffraction analysis. This unique behavior was due to the localized martensite formation in the PLC bands forming and propagating continuously during tensile straining. The PLC bands were characterized by the digital image correlation technique and their origin is further discussed.

6.2 Introduction

Strain-induced martensite transformations have been used for some time in designing modern advanced high strength steels (AHSS), such as the low alloy transformation-induced plasticity (TRIP) [6.1], carbide-free bainite (CFB) [6.2], and quenching and partitioning (Q&P) [6.3] steels, due to its role in the enhancement of work hardening and ductility. More recently, medium Mn steels containing 3 to 10 wt.% Mn were developed [6.4-6.6]; the higher Mn content ensures a large fraction of metastable retained austenite available to transform during room temperature deformation, which is the main contributor to the excellent strength-ductility balance of such steels. It is well established that plastic deformation provides new nucleation sites which consist of ε -martensite, stacking fault bundles and mechanical twins [6.7, 6.8], for α '-martensite embryos. As such, the amount of α '-martensite continuously increases with plastic strain at constant temperature; the overall transformation kinetics normally shows a sigmoidal shape [6.5, 6.7]. However, this relation is expected to be changed when the steels undergo inhomogeneous deformation.

It was remarked in the literature [6.5, 6.9] that some plastic instability phenomena such as the Lüders banding and PLC effect, may occur in medium Mn steels. The latter is generally characterized by serrated plastic flow in the tensile stress-strain curves and spatio-temporal organized deformation bands. The PLC effect is also commonly observed in ferritic steels [6.10] and austenitic high Mn twinning-induced plasticity (TWIP) steels [6.11, 6.12] tested at various temperatures and strain rates. Generally, it is proposed to be associated with dynamic strain ageing (DSA), which arises from the dynamic interaction between mobile dislocations and diffusing solute atoms. However, the PLC phenomenon in medium Mn steels is expected to be more complicated due to the multiphase structure and the strain-induced transformation feature; its origin and the correlation with the SIMT in such steels have rarely been studied. To this end, the present work investigates the relationship between the PLC phenomenon and SIMT in a ferrite-austenite duplex medium Mn steel, by a combination of digital image correlation and *in*

situ magnetic induction measurements complemented with ex situ X-ray diffraction analysis.

6.3 Experimental Procedure

The chemical composition of the investigated steel is Fe-0.2C-10.3Mn-2.9Al (in wt.%). The ingot was prepared in a vacuum induction furnace, reheated to 1230 $^{\circ}$ C and hot rolled to $^{\circ}$ 3 mm plates, followed by air cooling to room temperature, producing a predominately martensitic structure. The hot rolled plates were heat treated at 500 $^{\circ}$ C for 2 h in order to temper the martensite phase, after which cold rolling was conducted with a thickness reduction of $^{\circ}$ 50 $^{\circ}$ 6. Samples were then intercritically annealed at 700 and 750 $^{\circ}$ C for 5 min followed by water quenching, in order to produce various austenite conditions; they are referred to as IA-700 and IA-750 in this study for convenience.

Room temperature uniaxial tensile tests were carried out on the annealed specimens at a constant crosshead speed corresponding to a macroscopic engineering strain rate of 6×10^{-4} s⁻¹. The tensile samples were machined according to ASTM E-8 subsize standard (25 mm gage length) and oriented parallel to the rolling direction. Microstructure observations were performed with a field-emission scanning electron microscope (FE-SEM, FEI Inspect F-50).

The change in the fraction of retained austenite due to α' -martensite formation during tensile tests was analyzed by an *in situ* magnetic induction method implemented by a Feritscope (Fischer, FMP 30), combined with *ex situ* X-ray diffraction (XRD) analysis; the analyzed surface areas of the Feritscope and XRD were a 2 mm diameter circle and a 4.8×4.8 mm square, respectively. The probe of the Feritscope was tightly attached to the center of the tensile samples during the tensile testing, and the value was recorded every 2.5 s. Since the Feritscope was initially designed to measure the ferrite content in austenitic steels, it was calibrated in advance by comparing with the values generated by XRD on several prior cold rolled IA-750 samples. A linear relationship with a Pearson correlation coefficient of 0.994 exists between the two

measurements, as was observed by other researchers [6.8].

Digital image correlation (DIC) was used to investigate the localized deformation during tensile testing. Images were acquired with a G-504 Manta digital camera (Allied Vision Technologies GmbH, Stadtroda, Germany) with a telecentric lens at a rate of 9 frames per second. A field of view of ~14×5 mm² was characterized with numerical resolution of 7 µm/pixel. The strain fields were computed using the in-house OpenDIC software [6.13] and post-processed with the image analysis program Fiji [6.14].

6.4 Results and Discussion

Figure 6.1 shows the microstructures of the IA-700 and IA-750 sample, consisting of only ferrite (α) and austenite (γ) with sub-micron grains. The ultra-fine grain size is due to the phase transformation from martensite and static recrystallization concurrently taken place during intercritical annealing [6.6]. The measured fraction of austenite and its equilibrium composition calculated by FactSage 6.4 [6.15] with the FSstel database in the two samples are shown in Table 6.1. It is obvious that the higher annealing temperature increases austenite fraction but decreases austenite C and Mn content; thus, austenite stability is reduced at higher temperatures, as also indicated from the higher Md₃₀ temperature (the temperature at which half of the austenite is transformed to martensite after a strain of 30%) of the IA-750 sample. The lower C and Mn level of the austenite in the IA-750 sample also results in a lower stacking fault energy (SFE) compared with IA-700.

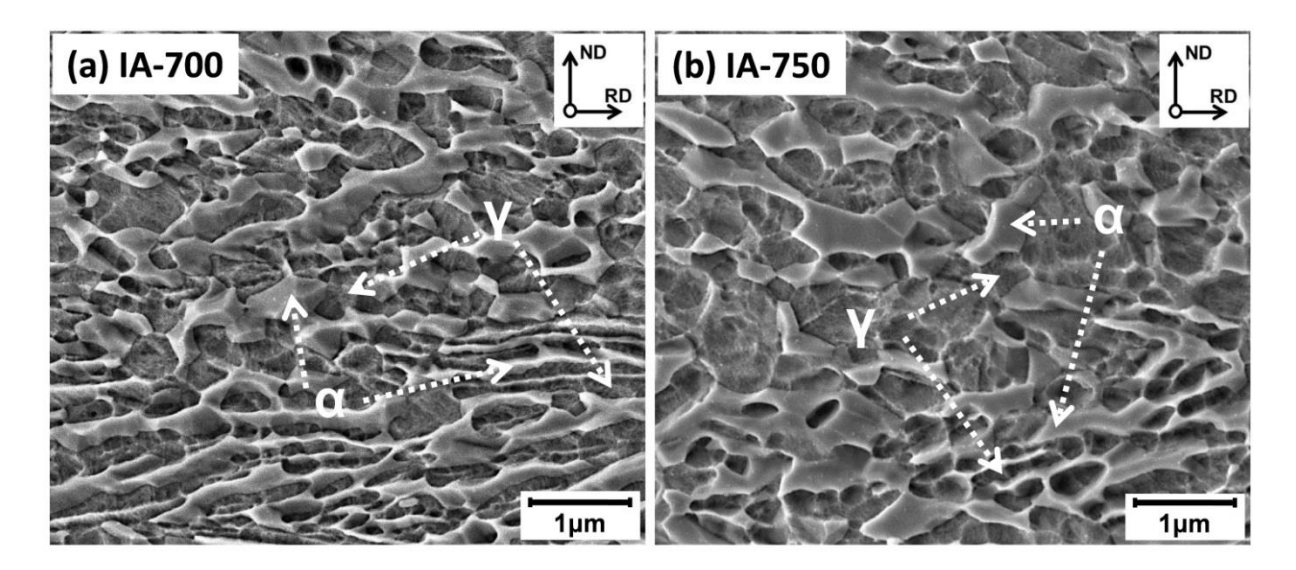


Fig. 6.1 SEM micrographs of the (a) IA-700 and (b) IA-750 sample.

Table 6.1 Fraction and equilibrium composition of austenite in the two samples

Sample	С	Mn	Al	Md (9C) *	Austenite SFE	Austenite Fraction
	(FactSage, wt. %)			$\mathrm{Md}_{30}\left(\mathrm{ extsf{C}} ight)*$	(mJ/m^2) **	(XRD, wt. %)
IA-700	0.32	13.1	2.5	289.2	18.2	33.1 (1.5)
IA-750	0.26	11.6	2.7	334.9	14.4	46.7 (2.5)

^{*} Md_{30} (°C) = 608 - 515C (wt. %) - 12Mn (wt. %) [6.16];

The true stress-strain curve and the work hardening rate of the two samples are shown in Figs. 6.2 (a) and (b). Two distinct flow behaviors can be observed: firstly, the IA-750 sample shows an obvious serrated flow phenomenon, beginning very early after the Lüders strain, whereas no distinct serrations can be observed for the IA-700 sample. Secondly, the IA-750 sample exhibits a much higher rate of work hardening ($d\sigma/d\varepsilon$) than the IA-700 and a larger elongation. The work hardening rate of the IA-750 sample, in general, first increases up to about 4000 MPa and then decreases after about 0.1 strain; however, the IA-700 sample shows a monotonic decrease after yielding. Several oscillations were observed in the work hardening curve of IA-750 (Fig. 6.2 (b)), which were associated with the serrations of the flow curve and the numerical derivative. Figure 6.2 (c) presents the change of transformed austenite fraction during tensile tests, which has been normalized by the initial austenite fraction ($\Delta y/\gamma_0$). The change of austenite fraction is due to the α' -martensite transformation; no ε -martensite was observed after deformation either from the microstructure or the XRD patterns. The value confirms a much more pronounced rate of SIMT (i.e. lower austenite stability) in the IA-750 sample, which is believed to be the main reason for the higher work hardening. However, the SIMT in the IA-750 sample is characterized by a

^{**}Austenite SFE was calculated by the thermodynamic model: $\gamma_{\rm SFE} = 2\rho\Delta G^{\gamma\to\epsilon} + 2\sigma_{\gamma/\epsilon}$, where ρ is the molar density along {111} planes, $\Delta G^{\gamma\to\epsilon}$ is the molar Gibbs energy of the γ to ϵ phase transformation, and $\sigma_{\gamma/\epsilon}$ is the interfacial energy, selected to be 5 mJ/m². The detailed calculation method was described in Curtze's work [6.17], and the thermodynamic data was selected from the references [6.17-6.21].

distinct discontinuous transformation behavior including consecutive pairs of martensite bursts and plateaus. This D-SIMT phenomenon was also confirmed by the XRD experiments, which were carried out on one tensile specimen characterized at very small strain intervals of ~0.005. The fact that this phenomenon only occurs in the IA-750 sample but not the IA-700 sample suggests that it is most likely a material feature pertaining to the composition and stability of austenite.

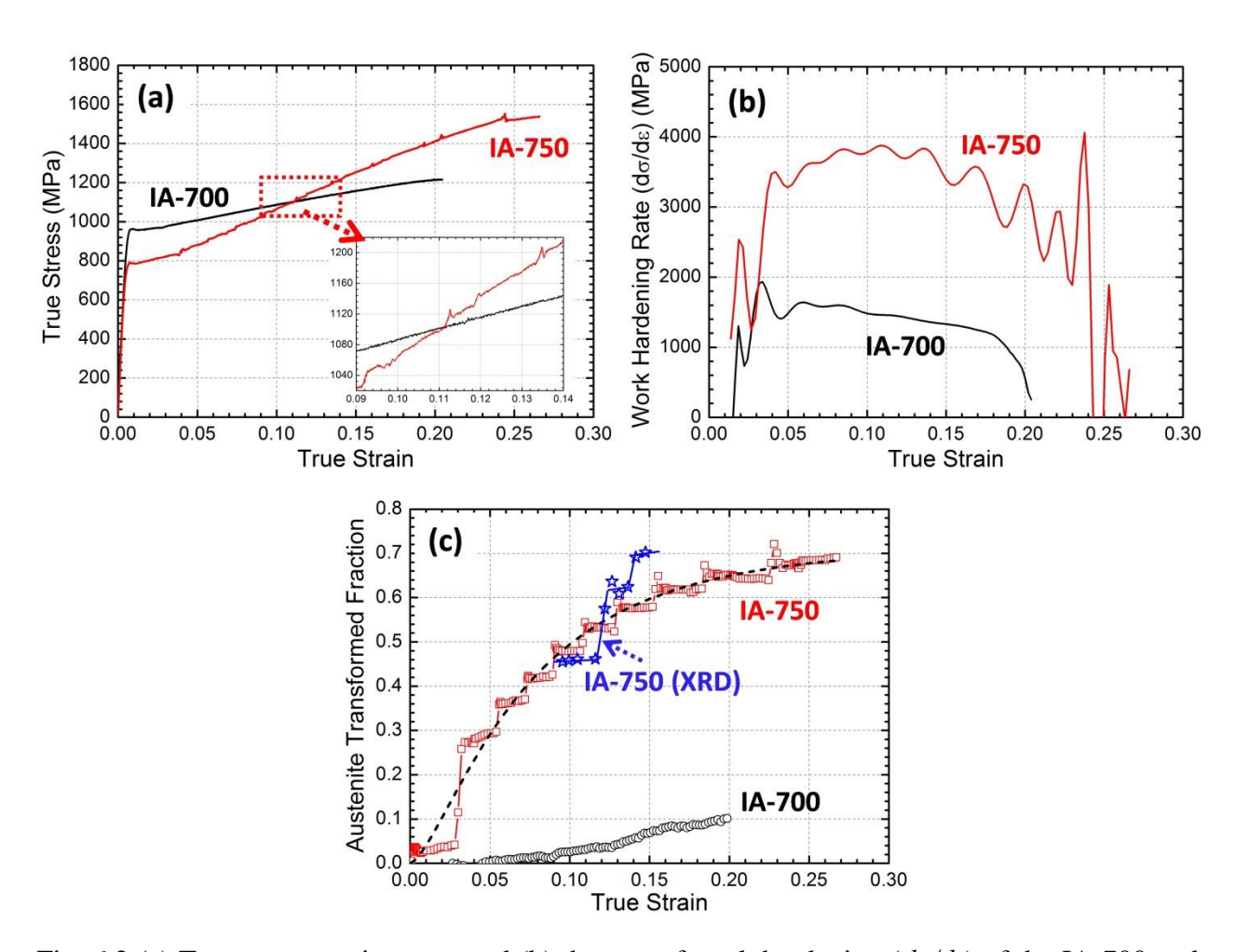


Fig. 6.2 (a) True stress-strain curve and (b) the rate of work hardening $(d\sigma/d\varepsilon)$ of the IA-700 and IA-750 sample; (c) Normalized austenite transformed fraction of the two samples during tensile straining, measured by Feritscope and XRD (the dash line is the fitting curve for the IA-750 sample based on the OC model).

It should be noted that this D-SIMT phenomenon has not been observed with *in situ* phase quantification methods in conventional TRIP steels [6.22] or similar medium Mn steels [6.5, 6.6]. The first martensite burst in the IA-750 sample in Fig. 6.2 (c) was most likely due to the localized SIMT inside the Lüders band, as reported by other researchers [6.9, 6.23], however, in contrast to the current study, the Lüders strain in their work was abnormally large such that the SIMT was almost saturated after the Lüders strain. Some SIMT models such as Burke-Matsumura and Olson-Cohen (OC) models [6.5, 6.7] also failed to explain this discontinuous behavior in the investigated alloy. However, the overall trend of the SIMT in the IA-750 specimen still follows the sigmoidal shape predicted by the OC model; the curve fitting, based on the OC model, yields the following relations between the fraction of martensite and global plastic strain:

$$f_{\alpha'} = [1 - \exp[-1.25 \times [1 - \exp(-11.1\varepsilon)]^{1.51}] \times f_{\gamma},$$

where f_{γ} is the initial austenite fraction before deformation. In order to explain this unique behavior, the strain localization in the IA-750 sample during tensile tests was investigated by DIC. Fig. 6.3 (a) shows the average engineering strain in the DIC analyzed area as a function of deformation time, and several strain maps corresponding to the propagation of two successive PLC bands. The strain behavior oscillates between strain increases and plateaus. It can be clearly observed that the passage of PLC bands in the DIC analyzed area results in strain increases, whereas the plateaus on the strain-time curve indicate that the banding behavior occurs outside of the detected area. The angle between the direction of the bands and the tensile axis is ~64°, which is larger than that reported in TWIP steels (~55°) [6.12]. The corresponding strain profile of the two bands along the tensile axis is plotted in Fig. 6.3 (b), from which the band strain can be estimated to be 0.013 and 0.018 for the 1st and 2nd band, respectively. Such local strains would result in around 2.3% martensite formation, calculated based on the OC model for the IA-750 sample by taking into account the local strain before and after the bands propagation. This number is very similar to the values of the martensite bursts (~2% in average) in the IA-750 sample detected by Feritscope in Fig. 6.2 (c) (excluding the first one which is due to the Lüders

band). This is the first indication that localized SIMT occurs in the PLC bands and moves following the bands propagation.

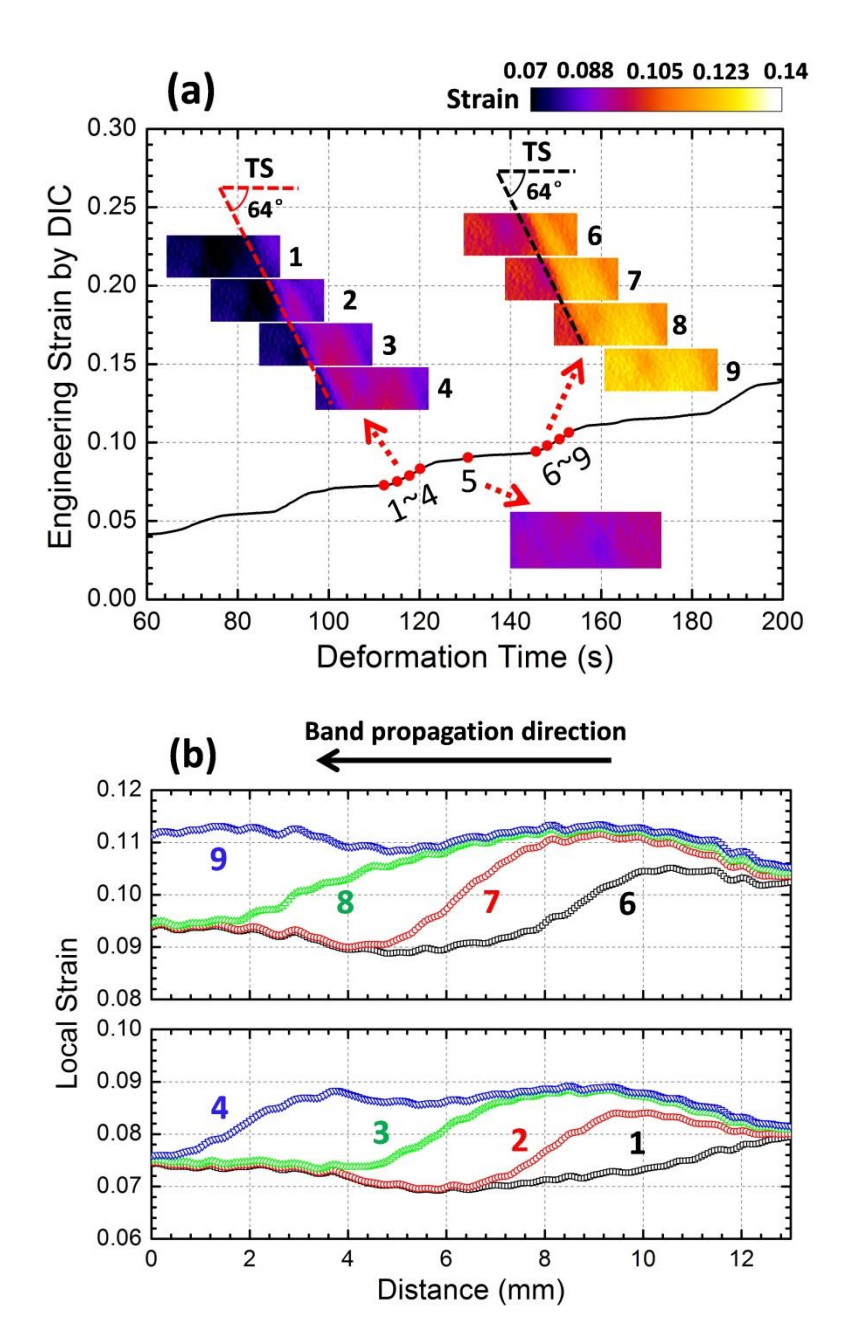


Fig. 6.3 (a) Average engineering strain generated by DIC as a function of deformation time and strain maps corresponding to the propagation of two successive bands in the IA-750 sample; (b) Corresponding strain profiles of the two bands along the tensile axis in the analyzed area.

The macroscopic engineering strain measured by the extensometer and the normalized austenite transformed fraction of the IA-750 sample as a function of deformation time in the plastic deformation range is shown in Fig. 6.4 (a). Ten distinct plateaus were observed and marked in the strain-time curve, indicating that ten PLC bands were initiated and propagated afterwards during tensile straining [6.12]. The same number of steps was also observed in the austenite transformed fraction curve. This also strongly suggests that the mechanism of D-SIMT correlates with the PLC bands, namely martensite forms locally in the PLC bands. Similar D-SIMT behavior was also reported by Hedström et al. [6.24] in a metastable austenite stainless steel using in situ high-energy X-ray diffraction techniques, although the strain localization was not investigated and no detailed explanation was given. However, it was found in his work that the discontinuous transformation event correlates with the stepwise increased lattice strains and peak broadening of the austenite phase, which would essentially occur if deformation bands propagate through the XRD detected area. Therefore, it is probable that the bursts of martensite fraction were derived from the bands passing through the austenite measurement range, followed by plateaus when the band fronts left the detected area. This idea can be verified by calculating the propagation velocity of the deformation bands, separately using DIC, the macroscopic strain-time curve and the transformed austenite-time curve in Fig. 6.4 (a). The propagation velocity can be calculated using the following equation: $v_p = L/\Delta t$, where L is the propagation length or distance, depending on the probed area of the detector (25 mm for the extensometer and 2 mm for the Feritscope), and Δt is the bands propagation time inside the detected areas, which can be read directly from the strain maps, and the two curves (the magnified part of the two curves as illustrated by the inset figure in Fig. 6.4 (a)). The average propagation speeds determined from DIC, the strain-time data and the austenite-time data are around 0.6 mm/s, 0.8 mm/s and 0.7 mm/s, respectively, which are quite comparable. These close values confirm the localized martensite formation in the propagating deformation bands occurred continuously during straining.

The dual phase nature of the investigated steel (ferrite-austenite) increases the complexity of interactions between the possible ongoing mechanisms. PLC bands are generally observed in ferritic structures upon straining of specimens at elevated temperatures where a sufficient diffusivity of solutes to trigger DSA is ensured [6.10]. However, austenitic TWIP steels can show DSA in conjunction with PLC effects at room temperature, which is very likely related to their high Mn content and low SFE [6.11, 6.12]. Considering the similarity in austenite characteristics between the investigated alloy and TWIP steels, it is not surprising to observe the PLC phenomenon in the present study which could most likely stem from the plastic instability of the austenite phase. In fact, the essential condition for the occurrence of localized SIMT in the PLC bands is the sufficient local deformation of austenite. However, the origin of the observed PLC effect in this study is more complex due to the fact that they correlate with the martensite transformation. Hence, the interplay between the SIMT and the PLC phenomenon is valuable to be discussed.

The engineering strain and stress as a function of deformation time for the IA-750 sample is shown in Fig. 6.4 (b), in which serrations in the stress curve can be clearly seen when the PLC bands are initiated and traverse the gage length. It appears that there is a localized SIMT associated with PLC bands, which could probably contribute to the overall work hardening but not the sudden intermittent rises in the overall flow stress. The subsequent small stress drops observed in Fig. 6.4 (b) are also difficult to explain by SIMT. The fact that the IA-700 sample and other medium Mn steels with similar or even higher fractions of SIMT [6.5, 6.6] compared with IA-750 do not show this noticeable serrated flow suggests that the discontinuous SIMT is an outcome of the PLC bands passage but not the reason for the observed PLC behavior and the jerky flow.

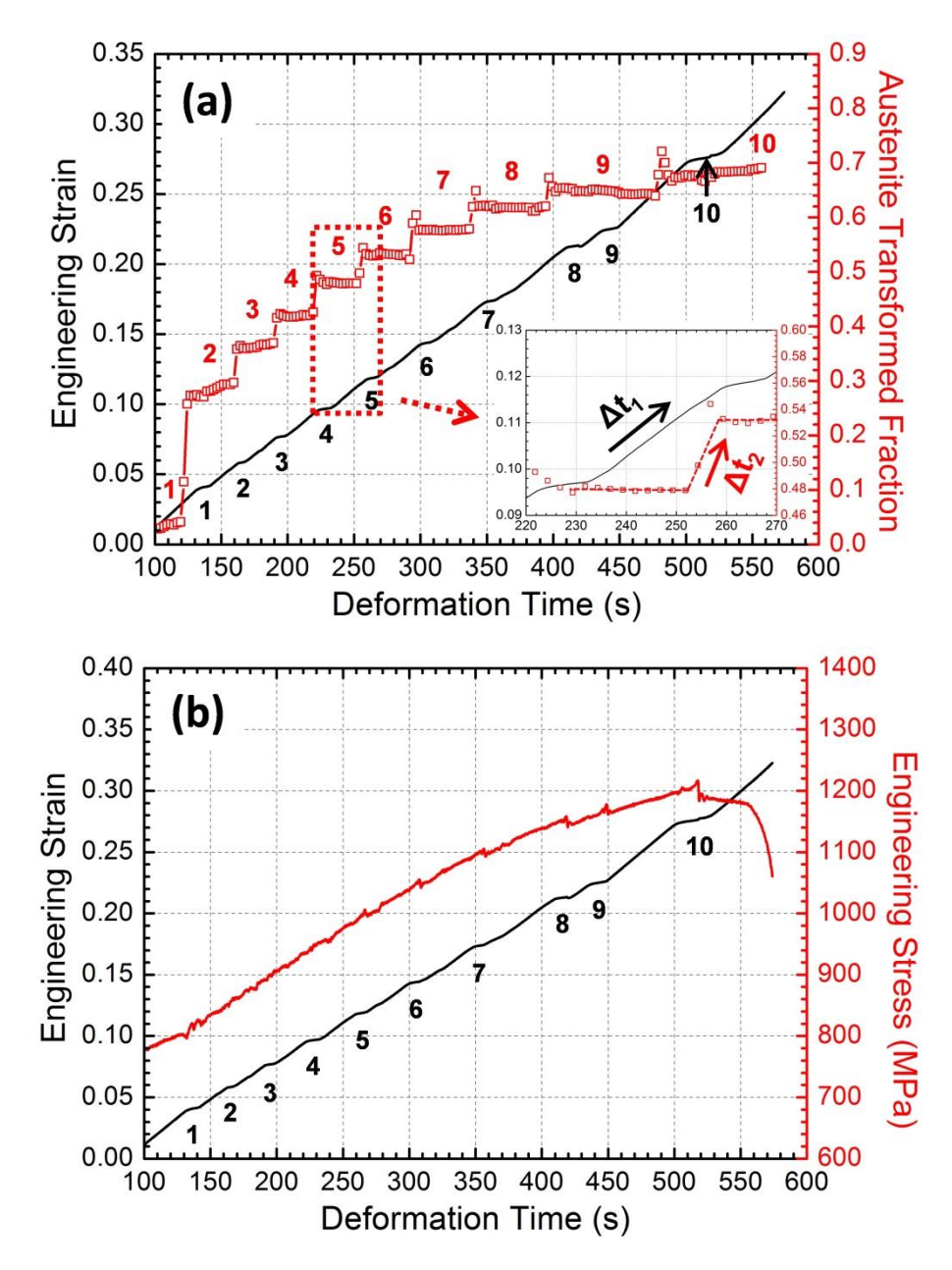


Fig. 6.4 Deformation time dependence of (a) engineering strain and normalized austenite transformed fraction and (b) engineering strain and stress for the IA-750 sample in the plastic deformation range.

On the other hand, the classical DSA theories initially proposed by Cottrell et al. [6.25] and further developed by other researchers [6.26, 6.27] can well explain these serrations; it is postulated that mobile dislocations can temporarily be pinned by interstitial carbon atoms

diffusing towards the dislocation cores. During the pinning time, the flow stress increases until it reaches a critical unpinning value which allows the dislocations to break away and move at high velocities, resulting in apparent drops of the flow stress. In TWIP steels, the estimated bulk diffusivity of C atoms at room temperature is too low to arrest dislocations for conventional DSA to occur [6.11]. The calculated thermal activation energy for PLC in TWIP steels is an order of magnitude lower than that for bulk C diffusion [6.28]. Note that the activation energy determined by conventional analysis for PLC could be inaccurate, due to the imprecise procedure to determine the critical strain for the onset of PLC bands [6.29]. Further, it is difficult to deconvolute the contribution of dislocation glide, twining and martensite formation to the occurrence of PLC in high/medium Mn steels, thus a conclusive estimation of the activation energy for the observed serrated flow might not be trivial. Nevertheless, the DSA effect in TWIP steels was therefore proposed to be associated with carbon reorientation between different interstitial lattice sites along with the interaction between C-Mn complexes and partial dislocations/stacking faults [6.11, 6.12]. The activation energy for the required single atomic jump of C inside the fault region between octahedral and tetrahedral sublattice sites was estimated to be around 0.75 eV [6.11], which is significantly lower than the determined value (1.78 eV) for C bulk diffusion in high Mn steels [6.30]. Higher C and Mn contents increase the probability of C-Mn complexes formation, which tends to impede the glide of dislocation lines thus facilitates the occurrence of DSA. However, the increased SFE due to C and Mn enrichment in austenite decreases the density of partial dislocations and stacking faults, which diminishes the intensity of DSA. As such the serrated flow could be seen merely within a suitable range of austenite compositions. For example, strain instability and tangible serrated flow were not found in the IA-700 sample regardless of its higher C and Mn contents in austenite. It has to be noted that in contrast to IA-750 and due to a lower intercritical annealing temperature, the IA-700 sample was not fully recrystallized, which could potentially influence the observed PLC response; this requires future studies. In addition, the counter effect of martensite formation on PLC in the investigated alloy is also suggested here in terms of: (1) Mobile dislocations might be

additionally pinned by the small martensite embryos until a higher stress is reached to unpin the dislocations. In order to maintain the martensite-induced pinning and associated unpinning process, enough numbers of martensite embryos should be continuously transformed, which is possible for the IA-750 sample due to its lower austenite stability; (2) higher amounts of martensite transformation might have a suppression effect on DSA associated with the trapping of trailing partials [6.31]. These two conflicting effects might further explain why the PLC effect and D-SIMT only occur in a certain range of austenite stability and would disappear in the samples with a higher amount of SIMT (even with lower SFE), which is evidenced in the work of other researchers [6.5].

6.5 Conclusions

In summary, the correlation between the SIMT and strain instability (the PLC effect) in a ferrite-austenite duplex medium Mn steel during tensile tests was investigated, using *in situ* magnetic induction measurements combined with *ex situ* XRD analysis and DIC techniques. It was shown that the SIMT in the IA-750 sample behaved discontinuously, which was due to the localized martensite formation within the PLC bands nucleating intermittently and propagating continuously during tensile straining.

6.6 References

- [6.1] P.J. Jacques, *Phase transformations in transformation induced plasticity (TRIP)-assisted multiphase steels*, in: E. Pereloma and D.V. Edmonds (Eds.), Phase Transformations in Steels, Vol. 2, Woodhead Publishing Ltd., Philadelphia, 2012.
- [6.2] C. Garc á-Mateo, F.G. Caballero, *The role of retained austenite on tensile properties of steels with bainitic microstructures*, Materials Transactions, 46 (2005), 1839-1846.
- [6.3] J.G. Speer, *Phase transformations in quenched and partitioned steels*, in: E. Pereloma and D.V. Edmonds (Eds.), Phase Transformations in Steels, Vol. 2, Woodhead Publishing Ltd., Philadelphia, 2012.
- [6.4] B. Sun, H. Aydin, F. Fazeli, S. Yue, *Microstructure Evolution of a Medium Manganese Steel During Thermomechanical Processing*, Metallurgical and Materials Transactions A, 47 (2016) 1782-1791.
- [6.5] P.J. Gibbs, E. De Moor, M.J. Merwin, B. Clausen, J.G. Speer, D.K. Matlock, *Austenite stability effects on tensile behavior of manganese-enriched-austenite transformation-induced plasticity steel*, Metallurgical and Materials Transactions A, 42 (2011), 3691-3702.
- [6.6] J. Han, S.J. Lee, J.G. Jung, Y.K. Lee, *The effects of the initial martensite microstructure on the microstructure and tensile properties of intercritically annealed Fe–9Mn–0.05 C steel*, Acta Materialia 78, (2014), 369-377.
- [6.7] G.B. Olson, M. Cohen, *Kinetics of strain-induced martensitic nucleation*, Metallurgical Transactions A, 6 (1975), 791-795.
- [6.8] J. Talonen, P. Aspegren, H. Hänninen, Comparison of different methods for measuring strain induced α -martensite content in austenitic steels, Materials Science and Technology, 20 (2004), 1506-1512.
- [6.9] X. Wang, L. Wang, M. Huang, Kinematic and thermal characteristics of Lüders and Portevin-Le Châtelier bands in a medium Mn transformation-induced plasticity steel, Acta Materialia, 124 (2017),17-29.
- [6.10] A.K. Sachdev, *Dynamic strain aging of various steels*, Metallurgical Transactions A, 13 (1982), 1793-1797.
- [6.11] S.J. Lee, J. Kim, S.N. Kane, B.C. De Cooman, *On the origin of dynamic strain aging in twinning-induced plasticity steels*, Acta Materialia, 59 (2011), 6809-6819.
- [6.12] L. Chen, H.S. Kim, S.K. Kim, B.C. De Cooman, *Localized deformation due to Portevin-LeChatelier effect in 18Mn-0.6 C TWIP austenitic steel*, ISIJ Internation, 47 (2007), 1804-1812.
- [6.13] N. Vanderesse, M. Lagac & F. Bridier, P. Bocher, An open source software for the measurement of deformation fields by means of digital image correlation, Microscopy and

- Microanalysis, 19 (2013), 820-821.
- [6.14] J. Schindelin, I. Arganda-Carreras, E. Frise, V. Kaynig, M. Longair, T. Pietzsch, S. Preibisch, C. Rueden, S. Saalfeld, B. Schmid, J. Tinevez, D. J. White, V. Hartenstein, K. Eliceiri, P. Tomancak, A. Cardona, *Fiji: an open-source platform for biological-image analysis*, Nature Methods, 9 (2012), 676-682.
- [6.15] C.W. Bale, E. Bélisle, P. Chartrand, S.A. Decterov, G. Eriksson, K. Hack, I.H. Jung, Y.B. Kang, J. Melan on, A.D. Pelton, C. Robelin, S. Petersen, *FactSage thermochemical software and databases-recent developments*, Calphad, 33 (2009), 295-311.
- [6.16] T.H. Lee, C.S. Oh, S.J. Kim, *Effects of nitrogen on deformation-induced martensitic transformation in metastable austenitic Fe-18Cr-10Mn-N steels*, Scripta Materialia, 58 (2008), 110-113.
- [6.17] S. Curtze, V.T. Kuokkala, Dependence of tensile deformation behavior of TWIP steels on stacking fault energy, temperature and strain rate, Acta materialia, 58 (2010), 5129-5141.
- [6.18] A.T. Dinsdale, SGTE data for pure elements, Calphad, 15 (1991), 317-425.
- [6.19] A. Dumay, J.P. Chateau, S. Allain, S. Migot, O. Bouaziz, *Influence of addition elements on the stacking-fault energy and mechanical properties of an austenitic Fe–Mn–C steel*, Materials Science and Engineering: A, 483 (2008), 184-187.
- [6.20] S. Allain, J.P. Chateau, O. Bouaziz, S. Migot, N. Guelton, *Correlations between the calculated stacking fault energy and the plasticity mechanisms in Fe–Mn–C alloys*, Materials Science and Engineering: A, 387 (2004), 158-162.
- [6.21] O. Grässel, G. Frommeyer, C. Derder, H. Hofmann, *Phase transformations and mechanical properties of Fe-Mn-Si-Al TRIP-steels*, Le Journal de Physique IV, 7 (1997), 383-388.
- [6.22] S. Brauser, A. Kromm, Th. Kannengiesser, M. Rethmeier, *In-situ synchrotron diffraction and digital image correlation technique for characterizations of retained austenite stability in low-alloyed transformation induced plasticity steel*, Scripta Materialia, 63 (2010), 1149-1152.
- [6.23] J.H. Ryu, J.I. Kim, H.S. Kim, C.S. Oh, H.K.D.H. Bhadeshia, D.W. Suh, *Austenite stability and heterogeneous deformation in fine-grained transformation-induced plasticity-assisted steel*, Scripta Materialia, 68 (2013), 933-936.
- [6.24] P. Hedström, U. Lienert, J. Almer, M. Odén, Stepwise transformation behavior of the strain-induced martensitic transformation in a metastable stainless steel, Scripta Materialia, 56 (2007), 213-216.
- [6.25] A.H. Cottrell, B. Bilby, *Dislocation theory of yielding and strain ageing of iron*, Proceedings of the Physical Society. Section A 62 (1949), 49.
- [6.26] A. Van den Beukel, *Theory of the effect of dynamic strain aging on mechanical properties*, Physica status solidi (a), 30 (1975), 197-206.

- [6.27] P. McCormigk, A model for the Portevin-Le Chatelier effect in substitutional alloys, Acta Metallurgica, 20 (1972), 351-354.
- [6.28] S. Allain, P. Cugy, C. Scott, J.P. Chateau, A. Rusinek, A. Deschamps, *The influence of plastic instabilities on the mechanical properties of a high-manganese austenitic FeMnC steel*, International Journal of Materials Research, 99 (2008), 734-738.
- [6.29] A. Roth, T.A. Lebedkina, M.A. Lebyodkin, *On the critical strain for the onset of plastic instability in an austenitic FeMnC steel*, Materials Science and Engineering: A, 539 (2012), 280-284.
- [6.30] T. Shun, C. Wan, J. Byrne, A study of work hardening in austenitic Fe-Mn- C and Fe-Mn-Al- C alloys, Acta Metallurgica et Materialia, 40 (1992), 3407-3412.
- [6.31] M. Koyama, T. Sawaguchi, K. Tsuzaki, Selective appearance of ϵ -martensitic transformation and dynamic strain aging in Fe–Mn–C austenitic steels, Philosophical Magazine, 92 (2012), 3051-3063.

CHAPTER 7

_

CONCLUSIONS

The main objective of the present investigation is to develop a better understanding on the processing-microstructure-property relationship of Al-Si added medium Mn steels with compositions of Fe-0.2C-(7~10)Mn-3Al-(0~3)Si (in wt.%). Specifically, the phase transformation behavior of the hot rolled samples during intercritical annealing (Chapter 3), the microstructural evolution during cold rolling and its effect on cold rollability (Chapter 4), and the detailed deformation and fracture mechanisms of the cold rolled and intercritical annealed samples (Chapter 5&6) were addressed. The following conclusions can be summarized:

1. The phase transformation behavior of two hot rolled medium Mn steels with compositions of Fe-0.2C-7/10Mn-3Al-3Si during intercritical annealing was investigated. The annealing temperature had a substantial influence on the microstructure of the 7Mn steel, including the variation of phase constituents, austenite morphology and composition, the Ms temperature and retained austenite fraction. However, the 10Mn steel was not sensitive to the annealing temperature, showing an invariant ferrite-austenite duplex microstructure with ~50 vol.% austenite regardless of the annealing temperature. The Mn content of austenite in the 10Mn steel also remained nearly unchanged at different annealing temperatures; this higher Mn value enhanced the austenite stability and maintained the Ms temperature below ambient temperature. Both steels possessed a large fraction of δ -ferrite (higher than 50 vol.%) before heat treatments, which was stabilized by Al and Si and maintained intact during intercritical annealing.

Transformation of initial ferrite-pearlite/bainite hot band microstructure into austenite was very rapid upon heating and additional isothermal holding in both steels. Austenite growth was believed to be first controlled by C diffusion in austenite following pearlite/bainite dissolution. Subsequently, Mn atoms tended to redistribute first in ferrite and at later stages in austenite. However, the amount of Mn partitioning and redistribution was too subtle (less than 0.5 wt.%) to result in a tangible change in austenite fraction for the examined annealing time. In addition, a modified thermodynamic database was evaluated using the experimental data. Although the new database achieved a better agreement with the experimental results for the 7Mn steel compared with TCFE7, some discrepancy in the predicted phase fractions and compositions over a range of intercritical temperatures still existed for the examined steels.

- 2. The medium Mn hot bands with same compositions (Fe-0.2C-7/10Mn-3Al-3Si) were intercritical annealed to produce a ferrite-austenite duplex microstructure, followed by a subsequent cold rolling. The 10Mn steel presented a much better cold rollability, which was believed to stem from two factors: (a) the larger strain partitioning in the 10Mn steel resulted in a less deformation accommodated by the brittle δ -ferrite, which delayed or even inhibited the micro-cracking formation inside the ferrite phase. The low ductility of the δ -ferrite was related to its high Si content and large grain size; (b) the deformation twinning (TWIP effect) activated in the 10Mn steel during rolling effectively enhanced the ductility of γ - α ' mixed phase. This showed that deformation twinning presented a superior contribution to the ductility of steels compared with strain-induced martensite.
- 3. The microstructure and the deformation and fracture mechanisms of three cold rolled and intercritical annealed medium Mn steels with different Si additions (Fe-0.2C-10Mn-3Al-0Si/1Si/3Si) were studied in detail. Silicon raised the austenite transition temperatures and enlarged the ferrite-austenite two phase domain. 3 wt.% Si added in the steel resulted in the formation of a large fraction of δ -ferrite, which remained coarse grained after

intercritical annealing. Similar austenite-ferrite duplex microstructures with fixed austenite fractions and C, Mn, Al contents were produced for different Si-alloyed steels by controlling annealing temperatures. All the investigated annealed samples showed a coupled TRIP and TWIP effect during tensile straining.

For the ferrite-austenite duplex structure with a lower fraction of austenite (~30 %), the tensile strength was only slightly changed by Si, whereas the total and uniform elongation was significantly influenced, with a first increase and then decrease trend with increasing Si contents. This was related to the different strain hardening behavior, resulted from the difference of strain distributions between austenite and ferrite and deformation twinning in austenite for different Si-alloyed samples. When the austenite fraction was higher (~45 %), the mechanical property became not sensitive to the Si content. Strain partitioning was only slight for this microstructure, due to the rapid martensite transformation at the beginning of deformation. The different strain hardening rate between the OSi and 1Si sample for this structure resulted from the different kinetics of strain-induced α'-martensite formation after yielding (i.e. the L üders strain).

The post-uniform elongation decreased with increasing Si content. The lower Si (0Si/1Si) samples were ductile with dimpled fracture, and voids formed mainly at the α/α' interfaces. However, the higher Si alloy (3Si) underwent premature fracture during tensile tests, and the fracture surface consisted of both dimple and cleavage/quasi-cleavage features. The failure of the 3Si sample was governed by the cracking in the brittle δ -ferrite phase or along the interfaces of δ -ferrite and γ/α' mixed phase. The embrittlement of δ -ferrite in this sample was due to the formation of B2 ordered phase.

4. The correlation between the strain-induced martensite formation and the PLC effect in a ferrite-austenite duplex medium Mn steel (Fe-0.2C-10Mn-3Al) during tensile tests was investigated, using *in situ* magnetic induction measurements combined with *ex situ* XRD

analysis and DIC techniques. It was shown that the strain-induced martensite formation in the sample annealed at 750 °C behaved discontinuously, which was due to the localized martensite formation within the PLC bands nucleating intermittently and propagating continuously during tensile straining. The PLC phenomenon in medium Mn steels was highly related to the stability of austenite. Based on this, an additional martensite-induced pinning mechanism promoting dynamic straining aging was proposed.

CHAPTER 8

_

CONTRIBUTIONS TO ORIGINAL KNOWLEDGE

The contributions to original knowledge made during the course of this study are summarized as follows:

- 1. The work investigated the phase transformation behavior of high Al-Si medium Mn steels upon intercritical annealing. This aspect has not been addressed in the previous literature, and accurate thermodynamic data for this group of medium Mn steels is currently not available. Such steels present a very different microstructure compared with medium Mn steels with lower Al and Si additions. Therefore, the study provides new information for the microstructural control of such alloys, and the acquired data can also benefit the development of more reliable thermodynamic database for similar steel systems.
- 2. The cold rollability of high Al-Si medium Mn steels and their microstructural evolutions during cold rolling were investigated in this work. It, for the first time, highlighted the critical role of strain partitioning between austenite and ferrite and deformation twinning on the cold rollability or ductility of medium Mn steels. The research can provide some guidelines for processing medium Mn steel sheets of similar compositions or other steels with similar microstructures.
- 3. The research, for the first time, studied the influence of Si on deformation and fracture mechanisms of medium Mn steels. The significance of the work also lies in revealing the fact

that austenite characteristics (fraction, stability and deformation mechanisms) are not single factors controlling the mechanical properties of medium Mn steels. The condition of the ferrite phase and the strain partitioning between austenite and ferrite are also important for achieving better mechanical performances.

4. The work investigated the correlation between strain-induced martensite formation and the PLC effect in medium Mn steels. For the first time, experimental validation was obtained concerning the localized formation of strain-induced martensite in the PLC bands, which provides new insights on the fundamentals of the room temperature PLC or DSA effect in steels.

CHAPTER 9

_

FUTURE WORK

- **1.** A full detailed characterization of the PLC banding behavior in medium Mn steels subjected to different strain rate tensile testing is required, in order to reveal the PLC and DSA mechanisms in such steels. The effect of the localized formation of the strain-induced martensite in the Lüders and PLC bands on the local and overall work hardening behavior should also be analyzed.
- **2.** The effect of different cold rolling parameters on the subsequent intercritical annealed microstructure and mechanical properties is recommended to be investigated.
- **3.** The relative contribution of TRIP and TWIP effect to the work hardening and mechanical property in medium Mn steels needs to be evaluated. This essentially requires a careful quantification of the nano-scaled deformation twins as a function of plastic deformation.
- **4.** A constitutive model describing the flow behavior of medium Mn steels would be the further step to understand the microstructure-property relationship. This model should include various factors such as the strength contribution from phase constituents, dynamic formation of strain-induced martensite and deformation twins, strain partitioning among different phases and the resulted geometrically necessary dislocations (GNDs).

APPENDIX A

_

SUPPORTING INFORMATION TO CHAPTER 5

The change of molar Gibbs energy upon γ to ε phase transformation $(\Delta G^{\gamma \to \varepsilon})$ is calculated using a subregular solution model [A.1]:

$$\Delta G^{\gamma \to \varepsilon} = \Delta G^{\gamma \to \varepsilon}_{chem} + \Delta G^{\gamma \to \varepsilon}_{mg} = \sum_{i} x_{i} \Delta G^{\gamma \to \varepsilon}_{i} + \sum_{ij} x_{i} x_{j} \Delta \Omega^{\gamma \to \varepsilon}_{ij} + \Delta G^{\gamma \to \varepsilon}_{mg} =$$

$$x_{Fe} \Delta G^{\gamma \to \varepsilon}_{Fe} + x_{Mn} \Delta G^{\gamma \to \varepsilon}_{Mn} + x_{Al} \Delta G^{\gamma \to \varepsilon}_{Al} + x_{Si} \Delta G^{\gamma \to \varepsilon}_{Si} + x_{C} \Delta G^{\gamma \to \varepsilon}_{C} + x_{Fe} x_{Mn} \Delta \Omega^{\gamma \to \varepsilon}_{FeMn} + x_{Fe} x_{Al} \Delta \Omega^{\gamma \to \varepsilon}_{FeAl}$$

$$x_{Fe} x_{Si} \Delta \Omega^{\gamma \to \varepsilon}_{FeSi} + \Delta G^{\gamma \to \varepsilon}_{mg}$$
(A.1)

with $\Delta G_{chem}^{\gamma \to \varepsilon}$ and $\Delta G_{mg}^{\gamma \to \varepsilon}$ the chemical and magnetic contribution to the free energy, respectively, x_i and $\Delta G_i^{\gamma \to \varepsilon}$ the molar fraction and molar Gibbs energy of the pure alloying elements, $\Delta \Omega_{ij}^{\gamma \to \varepsilon}$ the excess molar Gibbs energy due to mixing. For $\Delta \Omega_{ij}^{\gamma \to \varepsilon}$, only contributions caused by Fe were considered, whereas contributions of other element interactions as well as all ternary interactions and higher were neglected due to the small values [A.1].

The strain energy term, ΔG_{str} , has recently been evaluated by Lee et al. [A.2] using their experimental data and Eshelby's inclusion theory for Fe-15Mn-xC steel systems. It can be calculated by the following equation [A.2]:

$$\Delta G_{str} = [11.14 \exp(-w_C/0.56) - 3.49]/2\rho \tag{A.2}$$

where wc is C concentration in austenite (wt.%), ρ is the molar density along {111} planes, which can be calculated using the austenite lattice parameter a and Avogadro's constant N as:

$$\rho = \frac{4}{\sqrt{3}} \frac{1}{\alpha^2 N} \tag{A.3}$$

The functions describing $\Delta G_i^{\gamma \to \varepsilon}$ and $\Delta \Omega_{ij}^{\gamma \to \varepsilon}$ were acquired from the literature, as listed in Table A.1. Since the austenite C, Mn and Al contents and lattice parameter a (from XRD data) are similar for the three steels of the LA-structure, their values were averaged from the three samples and used in Eq. (A.1), in order to minimize the effect of the small concentration variations. $\Delta G_{mg}^{\gamma \to \varepsilon}$ was calculated based on the equations and parameters from Curtze's work [A.1]. The interfacial energy $\sigma_{\gamma/\varepsilon}$ was selected to be 5 mJ/m² [A.3].

Table A1 Numerical values and functions used for the calculations (Eq. A1)

Parameter	Function (J/mol)	Source
$\Delta G_{Fe}^{\gamma oarepsilon}$	-2243.38+4.309T	SGTE [A.4]
$\Delta G_{Mn}^{\gamma oarepsilon}$	-1000+1.123T	SGTE [A.4]
$\Delta G_{\!Al}^{\gamma oarepsilon}$	2800+5T	Dumay et al. [A.5]
$\Delta G_{Si}^{\gamma oarepsilon}$	-560-8T	Dumay et al. [A.5]
$\Delta G_C^{\gamma oarepsilon}$	$1246/x_{\text{C}} \times [1-\exp(-24.29x_{\text{C}})]-17.175x_{\text{Mn}}$	Dumay et al. [A.5], Curtze [A.1]
$\Delta arOmega_{FeMn}^{\gamma ightarrow arepsilon}$	$2180+532(x_{\text{Fe}}-x_{\text{Mn}})$	Huang [A.6]
$\Delta\Omega_{FeAl}^{\gamma oarepsilon}$	3328 (at 300K)	Yang et al. [A.7]
$\Delta\Omega_{FeSi}^{\gamma oarepsilon}$	1780	Grassel [A.8]

Reference

- [A.1] S. Curtze, V.T. Kuokkala, Dependence of tensile deformation behavior of TWIP steels on stacking fault energy, temperature and strain rate, Acta materialia, 58 (2010), 5129-5141.
- [A.2] S.J. Lee, J. Han, C.Y. Lee, I.J. Park, Y.K. Lee, *Elastic strain energy induced by epsilon martensitic transformation and its contribution to the stacking-fault energy of austenite in Fe–15Mn–xC alloys*, Journal of Alloys and Compounds, 617 (2014), 588-596.
- [A.3] A. Saeed-Akbari, J. Imlau, U. Prahl, W. Bleck, *Derivation and variation in composition-dependent stacking fault energy maps based on subregular solution model in high-manganese steels*, Metallurgical and Materials Transactions A, 40 (2009), 3076-3090.
- [A.4] A.T. Dinsdale, SGTE data for pure elements, Calphad, 15 (1991), 317-425.
- [A.5] A. Dumay, J.P. Chateau, S. Allain, S. Migot, O. Bouaziz, *Influence of addition elements on the stacking-fault energy and mechanical properties of an austenitic Fe–Mn–C steel*, Materials Science and Engineering: A, 483 (2008), 184-187.
- [A.6] W. Huang, An assessment of the Fe-Mn system, Calphad, 13 (1989), 243-252.
- [A.7] W. Yang, C. Wan, The influence of aluminium content to the stacking fault energy in Fe-Mn-Al-C alloy system, Journal of Materials Science, 25 (1990), 1821-1823.
- [A.8] O. Grässel, G. Frommeyer, C. Derder, H. Hofmann, *Phase transformations and mechanical properties of Fe-Mn-Si-Al TRIP-steels*, Le Journal de Physique IV, 7 (1997), 383-388.

APPENDIX B

_

ABSTRACT OF PUBLISHED ARTICLE RELATED TO THIS RESEARCH

Title: Microstructure Evolution of a Medium Manganese Steel during Thermomechanical Processing

Abstract: An as-cast Fe-0.2C-10Mn-3Si-3Al medium manganese steel with a FADP (ferrite plus austenite duplex) microstructure was subjected to hot compression tests at deformation temperatures within two phase $(\alpha+\gamma)$ range and various strain rates. The microstructure evolution of the experimental steel during hot deformation was investigated. The flow curves were characterized by a discontinuous yielding at the beginning of plastic deformation, followed by a weak work hardening to a peak and a subsequent mild softening stage. Two restoration processes took place during hot deformation, namely dynamic recrystallization (DRX) of austenite and continuous dynamic recrystallization of ferrite. The DRX of austenite was believed to dominate the softening stage of the flow curves. The discontinuous yielding stemmed from the existing Kurdjumov-Sachs (K-S) orientation relationship between ferrite and austenite in the initial undeformed microstructure, which gradually weakened during subsequent deformation.

• This part has been published as: Binhan Sun*, Huseyin Aydin, Fateh Fazeli, Stephen Yue, "Microstructure evolution of a medium manganese steel during thermomechanical processing", Metall. Mater. Trans. A, 47 (2016), 1782-1791.